Mode-Locked Pumped Continuous Wave Ce:LiCAF Lasers

by

Barbara Wellmann

A thesis submitted to Macquarie University
for the degree of Doctor of Philosophy
Department of Physics and Astronomy, Faculty of Science and Engineering
April 2016

MACQUARIE
University
SYDNEY · AUSTRALIA

Typeset in $\LaTeX\,2_{\varepsilon}$.

Except where acknowledged in the customary manner, the material presented in this thesis is, to the best of my knowledge, original and has not been submitted in whole or part for a degree in any university.

Barbara Wellmann

Abstract

At the MQ Photonics Research Centre of Macquarie University the project "Unlocking the Ultraviolet" was launched to establish a new laser platform based on Ce:LiCAF for continuous wave (CW) and ultrafast pulsed operations in the ultraviolet spectral region. The work presented in this PhD thesis was part of this project, with the main aim to develop a deep understanding of the dynamics in Ce:LiCAF lasers that are pumped by a mode-locked source. As a result, a novel mode of operation for CW solid-state lasers was identified and implemented successfully.

When setting up a mode-locked pumped laser system in a way that the normalized cavity length (that is the ratio between the length of the pump resonator and length of the laser cavity) is a rational number, ‘rational-harmonic mode-locking’ is obtained and short laser pulses are generated. In contrast, when the cavity length is detuned away from resonances, modulated continuous output is emitted. Such asynchronous pumping has never been substantially investigated before in solid-state lasers and led to the first ever CW Ce:LiCAF laser. The optimal normalized laser cavity length for asynchronously pumped CW Ce:LiCAF lasers was calculated to be 0.3964, which in the present case is a distance of 120 mm detuned from the third harmonic of the 78.75 MHz pump. The generated CW output featured a residual modulation of only 1% for frequencies below 1 GHz and 4% on faster timescales. The slope efficiency was 20% and the laser threshold 1.37 W. In the set-up used, the transition between CW behaviour and rational-harmonic mode-locking could be achieved easily by adjusting the length of the laser cavity, and thus in addition to the CW output, mode-locked output with pulse repetition rates up to 1.1 GHz was achieved.

Both mode-locked and CW laser output generation have been explored experimentally and theoretically by modelling the laser resonator based on the laser rate equations. Birefringent tuning of the CW Ce:LiCAF laser using single and multiple MgF_2 Brewster plates has also been investigated. Depending on the thickness of the MgF_2 plates used, continuous tuning over a range of up to 13 nm from 284.5 nm to 297.5 nm with a full width at half maximum linewidth of 50 GHz was achieved. By combining MgF_2 plates with etalons, the linewidth of the laser was narrowed down to 2.7 GHz.

Contents

1 Introduction

Since the first laser was demonstrated in 1960 [1] many research groups all over the world have worked on modifying and customising lasers and the characteristics of the achievable light output. As a result an enormously wide variety of lasers has been published over the last 55 years and there is still ongoing further development. The majority of the recent research aims to advance one or more of the crucial laser output parameters: broaden the tunability of the output wavelength, extend the (tunable) laser output to new wavelengths, narrow the output line bandwidth, improve the beam quality, increase the output power, and in pulsed laser systems shorten the pulse duration, increase the pulse repetition rate or heighten the pulse peak power.

Given that all these parameters are dependent on each other, by improving one of them the others may shift as well. While some of these dependencies are beneficial (e.g. the pulse peak power usually increases when the pulse duration decreases [2]), others are disadvantageous (e.g. high pulse repetition rates generally result in a fairly limited pulse energy [3]). Accordingly diverse laser platforms have emerged over time, each with a different focus area and with different advantages to improve distinctive laser output parameters. At the MQ Photonics Research Centre of Macquarie University the project "Unlocking the Ultraviolet" was launched to establish a new laser platform based on Ce^{3+}:$LiCaAlF_6$ (Ce:LiCAF) for continuous wave (CW) and ultrafast pulsed operation in the ultraviolet (UV) spectral region. The project was based on the results of the first ever mode-locked pulse Ce:LiCAF lasers, which were demonstrated by the LASER Group of the MQ Photonics Research Centre in 2009 [4, 5], and includes both CW pumped and mode-locked pumped Ce:LiCAF lasers. The work presented in this PhD thesis was part of "Unlocking the Ultraviolet", with the main aim to develop a deep understanding of the dynamics in Ce:LiCAF lasers that are pumped by a mode-locked source. Depending on the specific configuration of the Ce:LiCAF laser, such mode-locked pumped lasers can either generate short laser pulses when set-up for rational-harmonic mode-locking, or CW output when pumped asynchronously. The transition between mode-locked and CW behaviour can be achieved easily by adjusting the length of the laser cavity.

Both pulsed and CW UV lasers play a crucial role in scientific research and can be found in many applications and measurement tools. A large variety of atoms, molecules, and compound materials feature unique absorption bands in the UV, and thus the demand for UV lasers to detect, probe and control these materials is growing continuously. CW UV lasers can for example be used in high-resolution spectroscopy [6, 7], atom cooling and trapping [8, 9], and biological applications like flow cytometry for the detection of pathogens [10]. Ultrafast UV-pulses are also of high significance. They can, for example, greatly improve the time resolution of experiments that allows fast temporal characterisation of physical and chemical phenomena. Keller describes this vividly in her Nature article from 2003:

> In the same way that a strobe light at a disco "freezes" the motion of dancers, a mode-locked laser can "freeze" the motion of fast moving objects such as molecules or electrons [...]

By taking "pictures" of fast processes, chemical reactions or physical processes such as electronic transport in semiconductors can be retraced [11, 12]. In [13] femtosecond laser spectroscopy is described as an example of measurements using ultrafast pulses. Another application is the production of nanostructures in solid or glass materials. Traditionally nanosecond Q-switched lasers are used to fabricate patterns in the micrometer range, but more and more companies are changing to shorter pulses since the quality of the ablated holes and structures can be improved immensely when working with ultrafast pulses [14]. In semiconductors "cold" melting has been realised with ultrafast lasers [15] where a solid-to-liquid transition occurs so fast that sample heating can be minimised. Other applications include waveguide writing in bulk glasses [16], two photon laser scanning fluorescence microscopy [17], and medical applications where ultrafast lasers provide a higher resolution in surgery (e.g. corneal surgery [18] and tumor removal [19]). In these medical applications ultrafast pulses also promise to reduce secondary effects because the fluorescence threshold for optical damage decreases with a decreasing pulse duration [20].

This list of significant applications confirms the high value of the new laser platform proposed by "Unlocking the Ultraviolet" for both pulsed and CW lasing in the UV. In previous work Ce:LiCAF has only been used to generate ns and ps laser pulses. During the work presented here it was used to generate stable CW lasing and this thesis is the account of the development, simulation, and characterisation of the first ever mode-locked pumped CW Ce:LiCAF lasers. Chapter 2 provides an overview of some of the interesting history and fascinating developments of laser research relevant to the topic and summarises the principles of mode-locking which is the fundamental technique used in the laser system this thesis is based on. Then a summary of the development of UV lasers and the features of Ce:LiCAF as a laser material are reviewed in chapter 3, and a detailed description of the laser set-up is given in chapter 4. In the following chapters, the results and outcomes achieved during this PhD project are presented. Chapter 5 discusses the dynamics of mode-locked pumped Ce:LiCAF lasers based on simulation results and shows how the laser system can be used to generate short pulses when set up for rational-harmonic mode-locking and CW output when set up for asynchronous pumping. Chapter 6 then provides details about the tunability and linewidth narrowing of the generated CW output. The final Chapter 7 contains a comprehensive conclusion and gives recommendations for future work in Ce:LiCAF lasers. The main results presented in chapters 4 to 6 were also published in international research journals (see appendix A) and presented at prestigious international conferences that are listed in appendix B.

2

Theoretical Background

2.1 Q-Switching

Maiman's ruby laser from 1960 emitted a train of pulses with durations in the order of milliseconds and random fluctuations in intensity [2, 21, 22]. While this behaviour is typical for a free-running laser[1] pumped by a flash discharge, it is unsuitable for many applications and hence the search for stable laser solutions began. Just one year later, Hellwarth described the concept of Q-switching as a method to generate "giant" pulses with durations of about 10 ns [23, 24]. After Hellwarth's introduction of Q-switching, many others used this rather simple technique to produce high intensity pulses (with durations in the order of nanoseconds) and the theory of Q-switching has been reviewed many times over the years (e.g. [25–28]).

The idea of Q-switching is to prevent the initialisation of lasing in the resonator until the population inversion in the gain material has reached a high level (potentially up to the point where it is saturated). Lasing is then enabled abruptly, which causes the stored energy to be

[1] In contrast to a Q-switched or mode-locked laser

depleted rapidly and as a result a short light pulse with a high energy is emitted from the laser. This initial prevention and abrupt enabling of lasing is realised for example by inserting an attenuator in the laser resonator that can be switched on and off quickly. When the attenuator is activated, feedback in the resonator is suppressed by high losses in the cavity and can be expressed with a very low quality factor (Q-factor) of the optical resonator. When switching the attenuator off, losses in the cavity are low, which can be described with a high Q-factor. With the gain being now larger than the loss, lasing occurs. Combined the activation and deactivation of the attenuator modulates the Q-factor of the resonator, which is why the name "Q-switching" arose for this technique.

The Q-switch can be realised with different types of optical switches. These can be categorised in two main types: active Q-switches and passive Q-switches. Active Q-switches are externally controlled attenuators, which means the variable attenuator is operated by an external signal, e.g. an electrical signal. Passive Q-switches are saturable absorbers, which are materials whose transmission depends on the light intensity. This means, the initial loss of the absorber is high, but the material "bleaches" when the intensity of light rises above a certain threshold. This is for example given when a high energy pulse reaches the absorber. When pumped continuously, the gain builds up until threshold is reached when the intracavity field can bleach the saturable absorber. The laser can reach threshold despite the high absorption and a laser field can build up. It saturates the absorption and the laser switches quickly to a high gain condition and thus a short pulse is generated. After the pulse, the absorber reverts to its high-loss state and prevents the lasing until the population inversion reaches a high level again. Hence the laser pulses are self-triggered. The repetition rate can be controlled only indirectly when using passive Q-switches, e.g. by varying the amount of saturable absorber in the laser cavity or by varying the pump power. The materials that can be used as a saturable absorber depend on the wavelength. Typical examples are ion-doped crystals like chromium doped yttrium aluminium garnet (Cr:YAG), bleachable dyes or passive semiconductor devices.

2.2 Mode-Locking

An alternative approach to Q-switching that can be used to obtain even shorter pulses is a mechanism know as "mode-locking". Haus, who in 2000 wrote an invited paper for the IEEE

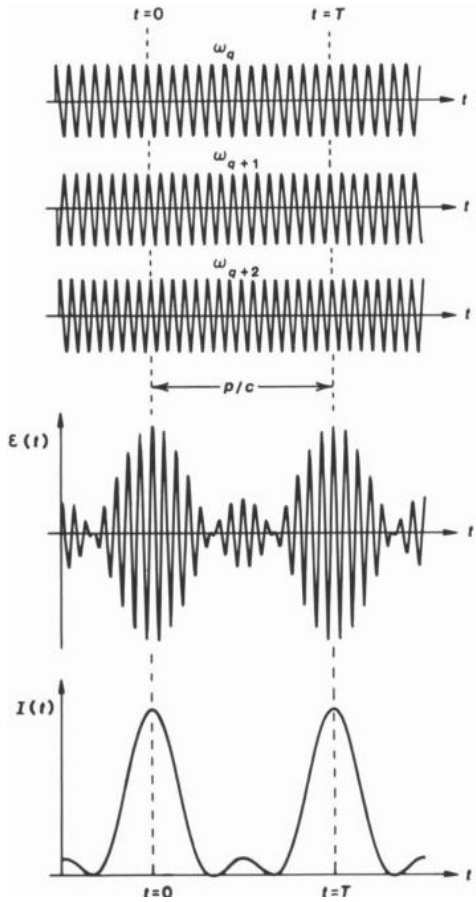

Figure 2.1: Beating of three locked frequencies which are all in phase at the time $t = 0$ [36]

Journal on Selected Topics in Quantum Electronics titled "Mode-Locking of Lasers" [29], summarises the early publications of mode-locking as follows:

> The first indications of mode-locking appear in the work of Gürs and Müller [30, 31] on ruby lasers, and Statz and Tang [32] on He-Ne lasers. The first papers clearly identifying the mechanism were written in 1964 by DiDomenico [33], Hargrove *et al.* [34], and Yariv [35].

The main principle of mode-locking is to use the superposition (also called "beating") of modes, which occurs when modes with a coherence between their phases oscillate simultaneously, to generate pulsed radiation. Figure 2.1 (taken from [36]) illustrates the beating of three equally spaced frequencies (ω_q, ω_{q+1} and ω_{q+2}) which are all exactly in phase at the time $t = 0$. In the middle part of the figure the time dependent field amplitude $\varepsilon\,(t)$ of the total signal (the sum of the three frequencies) is shown. Assuming all three signals have the same amplitude, the peak field amplitude of the superposed signal is three times the amplitude of each signal. Below the field amplitude the time dependent intensity $I\,(t)$ of the signal is

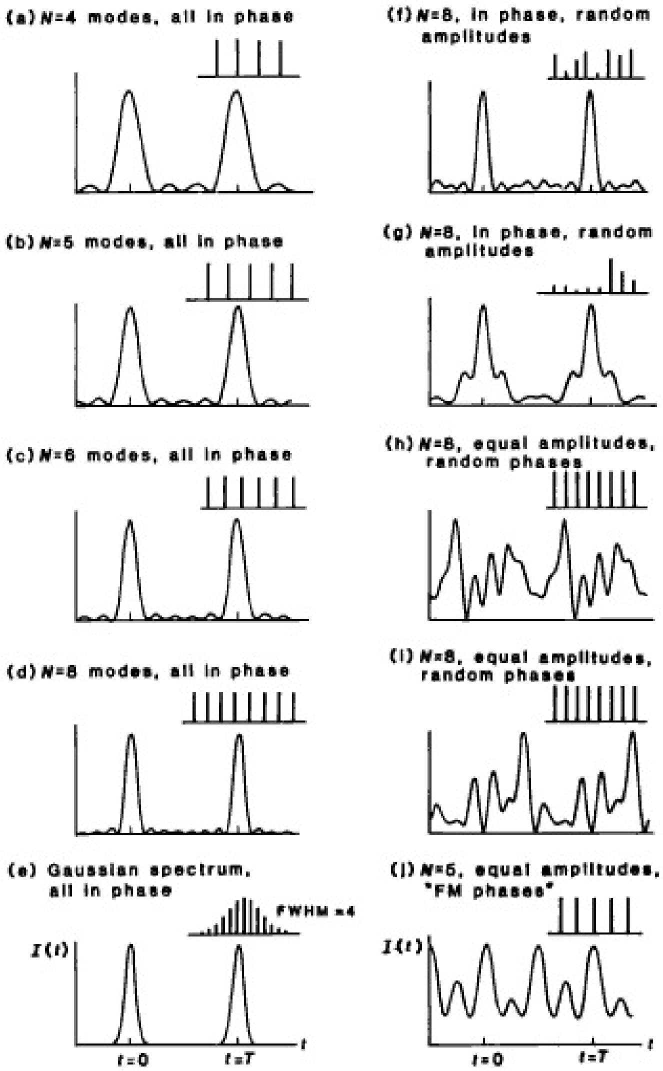

Figure 2.2: Examples of different intensity patterns in time that can be synthesized using N equally spaced frequency components with different relative amplitudes and phase angles. [36]

graphed. Since the peak intensity is proportional to the squared peak field amplitude, it is nine times the intensity of one signal.

An important factor is the fixed relative phase relationship between the oscillating modes - the modes have to be "locked". Otherwise modes with random phase relationships to each other generate outputs with random fluctuations of intensity. Figure 2.2 displays examples of different intensity patterns generated by equally spaced frequencies with different amplitude and phase relationships. Pictures a) to d) show the intensity patterns of N locked modes with the same amplitudes with varying N. Each time there is a primary mode-locked pulse per period and $N - 2$ much weaker subsidiary peaks. The higher N gets, the narrower the primary peaks become and the weaker the subsidiary peaks are. Picture e) shows the total

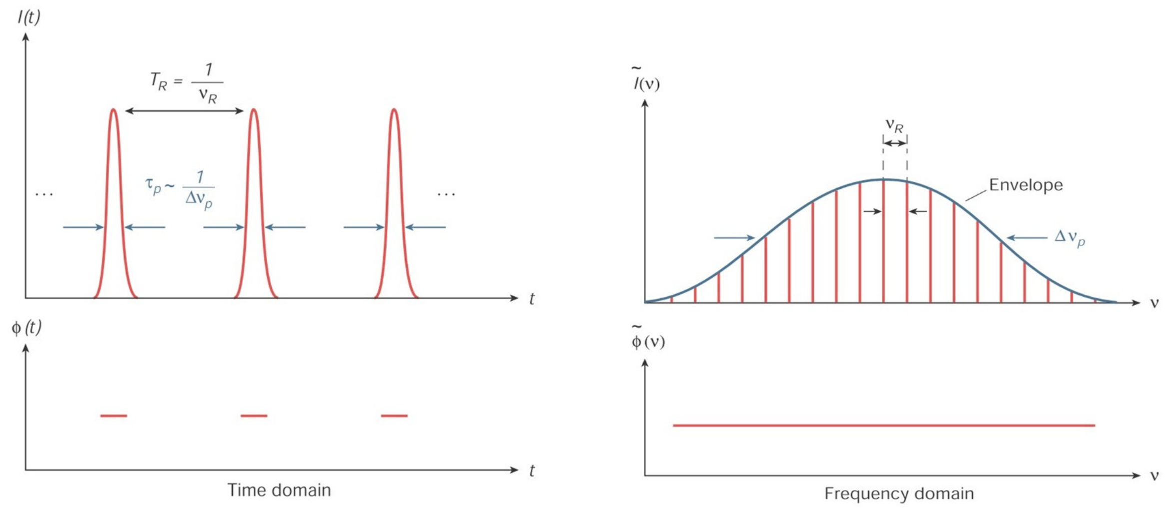

Figure 2.3: Keller 2003 in Nature: schematics of the intensity of mode-locked lasers in the time domain and in the frequency domain [3]

signal output assuming a gaussian shaped frequency input spectrum with all modes locked. As the Fourier transform of a gaussian spectrum is a gaussian pulse in time, the pulses now have a gaussian shape in time and no subsidiary peaks. Picture f) and g) illustrate the total signal with all oscillating modes locked but having different amplitudes. In this case pulses are still generated, but there is an irregular background of sub-pulses, which is higher the more the amplitudes of the modes vary.

Pictures h) and i) demonstrate the total signal when the modes are not locked. Even with all modes oscillating with the same amplitude, the intensity pattern does not show a clear single pulse but a random set of weaker fluctuations instead. Picture j) shows a frequency modulated signal where pulses are generated but the signal does not return to zero between the pulses.

Ultimately, mode-locked lasers generate an equidistant train of pulses in the time domain. The pulse repetition frequency ν_R of this pulse train is inversely proportional to the round-trip time T_R of the laser cavity $\nu_R = 1/T_R$, where T_R is defined by the length l of the laser cavity $T_R = 2l/\nu_g$ (with ν_g being the group velocity of the laser pulse). In the frequency domain mode-locked lasers feature a phase-locked frequency comb with a constant mode spacing that is equal to the pulse repetition frequency ν_R. The pulse duration τ_p in the time domain is inversely proportional to the spectral width of the envelope of the frequency comb of longitudinal modes in the frequency domain. These relationships between the pulse parameters are visualised in figure 2.3 (from [3]).

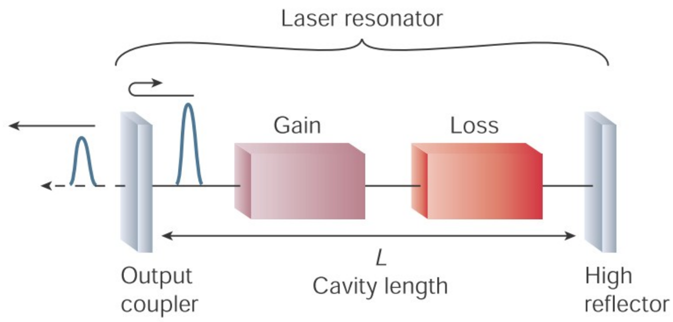

Figure 2.4: Schematic set-up of a mode-locked laser with a gain and a loss element inside a laser resonator [3]

Mode-locking is realised using a similar set-up as for Q-switching (see figure 2.4). A gain and a loss element are induced sequentially in a laser resonator; the difference to Q-switching is that the period of the loss (or gain) modulation must be adjusted carefully to the cavity round-trip time of the laser. Depending on how this modulation of the attenuator is realised, two types of mode-locking are distinguished: active mode-locking and passive mode-locking.

2.2.1 Active Mode-Locking

All early papers on mode-locking described results obtained due to active mode-locking. For active mode-locking, the loss of the laser resonator is changed periodically, e.g. by a modulator that is controlled by an external signal or by pumping the laser resonator with a train of pump pulses instead of a continuous source. In the early days of mode-locking, Hargrove et al. for example modulated the refractive index inside the resonator of a helium-neon laser acoustically at the period of one cavity round-trip time. Thereby they generated trains of pulses spaced by the cavity round-trip time of about 2.5 ns [34]. Commonly the resonator is changed by either modulating the loss of an attenuator or the optical path length (by modulating the refractive index n). As an example, a schematic of active mode-locking via loss modulation of an attenuator is shown in figure 2.5 [3]. The loss is modulated sinusoidally with a frequency ν_m, which is equal to the cavity mode spacing and hence equal to the pulse repetition frequency $\nu_m = \nu_R$. This causes an amplitude modulation of the field and results in a maximum oscillation at the centre frequency ν_0 with sidebands at $\nu_0 \pm \nu_m$. These sidebands are phase locked to the centre frequency. The process of sideband generation cascades and results in a comb of phase-locked modes in the time domain. The saturated gain at steady state

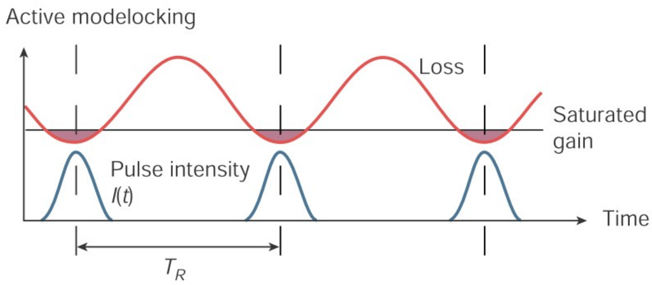

Figure 2.5: Schematic of active mode-locking [3]

only supports net gain around the minimum of the loss modulation and therefore generates short pulses with a period that is equal to $1/\nu_m$ which is equal to the cavity round-trip time T_R. To realise active mode-locking with a loss modulation, acousto-optical or electro-optical modulators are introduced into the laser resonator. Electro-optical modulation is achieved using Pockels cells or Kerr cells, acousto-optical modulation via standing acoustical waves.

Synchronous pumping is another type of active mode-locking and is realised by modulating the gain of the laser medium periodically, instead of modulating the loss in the cavity. This is achieved by using a pulsed laser as the pump source. The pump laser therefore must be a mode-locked laser itself and the repetition rate of the pump pulses must be adjusted to the resonator cavity length. Synchronous pumping (or synchronous mode-locking as it is also called) is commonly used in systems that have a short upper laser level lifetime (like dye, semiconductor or cerium lasers) and in systems that use non-linear frequency conversion processes [37, 38], and is the method we use in this PhD thesis. It is advantageous in our Ce:LiCAF system because it minimises the lasing threshold and provides a direct mode-locking mechanism. In Ti:sapphire lasers it has also been shown that synchronous pumping is compatible with simultaneous Kerr lens mode-locking (KLM, see below), which enables further compression of the output laser pulses [39, 40].

Synchronous pumping requires a precise matching of the laser cavity round-trip time to the pump cavity round-trip time or a harmonic, or rational-harmonic of the pump cavity round-trip time, particularly for ultrafast pulses. It is also possible to set up a laser system in a way that we call asynchronous pumping which basically avoids all laser cavity lengths where rational-harmonic mode-locking is influential and leads to CW laser output with only small residual modulation. This will be discussed in detail in chapter 5 as it is an important feature of the presented work.

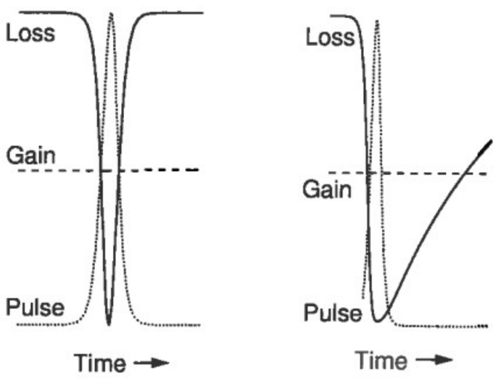

Figure 2.6: Mechanisms of passive mode-locking: left side - with a fast saturable absorber; right side - with a slow saturable absorber [41]

2.2.2 Passive Mode-Locking

For passive mode-locking no external signal is used to modulate the loss in the resonator. It can for example be achieved by introducing a saturable absorber into the laser cavity. Another technique is to use a Kerr medium as the gain medium for Kerr-Lens mode-locking (KLM). The dynamics of KLM can be described as a fast saturable absorber mechanism, which will be discussed later in this section. First consider passive mode-locking realised via a saturable absorber inside the laser cavity. The introduction of such a saturable absorber results in a self-amplitude modulation of the light inside the cavity. The absorber introduces a loss depending on the intensity of the light inside the cavity, which is higher the less the intensity is and smaller the higher the intensity is. A short pulse thus produces a fast loss modulation since the high intensity at the peak of the pulse saturates the absorber quickly and for a short time only. The profile of the pulse depends on the absorption and recovery of the saturable absorber. Figure 2.6 shows two different mechanisms. In the picture on the left side of the figure the mechanism is sketched for an ideal fast saturable absorber. When a light pulse is strong enough the saturable absorber is bleached quickly and the pulse can oscillate in the resonator. After the peak of the pulse the absorber recovers quickly and the resulting pulse shape is ideal and symmetric. In figure 2.6 on the right side, the mechanism with a slow saturable absorber is shown. The initial saturation of the absorber (and hence the reduction of the loss) is fast, followed by a slower recovery of the absorber after the peak of the pulse. A schematic of the resulting pulse pattern is shown in figure 2.7. The circulating pulse saturates the absorber to a level that is sufficient to allow it to oscillate in the resonator,

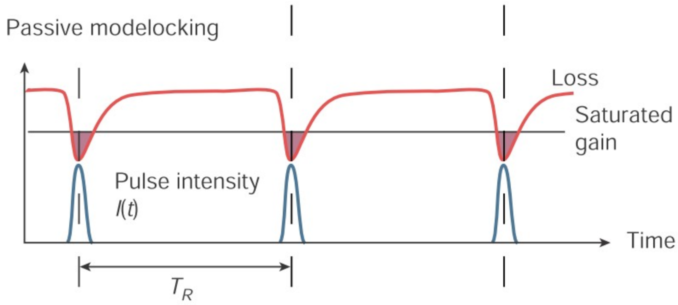

Figure 2.7: Schematic of passive mode-locking with a slow saturable absorber [3]

although any other circulating low-intensity light experiences more loss than gain and thus diminishes during the following cavity round-trips. Passive mode-locking can hence start from normal noise fluctuations in the laser as illustrated in figure 2.8. One noise spike is strong enough to significantly reduce the loss by saturating the absorber above the needed limit and thus will be more strongly amplified during the following cavity round trips, so that the stronger noise spike continues and grows until it reaches steady state, where a stable pulse train has been formed.

The first demonstration of passive mode-locking was in 1965 by Mocker and Collins [44], who proved that the saturable dye that was used for Q-switching in ruby lasers can also function as a saturable absorber for mode-locking. The passively mode-locked pulses were encased by a Q-switch envelope and this type of mode-locking was therefore called "Q-switched mode-locking". The shortest pulses Mocker and Collins achieved in 1965 with this new method were 1 ns long [44]. In the following year, 1966, DeMaria *et al.* published their results of generating pulses shorter than a nanosecond by passively mode-locking a Nd:Glass laser [45]. Given that "ultrafast pulses" usually refer to pulses with durations in the picosecond regime (or faster), DeMaria *et al.* hence demonstrated the first ever ultrafast pulses, which were - like Mocker and Collins pulses - Q-switched. Amplitude-modulation due to Q-switching occurred in all passively mode-locked solid-state lasers until 1992 when saturable absorbers from semiconductors were introduced [3, 46]. As a consequence in the '70s and '80s passively mode-locked dye lasers, which do not exhibit Q-switched mode-locking, dominated the field. In 1972 Ippen, Shank and Dienes generated the first CW saturable absorber mode-locking using a saturable dye in a dye laser [29, 47]. This achievement led them to the successful generation of sub-picosecond pulses in 1974 [48]. Research laboratories all over the world used the engineered reliable dye pulse lasers for time-resolved

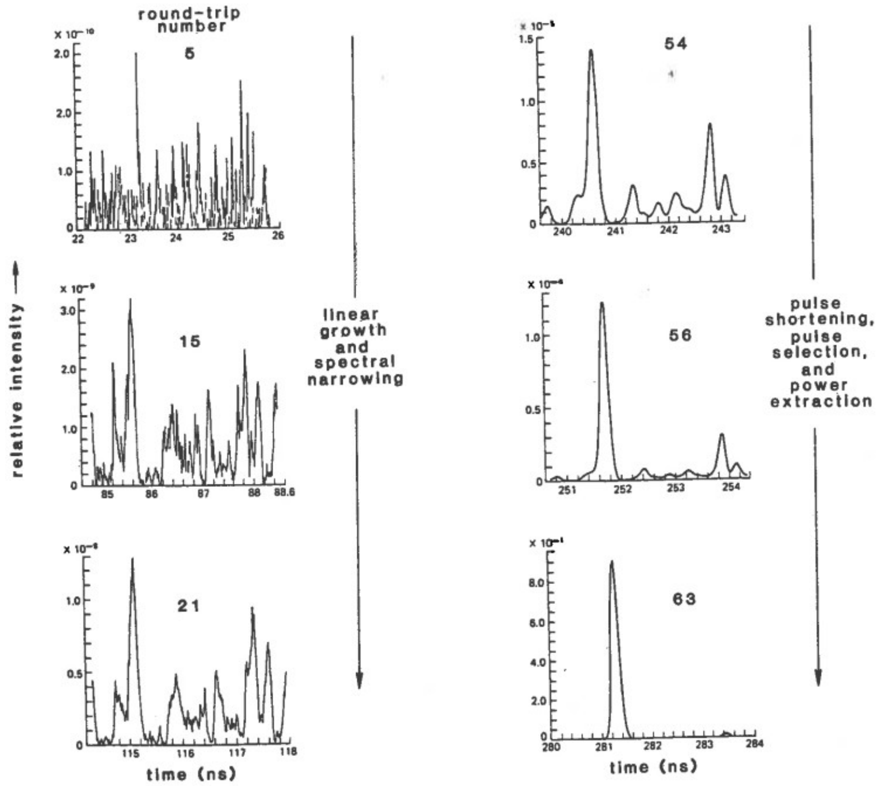

Figure 2.8: Computer simulation of the evolution of a single mode-locked pulse from the initial noise spikes in a passively mode-locked laser. Each plot shows the laser output intensity versus time during one round-trip cavity period; successive plots correspond to the output during successively later round trips. Note changes in the vertical intensity scale (taken from [42], where the results of [43] are summarised)

spectroscopy and scientists were encouraged to develop lasers with shorter and shorter pulse durations. In 1986 Valdmanis generated 27 fs pulses with around 10 mW average power with an ultrafast dye laser [49]. A final record was published 1987 by Fork et al., who used a passively mode-locked dye laser and additional external non-linear pulse compression [50] to achieve 6 fs pulses. The compression technique used was spectral broadening through an optical medium with Kerr nonlinearity followed by recompression.

In the late 1980s a new solid-state laser material was discovered that soon started off a triumphant course: titanium doped sapphire (also written as Ti:sapphire, or Ti:Al_2O_3). Moulton published in 1986 in the Journal of the Optical Society of America his paper "Spectroscopic and Laser Characteristics of Ti:Al_2O_3" and specified Ti:Al_2O_3 to have a broad enough gain bandwidth to support femtosecond pulses with a center wavelength at 800 nm [51]. In 1990 two papers on Ti:sapphire with very surprising results were written.

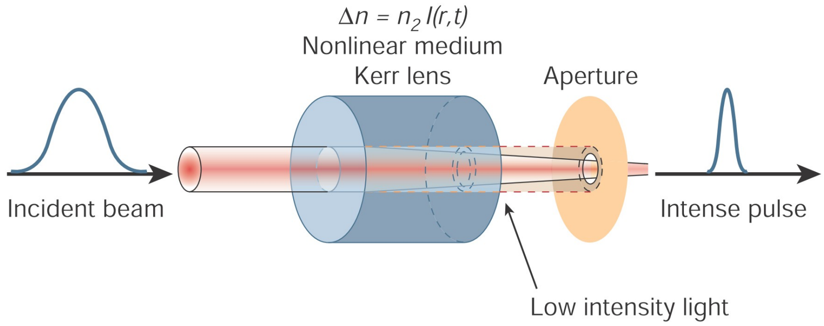

Figure 2.9: Schematic of Kerr-Lens mode-locking [3]

Keller in her 2003 Nature article "Recent Developments in Compact Ultrafast Lasers" wrote:

> In 1990, two important papers were presented at consecutive conferences. First, Ishida et al. [52] presented a passively mode-locked Ti:sapphire laser with an intracavity saturable absorber dye that produced stable 190 fs pulses. Second, Sibbett's group presented 60 fs pulses from a Ti:sapphire laser that appeared not to have a saturable absorber [53]. This second result - in the absence of a visible saturable absorber - had an instant impact on the research community, but the ultrafast laser experts realized that the first result was also very surprising, even though a saturable absorber was present. It was clear that the dye saturable absorber, with a recovery time in the nanosecond range, could not support ultrashort pulses with a Ti:sapphire laser as it could with dye lasers. Sibbett's mode-locking approach [53, 54] was initially termed 'magic mode-locking', and it triggered a major research effort into understanding passive mode-locking of solid-state lasers.

The explanation for "magic mode-locking" was soon found [55, 56] and since then the phenomenon has been known as "Kerr-Lens mode-locking".

With the discovery of KLM, enormous advances in the field of ultrafast lasers were possible. Kerr-Lens mode-locking is a form of passive mode-locking that can be described by the fast saturable absorber mechanism. The saturable absorption is produced by the intensity dependent self-focusing in a nonlinear Kerr medium. The Kerr medium is either the gain medium itself or a separate medium that is introduced to the laser resonator in addition to the gain material. With the gain medium being the Kerr medium, it is positioned at the intracavity focus. A schematic of the principle is shown in figure 2.9. The refractive index of the Kerr material increases with intensity $\delta n = n_2 I(r,t)$, where n_2 is the nonlinear refractive index and $I(r,t)$ the radial- and time-dependent intensity of a short-pulsed laser beam. Due to this refractive index profile the Kerr medium acts as a intensity dependent lens. In "soft aperture" Kerr-Lens mode-locking an increase of the gain is achieved due to an increased overlap of the laser mode with the (strongly focused) pump beam in the gain medium [57]. To obtain soft-aperture Kerr-Lens mode-locking the laser cavity has to be designed accurately near one of the stability limits of the cavity. A further increase of the loss for low intensities can be achieved using a hard aperture inside the cavity as illustrated in figure 2.9.

In contrast to other passive mode-locking techniques Kerr-Lens mode-locking does not normally start by itself from laser noise peaks. An additional starting mechanism is needed to switch the laser from CW to pulsed operation. Generally a short perturbation is used to increase the laser noise briefly, such as jolting one of the laser cavity mirrors mechanically. There have been a few exceptions published where self-started Kerr-Lens mode-locking was achieved [58, 59]. But in theses cases the cavities had to be aligned with sub-millimetre precision and required a very clean environment (since the intracavity losses need to be minimized particularly). Also self-starting Kerr-Lens mode-locking does not provide the features needed for the shortest pulses possible since the Kerr effect tends to be less strong in cavities designed to self-start the mode-locking. In 1992 Keller et al. also explained Ishida's result from 1990 [52] by Kerr-Lens mode-locking: the dye saturable absorber acts as a slow absorber and provides the needed conditions for KLM initialisation [60]. Kerr-Lens mode-locking is well established for Ti:sapphire as well as for Cr:LiSAF and Cr:LiCAF lasers, which use the same crystal host as Ce:LiCAF. It thus can most likely also be achieved in Ce:LiCAF.

Additionally, in 1992 suitable saturable absorbers from semiconductors for solid-state lasers were introduced [46]. They were designed as saturable semiconductor cavity laser mirrors (also known as semiconductor saturable absorber mirrors or SESAMs), where one or more layers of semiconductor saturable absorbers were arranged in a mirror structure [3, 61]. Dielectric Bragg mirrors for dispersion control (also known as chirped mirrors) followed in 1994 [62] and were soon further improved to double chirped mirrors [63, 64] and back-side coated chirped mirrors [65]. KLM, SESAMs and chirped mirrors were the keys to generate stable ultrafast pulse trains with solid-state lasers and as a result Ti:sapphire became more and more important. Soon Ti:sapphire lasers with stable pulses in the two cycle regime were developed (at a center wavelength of 800 nm, an optical cycle only lasts 2.7 fs). In 1999

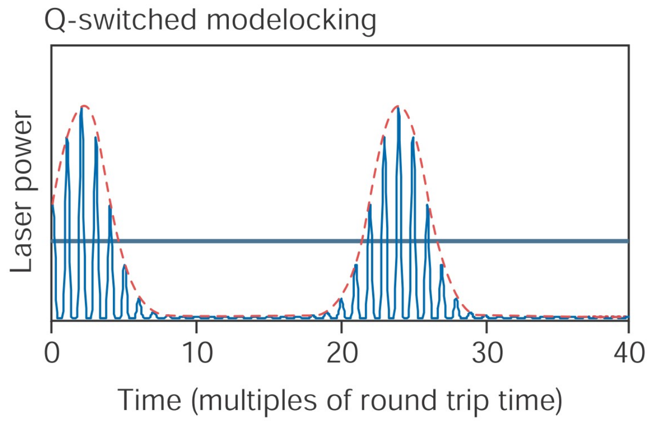

Figure 2.10: Q-switched mode-locking [3]

Sutter et al. demonstrated a SESAM assisted KLM Ti:sapphire laser that produced pulses in the two-cycle regime of only 5.8 fs with an average output power of 300 mW and a repetition rate of 100 MHz [66] and Ell et al. showed in 2001 a Ti:sapphire laser with double chirped mirrors that featured a spectrum extending from 600 nm to 1200 nm and emitting 5 fs pulses with 120 mW average power and 65 MHz repetition rate [67]. Using external non-linear pulse compression high energy pulses from Ti:sapphire lasers could be shortened even more to 4.5 fs [68] or 3.8 fs [69].

Ti:sapphire today is still the most important laser material for ultrashort pulses. The shortest pulses produced using a Ti:sapphire laser to date are just 2.6 fs long. They were achieved by induced phase modulation of 30 fs pulses generated directly from a Ti:sapphire laser [70]. Shorter laser pulses have only been produced by high harmonic generation to generate x-rays. [71–73].

2.2.3 Q-Switched Mode-Locking

As mentioned above, the first reported mode-locked pulse trains were encased in Q-switching envelopes leading to the term "Q-switched mode-locking". Saturable absorbers used for passive mode-locking are the same as the ones used for passive Q-switching. The only difference between a laser set-up for passive mode-locking in contrast to a laser set-up for passive Q-switching is a careful adjustment of the parameters of the saturable absorber to the cavity parameters such as round-trip time and generated intensity. If the adjustment is just slightly mismatched, self-Q-switching occurs in the laser. As a result the mode-locked picosecond pulses are emitted in bunches of pulses modulated with a much longer Q-switched pulse envelope, which occurs at a much lower repetition rate with fairly stable parameters (see figure 2.10). Q-switched mode-locking is normally considered an unwanted phenomenon. In 1999 Hönninger et al. published a comprehensive paper about the dynamics in passively mode-locked lasers [74]. According to Hönninger *et al.* Q-switched mode-locking occurs when the pulse energy is temporarily increased because of noise fluctuations in the laser, which then increases even further because of the stronger saturation of the saturable absorber. This has to be balanced by a stronger saturation of the gain. It is possible to derive stable passive mode-locking above a certain threshold. Hönninger *et al.* showed that Q-switching can be suppressed if $E_{pu}^2 > E_{sat,g}E_{sat,a}\Delta R$, where where E_{pu} is the intracavity pulse energy, $E_{sat,g}$ is the saturation energy of the gain medium, $E_{sat,a}$ is the saturation energy of the saturable absorber, and ΔR is the modulation depth of the reflectivity of the absorber.

2.3 Continuous Wave Lasing

In December 1961, the first continuous wave (CW) laser was built by Javan *et al.* and the results were published early the following year [75]. The laser consisted of a He-Ne gas mixture excited in a microwave discharge tube. Since the gain in the 80 cm long tube was quite small (approximately 1%), the system required highly reflecting mirrors at the operation wavelength of 1153 nm. During the experiments, the laser beam was made visible by a small image converter showing on a screen a bright green spot with a diameter of approximately 1 mm. In subsequent measurements it was determined that the beam divergence was smaller than 1 mrad and that linewidth of the laser $\Delta\nu_l$ was narrowband with $\Delta\nu_l/\nu_l \approx 10^{-10}$. The first CW laser in the visible was presented by White and Rigdenin in 1962, who operated a He-Ne laser in the red at 633 nm [76]. The availability of visible continuous wave laser light promoted the understanding of optimum laser structures and visualized the difference between coherent and incoherent light so that the demonstration of coherence and optical interference became evident [77]. Following these breakthroughs CW lasing has also been achieved in countless other lasers, including other gas lasers [78, 79], solid-state lasers [80], semiconductor lasers [81], and dye lasers [82].

Commonly the term "continuous wave laser" refers to a laser that continuously emits light (as opposed to pulse lasers) and is pumped by a continuous source. This PhD thesis shows that it is also possible to use a mode-locked source to generate continuous laser output.

Some lasers exhibit strong heating of the gain medium when being operated in CW mode. To avoid the resulting unwanted thermal effects, the lasers can be run chopped, also known as quasi-CW. Here, the pump power is only switched on for limited time intervals which can for example be realised by a chopper blade mounted on a rotor. The laser is on for sufficient time to reach steady-state operation in all respects except for thermal consideration.

Since the gain bandwidth of laser materials is normally very broad compared to the longitudinal mode spacing of a laser cavity, free running CW lasers typically operate on multiple longitudinal modes. This is accompanied by intrinsic amplitude and phase noise due to mode-beating between these modes. An effect that can increase the linewidth in CW lasers is inhomogeneous broadening [83]. Both homogeneous and inhomogeneous broadening are phenomena that shape the linewidth of a laser medium, but while homogeneous broadening is caused by events that impact all quantum emitters (that is the atoms, ions or molecules involved in the laser transition) equally, inhomogeneous broadening is related to interactions that affect each quantum emitter differently. Examples of the latter are different Doppler shifts in gas or liquid dye lasers due to the distinctive velocities of the various atoms present or different local electric fields for each quantum emitter in solid-state systems with dopants causing the Stark effect to change the energy levels inhomogeneously [84]. The result is a gain linewidth with a Gaussian profile (as opposed to a Lorentzian profile that is characteristic for a purely homogeneously broadened emission line) [83]. In inhomogeneously broadened lasers, a single laser mode cannot extract the energy stored in all quantum emitters, but just burns a spectral hole in the gain spectrum. Multimode operation is thus hard to prevent [85].

Both Ti:sapphire and Ce:LiCAF feature mainly homogeneous broadening, and do not suffer from spectral hole burning. Efficient single longitudinal mode (SLM) Ti:sapphire lasers can indeed be build. Still, SLM lasing is often obviated due to a different effect - spatial hole burning (SHB). SHB is a saturation effect that is caused by the field distribution of a standing wave. It occurs in the gain medium of bidirectional laser resonators due to the superposition of the counterpropergating light waves. The gain saturation is spatially modulated along the axis of the beam path with antinodes of the standing wave interference pattern (the period of which is half the wavelength) experiencing stronger saturation than nodes [85]. In consequence additional longitudinal modes that have antinodes in different places can be supported and build-up in the oscillator. SHB is most commonly avoided by using a unidirectional ring resonator set-up where no standing wave is formed. Even ring lasers do not tend to operate SLM when running freely, since the difference in gain between closely spaced modes is usually very small. Hence, in order to achieve SLM lasing, the linewidth needs to be controlled and narrowed by suitable optical components like birefringent filters or etalons. In this thesis we discuss the linewidth narrowing of our CW Ce:LiCAF laser using birefringent magnesium fluoride (MgF_2) filters in combination with etalons in chapter 6.

The theoretically achievable minimum laser linewidth is restricted by fundamental quantum processes described by the Schawlow-Townes limit. Schawlow and Townes presented their calculations of the laser linewidth limit $\Delta\nu_l$ in 1940 even before the first laser was built [86]. Their derivation was based on equations to estimate the linewidth of masers, which is limited by thermal fluctuations. Schawlow and Townes basically replaced the temperature dependency of the maser linewidth (given by the Boltzmann constant multiplied by the temperature $k_B T_p$) with the wavelength dependency of the laser linewidth (given by the Planck constant multiplied by the laser frequency $h\nu = e_p$). Their equation for the laser linewidth hence reads

$$\Delta\nu_l = \frac{4\pi e_p \left(\Delta\nu_c\right)^2}{P_l},$$

where e_p is the photon energy, $\Delta\nu_c$ is the half width at half maximum (HWHM) cavity bandwidth, and P_l the laser output power. The underlying assumption is that there are no parasitic cavity losses and the result must be interpreted as a half width at half maximum. It was later shown that above lasing threshold, the linewidth limit is actually two times smaller than calculated by Schawlow and Townes [87]. Considering this 0.5 factor and translating the equation from half width at half maximum values to full width at half maximum values (that is for the laser linewidth $\Delta\nu_l$ and the cavity bandwidth $\Delta\nu_c$), the converted equation is:

$$\Delta\nu_l = \frac{\pi e_p \left(\Delta\nu_c\right)^2}{P_l}.$$

Paschotta *et al.* derived a more general equation for the linewidth of a single frequency laser with quantum noise only that was not derived from linewidth equations for thermally limited masers, but on formulae for quantum noise [88]. This equation takes into account the parasitic cavity losses L_t and output coupling losses L_{OPC}:

$$\Delta\nu_l = \frac{e_p L_{OPC} \left(L_t + L_{OPC}\right)}{4\pi {T_R}^2 P_l}.$$

Here, T_R is the round-trip time of the resonator. For typical parameters, $\Delta\nu_l$ is of the order of a few Hz down to just a few μHz. While some CW lasers reach linewidths close to this theoretical limit with linewidths lower than 1 kHz, in most cases this limit is very hard to attain due to technical noise that is difficult to suppress (e.g. thermal fluctuations or vibrations of the cavity mirrors) and typical industry standard CW lasers have linewidth of the order of tens of kHZ up to GHz for wavelengths in the visible and infrared regime. The M Squared SolsTiS CW Ti:sapphire laser for example, an industry-leading SLM laser, features a linewidth of about 20 kHz.

3

UV Lasers

3.1 Generation of UV light

The first time UV light was generated using a laser was in 1961 [89], just one year after Maiman demonstrated his ruby laser. Franken *et al.* sent the light of a ruby laser (with a wavelength of 694 nm) through a quartz crystal onto a photographic paper in a spectrometer and obtained a spot at 347 nm. The published paper of this result in Physical Review Letters just had a little blemish - the spot that was supposed to be the evidence of the generated UV light was not visible (see figure 3.1). It was later told that one of the journal technicians had erased it, mistakenly believing it was a speck of dust[1] [90]. Ever since this day, second (and higher) harmonic generation is regularly used to produce CW and pulsed UV light. In fact, the fastest pulsed UV lasers to date are still realised by frequency conversion.

In 1963 the first directly generated UV laser light was observed [91]. Heard built a pulsed

[1]As legend has it, it was also the journal Physical Review Letters which refused Maiman's paper on the Stimulated Optical Radiation in Ruby, that was therefore published in Nature

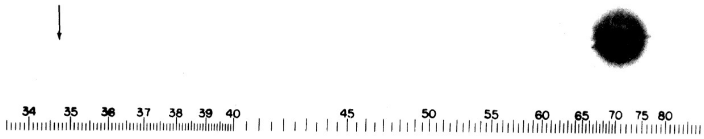

FIG. 1. A direct reproduction of the first plate in which there was an indication of second harmonic. The wavelength scale is in units of 100 A. The arrow at 3472 A indicates the small but dense image produced by the second harmonic. The image of the primary beam at 6943 A is very large due to halation.

Figure 3.1: FIG.1 of the paper "Generation of Optical Harmonics" by Franken et al. in Physical Review Letters, 1961 [89]

nitrogen-gas laser emitting in the ultraviolet spectrum from 300 nm to visible light at 400 nm in thirty lines. He noted that the strongest line was at 337.1 nm, which is still the most important and most commonly used laser line of N_2 gas lasers [25]. N_2 gas lasers typically emit laser pulses with a duration of about 15 ns at a low repetition rate of about 100 Hz.

Seven years after the demonstration of the first N_2 gas laser another type of gas laser emitting in the ultraviolet was realised: the excimer laser [92]. Excimers had already been proposed as a lasant species in 1960 by Houtermans [93] but it took 10 years until Basov built the first xenon excimer laser. "Excimer" is short for "excited dimer" with a "dimer" being a molecule consisting of two identical or similar parts [25]. In 1975 different research groups invented improved noble gas halides excimer lasers [94]. Noble gas halides are technically not excimers but exciplexs (short for "excited state complex"), since they consist of two different atoms and hence the correct name for these lasers would be "exciplex lasers", but this term is hardly used in literature and speech [25]. The wavelength of an excimer laser depends strongly on the molecules used and ranges from 126 nm for Ar_2 lasers to 351 nm for XeF lasers [25]. The average pulse energy also depends strongly on the molecules used and ranges from 10 mJ to 40 mJ for F_2 lasers to up to 1 J for XeCl and KrF lasers [25, 95]. All excimer lasers work in pulsed mode, and depending on the application pulse durations of 10 ns with a repetition rate of 100 Hz or pulse durations of 30 ns with a repetition rate of 8 kHz can be reached [25]. In 1982 Jain of I.B.M. demonstrated deep UV lithography for the first time using a XeCl excimer laser at 308 nm and a KrF excimer laser at 248 nm [96], which was the breakthrough for generating smaller and smaller feature sizes in microelectronic fabrication. Excimer lasers are also used for micromachining organic material, including human tissue during surgery (e.g. eye surgery such as LASIK) as well as certain organic polymers and plastics used for implants and artificial replacements.

In 1973 Elias *et al.* proposed another possible laser material type for UV lasers: trivalent lanthanides doped into solid-state crystals [97]. The first laser of this kind actually build was a $Ce^{3+}YLiF_4$ (also written as Ce:YLF) laser pumped by a KrF excimer laser in 1979 by Ehrlich *et al.* [98]. One year later Ehrlich *et al.* also demonstrated lasing in $Ce^{3+}LaF_3$ (Ce:LaF) [99]. The efficiency of the demonstrated laser was very low (<0.01% when pumped by a KrF laser) and Ce:LaF lasers have shown similar low efficiencies to date; therefore Ce:LaF is not regarded as laser material with a high potential [100]. The first laser action in Ce^{3+}:$LiCaAlF_6$ (Ce:LiCAF) and Ce^{3+}:$LiLuF_4$ (Ce:LiLuF) was demonstrated by Dubinskii *et al.* in 1993 and 1994 [101, 102], followed by Ce^{3+}:$LiSrAlF_6$ (Ce:LiSAF) lasers by Marshall *et al.* [103]. Since Ce:LiCAF is the laser material used for the presented PhD project, a detailed description of the properties of Ce:LiCAF and the achievements in Ce:LiCAF laser research is given in the following sections 3.2 and 3.3.

Ultrafast UV pulses are commonly produced by frequency conversion of ultrafast pulses in the picosecond or femtosecond regime of visible or infrared light with conversion efficiencies in the order of 10% [4]. The conversion efficiency of ultrafast pulses is significantly smaller compared to efficiencies for nanosecond pulses, where efficiencies often exceed 60% due to strong non-linear interactions and good phase-matching. For frequency conversion of ultrashort pulses, a group velocity mismatch occurs, which causes a temporal walk-off. Hence the effective interaction length is limited and only thin crystals can be used.

An example of UV pulses generated by frequency conversion are pulses achieved by frequency-tripled KLM Ti:sapphire lasers or fourth-harmonic generation from Nd-doped lasers. Using these methods, pulses in the range of 240 nm to 350 nm with sub-50 fs pulse durations have been shown [104]. UV pulses as short as 11 fs at 162 nm have been produced by the fifth harmonic of a Ti:sapphire laser in an argon gas jet, but this result was obtained accepting a very low efficiency resulting in pulse energies of only 4 nJ (when generated from 710 μJ, 12 fs pulses at 810 nm) [105]. Other methods such as Ti:sapphire pumped optical parametric oscillators (OPOs) can generate UV pulses with a relatively higher efficiency, but this comes with an highly increased complexity and cost as well as a restricted tunability [106]. By nondegenerate four-wave mixing in gases, high energy pulses (>20 μJ) with durations down to 8 fs at 260 nm have been shown [107, 108]. However, since the non-linear susceptibility of noble gases is very low, the technique of four-wave mixing in gases requires long waveguide capillaries which makes it very complex and bulky. Also the obtained repetition rates are very low (in the order of a few kHz) and the technique is very sensitive to alignment. Another solution to produce UV pulses out of ultrafast pulses with longer wavelengths is the supercontinuum generation [109] - pulses only 9.7 fs long at 290 nm have been demonstrated using this method [110]. There have also been reports of producing UV pulses by achromatic phase matching of visible ultrashort pulses in solids [111]. These pulses were sub-10 fs in a region of 275 nm to 335 nm and had energies of a few hundred nJ. The shortest UV pulses produced so far are only 3.7 fs long [112]. They were generated by high harmonic generation in noble gases at a wavelengths of 275 nm.

An alternative to generating ultrafast UV pulses by frequency conversion is to use a laser material that emits in the UV directly and has a broad enough bandwidth to support ultrafast pulses. We will see in the following sections 3.2 and 3.3 that Ce:LiCAF is such a material. Because of its very broad tuning range over 35 nm in the UV, Ce:LiCAF has even been described as the possible "Ti:sapphire of the UV" [113]. This substantial comparison will be reviewed in section 3.4. As will be discussed below, Ce:LiCAF has the potential to generate pulses with durations down to the attosecond regime [4].

Like ultrafast UV pulses, continuous wave UV laser light is also commonly generated by frequency conversion of visible or infrared light, using a combination of optical parametric conversion, and sum-frequency or higher-order harmonic generation to achieve the desired shorter wavelengths [114–116]. CW UV radiation can also be generated directly in the UV by excitation of ions such as argon or krypton. This is realised in gas lasers and the wavelength of these lasers is not easily tunable. Free electron lasers (FELs) can also be used to generate CW UV light. In fact they can produce a tunable output from the soft X-ray to the infra-red region, and are therefore a good alternative for applications like material processing. But since they require large scale infrastructures and are not commercially available, they are still not suitable for most CW UV applications. Again, the alternative approach is to use Ce:LiCAF, that can, as will be shown in the following chapters, be used to generate easily tunable CW light directly in the UV. As already mentioned in the introduction, the technique we use to generate CW laser output is asynchronous pumping, which to the best of our knowledge has never been exploited before in detail and led to the first ever CW Ce:LiCAF laser.

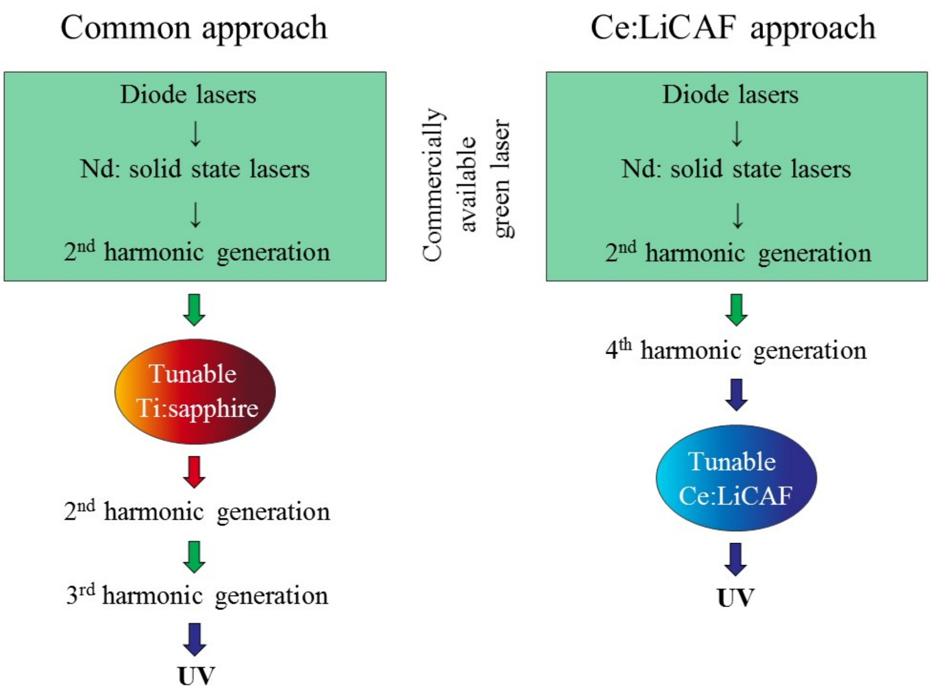

Figure 3.2: Comparison between the common approach to generate tunable UV laser output and the approach using Ce:LiCAF as a laser material.

3.2 Properties of Ce:LiCAF Laser Crystals

Trivalent lanthanides doped into solid state crystals were first considered as laser materials for the UV in 1973 by Elias *et al.* [97] and first laser action in Ce:LiCAF was demonstrated in 1993 by Dubinskii *et al.* [101], as mentioned in the previous section.

Using Ce:LiCAF as a solid-state laser crystal, laser light can be generated directly in the UV. This is immensely beneficial, especially when aiming to build a tunable UV laser. The comparison in figure 3.2 illustrates the advantages of using Ce:LiCAF as a laser material when building a tunable UV laser compared to the most common approach which is based on tunable Ti:sapphire lasers. Typically, tunable UV output is obtained by pumping a tunable Ti:sapphire laser with a commercially available green laser and subsequent frequency up-conversion of the infrared light via two harmonic generation steps to the desired UV wavelengths. The disadvantage is that the techniques to achieve cascaded non-linear conversion can often be complex. It presents substantial stability challenges, since the base laser and all conversion stages must be tuned and adjusted to the specific wavelength at all times simultaneously. Particularly for CW sources, the nonlinear frequency conversion is inefficient and requires elaborate sensitive locked resonant enhancement cavities to enhance the laser intensity to

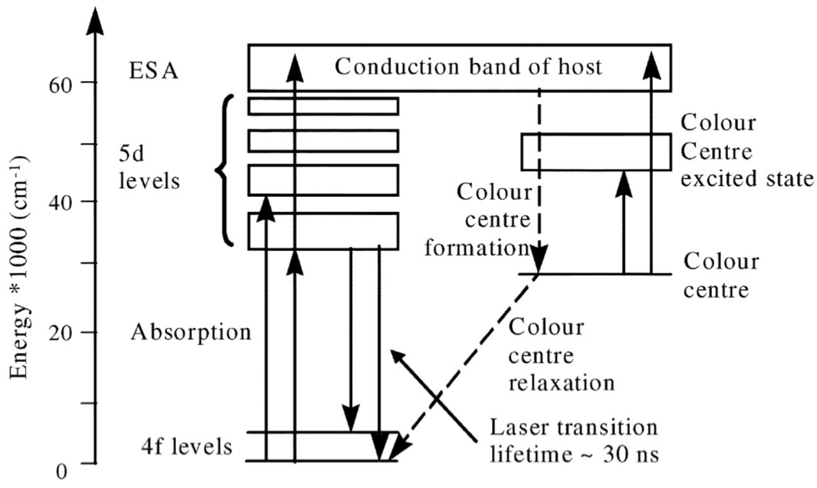

Figure 3.3: Schematic of the energy level structure for a trivalent cerium ion in a fluoride host [100]

obtain reasonable conversion efficiencies [117–119]. The alternative Ce:LiCAF approach is to convert a fixed wavelength pump light into the UV, and then to generate the tunable laser light directly in the UV. Since no wavelength-adjustment is needed in the frequency conversion stages, the set-ups required are equally feasible for pulsed and CW laser systems and are rather simple compared to those needed for other systems. Better efficiencies are reached and the laser output is easily tunable. The set-up used for the experiments conducted during the research phase of the presented PhD project is described in detail in the following chapter 4. As a pump source a Nd:YVO_4 laser was used whose infrared output was frequency quadrupled in two subsequent doubling stages. However, instead of working with an infrared source and two doubling stages it is also possible to use a commercially available green laser followed by just one frequency conversion stage, as indicated in figure 3.2. Indeed, recently high power (around 20 W average power) 40 MHz mode-locked 266 nm laser sources (EdgeWave GmbH, Ultrashort Pulse InnoSlab Lasers PX-Series) have become available commercially that could also be used to pump a Ce:LiCAF laser directly. In conclusion, working with Ce:LiCAF as a laser material to generate tunable UV output leads to simpler set-ups, better efficiencies and overall easier tunability than using the common approach based on tunable Ti:sapphire lasers.

Figure 3.3 shows the energy level structure for a trivalent cerium ion (Ce^{3+}) when doped into a fluoride host [100]. The desired UV lasing occurs on the $5d \rightarrow 4f$ transition. The gap between the laser levels is large enough (typically 20 000 cm^{-1} to 30 000 cm^{-1}) to restrain multi-phonon related nonradiative decay [120], which results in high (>90%) quantum efficiencies

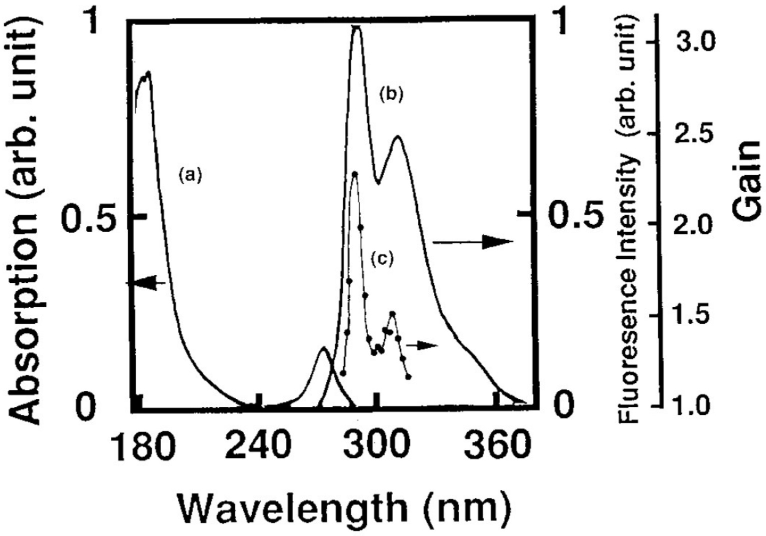

Figure 3.4: (a) Unpolarized absorption spectrum of a Ce:LiCAF sample (0.1 atomic %, 2.3 mm in length); (b) unpolarized fluorescence spectrum of Ce:LiCAF (0.9 atomic %); (c) single-pass small-signal gain dependence on the probe beam wavelength for a Ce:LiCAF sample (0.9 atomic %, 2.3 mm in length) from [122]

[101, 121]. As shown in the figure, aside from the laser transition, other transitions such as excited-state absorption (ESA) and colour centre (CC) formation can occur [100]. ESA describes the transition of an electron from the $5d$ levels of the Ce-ions to the conduction band (CB) of the host ($5d \rightarrow$ CB). If an excited electron then gets trapped at a lattice defect or impurity site instead of transitioning back from the CB to the $5d$ or $4f$ levels, a CC can be formed. The trapped electron can possibly remain at CC level in bound states of the trap or might be excited back to the CB by absorbing energy at pump or laser wavelengths, which causes losses. After transitioning back to the CB the electron can potentially return to a Ce^{3+} site, removing the colour centre. Hence CC lifetimes are dependent on impurity trap depths and temperature as they can be thermally deactivated. The upper laser level ($5d$) lifetime τ of Ce:LiCAF is 25 ns [103] and therefore even shorter than the lifetime in other Ce^{3+} doped fluorides (which is $\sim$ 30 ns as displayed in the figure). This very short upper laser level lifetime makes it difficult to get Ce:LiCAF lasers to operate in a CW mode, as will be discussed in detail later.

The non-polarized absorption spectrum, the fluorescence spectrum, and the single-pass small-signal gain dependence on the probe beam wavelength for Ce:LiCAF samples are shown in figure 3.4. The absorption spectrum (a) shows a high peak at 190 nm and a second (smaller) peak at 260 nm to 270 nm. Ce:LiCAF can therefore be pumped with the fourth-harmonic of Nd doped solid state lasers (266 nm). The fluorescence spectrum (b) displays a two-humped shape, which is typical for Ce^{3+} ions in most known hosts (due to the $5d \rightarrow 4f$ transition terminating at the $^2F_{7/2}$ and $^2F_{5/2}$ components of the spin-orbit split ground term [4]). The dominant emission of Ce:LiCAF is at 290 nm. The small-signal gain curve (c) has its highest peak also at 290 nm. It shows a gain bandwidth of 35 nm, so broad tunability from 280 nm to 315 nm can be achieved using Ce:LiCAF.

3.3 Previous Research in Ce:LiCAF Lasers

The first laser action in Ce:LiCAF was reported in 1993 by Dubinskii *et al.* [123]. In their experiments the cerium crystal was pumped quasi-longitudinally with a 12.5 Hz 266 nm pump beam converted from a Nd:YAG pump laser source. The laser cavity was a simple two mirror set-up consisting of one high reflective (HR) mirror with a radius of curvature (ROC) = 30 cm and an output coupling mirror with ROC = 30 cm and a reflectivity (R) = 32% at the lasing wavelengths, separated by 20 cm. They achieved 0.15 mJ output at 288 nm with a slope efficiency of 8.7%, and tuning from 281 nm to 297 nm by using an intracavity tuning prism. The pulse half-width was reported to be of about 8 ns. They also conducted a long-time experiment, during which they irradiated the cerium crystal with a pump fluence of 1 J/cm^2 over 5 hours. No colour centre induced crystal colouration was observed over the full 5 hour runtime.

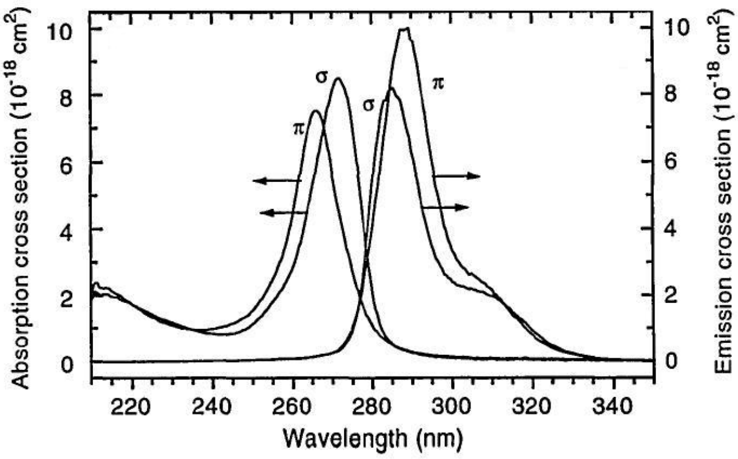

Figure 3.5: Polarisation dependent absorption and emission spectrum of a Ce:LiCAF sample as published in [103]

Marshall *et al.* published a detailed analysis of the spectroscopic properties of Ce:LiCAF in 1994 [103]. They used samples grown by both Czochralski and the Zone-Melt methods and postulated that the Ce^{3+} ions substitute the Ca^{2+} on the octahedral sites in the LiCAF lattice. Using these crystals they built simple two mirror resonators consisting of one HR mirror with ROC = 10 cm and an output coupling mirror with ROC = 10 cm and R = 50%, separated by 10 cm. By pumping this cavity with 10 Hz repetition rate frequency quadrupled Nd:YAG light, they achieved a slope efficiency of 21%. They also investigated the small signal behaviour of Ce:LiCAF using a frequency doubled dye laser as a probe source. They found that the small signal gain was dependent on the polarisation of pump and probe beam. When pump and probe both were π-polarised, the small signal gain was higher than when either pump or probe were σ-polarised. It was concluded that the ESA cross section must be higher for σ-polarisation than for π-polarisation, and the ESA cross sections were estimated to be 5.5×10^{-18} cm^2 and 3.6×10^{-18} cm^2 for π- and σ-polarisation respectively, while the laser emission cross section was estimated to be in the same range of approximately 10×10^{-18} cm^2. The polarisation dependent absorption and emission spectrum as measured by Marshall *et al.* is shown in figure 3.5.

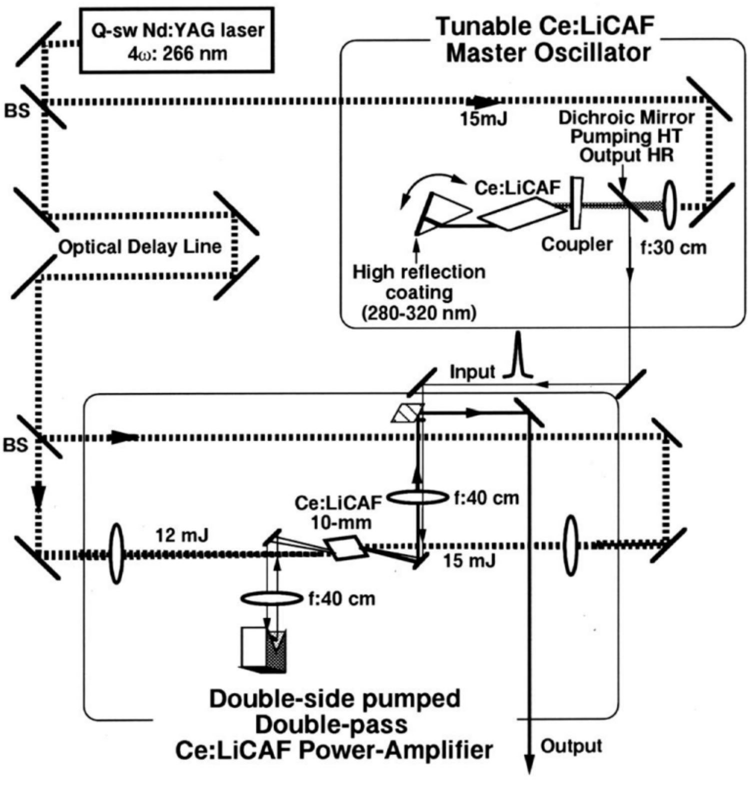

Figure 3.6: Set-up of Ce:LiCAF laser cavity and amplifier system as used in [124]

Following these results improvements in the performance of Ce:LiCAF lasers have been made by using higher quality crystals cut at Brewster's angle to favour π-polarisation and so minimise ESA. Pinto *et al.* for example reported a slope efficiency of 39% for a two mirror cavity set-up with a HR mirror with ROC = 2 m and a flat output coupler with R = 15%, separated by 7 cm, transversely pumped by a 10 Hz frequency quadrupled Nd:YAG laser [125]. Tunability was achieved, using an intracavity prism, from 281 nm to 315 nm. Like Dubinskii *et al.*, Pinto *et al.* also observed no long-lifetime colour centre effects.

In 1996 the first high repetition rate Ce:LiCAF laser was reported by Petersen *et al.* [126]. They used a 1.35 W 10 kHz frequency quadrupled Nd:YVO_4 laser to longitudinally pump the cerium crystal in a two mirror cavity with a HR mirror with ROC = 10 cm and an output coupling mirror with ROC = 10 cm and R = 50%, separated by 6 cm. They achieved up to 350 mW and a slope efficiency of 28% at 292 nm, and tuning from 289 nm to 312 nm by placing a Brewster prism in the cavity and reducing the output coupling to 5%.

In 1998 Dubinskii *et al.* and Liu *et al.* demonstrated the first amplified Ce:LiCAF oscillators [124, 127]. The set-up used by Liu *et al.* can be seen in figure 3.6. They used the fourth harmonic of an Nd:YAG laser horizontally polarised with pulse energies up to 200 mW at 266 nm with pulse durations of 100 ns at 1 Hz repetition rate that was longitudinally focused into the cerium crystal. Their cavity was 1.5 cm long and consisted of a flat HR mirror and a flat output coupling mirror with a transmission (T) of 80%. The generated output pulses were 600 ps long with an energy up to 1 mJ, tunable from 281 nm to 314 nm. Subsequently these pulses were amplified to 4 mJ by double-passing through the amplifier that consisted of a Ce:LiCAF crystal pumped with the remaining power of the fourth harmonic of the Nd:YAG pump laser. Additionally the tunability of output wavelength was extended in the same experiment by sum-frequency mixing of the cerium UV output and a 1064 nm beam from the same Nd:YAG pump source. The mixed UV pulses had a wavelength around 230 nm, pulse energies of 0.5 mJ, and pulse durations of 1 ns.

Liu *et al.* also achieved shorter pulses with a similar set-up in 1999. This time, they used a Nd:YAG laser with a repetition rate of 10 Hz that produced 75 ps pulses as a pump source [128]. The output coupling mirror had R = 30% and the Ce:LiCAF crystal was a 10 mm long Brewster cut crystal with 1% cerium doping. The output pulse duration measured was 150 ps, which was a record held for 10 years until Granados *et al.* published their results in 2009 [5] (see later). Following these achievements, Liu *et al.* worked on chirped pulse

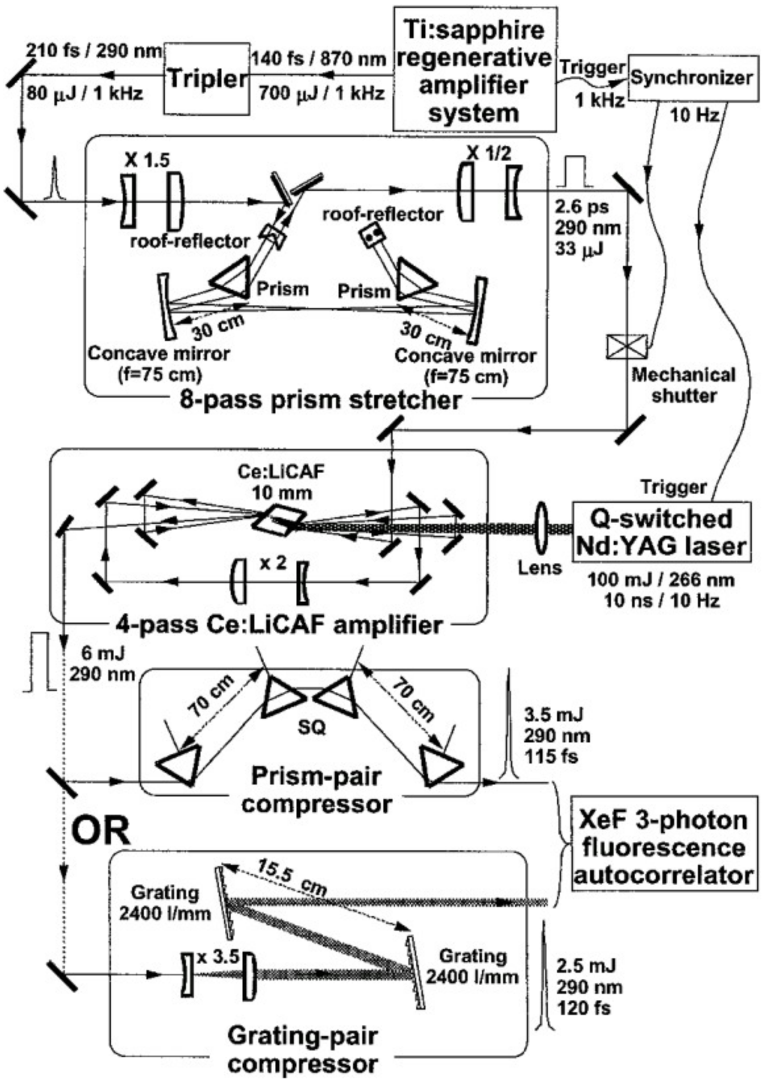

Figure 3.7: Set-up of the Ce:LiCAF chirped pulse amplifier as used by [129]

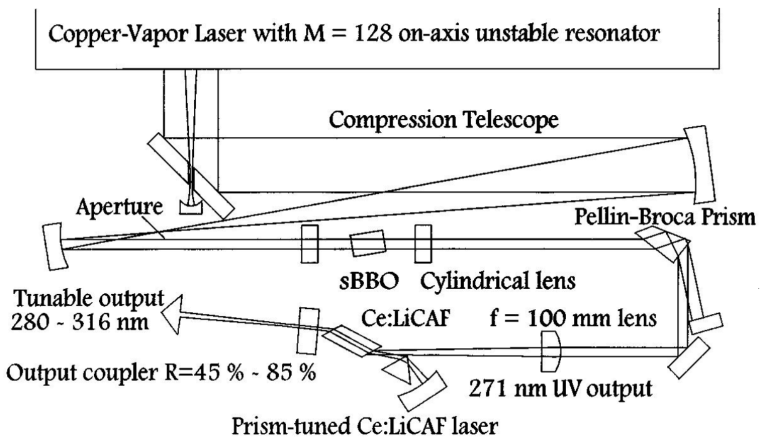

Figure 3.8: Set-up of the sum-frequency mixed CVL pump source and the Ce:LiCAF laser as used by [130]

amplification (CPA) systems using Ce:LiCAF as a broadband gain medium [129]. They used a 1 cm x 1 cm x 1 cm Brewster-cut Ce:LiCAF crystal at the centre of a modified bow-tie-style four-pass amplifier as shown in figure 3.7. The seed beam was a frequency tripled Ti:sapphire 290 nm pulses with a duration of 210 fs at a repetition rate of 1 kHz and a spectral bandwidth of 1 nm. These pulses were extended to 2.6 ps pulses of 33 µJ by an eight-pass quartz-prism pulse stretcher and then guided into the Ce:LiCAF amplifier. The seed beam diameter was approximately 1.5 mm for the first and second pass and was expanded to approximately 3 mm for the third and forth pass to avoid deep gain quenching and possible damage to the optics in the amplifier. A synchronously operated 10 Hz Q-switched Nd:YAG laser emitting 100 mJ pulses at 266 nm with a pulse duration of 10 ns was used as a pump beam. It was softly focused into the Ce:LiCAF crystal to a diameter of 4 mm. The gain factor achieved with this configuration was 370, delivering 6 mJ pulses at 290 nm with a pulse duration of 10 ns. After amplification, the beam was compressed by dispersion-compensation via a double-pass through a quartz Brewster prism pair to just 115 fs. Liu *et al.* noted that this achievement is just the first step towards all-solid-state UV terawatt laser systems that will become available with future scaling of the Ce:LiCAF laser system and higher pumping power. With shorter seed pulses and better dispersion control, much shorter pulse durations will also be achievable as the bandwidth of the Ce:LiCAF gain material was not fully utilized yet.

In 1999 McGonigle *et al.* demonstrated with the set-up shown in figure 3.8 that copper vapour lasers (CVL) can also be used as a pump source for cerium lasers [130]. Pumping by CVL instead of a frequency quadrupled Nd doped laser, has the advantage, that all cerium-doped lasers can be pumped by a single frequency doubling step. CVLs have two fundamental lines at 511 nm and 578 nm and these lines can generate three UV wavelengths: 255 nm (frequency doubled 511 nm), 271 nm (sum-frequency-mixed), and 289 nm (frequency doubled 578 nm). The 271 nm line can be used to pump Ce:LiCAF and Ce:LiSAF, and the 289 nm line can be used to pump Ce:LiLuF, which broadens the possible tuning range from 280 nm to approximately 340 nm in a set-up that consists of a CVL pump and both a Ce:LiCAF (or Ce:LiSAF) and a Ce:LiLuF laser cavity. Figure 3.9 shows the absorption and emission spectra of different cerium doped fluoride crystals. McGonigle *et al.* achieved in their set-up - using a CVL with a repetition rate of 7 kHz to pump a Ce:LiCAF crystal - 530 mW at 288.5 nm with a slope efficiency of 32% and tuning from 280.5 nm to 316 nm by placing a tuning prism in the cavity.

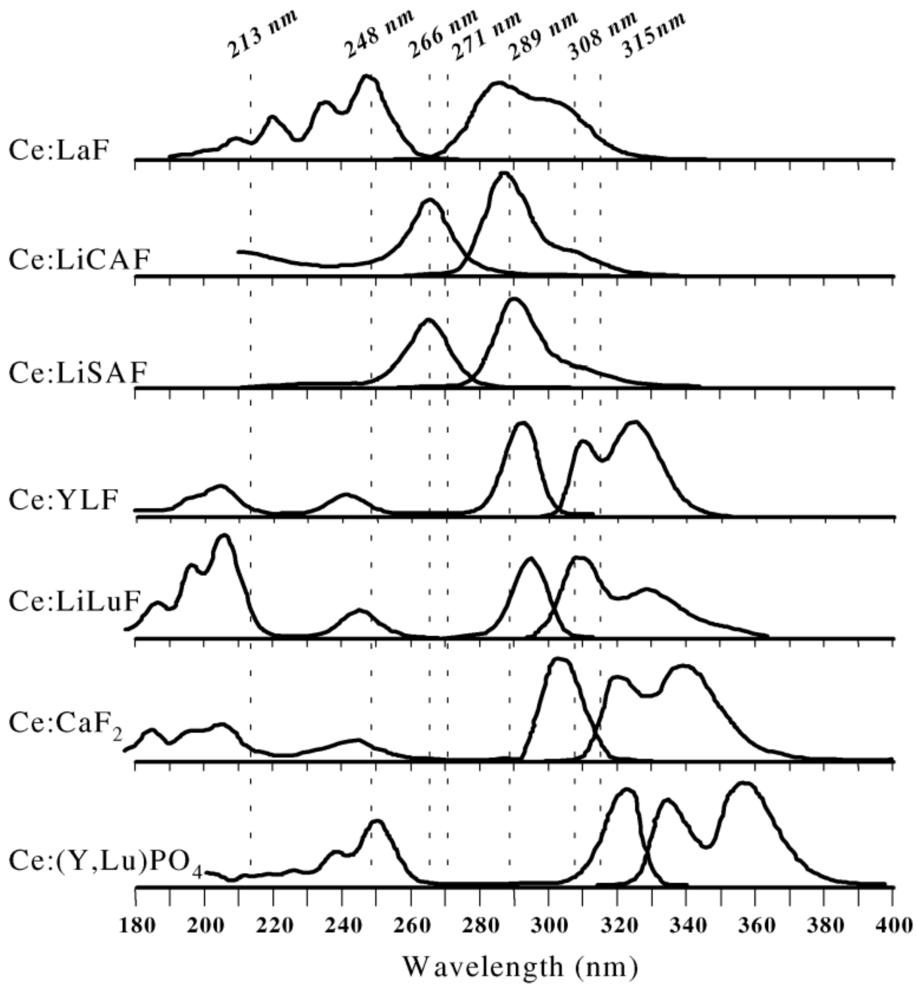

Figure 3.9: Absorption and emission spectra for trivalent cerium in different fluoride crystals [100]

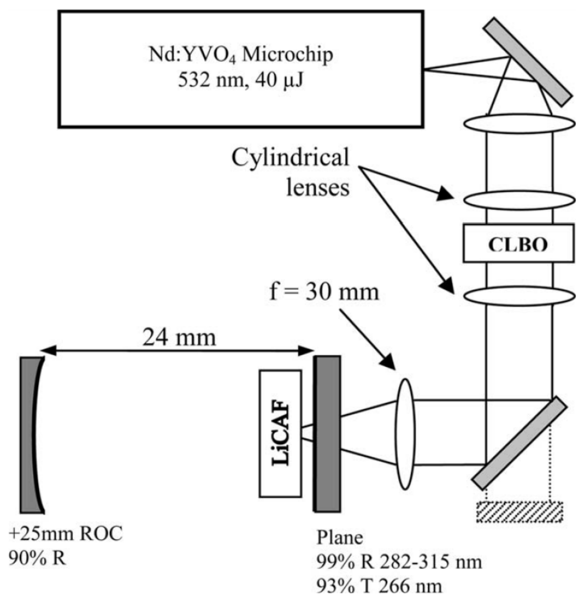

Figure 3.10: Set-up of the miniature Ce:LiCAF laser as reported in [131]

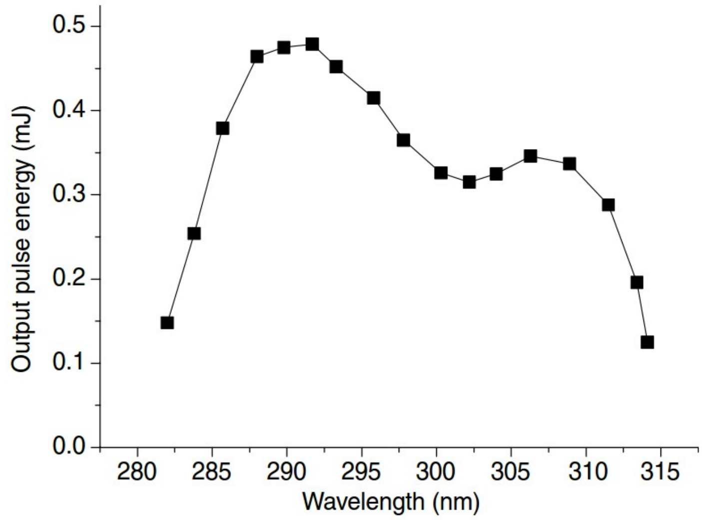

Figure 3.11: Output power of the prism-tuned Ce:LiCAF laser across its 283 nm to 314 nm tuning range, for a pump pulse energy of 2 µJ, as published in [131].

In 2006 Spence *et al.* published results on miniature Ce:LiCAF lasers [131]. This type of Ce:LiCAF laser was intended to be of use in small laboratories or industrial environments where the size of a laser might present a problem for practical implementation. Another advantage of the presented miniature Ce:LiCAF lasers was the use of a commercially available inexpensive pump laser: Spence *et al.* used a frequency doubled Nd:YVO_4 laser that generated 750 ps 40 µJ pulses at 532 nm with a repetition rate of 1 kHz as a pump source and frequency doubled this green light using a CLBO crystal to achieve 550 ps 12 µJ pulses at 266 nm (see figure 3.10). However, they found that a pump energy of just 2 µJ is sufficient to achieve continuous tuning over the full range of the Ce:LiCAF gain spectrum. Using 2 µJ pump pulses, their laser output was as high as 550 nJ for output pulses of a duration of 1.7 ns in the tuning range of 283 nm to 314 nm (figure 3.11). The lasing threshold was as low as 200 nJ and the absolute efficiency of this laser was 31%. This work showed that Ce:LiCAF lasers can be miniaturised and be pumped by very small 266 nm microchip lasers for applications such as fluorescence spectroscopy.

So far cerium lasers have mainly been operating in pulsed mode with pulse durations in the nanosecond regime. Today average output powers of cerium lasers are in the 1 W level [100], with output pulse energies in the order of 100 mJ [132] and >50% efficiencies [133]. While the achievements in ns-Ce:LiCAF lasers have been progressing ever since the first Ce:LiCAF laser in 1993, and even though Ce:LiCAF has the potential to generate pulses as short as 3 fs, to date no one has come near producing Ce:LiCAF pulses in the

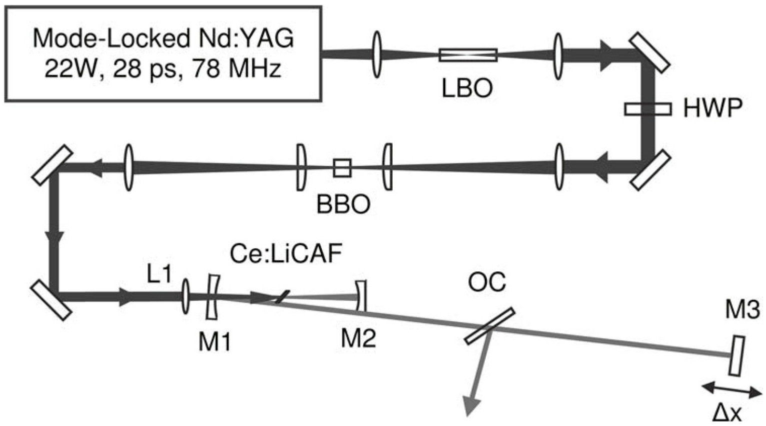

Figure 3.12: Experimental set-up as used in [5]. L1: sherical lens with a focal length of $f = 5$ cm; M1, M2: concave sherical mirrors with ROC (radius of curvature) = 10 and 5 cm respectively; M3: plane mirror; OC: output coupler; HWP: half-wave plate at 532 nm.

few fs regime. The shortest pulses reported so far, have been demonstrated by Granados *et al.* of the MQ Photonics Research Centre in 2009 and were 6 ps long at 291 nm [5]. The set-up Granados *et al.* used (shown in figure 3.12) was similar to the set-up used during the experiments presented in this thesis (see chapter 4). In the three-mirror cavity, the dichroic input coupling mirror M1 was used as the folding mirror and a 6 mm thick UV-grade silica plate placed in the long cavity arm at close-to Brewster's angle was used as a variable output coupler. The maximum output coupling was 3%. The cavity lengths of the 78 MHz pump and the Ce:LiCAF laser were matched for synchronous pumping at the 1^{st} harmonic of the pump. The laser threshold was 580 mW and the slope efficiency 13%, generating a maximum output power of 52 mW. It was reported that the output power was strongly dependent on the cavity length (see figure 3.13), with a cavity length detuning from the 1^{st} harmonic of only 0.5 mm leading to a decrease of the output power by 50%. To measure the pulse duration of the UV pulses, an asynchronous sampling method using a $\chi^{(2)}$ cross-correlation technique was used. A 400 mW Ti:sapphire laser running at 800 nm, emitting 14 fs transform-limited pulses at 78 MHz was difference-frequency mixed with the 291 nm pulses of the Ce:LiCAF laser, generating a signal at 457 nm. The cavity length of the Ti:sapphire laser was adjusted so that there was a small difference in pulse repetition frequency to the Ce:LiCAF laser of $\Delta\nu_R = 2.8$ kHz, giving a time resolution of 466 fs. The laser pulses were difference-frequency mixed in a 4-mm-long BBO crystal whose acceptance bandwidth limited the time resolution further to ~1 ps. Due to the difference in repetition rates, successive pairs of pulses arrived at the BBO with a different relative delay mapping

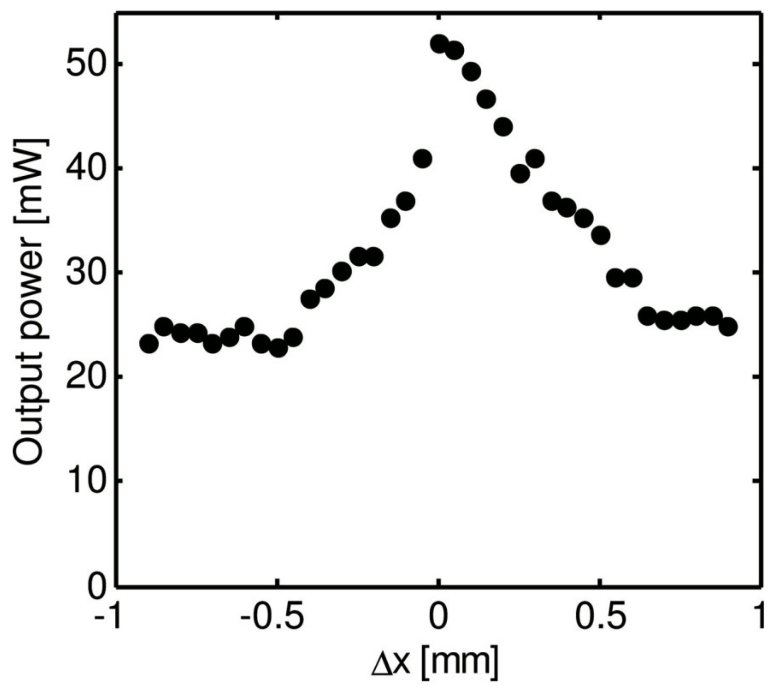

Figure 3.13: Output power of the cerium oscillator as a function of cavity length detuning as reported in [5].

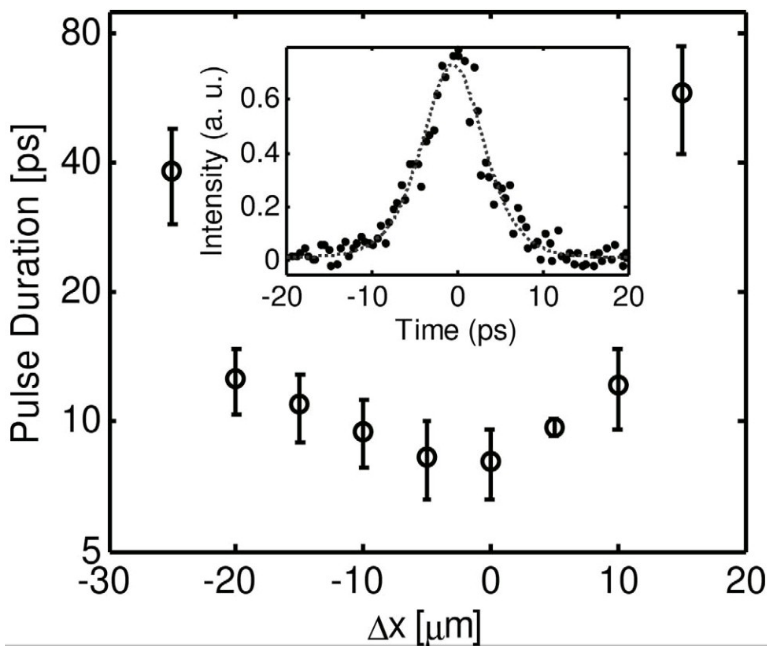

Figure 3.14: Output pulse duration as a function of cavity length detuning and (inset) cross-correlation data for the measurement of the output pulse for zero detuning as reported in [5].

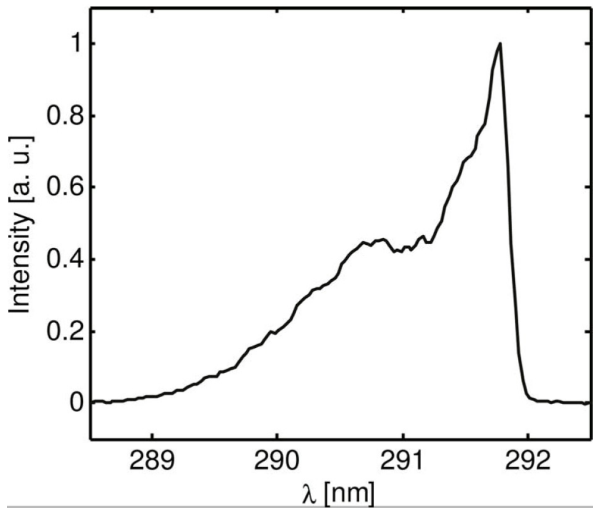

Figure 3.15: Output spectrum as reported in [5].

out the cross-correlation and enabling the determination of the Ce:LiCAF pulse duration. The cross-correlation data for the measurement of the output pulse at zero detuning is plotted in the inset of figure 3.14. Figure 3.14 also shows the pulse duration as a function of cavity length detuning, evincing that the shortest pulses (with a duration of 6 ps) are generated when the oscillator is mismatched by less than 20 µm from the 1^{st} harmonic of the pump. Granados *et al.* also presented the output spectrum of the 6 ps Ce:LiCAF laser (see figure 3.15). The peak wavelength was at 291.7 nm, and featured a bandwidth greater than 1 nm. This bandwidth can support pulses of less than 100 fs, suggesting that the pulses were not close to being transform limited. At the side of the spectrum with the longer wavelength, the spectrum exhibited a sharp edge. Granados *et al.* reported that the specific wavelengths at which this edge occurred was dependent on alignment and pump power and appeared to be a genuine response to the decreasing gain for longer wavelengths rather than an artefact from an unwanted absorption edge.

A Ce:LiCAF laser based on a whispering gallery modes (WGM) ring resonator was published in 2012 by Le *et al.* [134]. Figure 3.16 (a) illustrates the set-up of the WGM laser. Le *et al.* report a lasing threshold of 1.6 µJ and an effective slope efficiency of 25%. They claim to have achieved wide-bandwidth lasing from 280 nm to 330 nm (see figure 3.16), however it is questionable if the generated output truly was lasing output rather than fluorescence. Wide-bandwidth lasing as reported is not very likely in a homogeneously broadened laser medium and in absence of any mode-locking mechanism, and the measured output spectra actually look like typical fluorescence spectra of Ce:LiCAF.

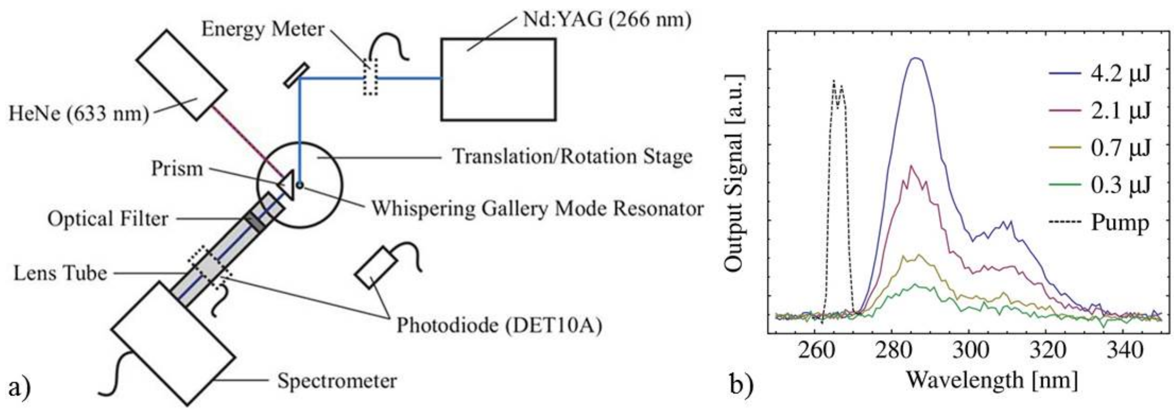

Figure 3.16: a) Schematic of the WGM laser set-up, b) WGM laser output spectrum at several pump energies [134].

Through all the above summarized key milestones, Ce:LiCAF has been used as a laser material for pulsed laser operation, and still the most common Ce:LiCAF lasers generate pulses in the ns regime. Studies on continuous wave Ce:LiCAF lasers have been only theoretical until very recently, when Eduardo Granados Mateo reported the generation of chopped CW Ce:LiCAF lasing with small residual modulation in his PhD thesis in 2010 [4] (see below). The first theoretical study on the CW laser threshold of Ce:LiCAF was done by Marshall *et al.* in 1994 [103]. The estimation was given for longitudinal pumping conditions, pump and laser beams were assumed to have a Gaussian profile with the pump spot radius being much smaller than the laser mode radius, the output coupling was assumed to be only 1%, the single-pass losses were considered negligible, and the quantum efficiency was set to 1 for simplification. In addition, Marshall *et al.* assumed the total absence of excited-state absorption (ESA), because they postulated the population of the excited laser level to be low in the CW pumping regime. A study by Alderighi *et al.* later found that ESA can in fact not be neglected, as ESA causes a significant reduction of the single ion emission cross section and in turn reduces the gain [135]. In the same study, Alderighi *et al.* presented an estimation of the Ce:LiCAF CW laser threshold based on the derivation of Payne *et al.* for the CW threshold of the quasi-three-level laser system in Cr^{3+}:LiCAF [136]. Alderighi *et al.* compared their theoretical estimation with experimental results achieved by means of time-resolved measurement in the pulsed regime. A long-pulse-duration source was used to pump two Ce:LiCAF based laser configurations: one tunable laser and one high-efficiency nondispersive laser in a quasi-stationary lasing regime. The experimental values obtained for the CW threshold intensities of Ce:LiCAF were I_{CW}^{th} = 4.5 ± 0.2 MW/cm^2 and

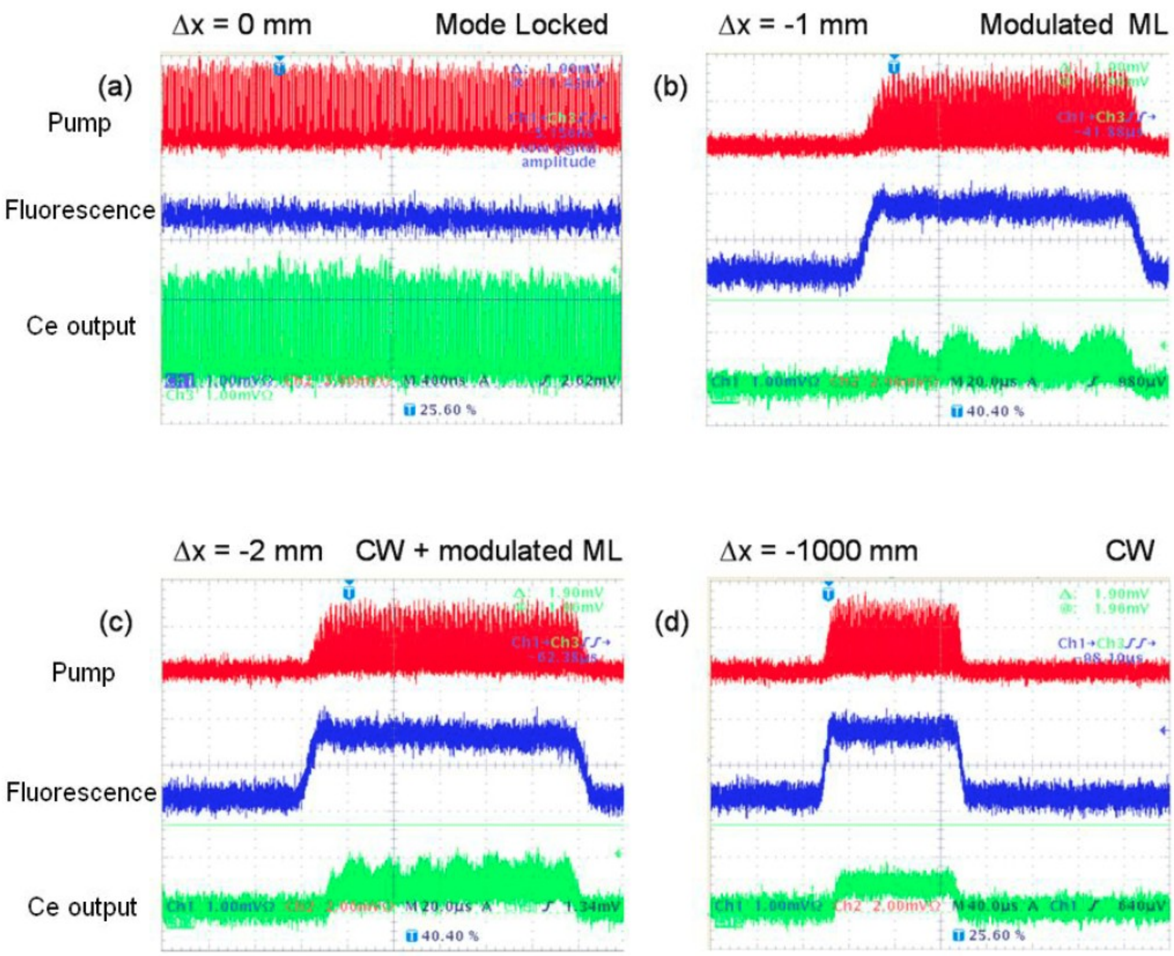

Figure 3.17: Output of the laser for four different cavity lengths as reported in [4]: (a) Δx = 0 mm produces a stable mode-locked output, (b) Δx = -1 mm produces a modulated mode-locked output, (c) Δx = -2 mm the output has CW components, (d) Δx = -1000 mm the laser operates in CW mode. The window of output in (b), (c) and (d) corresponds to the chopper open period.

1.9 ± 0.2 MW/cm^2 for the dispersive laser with quasi-collinear pumping and the nondispersive laser with longitudinal pumping respectively. On basis of their model and validated through their experiments, the lower limit of the CW threshold for Ce:LiCAF was extrapolated to be I_{CW}^{th} = 93 kW/cm^2 and it was postulated that CW lasing is obtainable with 590 mW absorbed CW pump power tightly focused in a 20 µm spot radius, and hence the feasibility of a tunable UV all-solid-state CW Ce:LiCAF laser was concluded.

As already mentioned, Eduardo Granados Mateo reported the generation of chopped CW Ce:LiCAF lasing with small residual modulation in his PhD thesis in 2010 [4]. With a chopped pump beam, quasi-CW lasing was achieved over the 100 ms opening time of the chopper by asynchronously pumping a three mirror laser cavity. The basic set-up used was the same as for the synchronous pumping (see figure 3.12), except that the length of the long

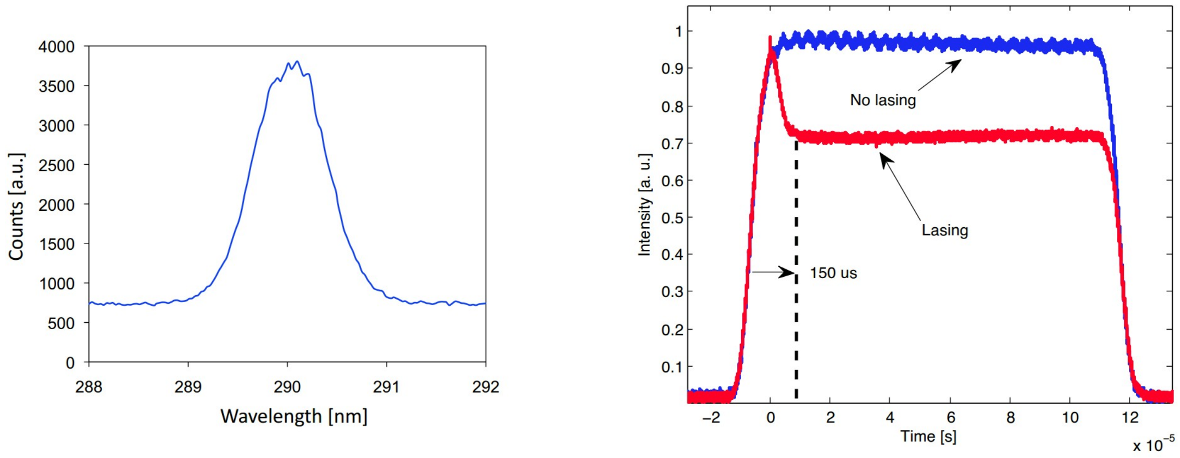

Figure 3.18: (a) Output spectrum of CW Ce:LiCAF laser without prism and (b) experimental pump depletion obtained for CW operation as reported in [4].

cavity arm was detuned from the 1^{st} harmonic. Figure 3.17 shows the laser output for different cavity length detunings as reported by Granados. To obtain the images, a 6 GHz oscilloscope and a photodiode with a 1 ns response was used, limiting the resolution of the presented time traces. Granados postulated that for cavity detunings larger than $\Delta x = -1000$ mm from the 1^{st} harmonic CW output is being generated, except when the length of the cavity matches an integer multiple of the pumping laser repetition rate. He achieved best CW output with the long cavity arm set to a length of 30 cm. Granados noted that there will always be small fluctuations in a pulse pumped CW output due to modulated gain and the short upper laser level lifetime of just 25 ns. The spectrum of the achieved CW output and the measured pump depletion were also presented in Granados' PhD thesis (see fig 3.18). The output spectrum of the free running laser without a tuning prism was determined as being broad (larger than 1 nm) and the depletion of the crystal fluorescence due to lasing action measured to be greater than 20% with a stabilization time of approximately 150 µs. Since CW lasing was achieved over a time period of 100 ms, it was concluded that the effects of colour centres is indeed small for CW mode-locked Ce:LiCAF lasers. While Granados' findings on the generation of CW Ce:LiCAF laser output are the first known achievements in this area, the obtained output was never characterised thoroughly and the noted residual modulation of the output was never quantified or investigated in detail.

3.4 Ce:LiCAF - The Ti:sapphire of the UV?

Ti:sapphire had a tremendous impact on science and applications and is arguably the most important laser material in the world today. In 2002 Ono *et al.* stated in their paper on a high-energy UV power-amplifier module based on Ce:LiCAF, that "Ce:LiCAF is a Ti:sapphire in the UV region" [113]. The encouraging comparison is based on the fact that Ce:LiCAF and Ti:sapphire feature many similarities as laser materials. Both are efficient, robust, and convenient to set up in all-solid-state laser systems. Yet the most important common feature is certainly the immense bandwidth of both materials of order 133 THz. In figure 3.19 the emission cross sections of Ce:LiCAF and Ti:sapphire are plotted in the same graph to highlight the similar frequency bandwidths. When operating in mode-locked mode, the theoretical directly achievable pulse duration when using Ce:LiCAF and Ti:sapphire based on their large bandwidth is around 4.5 fs (see figure 3.20). Indeed Ti:sapphire lasers can be mode-locked to directly generate 4.4 fs pulses [137]. With its gain bandwidth ranging from 600 nm in the red to 1100 nm in the infrared (IR) spectral region, the single cycle limit of Ti:sapphire at the 800 nm centre wavelength is 2.7 fs. Matsubara *et al.* reached this limit by induced phase modulation of 30 fs Ti:sapphire pulses [70]. Since the emission band of Ce:LiCAF covers a range of much shorter wavelengths in the deep UV from 280 nm to 315 nm, the single cycle limit of its peak wavelength of 290 nm is much shorter as well. As figure 3.20 illustrates, it is as narrow as 970 as. To date no-one has come even close to reaching this theoretical limit, but it confirms the potential of Ce:LiCAF as a laser material.

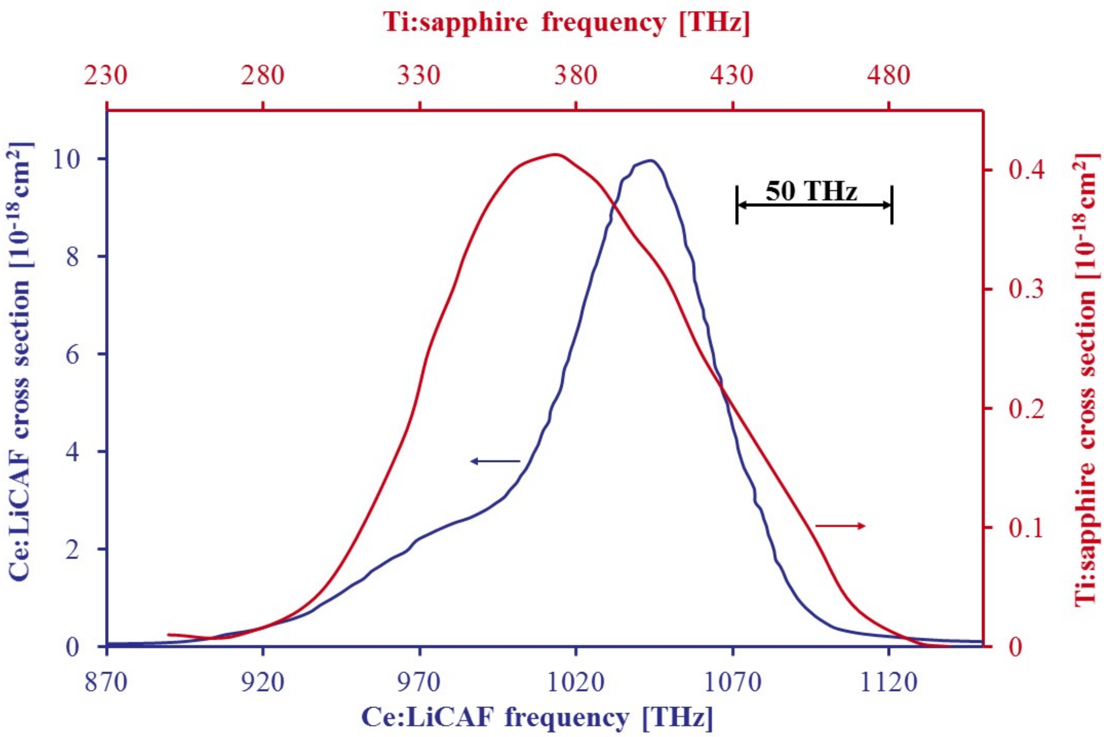

Figure 3.19: Emission cross-section of Ce:LiCAF (blue, left vertical axis) and Ti:sapphire (red, right vertical axis) as a function of frequency. The horizontal frequency axis for Ti:sapphire is on top of the graph and the one for Ce:LiCAF on the bottom. The plot illustrates the similar frequency bandwidths of both materials.

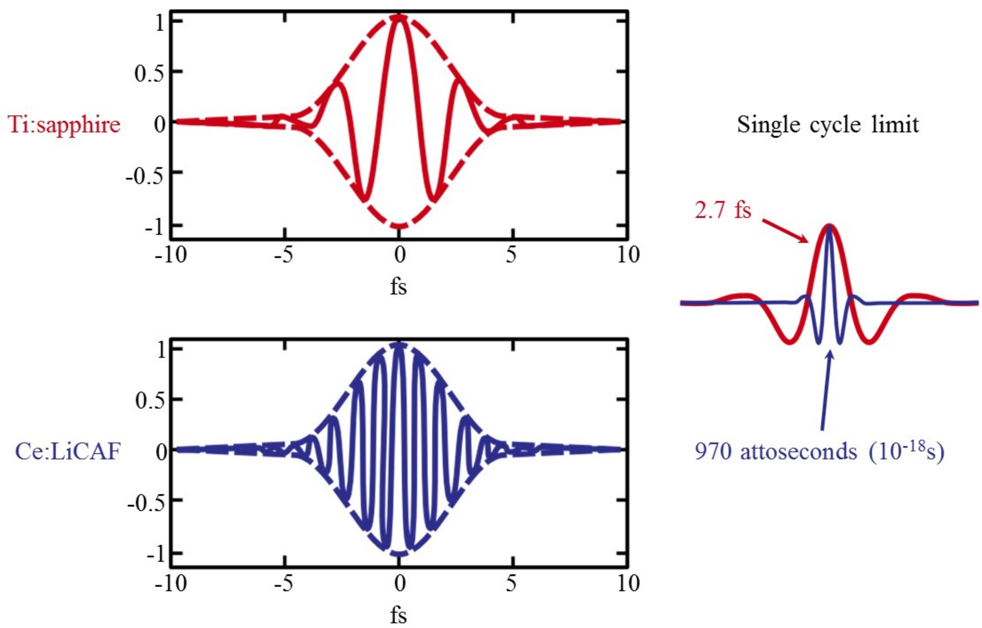

Figure 3.20: Achievable pulse duration and single cycle limit for Ce:LiCAF and Ti:sapphire.

4

Continuous Wave Ce:LiCAF laser

All experimental results presented and discussed in this thesis were achieved using the same basic set-up, which is described and explained in this chapter. The individual settings and modifications to this layout, which were made in order to meet the distinct requirements for each experiment (e.g. different cavity lengths, integration of measurement tools, etc.) are specified later in this thesis where the relevant experiment is discussed.

An overview of the basic set-up of the developed laser system is given in figure 4.1. It consists of an infrared (IR) pump source followed by two frequency doubling stages (which convert the pump light into the UV), a focussing optic and a three-mirror laser cavity. The generation of the UV pump light is discussed in detail in section 4.1. In section 4.2 the laser cavity design is presented and section 4.3 describes the alignment procedure of the laser cavity. The following sections examine characteristics of the continuous wave (CW) laser built: section 4.4 studies the output coupling features, section 4.5 the time domain behaviour, section 4.6 the slope efficiency and laser threshold, and section 4.7 the free running laser spectrum.

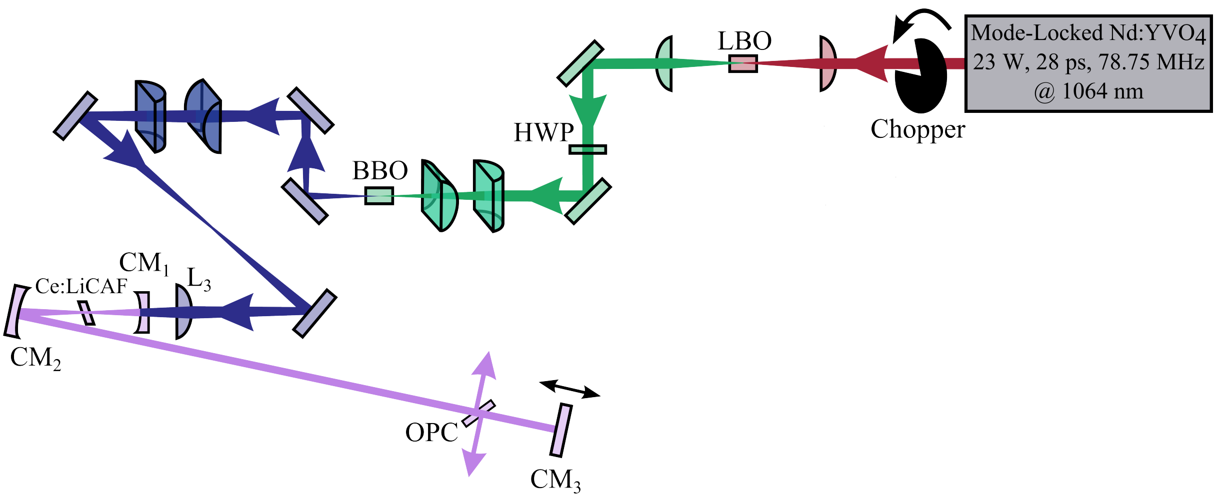

Figure 4.1: Schematic of the experimental set-up. LBO, BBO: frequency doubling stages; HWP: half-wave plate at 532 nm; L_3: spherical focussing lens; CM_1: dichroic cavity mirror with a radius of curvature (ROC) = 5 cm; CM_2: high reflective (HR) cavity mirror with ROC = 10 cm; OPC: output coupler; CM_3: HR plane cavity mirror.

4.1 Laser Pump Light Generation

The basic concept of the pump light generation was adopted from Eduardo Granados Mateo's approach, who developed mode-locked Ce:LiCAF lasers during the first part of his PhD at Macquarie University in 2009 [4]. It has been optimised successfully and as a result stable UV pump pulses can be generated at 266 nm. As a pump source a commercial diode-pumped mode-locked picosecond Nd:YVO_4 laser (Photonic Industries PS-1064-25) was used, which generates 1064 nm 28 ps pulses at a repetition rate of 78.75 MHz with an average output power of 23 W. This pump light was focused into the first frequency doubling stage using an 8 cm focal length spherical plano-convex lens, anti-reflection coated for 1064 nm (L_1). Figure 4.2 shows a schematic of the first doubling stage.

The frequency doubling in this stage is realised via a single pass through a plane cut anti-reflection (AR) coated lithium triborate (LBO) crystal. LBO is a biaxial nonlinear optical material that is well known for temperature-tuned, noncritically phase-matched second-harmonic generation (SHG) [138] and optical parametric oscillation with nanosecond and picosecond laser pulses [139]. Advantageous characteristics of LBO for frequency conversion are the wide transparency range (0.16 µm - 3.5 µm), the moderate nonlinear optical coefficient, the high optical damage threshold (25 GW/cm^2 for a 0.1 ns pulse at 1064 nm) [140] and its suitability for temperature-tuned noncritical phase-matching, which drastically increases

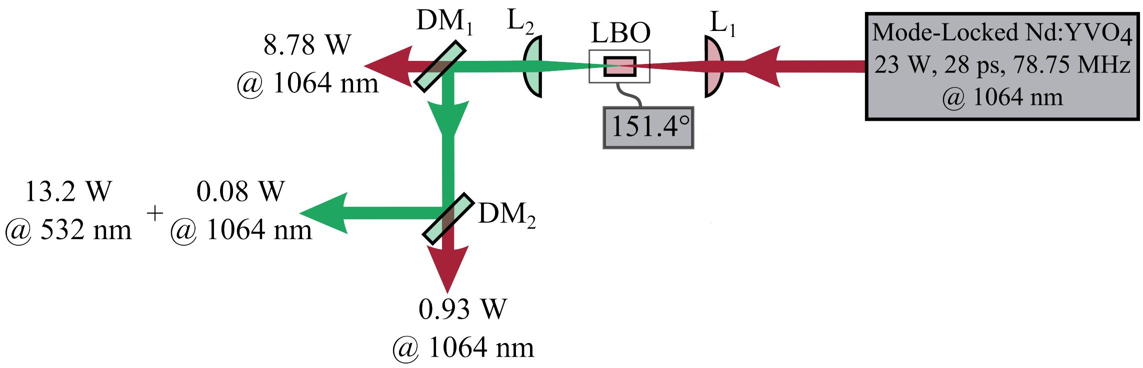

Figure 4.2: Set-up of the first doubling stage.

the angle of acceptance and eliminates beam walk-off [140, 141]. The maximum effective nonlinearity of LBO (d_{eff} = 0.85 pm/V) can be achieved when type-I phase matching becomes noncritical at the crystal orientation $\theta = 90°$ and $\phi = 0°$ [4]. In order to obtain this nonlinearity for the wanted SHG, the LBO crystal used was cut at $\theta = 90°$ and $\phi = 0°$. Its cross-sectional area was 5 mm x 5 mm and it was 3.5 cm long along the optical axis. The focused 1064 nm pulses generated a spot size of approximately 60 µm in the LBO. The crystal was mounted in an oven and heated to 151.4°C (thermally controlled with a temperature resolution better than 0.1°C) where non-critical phase matching occurred. After the LBO, the frequency doubled light at 532 nm was re-collimated using a second 8 cm focal length spherical plano-convex lens (L_2). To separate the residual infrared light after the LBO, two plane dichroic mirrors that transmitted at 1064 nm and reflected at 532 nm were placed in the beam path (DM_1 and DM_2). With a total reflectivity of approximately 98%, the total output power of the frequency doubled light at 532 nm was 13.2 W after the two dichroic mirrors. The residual reflected portion of the 1064 nm light after the two dichroic mirrors was approximately 0.8%.

Subsequent to the first doubling stage, the pump pulses were frequency doubled again in the second doubling stage. For the SHG of the 532 nm light (fourth harmonic of the fundamental infrared 1064 nm) a plane cut AR coated β-barium borate (BBO) crystal was used. BBO has been used in deep UV lasers with pulse repetition rates in the kHz range [142], and in low power CW systems. For low power CW systems, resonant ring cavities must be used in order to achieve adequate efficiencies [143–145]. As Eduardo Granados Mateo established in his work, a single pass arrangement is sufficient for SHG at the peak powers we are working with [4]. There are (more efficient) alternatives to using BBO (e.g. CLBO), but these alternatives present challenges in terms of stability, durability and robustness. The

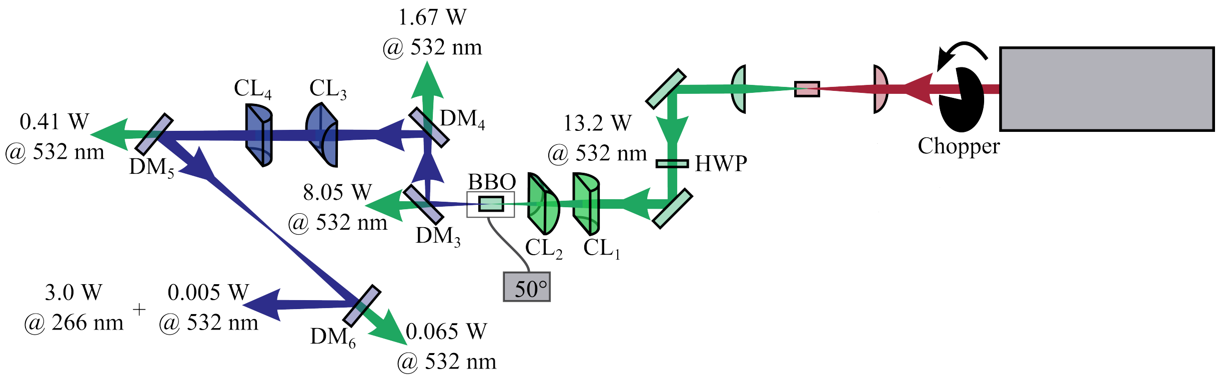

Figure 4.3: Set-up of the second doubling stage.

BBO single pass solution allows a relatively simple set-up for our second doubling stage (see figure 4.3). The crystal used had a cross-sectional area of 5 mm x 5 mm, was 4 mm long, and was cut for type-I SHG. To minimise absorption in the slightly hydroscopic BBO, the crystal was heated to 50°C. The pump light was chopped before being focused into the LBO in order to avoid thermal effects in the second doubling stage. The chopper had an open:closed ratio of 1:11, passing 400 µs bursts of mode-locked pulses every 4.8 ms. Note that all powers are given as the average power during the 400 µs burst; the average powers over the full chopper cycle therefore are 1/12 of the stated powers. To prevent the effects of a large walk-off angle, the 532 nm beam is focussed elliptically into the BBO crystal after passing through a half-wave plate (HWP). This was achieved by using two crossed cylindrical lenses (CL$_1$ with focal length f_{CL1} = 30 cm, and CL$_2$ with focal length f_{CL2} = 10 cm). The resulting elliptical 532 nm focal spot in the BBO crystal had the dimensions of 12 µm x 180 µm (see figure 4.4). The power of the UV light at 266 nm generated by the second doubling stage was 3.0 W, with individual mode-locked pulses having a duration of 23 ps. The 266 nm light was subsequently reshaped using two cylindrical lenses (CL$_3$ with focal length f_{CL3} = 10 cm, and CL$_4$ with focal length f_{CL4} = 10 cm).

Over the course of day-to-day experiments, the second doubling stage exhibited noticeable

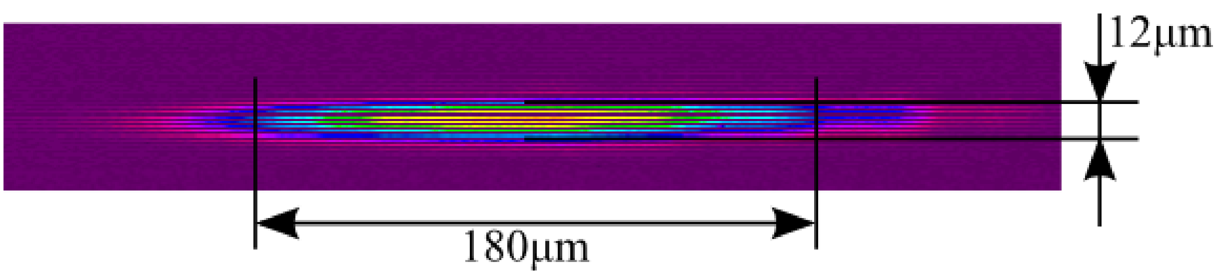

Figure 4.4: Elliptical 532 nm focal spot in the BBO crystal.

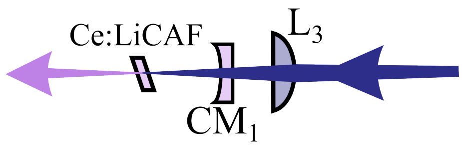

Figure 4.5: Focussing the 266 nm pump beam into the Ce:LiCAF laser crystal.

variabilities. Specifically, every time the system was switched on, the beam path of the 266 nm light generated in the BBO was slightly shifted. This shift was marginal, but nevertheless affected the overall performance of the system. As a result, the positioning of the BBO crystal had to be tweaked slightly for optimal performance each time the system was switched on. In particular, the phase matching angle of the BBO needed to be adjusted. The reason for the shift of the 266 nm beam between on-times could not be clearly identified. Most likely the mount of the BBO, that featured clamps to hold the BBO in place, was altered slightly by temperature and humidity changes in the laboratory and during use. As the air conditioning system in the whole building was unreliable at times, especially during the very hot summer months, temperature and humidity changes could not be avoided over the course of the experiments. In addition, the BBO crystal showed inconsistency in performance. By scanning through the crystal, "sweet spots" with high performance and weak spots with low performance were clearly distinguishable. Coming across a damage spot was also distinctively noticeable when adjusting the crystal for peak performance. The number of damage spots in the BBO crystal increased over time by hitting weak spots during the daily adjustments. BBO crystals hence needed to be replaced every couple of months depending on usage due to failure when hitting clustered damage spots.

Due to the necessary daily tweaking of the BBO positioning, it was easier not to collimate the beam using CL_3 and CL_4, but to form a convergent beam. Four dichroic mirrors that transmitted at 532 nm and reflected at 266 nm were used to separate the residual 532 nm light (DM_3 - DM_6). After DM_6 we measured approximately 3.0 W of 266 nm light and 0.005 W of 532 nm light. The 266 nm pump pulses were then focused by a spherical plano-convex lens (L_3), anti-reflection coated for 266 nm with focal length f_{L3} = 75.6 mm, through the dichroic cavity mirror (CM_1) into the Ce:LiCAF laser crystal (see figure 4.5).

The position of L_3 was adjusted accordingly to the tweaking of the BBO crystal for each experiment to get optimal pumping of the laser crystal. The power of the 266 nm pump beam inside the laser cavity (after CM_1) was 2.8 W. Thus the overall pump efficiency from

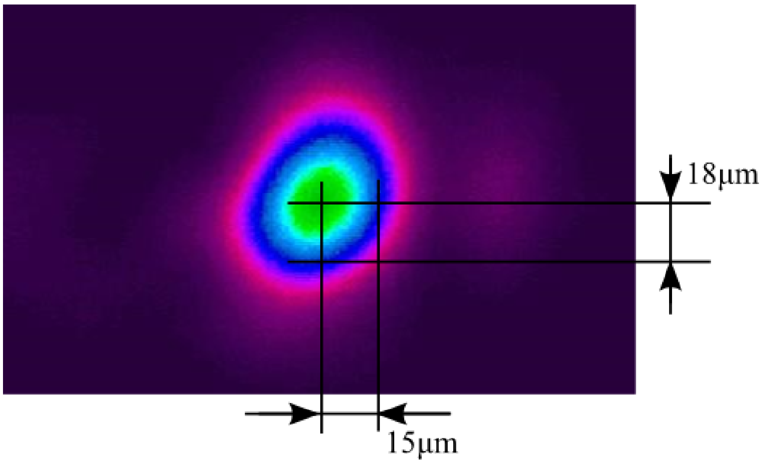

Figure 4.6: 266 nm focal spot in the laser cavity.

23 W of 1064 nm light to 2.8 W of 266 nm light was 12.2%. The 266 nm focal pump spot in the laser cavity was slightly elliptical with a waist (radius at $1/e^2$ of the peak intensity) of 15 μm x 18 μm (measured using a UV camera and verified via knife-edge test). An image of the 266 nm pump spot can be seen in figure 4.6.

4.2 Cavity Design

As shown in figure 4.7, the laser cavity was set up as a three-mirror resonator. All three mirrors were custom coated by Advance Thin Film (ATF) via ion-beam sputtering (IBS). IBS coatings feature lower scatter and absorption losses and fewer pinhole defects in the coated surface than coatings fabricated using standard technologies. CM_1, the dichroic input mirror, was measured to be 92.7% transmissive at 266 nm and highly reflective between 285 nm and 305 nm (0.07% transmittance at 285 nm and 305 nm, with minimum transmittance of approximately 0.04% at 295 nm). It had a radius of curvature (ROC) of ROC_{CM1} = 5 cm. CM_2 and CM_3 were high reflective (HR) coated at 285 nm - 310 nm with ATF stating a transmittance of 0.002% at 285 nm - 300 nm and 0.016% at 310 nm. However, since IBS coatings are designed for maximum reflectivity, absorption losses and scattering dominate the performance rather than transmission, and hence characterising HR mirrors in the UV by measuring the transmittance is not really suitable. Thus, the losses of these mirrors were determined using a ringdown approach as described in the following section 4.3 "Cavity Alignment and Loss Measurement".

CM_2 was a curved HR mirror with ROC_{CM2} = 10 cm and CM_3 was a plane HR cavity

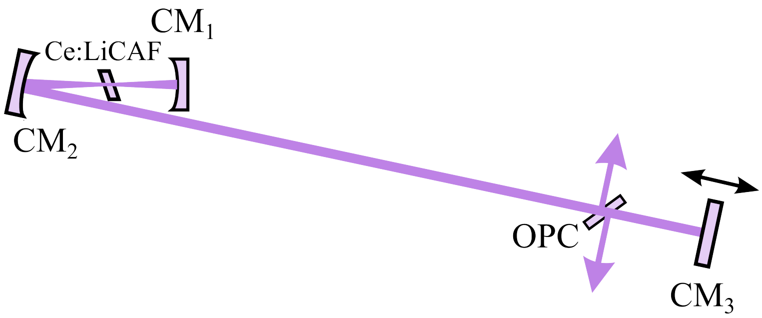

Figure 4.7: Laser cavity set-up.

mirror. The Ce:LiCAF laser crystal was placed in the focal position in the short cavity arm between CM_1 and CM_2. It was a 1.25 mm long 3.5% cerium-doped LiCAF crystal from VLOC, cut at Brewster's angle with the c axis perpendicular to the propagation direction and in the horizontal plane. This cut type was chosen to achieve best laser efficiency for the π-polarised pump and laser beams. The single pass absorption at 266 nm of this crystal was measured to be 70% and the single pass loss at 290 nm was 0.7% (see section 4.3). A 4 mm thick UV-grade silica plate at close-to Brewster's angle was placed in the long cavity arm near to CM_3 as an output coupler (OPC). Using a Brewster plate in this way allows tuning the output coupling fraction to optimise the efficiency of the laser. The folding angle of the laser cavity was set according to the analysis presented by Kogelnik *et al.* in [146] regarding astigmatism compensation for a folded three-mirror cavity. In a three-mirror cavity astigmatism is introduced at the folding mirror and in the Brewster-cut crystal. When using a mirror at oblique incidence, the beam focusses at a different location in tangential and sagittal planes, which leads to two different focal lengths f_s and f_t, which can in terms of the actual focal length f of the mirror be expressed as

$$f_s = f / \cos\theta \quad \text{and} \quad f_t = f \cdot \cos\theta,$$

where θ is half the folding angle α. In a Brewster crystal the beam also travels two different effective distances d_s and d_t in the sagittal and tangential plane.

$$d_s = d\sqrt{n^2+1}/n^2 \quad \text{and} \quad d_t = d\sqrt{n^2+1}/n^4,$$

with n being the refractive index of the Brewster cell (in our case the refractive index of Ce:LiCAF for 290 nm, $n = n_{c290\ nm}$) and d being the thickness of the Brewster cell. Astigmatism can always be compensated at one point in the cavity. Since our OPC is located close to CM_3 we choose CM_3 to be this point. To compensate the astigmatism introduced,

$$f/\cos\theta - f\cdot\cos\theta = d\sqrt{n^2+1}/n^2 - d\sqrt{n^2+1}/n^4$$

must be fulfilled. Since in our case $f = f_{CM2} = 50$ mm, $t = l_c = 1.25$ mm, and $n = 1.41$, $\theta = 6°$ and hence the folding angle α is set to $\alpha = 12°$.

Ideal positioning of the three mirrors within the stability range and important characteristics of the mode inside the laser cavity (e.g. the position and sizes of beam waists) can be calculated via an ABCD transfer matrices analysis of the resonator. The transfer matrix equations for the sagittal (T_s) and the tangential (T_t) plane for our laser cavity are

$$T_s = \begin{bmatrix} A_s & B_s \\ C_s & D_s \end{bmatrix} = \begin{bmatrix} 1 & 0 \\ -f_{CM2}/\cos(\theta) & 1 \end{bmatrix} \begin{bmatrix} 1 & 2l_1 \\ 0 & 1 \end{bmatrix} \begin{bmatrix} 1 & 0 \\ -f_{CM2}/\cos(\theta) & 1 \end{bmatrix}$$
$$\begin{bmatrix} 1 & l_2 + l_3 + l_c\sqrt{n^2+1}/n^2 \\ 0 & 1 \end{bmatrix} \begin{bmatrix} 1 & 0 \\ -1/f_{CM1} & 1 \end{bmatrix} \begin{bmatrix} 1 & l_2 + l_3 + l_c\sqrt{n^2+1}/n^2 \\ 0 & 1 \end{bmatrix}$$

and

$$T_t = \begin{bmatrix} A_t & B_t \\ C_t & D_t \end{bmatrix} = \begin{bmatrix} 1 & 0 \\ -1/(f_{CM2}\cdot\cos(\theta)) & 1 \end{bmatrix} \begin{bmatrix} 1 & 2l_1 \\ 0 & 1 \end{bmatrix} \begin{bmatrix} 1 & 0 \\ -1/(f_{CM2}\cdot\cos(\theta)) & 1 \end{bmatrix}$$
$$\begin{bmatrix} 1 & l_2 + l_3 + l_c\sqrt{n^2+1}/n^4 \\ 0 & 1 \end{bmatrix} \begin{bmatrix} 1 & 0 \\ -1/f_{CM1} & 1 \end{bmatrix} \begin{bmatrix} 1 & l_2 + l_3 + l_c\sqrt{n^2+1}/n^4 \\ 0 & 1 \end{bmatrix}.$$

Here, l_1 is the length of the long cavity arm, l_2 is the distance between CM_2 and the laser crystal and l_3 is the distance between the laser crystal and CM_1.

To determine the stability range of the cavity and to calculate the mode characteristics, the complex Gaussian beam parameter q is used. In our case q is the parameter for the beam propagating through the cavity starting on CM_2 in the direction towards the laser crystal (travelling along z). q is transformed by the ABCD matrix as

$$q' = \frac{Aq + B}{Cq + D}.$$

To ensure laser cavity stability, after each round trip time $q = q'$ must be satisfied. Thus the laser cavity is stable when

$$q = \frac{\frac{A-D}{C}\sqrt{\left(\frac{D-A}{C}\right)^2 + 4\frac{B}{C}}}{2}.$$

In terms of the laser beam size $\omega_l(z)$ and curvature $R_l(z)$, q can be written as

$$\frac{1}{q(z)} = \frac{1}{R_l(z)} - i\frac{\lambda}{\pi n \omega_l(z)^2}.$$

At beam waist locations $q(z)$ must satisfy the condition of a plane wave, that is the condition of infinite curvature. Thus at these locations $q(z)$ is purely imaginary. The size of the waist can then be calculated by

$$\omega_{l,0} = \sqrt{\frac{\lambda_0}{\pi \mathrm{Im}(q)}}.$$

When setting up the cavity for synchronous pumping, the cavity round-trip time must match the round-trip time of the pump pulses, hence

$$l_{syn} = 2 \cdot (l_1 + l_2 + l_3 + l_c) = c/\nu_{R,pump},$$

where c is the speed of light and in our case $\nu_{R,pump}$ = 78.75 MHz. Thus, when calculating the stability range and beam characteristics for this case, the only free parameter is the term $(l_2 + l_3)$, that is the length of the short cavity arm (the length of the crystal excluded). Figure 4.8 shows the calculated results as functions of $(l_2 + l_3)$ for synchronous pumping and astigmatism compensation at CM_3. In figure 4.8 (a) the waist size in the crystal can be seen, in figure 4.8 (b) the distance between the waist in the short cavity arm and CM_2, and in figure 4.8 (c) the waist size in CM_3. In all three graphs the strong dependency on $(l_2 + l_3)$ is clearly visible. As the graphs show, the cavity is stable for 99.3 mm < $(l_2 + l_3)$ < 108.6 mm. In figure 4.8 (c) the waist sizes in the sagittal plane and the tangential plane are identical, which confirms the astigmatism compensation at this point, while in figure 4.8 (a) and figure 4.8 (b) the results are differing between sagittal and tangential plane. The distance between the position of the waist in the sagittal and the tangential plane is approximately 0.6 mm. This is shorter than the thickness of the laser crystal (l_c = 1.25 mm). While at the shorter end of the stability range (around $(l_2 + l_3)$ = 100 mm) the position of the waist is in the centre between CM_1 and CM_2 (the distance between the mirrors here is $(l_2 + l_3) + l_c$ = 101.25 mm and the waist is positioned at approximately 50.6 mm and 51.3 mm from CM_2 for sagittal and tangential plane respectively), it shifts towards CM_1 for larger $(l_2 + l_3)$. At $(l_2 + l_3)$ = 108 mm, that is $(l_2 + l_3) + l_c$ = 109.25 mm, the waist is positioned at approximately 58.4 mm and 59.0 mm from CM_2 for sagittal and tangential plane respectively. Furthermore, the waist size is identical in the sagittal and tangential plane at at shorter end of the stability range, while it diverges towards the longer end of the stability range. Hence we set up the cavity at the

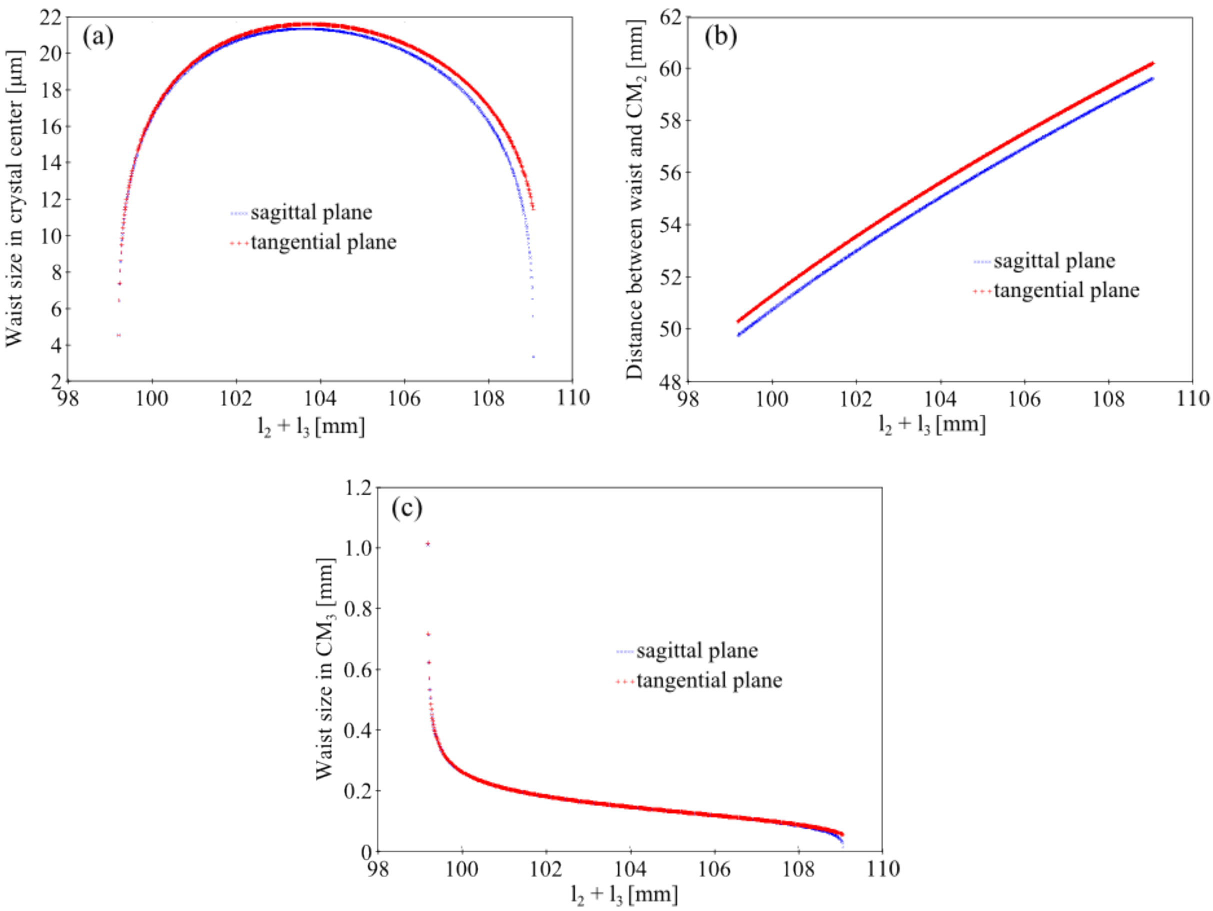

Figure 4.8: Results for synchronous pumping, astigmatism compensation at CM_3.

shorter end of the stability range with a distance between CM_1 and CM_2 of 102 mm and the Ce:LiCaF crystal at 50 mm from CM_1.

4.3 Cavity Alignment and Loss Measurement

As a matter of course, precise alignment of the laser cavity is crucial to achieve lasing. The first thing to ascertain when setting up the laser cavity is the size and position of the pump focus. As mentioned in section 4.1, there was an intermediate focus in the pump beam behind CL_4. The focussing lens L_3 and the dichroic cavity mirror CM_1, through which the pump beam is focussed, act as a compound lens and produce a demagnified version of the intermediate pump focus in the laser cavity (CM_1 is a negative lens in transmission). The size and position of the pump spot can be determined using a knife edge test. The desired distance between the pump spot and CM_1 was a given value predetermined by the calculations described in section 4.2. To adjust the focal position L_3 must be translated. The size of the

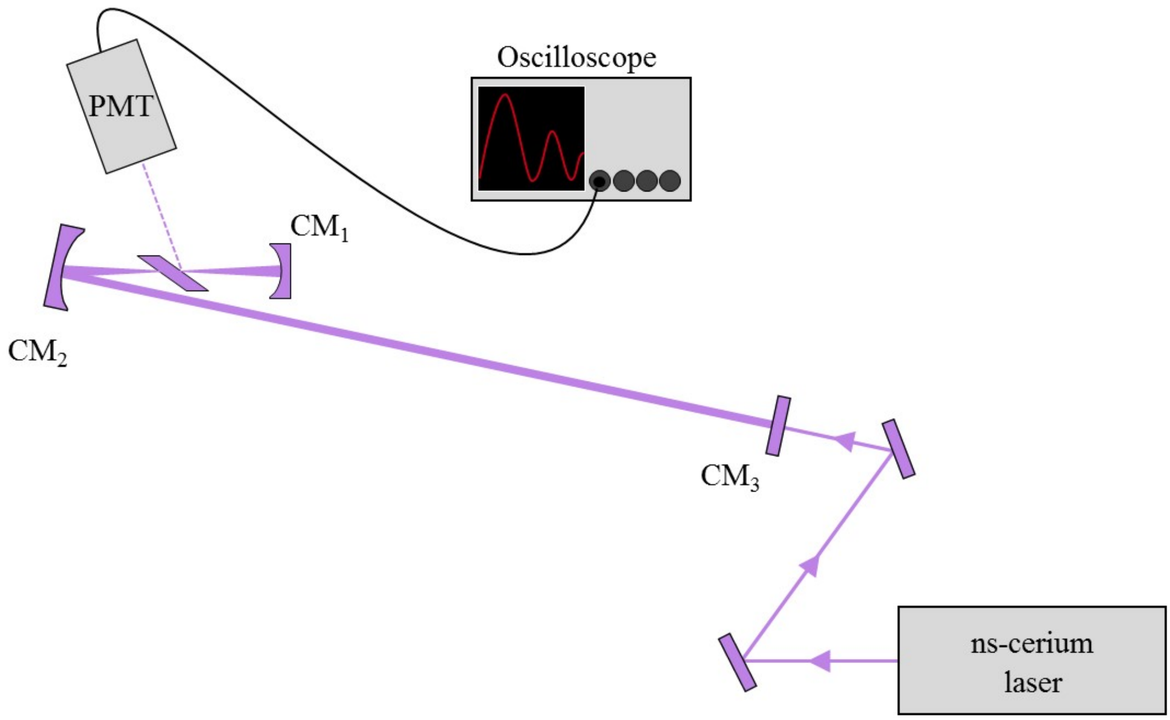

Figure 4.9: Set-up for cavity alignment and loss measurement.

focal spot is determined by the distance between the intermediate pump focus and L_3, which means the separation between the dichroic mirrors DM_5 and DM_6 is decisive. To get a good overlap with the waist of the 290 nm laser beam in the cavity, which was calculated to be around 17 μm when working at the shorter end of the stability range (see figure 4.8), a pump spot radius of 17 μm was desired. As shown in figure 4.6, a slightly elliptical pump spot with a waist of 15 μm x 18 μm was achieved.

Next, the Brewster cut Ce:LiCAF crystal was placed at the focal position of the pump spot. The angle of reflection θ_r, which is the full angle between the incident ray and weak reflected ray with the crystal surface at Brewster's angle, is

$$\theta_r = 2 \cdot \theta_B = 2 \cdot \arctan\left(\frac{n_{c290nm}}{n_{air}}\right) = 109.31°,$$

with $n_{c290nm} = 1.41$ and $n_{air} = 1$. To place the crystal roughly at the right angle in the cavity, the direction of the reflection of the 266 nm pump beam was measured using a protractor. Once the cavity was fully set up, the angle of the crystal was fine tuned by observing the reflection of the 290 nm laser beam. CM_2 was then placed at the predetermined distance from the focal spot with the calculated folding angle (see section 4.2). To align the laser cavity, a separate ns-cerium laser [131] was used as a probe laser. It was aimed at CM_2 at an angle of

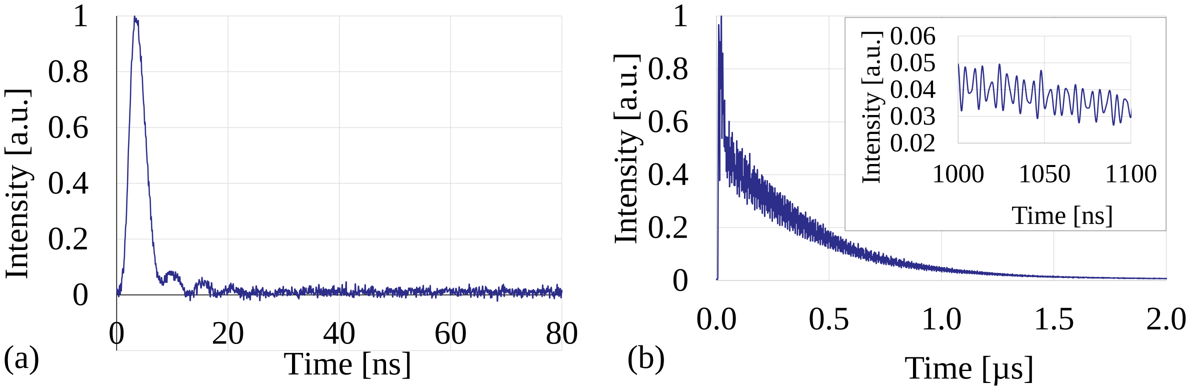

Figure 4.10: PMT-measurements (a) single pulse in open cavity (without CM_3), (b) ringdown pulse decay in aligned cavity.

12° to overlap the pump beam (see figure 4.9). The idea was to align the probe laser beam with the pump as well as possible and then to use a ringdown approach to align the laser cavity precisely and to ensure that cavity losses are minimised. Once the probe laser beam and the pump were overlapped on CM_2 and the short cavity arm (using pinholes and targets marked on paper), CM_3 was put in the beam and aligned giving the best back reflection of the probe laser (checked with pinholes in the probe beam). To measure the ringdown signal, a Hammamatsu H10721-210 compact photomultiplier tube (PMT) connected to an oscilloscope, was used as a detector. It collected the 290 nm reflection of the probe laser beam coming off the surface of the Ce:LiCAF crystal (or the transmitted 290 nm light through the dichroic CM_1 when measuring without the crystal in the cavity). This way the decay time of the probe pulses in the cavity could be displayed on the oscilloscope. The longer the decay time, the lower the losses of the cavity and the better the alignment. Figure 4.10 (a) shows a single nanosecond probe pulse in the open cavity without CM_3 and figure 4.10 (b) shows the ringdown pulse decay for the aligned cavity with CM_3 in place. In the inset of figure 4.10 (b) a zoomed version of the ringdown trace is given. The separate peaks of the round-trip pulses are clearly visible. Here, the cavity had a total length of 1.43 m, thus the round-trip time was 4.8 ns.

The ringdown approach can also be used to measure the losses introduced by the cavity elements. The pulse decay follows $1/e$ on average. Thus on a logarithmic scale it comprises a straight line. The peak intensity I of the pulse after each round-trip time can be fitted using the equation

$$I = I_0 \left(1 - e^{-T_R/\tau_I}\right) + I_b,$$

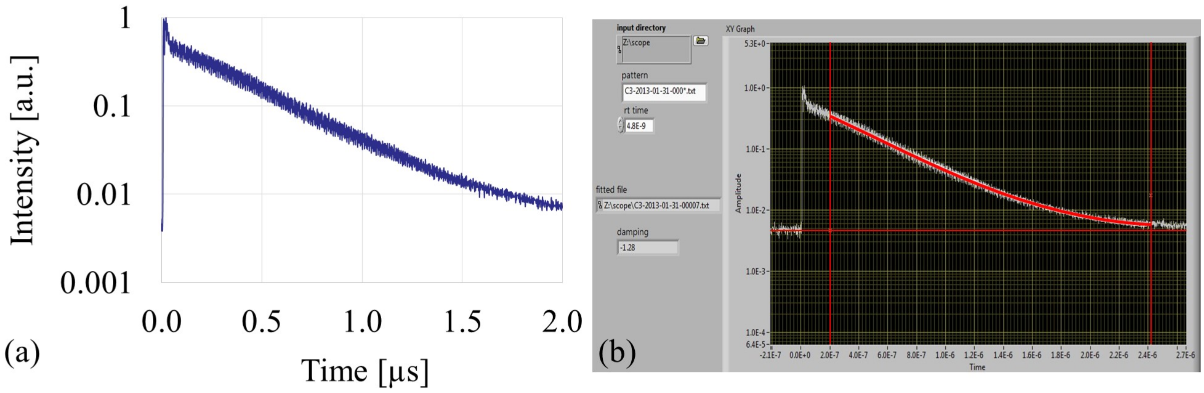

Figure 4.11: (a) Ringdown pulse decay shown on a logarithmic intensity-axis, (b) control-panel of the LabView program witten to calculate the losses of the ringdown cavity showing the fit to the data in red.

where T_R is the cavity round-trip time, τ_I the decay time of the peak intensity, and I_b is the intensity of the background noise. The ringdown pulse decay of figure 4.10 (b) can be seen on a logarithmic intensity scale in figure 4.11 (a). In figure 4.11 (b) the control panel of a LabView Program to calculate the cavity losses of a ringdown cavity is displayed. The red curve is the fit to the data. In the given example the cavity had a total loss of 1.28%. To measure the combined loss of the three cavity mirrors without the crystal in the cavity, the PMT was placed behind the dichroic CM_1. This was possible because the pump beam was not needed for these measurements. The ringdown measurements revealed the importance of keeping the cavity mirrors in a scrupulously clean state, and it affirmed that even if the mirrors seemed clean to the naked eye, they might actually not be. Cavity losses were measured multiple times with cleaning of one mirror at a time between measurements using different cleaning techniques. As a result, drag-wiping was identified as a poor cleaning method for the cavity mirrors. Instead, cleaning by firmly swiping a lens cleaning tissue dampened with methanol over the mounted mirror provided best results. It became clear that monitoring the mirror cleanliness via ringdown measurement is important to guarantee best overall performance of the Ce:LiCAF laser.

The total round-trip loss of the cavity with all three mirrors featuring best possible cleanliness, but without the crystal and without the OPC was measured to be 1.1%. Placing the crystal in the cavity increased the loss to 2.5%, thus the double pass loss of the crystal was determined to be 1.4%, that is the single pass loss of the crystal is 0.7%. The ringdown approach was also used to optimise the cavity fold angle. With losses featuring a distinct

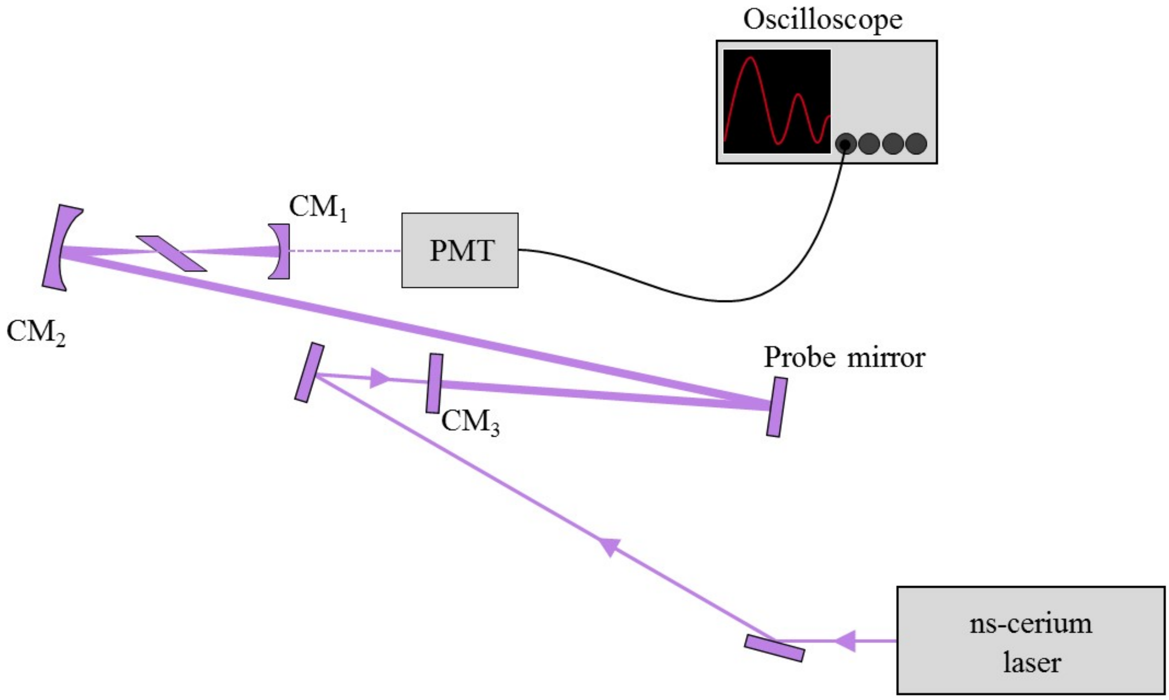

Figure 4.12: Set-up for loss measurement of cavity elements.

minimum at the astigmatism compensating angle, the fold angle can be adjusted precisely.

To measure the loss of the individual cavity mirrors, the set-up was rearranged as drawn in figure 4.12. The total cavity length was kept identical (thus the round-trip time was kept identical), but a fourth mirror was placed in the long cavity arm, so that a third arm was formed. The probe beam still entered the cavity through the back of the cavity end mirror (CM_3). Since the loss of the three mirror cavity was already measured before, by placing different mirrors as the probe mirror, the losses of these individual mirrors could be determined as half the measured increase in loss. We measured plane mirrors that were coated by ATF in the same coating run as the mirrors we use to build the cavity. The measured losses of the cavity elements are summarised in table 4.1. Thus, according to the measurements, the total loss of our cavity without the crystal and without the OPC (L_{em}) should be

$$L_{em} = L_{CM1} + L_{CM2} + L_{CM3} + L_{CM2} =$$

$$= 0.45\% + 0.2\% + 0.2\% + 0.2\% = 1.05\%.$$

This is in agreement with our previously measured value of 1.1%, which confirms the underlying assumption that mirrors coated in the same coating run feature the same loss.

Table 4.1: Measured losses of the cavity elements.

Cavity Element	**Loss**
ATF coated HR mirror	0.2%
AFT coated dichroic mirror	0.45%
Ce:LiCAF crystal (single pass)	0.7%

Quantification of the losses of each cavity element reveals why it is sensible to use an HR mirror as the folding mirror of the three-mirror cavity. Since the beam inside the cavity gets reflected twice per round trip by the folding mirror, but only once by the two end mirrors, by using a dichroic mirror as the folding mirror and two HR end mirrors, L_{em} would increase by 0.25% to 1.3%. Similarly, setting up the laser cavity as a symmetrical four-mirror cavity with two curved folding mirrors (two reflections per round trip each) and two plane mirrors (one reflection per round trip each), would lead to L_{em} = 1.45% using one of the plane mirrors as a dichroic input coupling mirror, or even L_{em} = 1.7% using one of the folding mirrors as a dichroic input coupling mirror.

In addition to the ATF mirrors used for the set-up of the presented laser system, the mirrors coated by Melles Griot that were used by Eduardo Granados for the experiments were also diagnosed. Their losses were determined to be 0.5% each, with no significant difference between the dichroic and HR mirrors. Moving from these mirrors to the ATF coated mirrors when starting the experiments for the presented PhD project, hence reduced the losses of the three-mirror cavity by 0.95%.

4.4 Output Coupling

As mentioned in section 4.2, a 4 mm thick UV-grade silica plate was used as an output coupler (OPC). The OPC was placed in the long cavity arm of the laser cavity close to the HR end mirror CM_3 at close-to Brewster's angle. Using this type of OPC instead of an output coupling end mirror has many advantages: It can be rotated, removed or added easily without changing the cavity alignment, since the end mirror CM_3 is a plane mirror. Thus the laser cavity can be initially aligned with a high Q cavity. The total cavity loss of the mirrors and the crystal, but without the output coupler was L_t = 2.45%. The OPC provided a variable

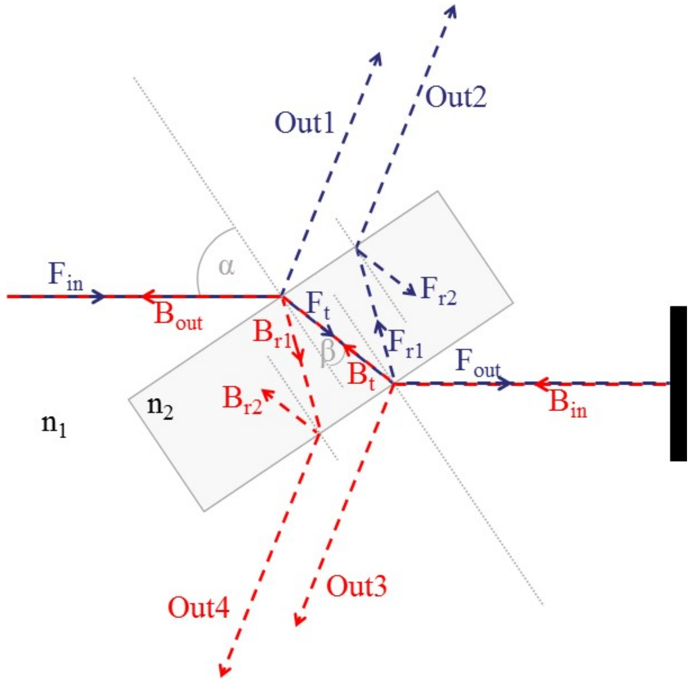

Figure 4.13: Schematic of the beam paths through the OPC

additional loss to the cavity, that was highly dependent on the angle of the OPC relative to the beam inside the laser cavity. In figure 4.13 a schematic of the geometry of the beam paths is given. The forward travelling beam F_{in} coming from CM_2 is incident on the OPC under the angle α. Part of F_{in} is transmitted into the OPC (F_t) with the internal refractive angle β, the rest is reflected and becomes part of the laser output ($Out1$). Similarly, F_t is split at the second interface. The transmitted beam F_{out} that is backreflected at CM_3, travels back as B_{in} and is split into B_t and $Out3$ when hitting the OPC again.

Due to the geometry of the plane-parallel OPC, all external angles to the normal of the interface are the same (angle α), and all internal angles to the normal are also the same (angle β). The relationship of the angles α and β is given by Snell's law

$$n_1 \sin\alpha = n_2 \sin\beta,$$

with n_1 being the refractive index of the surrounding air ($n_1 = 1.0002931$ for $\lambda = 290$ nm) and n_2 being the refractive index of the quartz OPC ($n_2 = 1.4908$ for $\lambda = 290$ nm). The reflectivity R and the transmission T at the interfaces for the π-polarized light are given by the Fresnel equations

$$R = \left[\frac{n_1\sqrt{1 - \left(\frac{n_1}{n_2}\sin\alpha\right)^2} - n_2\cos\alpha}{n_1\sqrt{1 - \left(\frac{n_1}{n_2}\sin\alpha\right)^2} + n_2\cos\alpha} \right]^2$$

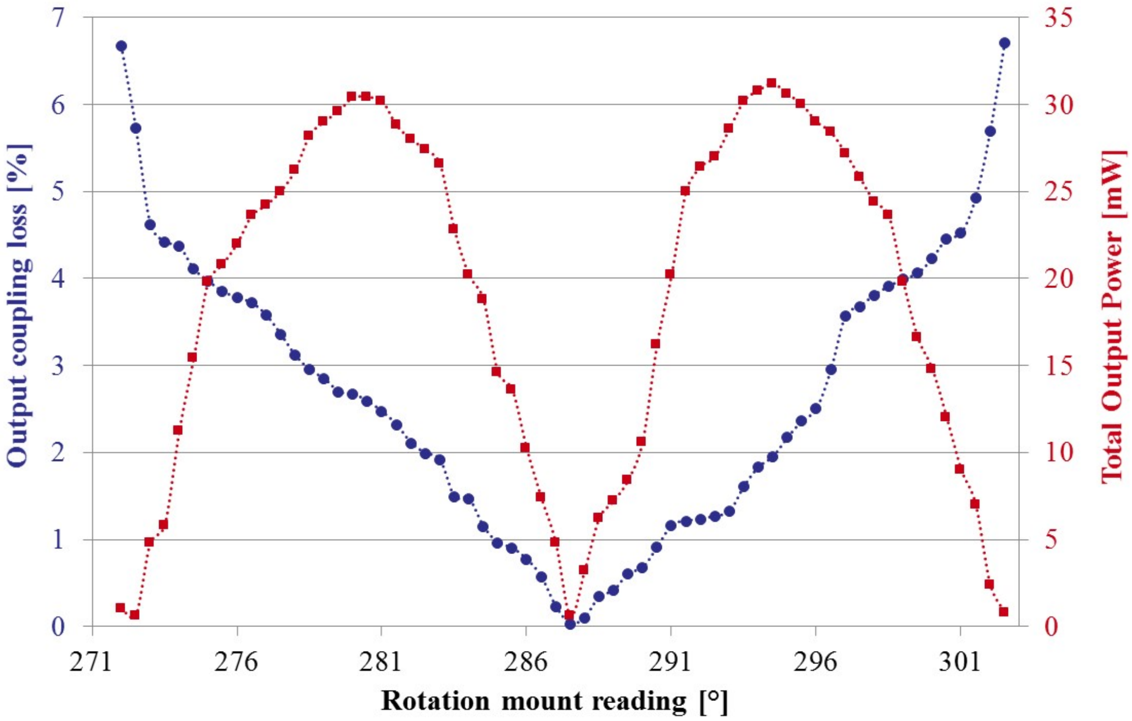

Figure 4.14: Measured output coupling loss in % and laser output power in mW as a function of the reading on the rotation mount holding the output coupling SiO_2 plate.

and

$$T = 1 - R.$$

The total loss L_{OPC} introduced by the OPC is

$$L_{OPC} = \frac{F_{in} - B_{out}}{F_{in}} = 1 - T^4,$$

with $F_{out} = F_t T$, $F_t = F_{in} T$, $B_{out} = B_t T$, $B_t = B_{in} T$, and $B_{in} = F_{out}$, since the loss of CM_3 is included in the cavity loss L_t (see above) and does not need to be taken into account here.

The total laser output is

$$Out = \frac{Out1 + Out2 + Out3 + Out4}{F_{in}} = R + RT^2 + RT^2 + RT^4 = R\left(1 + T^2\right)^2,$$

with $Out1 = F_{in}R$, $Out2 = F_{r1}T$, $F_{r1} = F_t R$, $Out3 = B_{in}T$, $Out4 = B_{r1}T$, and $B_{r1} = B_t R$. The different output beams do not overlap and hence do not interfere.

The total laser output can also be written as

$$Out = L_{OPC} - \frac{F_{r2} + B_{r2}}{F_{in}},$$

with $F_{r2} = F_{r1}R$, and $B_{r2} = B_{r1}R$.

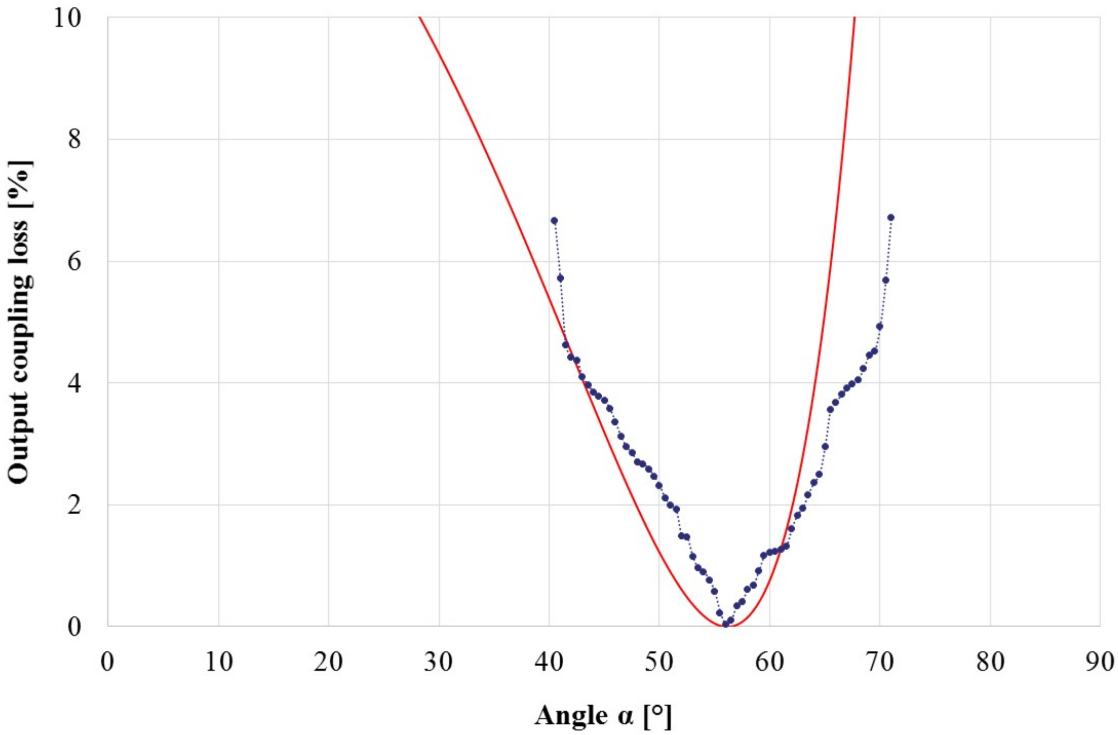

Figure 4.15: Predicted and measured output coupling loss in % as a function of the angle of incidence α. Based on the measurement results, the Brewster's angle was determined to be at the 287.5° mark on the rotation mount, the x-axis of the measurement was translated accordingly.

Experimentally, the loss introduced by the OPC was measured using the ringdown approach. At the same time, the output power off the OPC was measured, with all reflections from the OPC plate being included in this power measurement. The output power coming off the surfaces of the laser crystal at Brewster's angle was not substantial and was thus neglected. The measured output coupling loss and the laser output power as a function of the reading on the rotation mount holding the OPC can be seen in figure 4.14. At Brewster's angle, theoretically $L_{OPC} = 0$, with L_{OPC} increasing as the plate is rotated away from Brewster's angle in both directions. Experimentally, the additional loss due to the OPC at Brewster's angle was less than the error on our measurement, <0.05%. Hence, Brewster's angle was determined to be at the 287.5° mark on the rotation mount. For angles close to Brewster's angle as used for the output coupling here, F_{r2} and B_{r2} are very small, hence Out$\approx L_{OPC}$. In figure 4.15, the predicted output coupling loss L_{OPC} is plotted over the angle of incidence α, in addition to the measured output coupling loss. The x-axis of the measurement was translated based on the determination of the location of Brewster's angle on the rotation mount. Predicted and measured results are in good agreement. Figure 4.16 finally shows the laser output power in

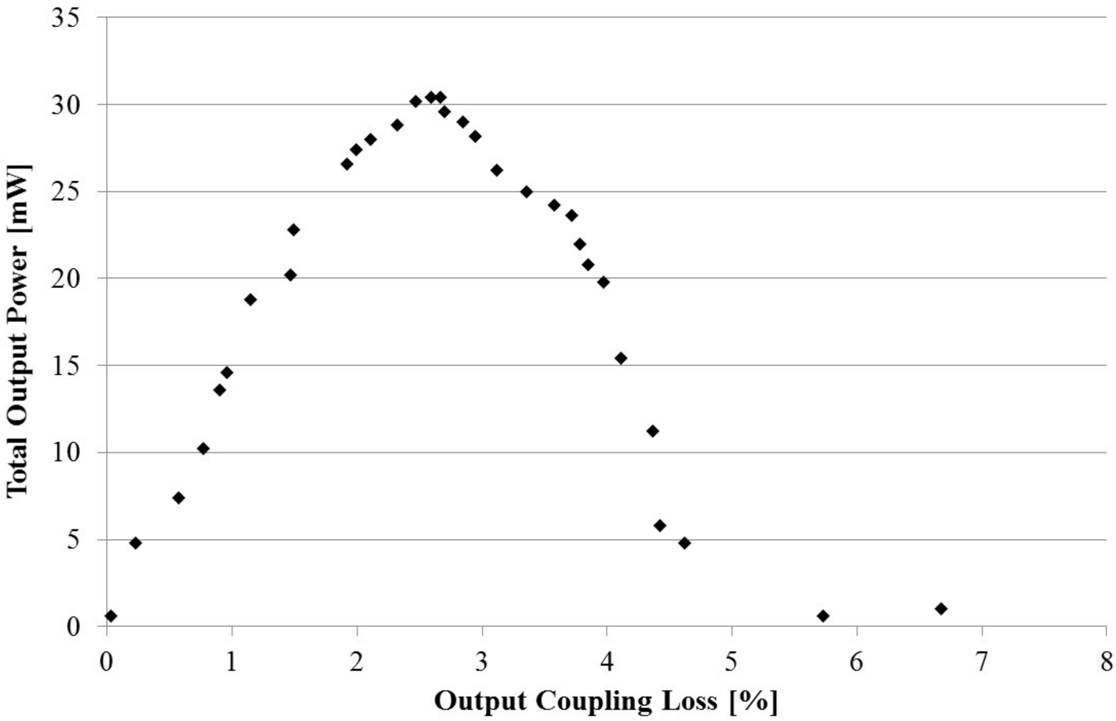

Figure 4.16: Measured laser output power in mW as a function of the output coupling loss.

mW as a function of the round-trip output coupling loss introduced by the OPC. As the graph illustrates, the maximum laser output power was observed for a measured output coupling loss of L_{OPC} = 2.5% (which corresponds to an angle of 7.5° relative to Brewster's angle). The following power measurements were taken with the OPC at this optimum angle.

4.5 Time Domain Behaviour

In this section and in the following sections 4.6 and 4.7, the laser output is characterised for a laser cavity with a length of 0.754 m, where the modulation of the laser output is at a minimum and can be described as CW. In the next chapter 5, theory to explain why this cavity length is optimal for CW lasing will be presented and the laser behaviour is compared to a numerical model. Figure 4.17 shows the measured Ce:LiCAF laser output during one opening of the chopper plotted as a function of time. Note that the chopper was placed in the pump beam to avoid thermal effects in the second doubling stage (see section 4.1) and all given powers in this chapter are average powers during the open-period of the chopper. The time trace given in figure 4.17 was measured with a ns-photodiode (accordingly with a maximum bandwidth of 1 GHz) displayed with an oscilloscope sample rate of 10 GBit/s. After an initial build-up

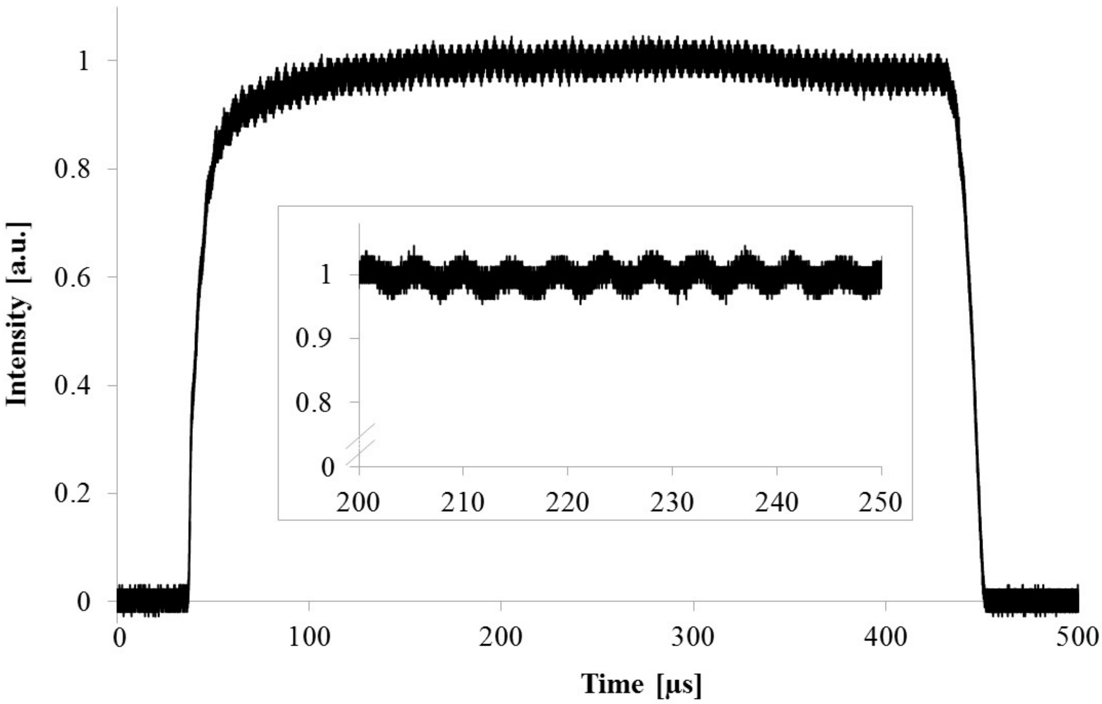

Figure 4.17: CW-laser output during one opening of the chopper, measured on a ns-photodiode displayed with an oscilloscope sample rate of 10 GBit/s.

time of around 20 µs, the laser output is stable over the rest of the 400 µs chopper opening time. In the inset of figure 4.17, the laser output is given over a time frame of 50 µs, which clearly reveals a 4.55 µs ripple. This ripple, which produces an approximately 5% amplitude modulation on the Ce:LiCAF output, is caused by a small 220 kHz modulation on the pump laser pulse train. This modulation is not related to the mode-locked pumped CW dynamics and would be absent with a smooth mode-locked pump laser. A zoom of the time trace over 150 ns and 42 ns is shown in Fig. 4.18. It is on these timescales that we see dynamics caused by mode-locked pumping. These dynamics are discussed in detail in the next chapter 5. The modulation was measured to be just ±1% for frequencies below 1 GHz.

4.6 Slope Efficiency

For a cavity length of 0.754 m, the laser output power as a function of the pump input is shown in Fig. 4.19. Using a polariser and $\lambda/2$-waveplate to attenuate the pump, the laser threshold was determined to be 1.37 W, and the maximum laser output power achieved was 288 mW at an input power of 2.80 W. In [136] Payne et al. discuss models to calculate the slope

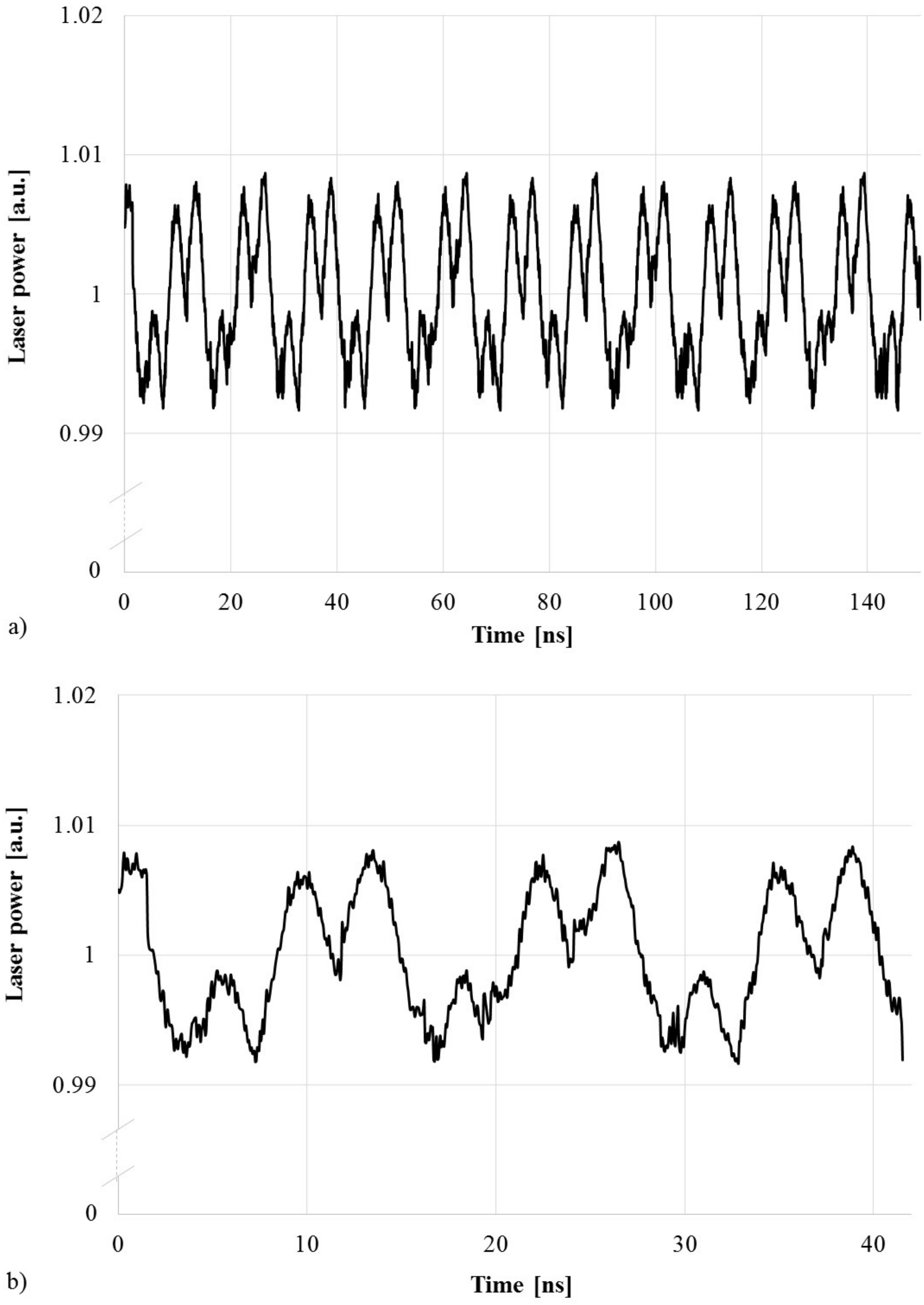

Figure 4.18: Measured CW laser output over a time frame of a) 150 ns and b) 42 ns. The modulation is of the order of 1% for frequencies below 1 GHz.

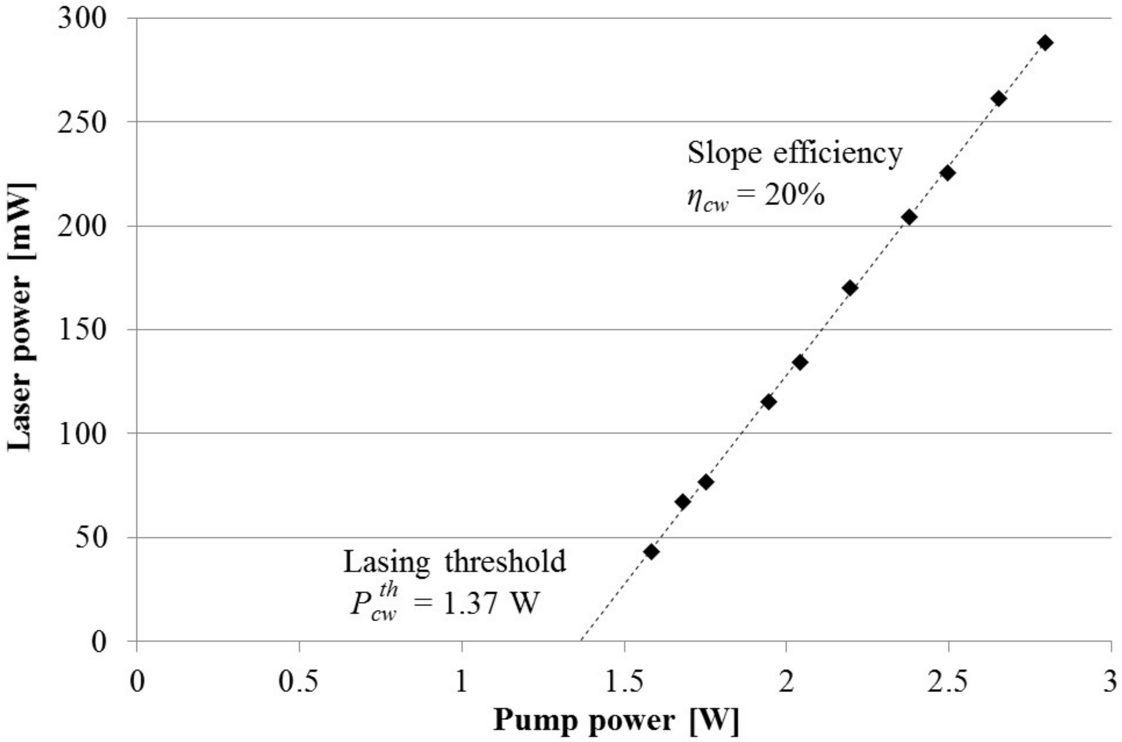

Figure 4.19: Slope efficiency for maximum power output coupling.

efficiency and the lasing threshold for Cr^{3+}:LiCAF CW-lasers theoretically. Alderighi *et al.* transferred and verified these equations in [135] for Ce:LiCAF. The CW-slope efficiency η_{CW} can thus be calculated as

$$\eta_{CW} = \eta_p \eta_a T_{DM} \left(\frac{\lambda_p}{\lambda_l}\right) \left(\frac{L_{OPC}}{L_{OPC} + L_t}\right) \left(\frac{\sigma_{em} - \sigma_{ESA}}{\sigma_{em}}\right).$$

Here, η_p is the pump efficiency, η_a is the pump absorption, T_{DM} is the transmission of the dichroic input mirror for the pump beam; the term in the first bracket describes the quantum efficiency η_q, and the term in the second bracket is the output coupling efficiency η_{opc}. η_p was set to 1, $\eta_a = 90\%$ (this includes absorption of the residual pump during its second pass through the cerium crystal, as discussed later), and $T_{DM} = 91\%$. The effect of excited-state absorption (ESA) of the laser radiation in Ce:LiCAF is taken into account by the term in the third bracket. The importance of ESA in Ce^{3+} doped materials was first noted in 1978 by Jacobs *et al.* [147] and Miniscalco *et al.* [148], who reported intense ESA in Ce:$Y_3Al_5O_{12}$ (Ce:YAG), which is high enough to prevent any gain. Pedrini *et al.* [149] and Hamilton *et al.* [150] confirmed later that ESA is caused by the transition of an electron from the 5d orbital of the Ce^{3+} ion to the conduction band (CB) of the host medium (a schematic of the energy levels in Ce^{3+}-doped fluoride lasers emphasizing the excited-state absorption is given in figure 4.20). 5d → CB ESA was also found in other rare-earth-doped materials like

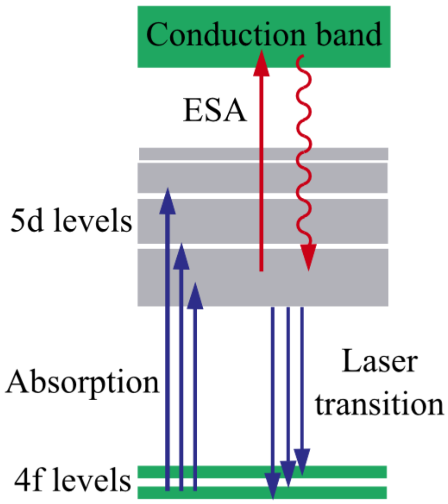

Figure 4.20: Schematic of the energy levels in Ce:LiCAF, showing the excited state absorption (ESA) from the $5d$ levels to the conduction band.

Sm^{2+}:CaF_2 [151], Eu^{2+}:CaF_2 [152], and other Eu^{2+} crystals [153], substantiating ESA as general feature in this type of material and linking it to the observed lack of UV laser emission or relatively low laser slope efficiencies for rare-earth-doped crystals. It was reported that the peak energy at which ESA occurs is related to the relative positions of the impurity energy levels within the band gap of the host [103, 149, 153]. In [103] Marshall *et al.* investigated the emission properties of Ce:LiSAF and Ce:LiCAF in detail. It was found that, while in both Ce:LiSAF and in Ce:LiCAF the $5d \rightarrow$ CB ESA transition is present, it is less prominent leading to high laser efficiencies relative to the other solid-state UV laser materials. One of the most important discoveries of Marshall *et al.* was the finding that ESA in Ce:LiSAF and in Ce:LiCAF is anisotropic, being two times larger for σ-polarized light than for π-polarized light in Ce:LiCAF. The anisotropy was attributed to the crystal structure and the direction of the electron transfer within the crystal. Anisotropic ESA had not been observed before in any other $5d \rightarrow$ CB transition. The ESA cross section σ_{ESA} was quantified by relating it directly to the effective gain cross section σ_{eff} and the emission cross section σ_{em}

$$\sigma_{eff} = \sigma_{em} - \sigma_{ESA}.$$

σ_{em} was determined experimentally from the π- and σ-polarized emission spectrum to be $9.6 \cdot 10^{-18}$ cm^2 (see figure 3.5 in chapter 3.3), and σ_{eff} from the π- and σ-polarized small-signal single-pass gain spectrum. As a result, Marshall *et al.* estimate the ESA cross section σ_{ESA} of Ce:LiCAF for π-polarized light to be $3.6 \cdot 10^{-18}$ cm^2. With this value, the theoretically-predicted slope efficiency can be calculated to be $\eta_{CW} = 23.7\%$. This theoretical value is in good agreement with the measured value of 20%. To adapt the theoretical value of the slope efficiency to the measured result, a factor $\eta_o = 0.81$, the overlap efficiency, was included in the above equation.

The CW-lasing threshold P_{CW}^{th} is calculated using the model

$$P_{CW}^{th} = \frac{\pi \omega_l^2 h \nu_l \left(L_{OPC} + L_t\right) n}{2\left(\sigma_{em} - \sigma_{ESA}\right) \tau \eta_p \eta_a T_{DM}},$$

where ω_l is the radius of the cavity mode waist in the laser cavity, ν_l is the laser frequency, τ is the fluorescence lifetime, and $n = 1.41$ is the refractive index (which appears here owing to the Brewster crystal). With a radius of the cavity mode waist ω_l of 17 µm, as calculated in chapter 4, the model gives a lasing threshold of $P_{CW}^{th} = 1.91$ W, which is slightly larger than the observed value of 1.37 W. However, the laser cavity mode size of $\omega = 17$ µm assumed a laser cavity length equal to the pump cavity length for synchronous mode-locking and the actual result was the waist size as a function on the length of the short cavity arm (between CM_1 and CM_2). The limits for the waist size are ≈5 µm (for a mirror separation close to the ends of the stability range at around $(l_2 + l_3) = 9.95$ cm and $(l_2 + l_3) = 10.9$ cm) and 22 µm in the middle of the stability range at around $(l_2 + l_3) = 10.4$ cm (see fig 4.8). Given that the dynamics in our configuration used for CW output with a cavity length of 0.754 m may differ from the synchronous set-up, it is likely that the calculated waist size is inaccurate. Varying the waist size to $\omega_l = 12.9$ µm matches the measured result of a laser threshold of 1.37 W.

It should also be mentioned that in [154], for the same laser, a slope efficiency of 33% and a laser threshold of 2.2 W was reported. It was stated that the high discrepancy between the measured slope efficiency of 33% and the theoretical slope efficiency of 23.7% is most likely due to a lower value for the ESA cross section than the estimated value of $\sigma_{ESA} = 3.6 \times 10^{-18}$ cm^2 given by Marshall et al., which was used in the calculation. However, when repeating the experiments, a calibration issue in the powermeters used to previously measure the slope efficiency became clear. Replicating the measurement with a new, accurately calibrated powermeter, led to the above stated slope efficiency of 20%. Also, it was determined that the pump laser repetition rate was precisely 78.75 MHz, instead of 80 MHz as stated in [154].

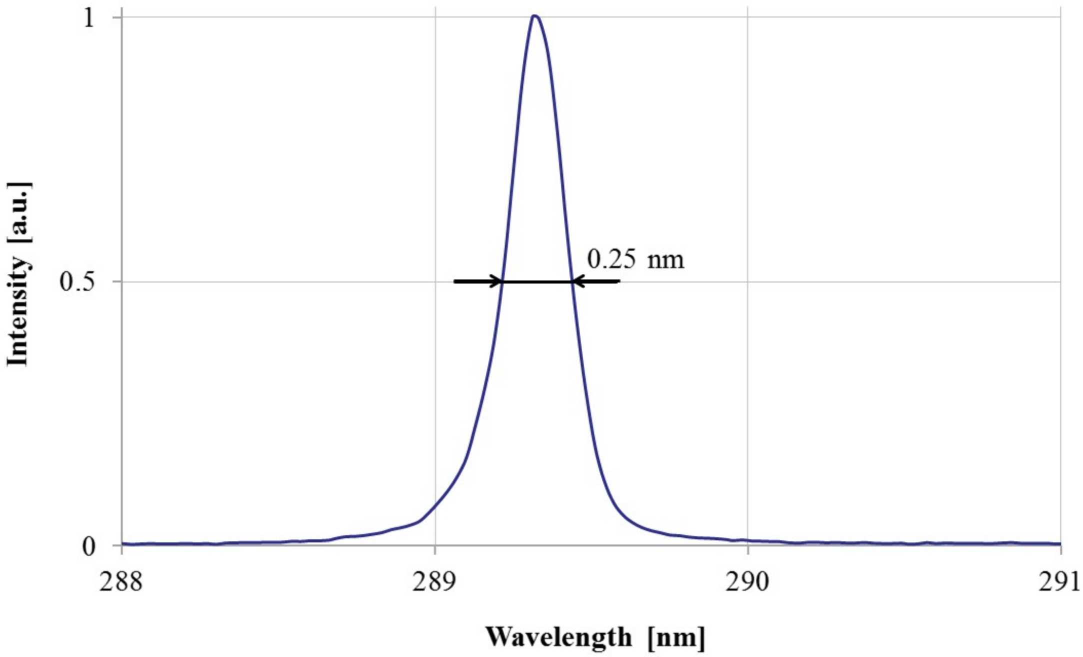

Figure 4.21: Spectrum of the free running laser without OPC.

4.7 Free Running Laser Spectrum

The output spectrum shown in figure 4.21 was measured for a free-running laser with a cavity length of 0.754 m without the OPC in the long cavity arm. The laser signal was captured off the Brewster's angle of the Ce:LiCAF crystal and measured with an Ocean Optics HR4000 spectrometer with a resolution of 0.05 nm. As shown in the figure, the peak wavelength of the laser was at 289.30 nm with a full width at half maximum (FWHM) linewidth of 0.25 nm. With the OPC in the long cavity arm for maximum output power the laser operated at 289.50 nm with a linewidth of 0.20 nm.

The main results of this chapter were published in: B. Wellmann, D.J. Spence, and D.W. Coutts, "Tunable continuous wave deep-UV laser based on Ce:LiCAF", Optics Letters, Vol.39, No.5, 1 March 2014, pp. 1306-1309 (see appendix A "Publications Arising from this Thesis").

5

Analysis of Mode-Locked Pumped CW Lasers

5.1 Synchronous and Asynchronous Pumping

When pumping a solid-state laser with a mode-locked pump source, the length of the laser cavity determines the laser operation mode. Each successive pulse from the mode-locked pump is incident at the laser crystal with some specific timing relative to the circulating laser cavity field. If that timing is the same for every pump pulse, then we have synchronous mode-locking, where a single pulse is formed in the laser cavity field, and that pulse arrives at the gain crystal synchronised with each pump pulse. Clearly this occurs when the pump cavity length and laser cavity lengths are matched; it also occurs when the laser cavity length is any integer fraction of the pump cavity length. For N-th harmonic locking, the laser cavity is N-times shorter than the pump cavity, and the pulse in the laser cavity makes N round trips between each synchronised pump event. The relative timing of the pump pulse and the

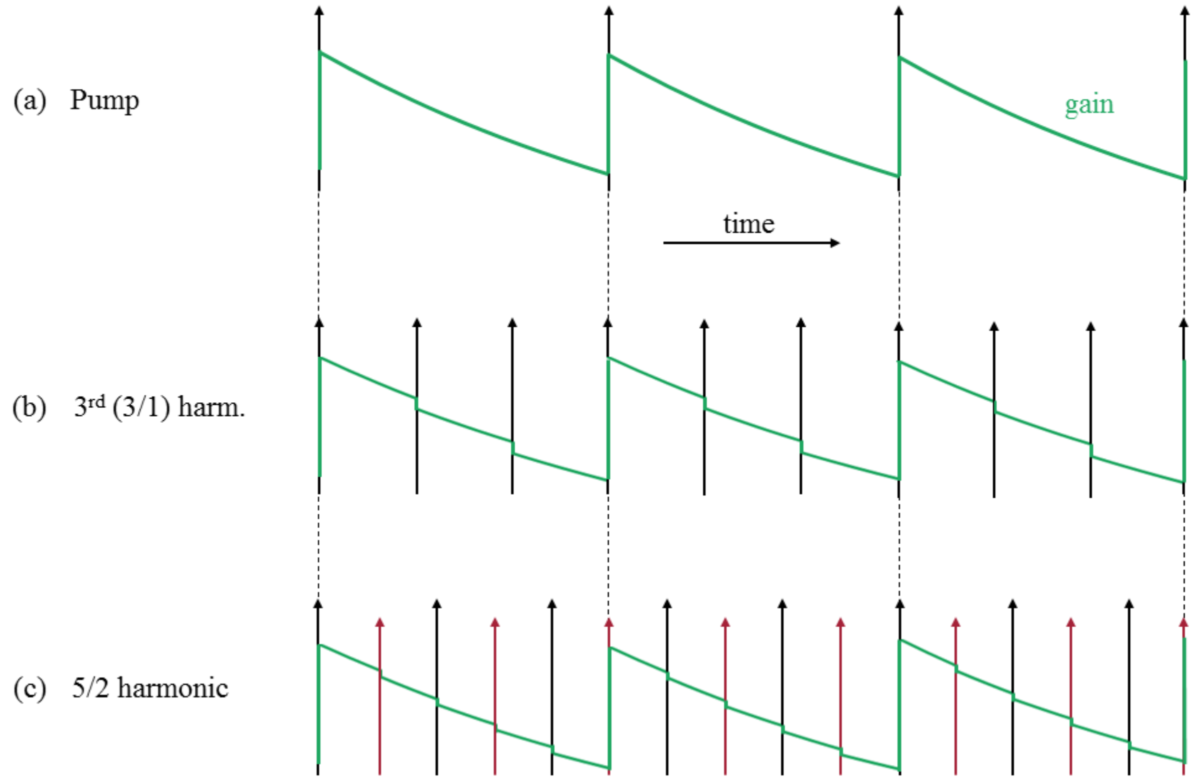

Figure 5.1: (a) The pump pulse train arriving at the laser crystal. The green line represents the gain curve. (b) The laser pulse train of the 3^{rd} harmonic of the pump. There is one pulse in the cavity which is synchronized with a pump pulse every 3^{rd} round-trip. (c) The laser pulse train for the 5/2 harmonic. There are two pulses in the cavity (represented by the black and red arrows, arbitrarily drawn with different heights to distinguish them), each synchronous with a pump pulse every 5th round-trip.

intracavity laser pulse for the third harmonic are shown schematically in figures 5.1(a) and 5.1(b).

There are also more complex harmonics, for which multiple locations in the laser cavity field are each synchronised with a subset of the arriving pump pulses, and each of the locations experience pump events in sequence. This occurs when the ratio of the cavity lengths is any rational number, giving rise to 'rational-harmonic' mode-locking. For example, if the laser cavity length is 2/5 of the pump cavity length, there are two locations in the laser field that are each synchronised with every second pump pulse. We can call this the 5/2 harmonic. Figure 5.1(c) illustrates the timing for the 5/2 harmonic; there are two laser pulses in the cavity with each pulse synchronous with a pump pulse every five round trips. In general, the x/y harmonic has y pulses in the laser cavity, each of which makes x round trips between its

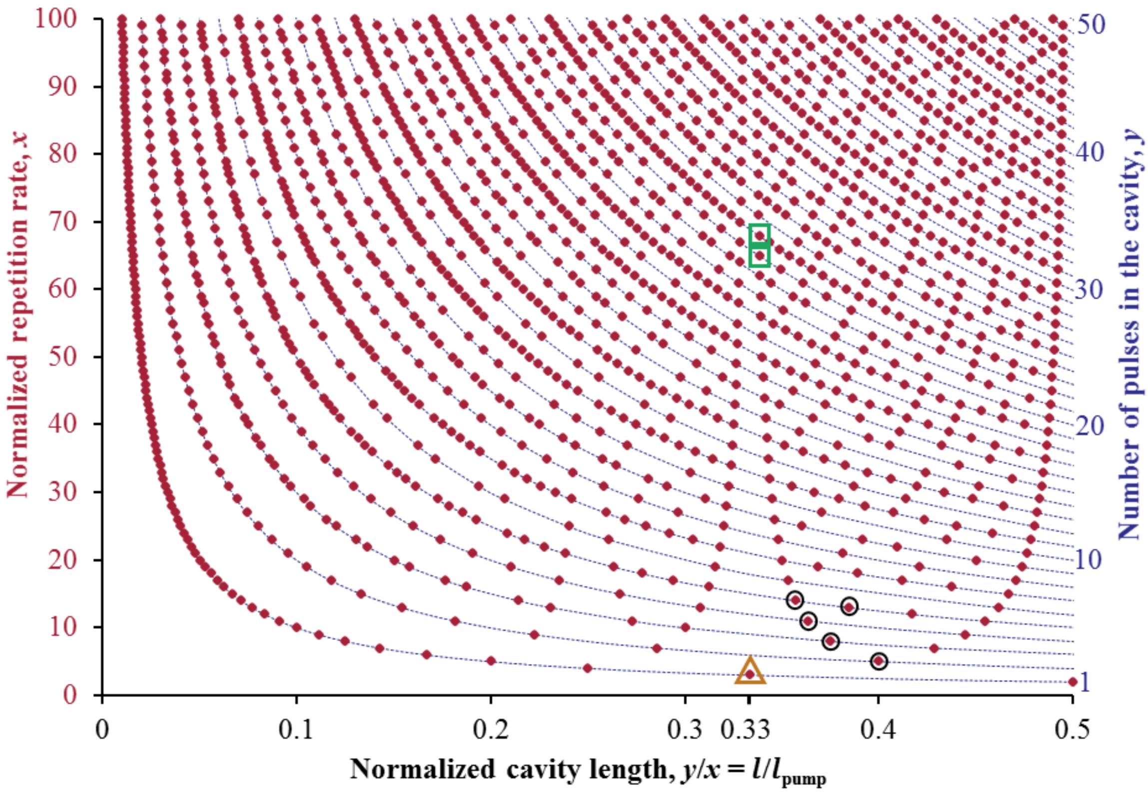

Figure 5.2: A visualization of harmonics as a function of the normalized cavity length (l/l_{pump} = y/x). The vertical axis is the normalized laser repetition rate $R_c/R_{pump} = x$. The plot includes all harmonics for which $x \leq 100$, and $y/x \leq 0.5$. The solid lines connect harmonics with the same y thus having the same number of intracavity pulses. Harmonic points marked are explored in detail later in this work.

pump events. The output repetition rate is x times that of the pump laser. Note that for the presented Ce:LiCAF laser, featuring an upper laser level lifetime of $\tau = 25$ ns, and a pump pulse repetition rate of $R_{pump} = 78.75$ MHz, which corresponds to a pump pulse round trip time of 12.7 ns, the gain persists between pump events (shown schematically in figure 5.1), so that the laser pulses (and indeed all parts of the cavity field) see gain at every pass through the crystal whether or not that pass is synchronous with a pump pulse.

Figure 5.2 shows a plot of the range of rational harmonics, where the horizontal axis is the normalized cavity length $l/l_{pump} = y/x$, and the vertical axis the normalized laser repetition rate $R_c/R_{pump} = x$. The plot includes all harmonics for which $x \leq 100$, and $y/x \leq 0.5$. The blue dotted lines connect harmonics with the same y thus having the same number of intracavity pulses. So the lowest line connects the 2^{nd}, 3^{rd}, etc. harmonics with cavity lengths 0.5, 0.33, etc. The next lowest line connects the 5/2, 7/2, etc. harmonics with normalized cavity lengths 2/5, 2/7, etc. The complete set of reduced rational fractions that define the harmonics are known as the Farey sequence [155]. Rational-harmonic mode-locking allows access to a wide range of repetition rates for relatively minor changes in the laser cavity length.

Rational-harmonic mode-locking was first observed in 1986 in a dye laser [156], where it was called "periodicity multiplication" and was discovered again by Onodera *et al.* in 1993 [157], where it was proposed as a new method for high repetition rate actively mode-locked semiconductor lasers. Since then it has also been reported in synchronously pumped ring optical parametrical oscillators (OPOs) [158, 159], and fiber lasers [160, 161], and has also been referred to as "higher order frequency modulation (FM) mode-locking" e.g. in [162], or "quasi-synchronous pumping", e.g. in [159]. In all cases, it was noted that the pulses achieved by rational-harmonic mode-locking showed non-constant pulse energies. Especially rational-harmonic mode-locked ring OPOs have pronounced pulse energy variation, since pulses see gain only during their own pump events and thus decay in amplitude on each round trip between pump events [159]. In fiber lasers that feature a long energy storage time compared to the laser round trip time, strong Q-switching has been observed when the laser cavity is detuned from a harmonic [161]. As a result, pulse-amplitude equalization has been established in high repetition rate rational-harmonic mode-locked fiber lasers [163–165]. Besides pulse energy variations, other challenges associated with rational-harmonic mode-locking (as well as harmonic mode-locking, which can be seen as a special case of ration-harmonic mode-locking) are phase-incoherency and in the case of passively mode-locked lasers unstable pulse spacing. This is why the technique is not suitable for all applications that require high repetition rates and some researchers favour fundamental mode-locking even though it requires very short laser cavities to achieve high repetition rates [166].

In the presented Ce:LiCAF lasers, the pulse trains generated at rational harmonics will have relatively uniform energy, since the gain persists between pumping events and so pulses are amplified even on round trips for which they are not synchronous with the pump as previously mentioned; the precise variation between the pulse heights will be different for each harmonic. Due to the short upper laser level lifetime of Ce:LiCAF (τ = 25 ns), Q-switching modulation is also not expected to be significant.

For a fixed pump power, the more pulses there are in the laser cavity (y), the less energy is in each. Hence the extent of gain saturation decreases as the number of pulses increases, and

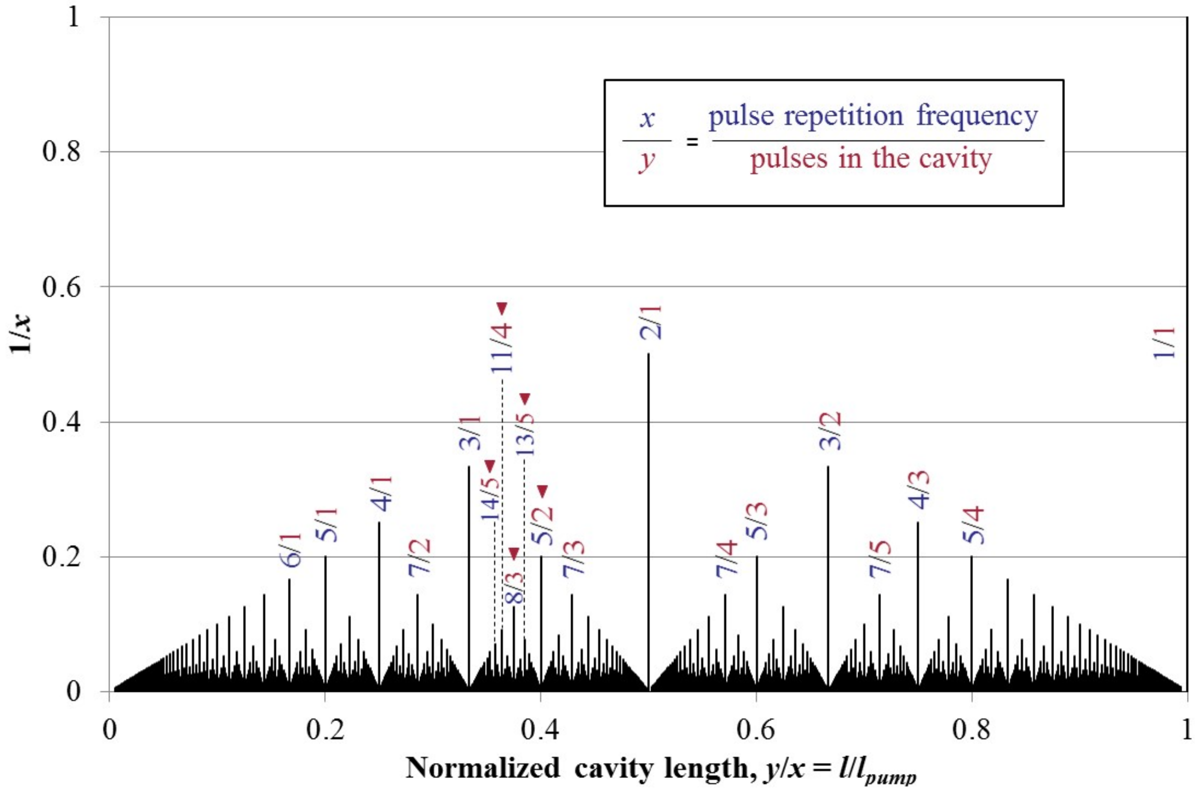

Figure 5.3: A visualization of harmonics as a function of the normalized cavity length (l/l_{pump} = y/x). The vertical axis indicates the strength of the harmonics: harmonics with smaller numerator x feature taller bars. The plot includes all harmonics for which $x \leq 200$. The higher harmonics that were detected experimentally (see section 5.2) are labelled and marked with red triangles.

as a result the strength of the pulse-forming effect decreases as well. The underlying dynamics are similar to those of a slow saturable absorber in a passively mode-locked laser, where the net gain window is opened when an incoming light pulse is strong enough to bleach the absorber sufficiently which might be accompanied by a sharpening of the rising edge of the pulse. In a slow saturable absorber that features a long recovery time compared to the laser pulse duration the net gain window is then closed by gain saturation by the pulse itself, resulting in an asymmetric pulse shape. If the pulse energy of the incoming pulses is not high enough to bleach the absorber sufficiently during a single pass, the initiation of stable mode-locking is prevented. Analogously stable-mode locking in our system is prevented when in cavities with a large number of pulses y the energy in the pulses is too low to open a net gain window for mode-locking. We thus expect the laser cavity field for complex rational harmonics (x/y) with larger denominators y to become progressively less modulated. At the same time, the pressure to mode-lock also decreases with increasing numerator x, since with increasing

x each circulating pulse becomes synchronous with a pump pulse less frequently. Both effects are limiting the theoretically-infinite set of complex harmonics to a more restricted number in practice. In figure 5.3 all rational harmonics with $x \leq 200$ are plotted over the normalized cavity length $l/l_{pump} = y/x$, with the vertical axis indicating the strength of the harmonic: harmonics with smaller numerator x feature taller bars. The resonances also get narrower as the numerator x increases, imposing tighter limits on the cavity length range where fully modulated pulse trains can be observed. Hence, at cavity lengths between those corresponding to harmonics that have small numerators and denominators, there are cavity lengths for which there is no strong modulation of the laser cavity field. Setting up the cavity intentionally at those lengths we call "asynchronous pumping".

5.2 Rational Harmonics

Using the presented Ce:LiCAF laser system, the rational harmonics close to the 3^{rd} harmonic (alternatively called the 3/1 harmonic), that is located at a cavity length $l_3 = l_{pump}/3 \approx 0.634$ m, where l_{pump} is the length of the pump laser resonator, were studied. The 3^{rd} harmonic is marked with an orange triangle in figure 5.2. From here on, the cavity lengths are given as cavity length mismatch $\Delta l = l - l_3$, which is the cavity length referenced to that for the 3^{rd} harmonic. The focus is on harmonics that occur for cavity lengths close to but longer than for the third harmonic, i.e. $x/y \leq 3$ and $l_{x/y} = l_{pump} \times y/x \geq l_3$, as this length range probes the full range of expected behaviour for a synchronously pumped Ce:LiCAF laser.

Experimentally, a range of rational harmonics were observed using a fast photodiode. The traces shown in figures 5.4(c) - 5.4(g) were measured using an ALPHALAS UPD-50-UP ultrafast photodetector with a 50 ps rise time, and a 6 GHz oscilloscope. Thus it is expected to be able to detect harmonics with repetition rates $\ll$ 6 GHz; with the 78.75 MHz pump laser, this corresponds to harmonics x/y with $x \ll 75$. Figure 5.4 shows a selection of the observed higher order harmonics corresponding to the group of rational harmonics circled in black in figure 5.2, which are also labelled and marked (red triangles) in figure 5.3, each appearing at the predicted cavity length $l_{pump} \times y/x$, showing fully modulated pulse trains; the maximum measured repetition rate is 78.75 MHz $\times$ 14 = 1.103 GHz corresponding to the 14/5 harmonic.

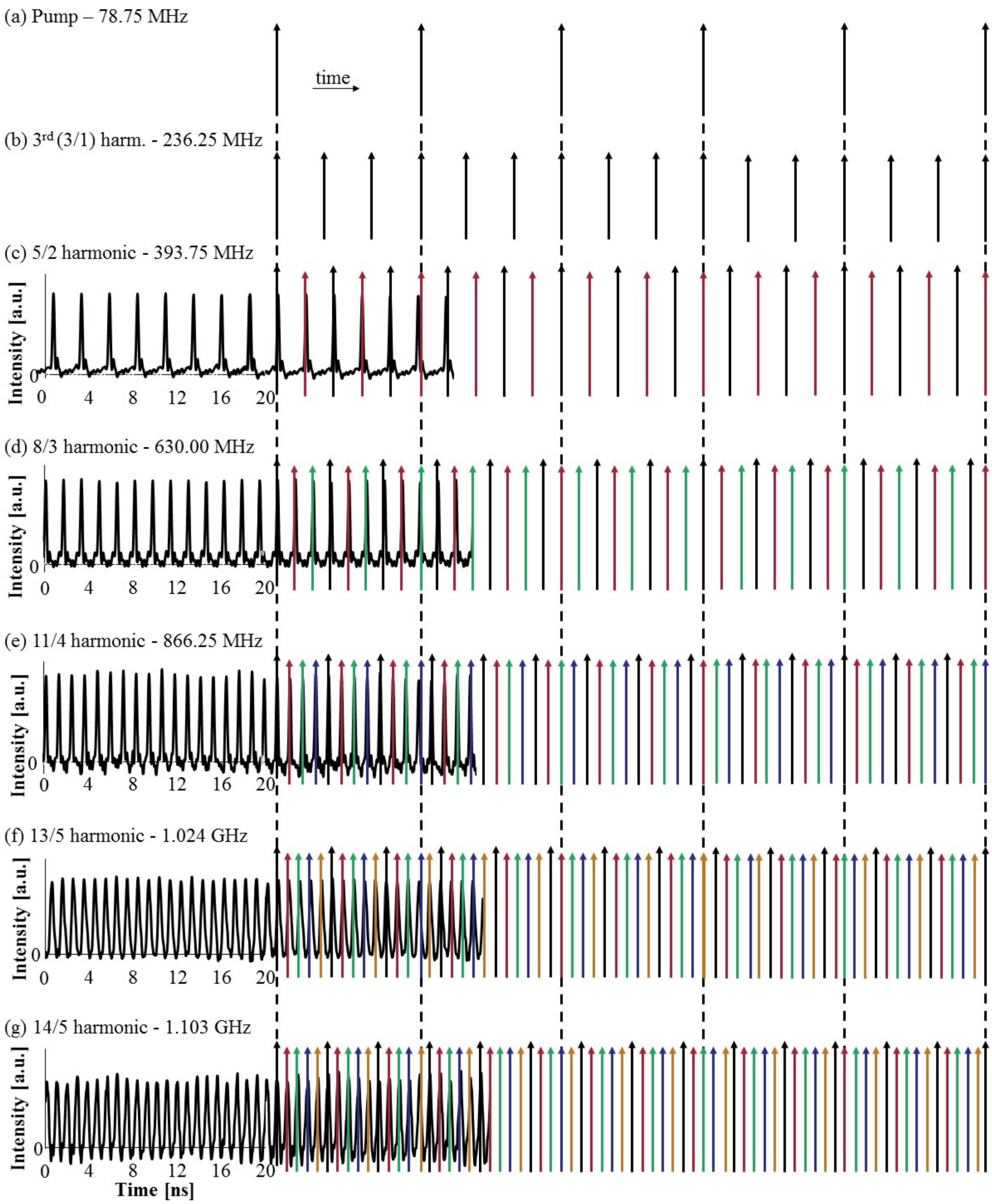

Figure 5.4: Time domain measurement of a selection of rational harmonics, showing full modulation of the cerium laser cavity field overlapped with the schematic diagram showing the pulse timing for the pump laser and the harmonics. For each harmonic, each of the distinct pulses within the laser cavity is marked with a different color, with one arbitrarily marked taller to assist the reader.

Figure 5.4 also shows schematically the timing for each of these different harmonics. The timing of the arrival of pump pulses at the laser crystal is shown in panel (a); the remaining panels show the timing of arrival of pulses in the laser cavity. The colour-coded arrows represent the distinct pulses within the laser cavity at the higher harmonics - recall that for the x/y harmonic, there are y distinct pulses in the laser cavity. The arrow marking the specific pulse that is synchronous at the left is drawn slightly larger to assist the reader to track the different pulses in the cavity. Comparing the 13/5 and the 14/5 harmonic [figures 5.4(f) and 5.4(g)] is particularly instructive; in both cases there are 5 distinct pulses in the cavity. For the 13/5 harmonic, the repetition rate is 78.75 GHz $\times$ 13 = 1.024 GHz, and each pulse is synchronous after making 13 round trips - the pulses are synchronous with the pump pulse in the order 1-3-5-2-4-1-3-... For the 14/5 harmonic, the repetition rate is 78.75 GHz $\times$ 14 = 1.103 GHz, and each pulse is synchronous after making 14 round trips - the pulses experience pump events in the order 1-5-4-3-2-1-5-...

The main aim of the work presented here is to discuss the general form of the laser operation mode of mode-locked pumped lasers for a large range of cavity lengths, concentrating on the transition between mode-locked and CW behaviour. A detailed characterisation of the pulses at rational harmonics (e.g. pulse widths, stability) is thus not included in this work. Previously, the pulse duration of a similar laser, mode-locked at the fundamental harmonic, was measured to be 6 ps [5].

5.3 Numerical Model

To analyse the behaviour of the laser system for various cavity lengths, a numerical model was compiled based on the laser rate equations. The MatLab code of the model including explanatory comments can be found in appendix C "MatLab Code of Cavity Model". In this model, the bi-directional cavity field is divided into an integer number (typically 1000) of small elements, and the evolution of that laser field is calculated as the field circulates in the cavity. It is assumed that the laser crystal is thin. To determine the rate of change of the inversion, the current left and right travelling laser field at the crystal location (I_L^+ and I_L^-) are used. Combined with time dependent absorbed pump power $P_P^{abs}(t)$ that tracks the train of pump pulses arriving at the crystal, the total number N of inverted ions in the laser crystal can be written

$$\frac{dN}{dt} = \frac{P_P^{abs}(t)}{e_p} - \frac{\sigma_{em} N \left(I_L^+ + I_L^-\right)}{e_l} - \frac{N}{\tau},$$

in which e_p and e_l are the photon energies of the pump and laser photons, τ is the upper laser level lifetime, and σ_{em} is the emission cross section of the laser transition. The incident pump pulse train is modelled as a sequence of pulses with temporal Gaussian profile. The single-pass absorption of our crystal was measured to be $\alpha_p = 70\%$. The cavity mirrors (CM_2 and CM_3 in Fig. 4.7) were not only highly reflective for the laser wavelength, but also for the pump wavelength. Thus, in addition to being pumped by the forwards travelling pump light through CM_1, the crystal is also pumped by the backwards travelling residual pump that is reflected inside the cavity. This second pump pass results in absorption of a further 21% of the initial pump energy - we include this secondary absorption in the model, suitably offset in time from the main absorption pass. The laser field is amplified during its forward and backward pass through the crystal according to

$$dI_L^{\pm} = \frac{\sigma_{eff} N I_L^{\pm}}{An},$$

where $\sigma_{eff} = \sigma_{em} - \sigma_{ESA}$ is an effective gain coefficient that accounts for the reduction in effective gain caused by excited state absorption with coefficient σ_{ESA}. Parameter A is the focal area of the pump laser, which is expanded by the refractive index of the crystal n in the tangential plane within the Brewster cut crystal. The output coupling is modelled as a loss L_{OPC} applied at a single specific location in the cavity with current field value I_L^{OPC}; the remaining cavity losses L_t are also collected here, resulting in

$$dI_L^{OPC} = (L_{OPC} + L_t)\, I_L^{OPC}.$$

The output coupling $L_{OPC} = 2.5\%$ and the round trip loss $L_t = 2.45\%$ were measured accurately (to $\pm 0.05\%$) using a cavity ringdown method, and sum to a total loss of 4.95% (see chapter 4). Finally, the laser output power P_L is calculated as

$$P_L = L_{OPC} I_L^{OPC} An.$$

The model was used to predict the behaviour and the form of the output of Ce:LiCAF lasers with parameters summarized in Table 5.1 as a function of cavity length. Note that the behaviour is insensitive to minor changes in the listed parameters other than the cavity length. The model neglects dispersion and gain bandwidth that will affect the duration of

Table 5.1: Input variables for the numerical model used for simulating the Ce:LiCAF laser.

Variable	**Value**
Measured (average) pump power P_P	2.76 W
Pump repetition rate R_{pump}	78.75 MHz
Pump cavity length $l_{pump} = c/(2 \times R_{pump})$	1.902 m
Pump pulse duration	23 ps
Transmission of the dichroic input coupling mirror (CM_1)	91%
Single pass absorption of the crystal α_p	70%
Overlap efficiency η_o	81%
Pump wavelength	266 nm
Laser wavelength	290 nm
Laser beam waist in crystal ω_l	12.9 μm
Upper laser level lifetime τ	25 ns
Emission cross section σ_{em}	9.6×10^{-18} cm^2 [103]
ESA cross section σ_{ESA}	3.6×10^{-18} cm^2 [103]
Refractive index of the crystal (at laser wavelength) n	1.41
Output coupling loss L_{OPC}	2.5%
Loss of cavity elements L_t	2.45%

strongly mode-locked pulses; it also neglects non-linear effects such as self phase modulation and self-focusing that can cause passive mode-locking and soliton generation. Thus the model is not suitable for understanding the laser performance at locations that generate very short pulses, and pulse durations for strongly mode-locked pulse trains are not considered or presented in this work. The model is designed for investigating the behaviour for cavity lengths between strongly mode-locked locations, where the peak intensities are low, and the structure in the cavity field is on multi-picosecond time-scales: here the laser behaviour is determined mostly by gain modulation and gain saturation. The good agreement shown below between the model and experiment for such asynchronous cavity lengths attests that the simplified model provides a useful tool for understanding the behaviour of this laser.

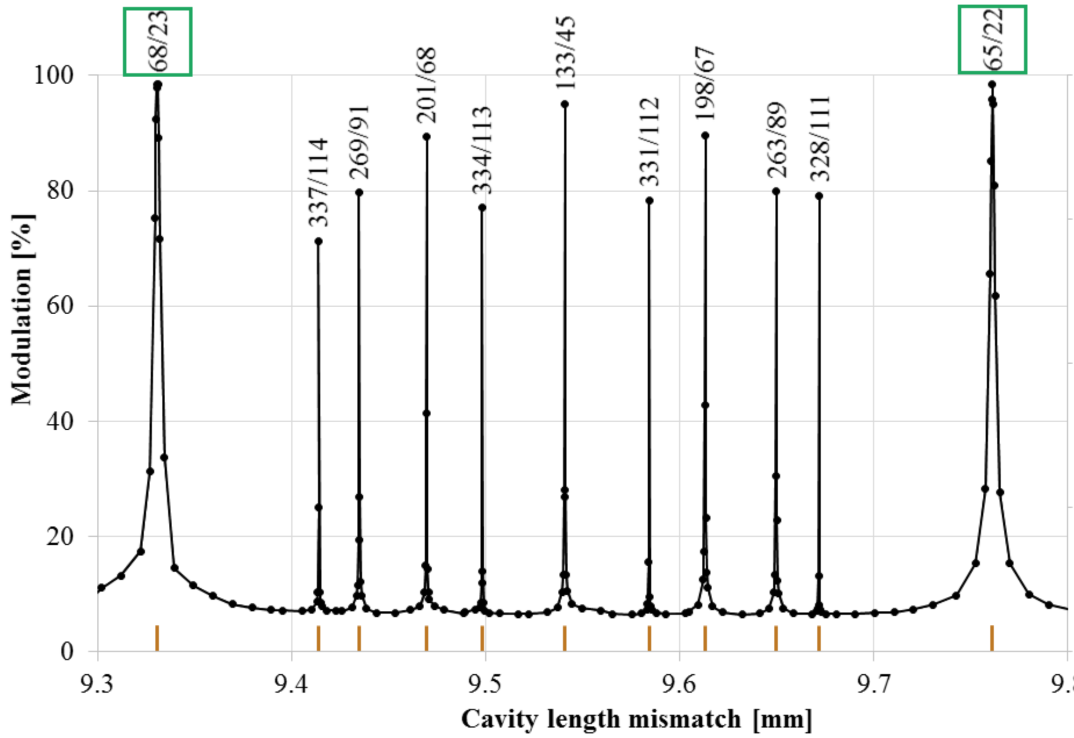

Figure 5.5: Modulation depth of the laser output from numerical simulation as a function of cavity length mismatch Δl, showing a set of higher harmonics interspersed by regions of lower modulation. The location of harmonics with $x < 390$ are indicated near the x-axis. The harmonic labels marked with a square correspond to the points marked with a square in figure 5.2.

5.4 Modelling of Higher Harmonics

The simulated output from the model is used to explore the behaviour of the laser for a small range of cavity lengths. Figure 5.5 shows the modulation depth of the simulated laser output, defined as $(I_{max} - I_{min}) / (I_{max} + I_{min})$, as a function of cavity length mismatch. Also marked are the expected positions of all rational harmonics with $x < 390$ in this cavity length range. Note that this cavity length mismatch range of 9.3 mm to 9.8 mm, corresponds to a very narrow selection of potential harmonics, covering normalized cavity lengths of 0.3382 to 0.3385; the two dominant harmonics (68/23 and 65/22) are marked with green squares both in figure 5.5 and in figure 5.2. Using the model, the locations and surrounding cavity lengths for the harmonics with $x < 390$ are sampled specifically, to find the range of cavity lengths over which each harmonic has influence. Locations of harmonics with larger x are not specifically sampled, and hence are not resolved or do not feature a modulation significantly larger than the background modulation and are thus not detected. As a result, the model predicts strong modulation of the cavity field at the location of each $x < 390$ harmonic,

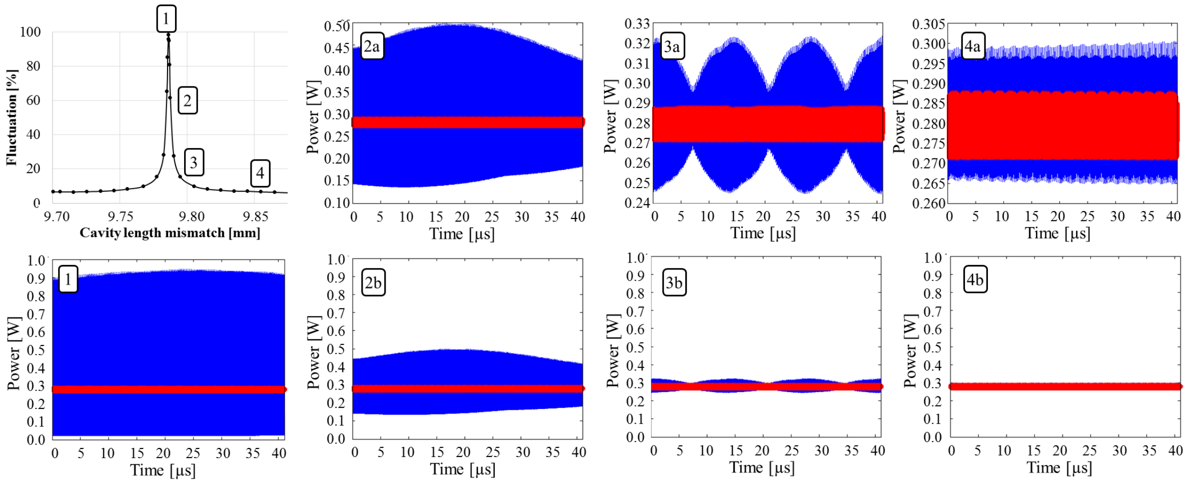

Figure 5.6: Beating around the 65/22 harmonic. Blue line: unfiltered model output; red line: model output convolved with the response function of a 1 ns response and an oscilloscope with a 6 GHz bandwidth ("filtered model output"). (1) output directly at the 65/22 harmonic, (2) - (4) at lengths further and further away from the harmonic. The lower row are plotted with an equally ranged y-axis; the y-axes in the upper row are zoomed in on the data range.

with the modulation depth decreasing somewhat with increasing x; thus there is a continuous transition between trains of well separated pulses and a modulated CW cavity field as the number of pulses in the cavity increases.

5.5 Beating Around Rational Harmonics

Now the regions close to higher harmonics are considered in more detail. Figure 5.5 shows the shoulders of some higher harmonics, where it is clearly visible that harmonics with smaller y have influence over a larger region of cavity lengths. Figure 5.6 provides an overview of the laser output around the 65/22 harmonic. In addition to the model output (blue line), the model output convolved with the response function of a photodiode with a 1 ns response and an oscilloscope with a 6 GHz bandwidth is plotted (red line). Such a measurement system was used when the instantaneous output power was not sufficient for the faster photodiode that detected the higher harmonics in figure 5.4; see section 5.6 below. All outputs shown are plotted over 10,000 round trip times. Figure 5.6 (1) is taken directly at the harmonic, while figures 5.6 (2) to (4) are for lengths further and further away from the harmonic. The lower row (figures 5.6 (1), (2b), (3b), and (4b)) are all plotted with an equally ranged y-axis which illustrates nicely how the fluctuation becomes smaller and smaller the further away from the

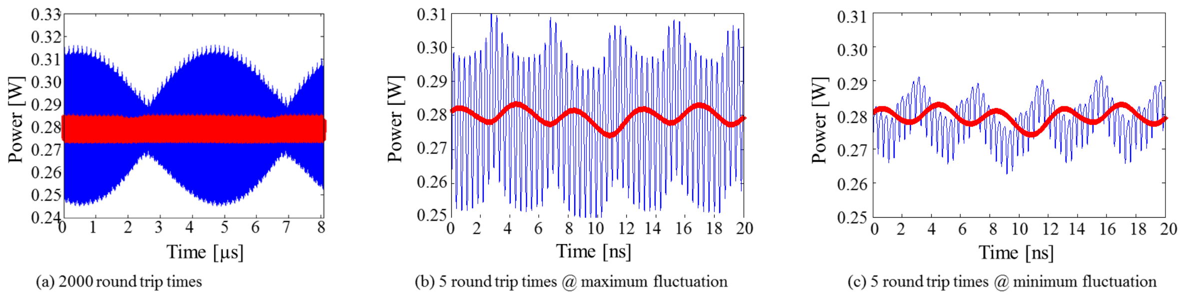

Figure 5.7: Beating at Δl = 18 mm. Blue line: unfiltered model output; red line: filtered model output. (a) over 2,000 round trip times, (b) over 5 round trip times at the maximum fluctuation, and (c) over 5 round trip times at the minimum fluctuation.

harmonic we are. The upper row (figures 5.6 (2a), (3a), and (4a)) are pictures taken at the same cavity lengths as the lower row, but the y-axis are scaled to zoom in on the data range. Looking at the convolved output in the lower row (red lines) it becomes clear, that these fast modulations cannot be seen when measuring the laser output with a nanosecond photodiode - the height of the simulated filtered output stays the same over the whole displayed range.

Figure 5.7 gives an insight into the beating phenomenon. The output plots are taken at Δl = 18 mm, close to the 35/12 harmonic. Figure 5.7 (a) shows the output over 2,000 round trip times, figures 5.7 (b) and (c) are over five round trip times, where figure 5.7 (b) is zoomed in at the maximum fluctuation and figure 5.7 (c) is zoomed in at the minimum fluctuation. The number of peaks per round trip time is the same for maximum and minimum fluctuation. In figure 5.7 (c) it appears that the modulation of the simulated filtered output is shifted slightly compared to the modulation of the unfiltered output, which is as expected due to the pulse response that is the basis of the filter simulation. Again there is no difference in the filtered output for maximum and minimum fluctuation.

5.6 CW Laser Output

The resonances become much sharper for higher harmonics: e.g. for the 68/23 harmonic, the resonance has a width of Δl = 100 μm, but for the 198/67 or 263/89 harmonic, the resonances have a width of only Δl = 10 μm. The decreasing modulation depth and decreasing width of the resonances for the higher harmonics means that despite there being an infinite number of possible harmonics, in practice there are significant regions between the resonances that have relatively little modulation. Figure 5.8 shows the predicted fast output modulation in

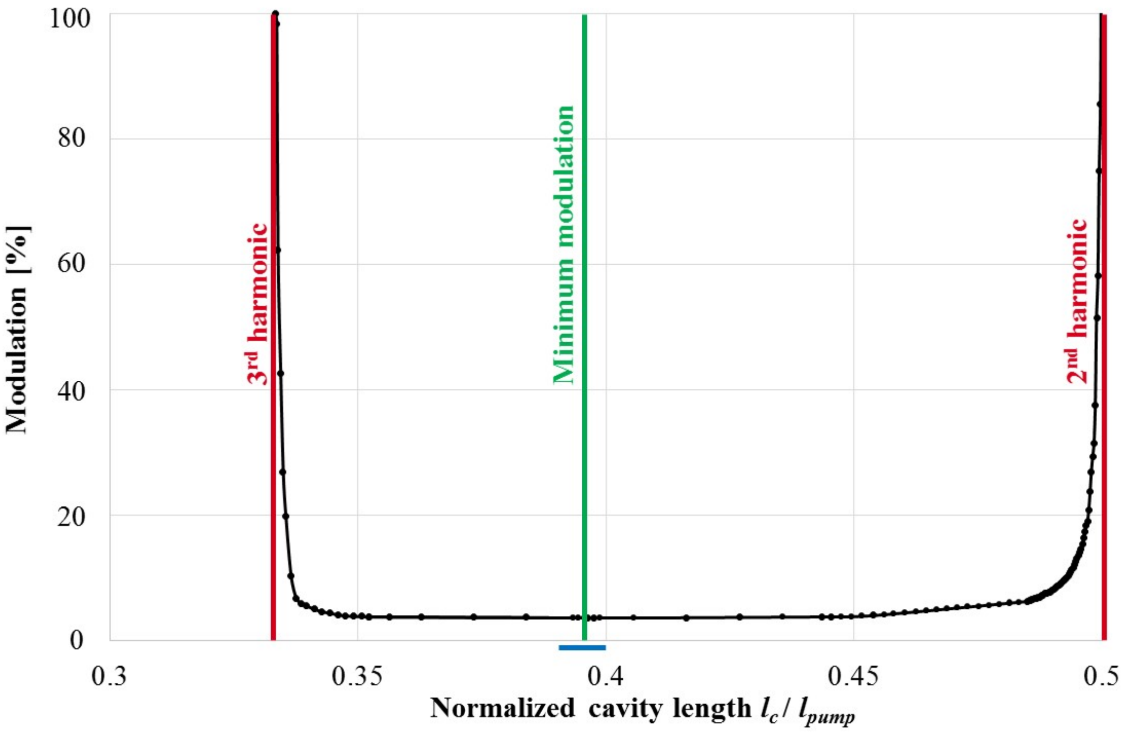

Figure 5.8: Simulated laser output modulation as a function of normalized cavity length between the 3^{rd} and 2^{nd} harmonic. The simulations were carried out at cavity lengths representative of the low-modulation regions.

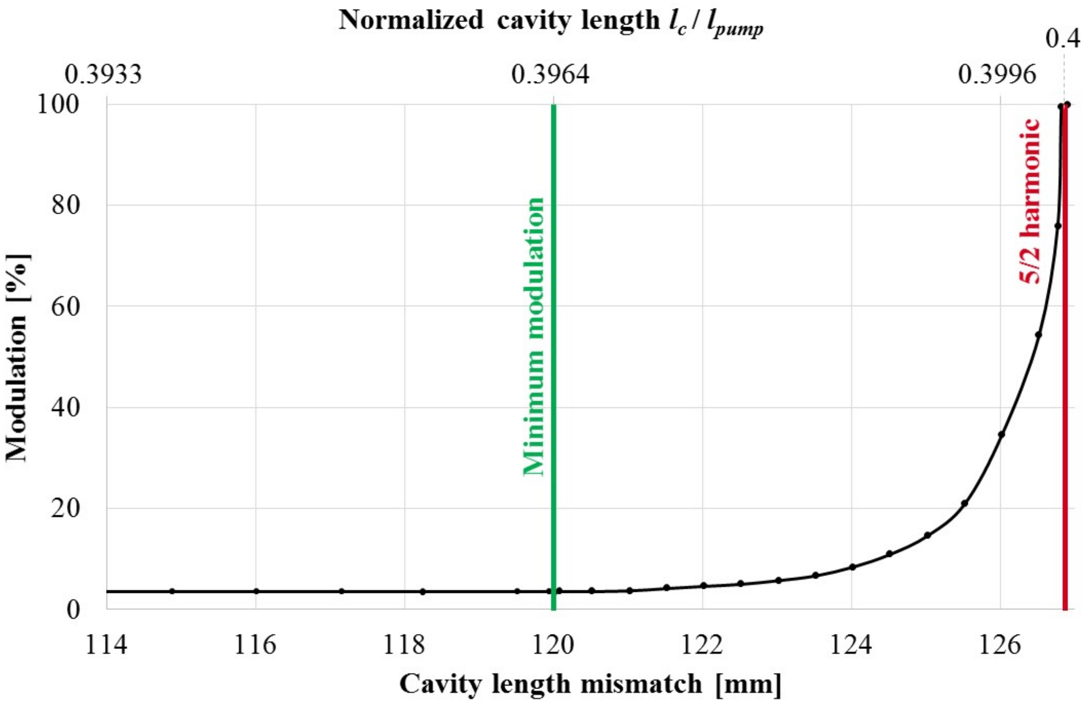

Figure 5.9: Simulated laser output modulation as a function of cavity length mismatch from the 3^{rd} harmonic, close to the 5/2 harmonic.

% between the 3^{rd} and 2^{nd} harmonic. The simulations were carried out at cavity lengths representative of the low-modulation regions, avoiding the narrow peaks corresponding to harmonics with $y > 1$ (that is all harmonics except the 3/1 (= 3^{rd}) harmonic at 0.3333 normalized cavity length and the 2/1 (= 2^{nd}) harmonic at 0.5 normalized cavity length). The curves were plotted for an input power of 2.80 W, so about twice above threshold (see chapter 4). By avoiding all harmonics with $y > 1$, the graph reveals the shoulders of the 3^{rd} and 2^{nd} harmonic, and the underlying unavoidable minimum residual modulation (see section 5.8). The model predicts that for cavity lengths around a normalized cavity length of 0.3964 the residual modulation is minimized. This normalized cavity length corresponds to an absolute length of $l = 0.754$ m and a mismatch from the 3^{rd} harmonic of $\Delta l = 120$ mm. Since this location is very close to the 5/2 harmonic at 0.4 normalized cavity length (at $\Delta l = 126.8$ mm), the region close to the 5/2 harmonic was investigated further. In figure 5.9 the predicted modulation is plotted over a cavity length mismatch of 13 mm approaching the 5/2 harmonic. The cavity region shown corresponds to a normalized cavity length ranging from 0.3933 to 0.4, this range is marked in figure 5.8 with a blue bar under the x-axis for comparison. The shoulder of the 5/2 harmonic is thus predicted to meet the underlying minimum residual modulation at around 121 mm cavity length mismatch and hence does not have significant influence at the location of the minimum modulation.

The shoulder of the 3^{rd} harmonic has also been explored experimentally. Figure 5.10 shows a series of experimental measurements at different cavity mismatch lengths that avoid rational-harmonic mode-locking, and where the resulting modulation is small. Note that these experimental measurements were recorded using a photodiode with a 1 ns response and an oscilloscope with 6 GHz bandwidth, since the instantaneous output power was not sufficient for the faster photodiode. These measurements are compared to the model output, as well as the model output convolved with the response function of our measurement system to simulate the experimental results (the curve marked "simulated, filtered" in figure 5.10). Like before, the simulations were carried out at cavity lengths representative of the low-modulation regions, avoiding the narrow peaks corresponding to high-order harmonics, and an input power of 2.80 W was chosen. The modulation decreases with increasing cavity length mismatch Δl from the third harmonic, as expected, and the modulation of the simulated filtered output and the experimentally measured output match each other closely, giving confidence in the output of the model. At the location of the predicted minimum

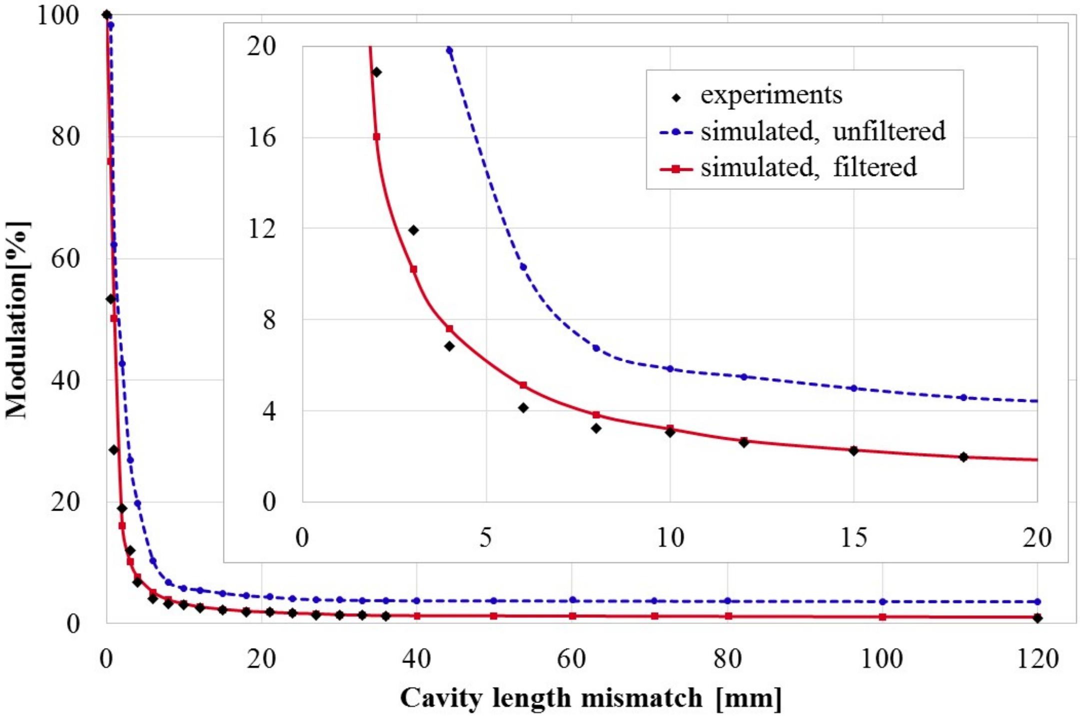

Figure 5.10: Measured and simulated laser output modulation as a function of the cavity length mismatch. These points cover normalized cavity lengths from 0.3333 to 0.3964.

modulation, the measured modulation and the simulated filtered modulation are in the order of 1%, while the simulated unfiltered modulation is in the order of 4%.

5.7 RF Spectrum

The RF spectrum of the simulated laser output was calculated via Fourier Transformation, and in figure 5.11 the resulting RF spectra of the output at Δl = 120 mm (CW cavity length) and important harmonics are displayed. Figures 5.11 (a) - (e) are all plotted over the same frequency range (up to 1 GHz), while figure 5.11 (f) covers a larger frequency range (up to 64 GHz). At Δl = 120 mm, the major part of the total output power is in the CW component of the signal (at 0 Hz - please note that all y-axes are logarithmic axes). All other major frequency components are associated with the important harmonics of the pump. Clearly noticeable is the 5/2 harmonic component, which is due to the fact, that the CW cavity length is close to the cavity length of that harmonic (see figure 5.9). In figure 5.11 (f), there is an additional mark at 8.741 GHz visible, with associated smaller marks at harmonics of 8.741 GHz. These marks correspond to the 111/44 harmonic, that is located at 0.396396

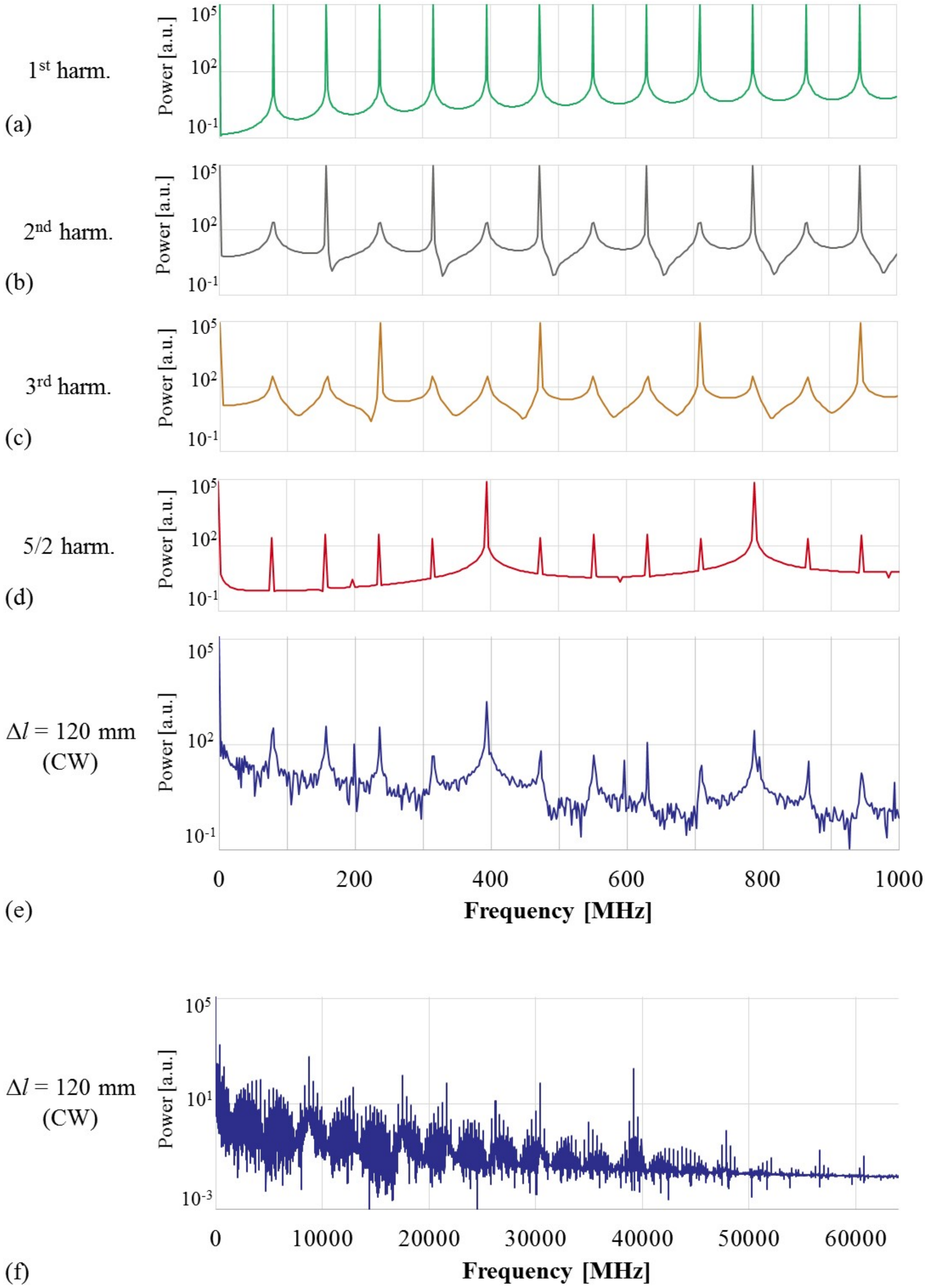

Figure 5.11: RF spectra of the simulated laser output (a) - (d) for different harmonics and (e), (f) at Δl = 120 mm. The spectra (a) - (e) are all plotted over the same frequency range (up to 1 GHz), the spectrum in (f) covers frequencies up to 64 GHz.

normalized cavity length (l = 0.75399 m, Δl = 119.99 mm). The 111/44 harmonic is just 10 µm away from the CW location and can be found in the RF spectrum. Nevertheless, it is of minor influence for the overall residual modulation featured at Δl = 120 mm, where the 5/2 harmonic, and the y = 1 harmonics are much more prominent (see also the time traces taken at Δl = 120 mm below).

5.8 Gain Step

The residual modulations in the laser output are due to the unavoidable effect that when pumping with a mode-locked pulsed laser, each pump pulse produces a step increase in the inversion N_i which implicates a step increase in the gain G. During the 23 ps pump pulse, the inversion reaches its maximum and subsequently decays due to stimulated and spontaneous emission until the next pump pulse arrives, leading overall to a saw-tooth inversion curve (see figure 5.12). Below threshold, the step in the inversion ΔN at each pump pulse is

$$\Delta N = N_{max} - N_{min} = N_{max}\left(1 - \mathrm{e}^{-t_p/\tau}\right),$$

where t_p is the pump pulse period, and τ = 25 ns is the fluorescence life-time. The gain is dependent on the inversion,

$$G = \sigma_{eff} l N_i,$$

where σ_{eff} is the effective gain cross section of the active medium ($\sigma_{eff} = \sigma_{em} - \sigma_{ESA}$), and l is the length of the active medium, this also leads to a saw-tooth gain curve. To estimate the magnitude of the gain step ΔG, the gain at lasing threshold has to be calculated.

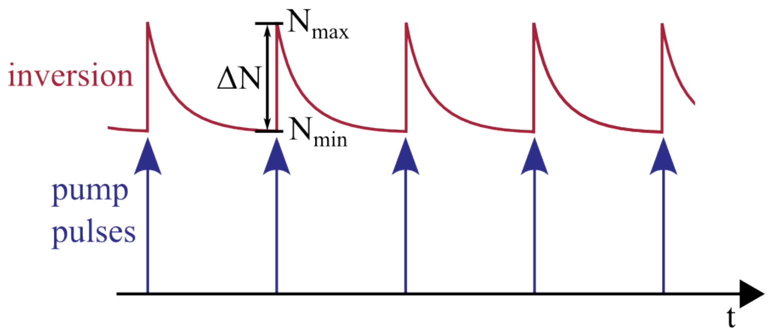

Figure 5.12: Schematic of the inversion curve for an asynchronous pumped CW laser. Blue arrows represent the times when a pump pulse arrives at the laser crystal.

At threshold, the average gain $< G_{th} >$ has to be equal to the loss L

$$L =< G_{th} >= \sigma_{eff} l < N_{th} >$$
$$= \frac{1}{t_p} \int_0^{t_p} \sigma_{eff} l N_{th}(t)\ \mathrm{d}t = \frac{\sigma_{eff} l N_{th,max} \tau}{t_p} \left[1 - e^{-t_p/\tau}\right].$$

We can rewrite this equation in terms of ΔN_{th} as

$$L = \frac{\Delta N_{th} \sigma_{eff} l \tau}{t_p}.$$

Since we can also deduce ΔN from the number of photons in each pump pulse

$$\Delta N = \frac{E_p}{ALe_p},$$

where E_p is the pump energy, A is the pump area, and e_p is the photon energy, we can rewrite the equation for L in terms of $E_{p,th}$ as

$$L = \frac{E_{p,th} \sigma_{eff} \tau}{Ae_p t_p}.$$

This equation can be rearranged to

$$\frac{\sigma_{eff}}{Ae_p} = L \frac{t_p}{\tau E_{p,th}}.$$

Above threshold,

$$\Delta G = \sigma_{eff} \Delta N l = \frac{\sigma_{eff}}{Ae_p} E_p = \frac{E_p}{E_{p,th}} L \frac{t_p}{\tau}.$$

Setting $E_p / E_{p,th} = \gamma$, thus γ being the number of times above threshold, and $L = (L_{OPC} + L_t)$, where L_{OPC} is the output coupling loss, and L_t is the round-trip loss, the step in the gain for each round trip becomes

$$\Delta G = \gamma \cdot (L_{OPC} + L_t) \cdot \frac{t_p}{\tau}.$$

Since the intracavity field passes through the gain medium twice on each round-trip, the single pass step in the gain has an amplitude ΔG_{sp} given by

$$\Delta G_{sp} = \frac{1}{2} \cdot \gamma \cdot (L_{OPC} + L_t) \cdot \frac{t_p}{\tau}.$$

For the 78.75 MHz pump laser used, the pump pulse interval equals half the Ce:LiCAF fluorescence lifetime, and with 4.95% total cavity loss, the gain step is predicted to be just 2.57% at the maximum output power obtained. The resulting modulations in the intracavity field and laser output depend on the cavity length mismatch and are expected to be of the same order of magnitude as the gain step for optimum mismatching.

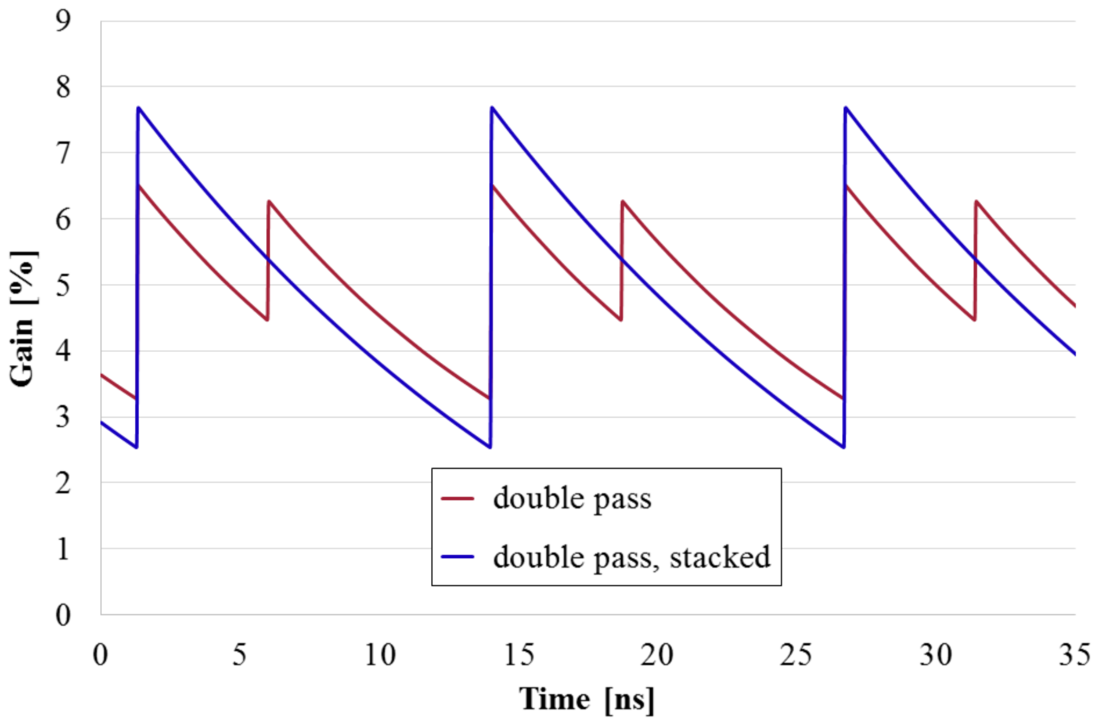

Figure 5.13: Gain step for double pass pumping and stacked double pumping (forwards and backwards pumping are simulated to occur simultaneously, so that the two steps are combined to one step).

The simulated percentage gain over time from the numerical model is shown in figure 5.13. Here, the average gain is 4.95%, which agrees with the total cavity losses. Recall that in the experiment only part of the pump pulse is absorbed during the first pass through the crystal and that there is a second pump event after the residual pump pulse is back-reflected into the crystal. The red line shows the gain for a double pass pumped crystal where the backwards pumping occurs with a time delay as given in the laser. The maximum gain step for the forwards pumping in this case is $\Delta G = 1.69\%$. The blue line is the result for 'stacked double pass pumping', where the backwards pumping is simulated to occur simultaneously with the forwards pumping, so that the otherwise separately occurring two steps in the gain are combined to one gain step. The maximum simulated gain step in this case is $\Delta G = 2.57\%$ and hence agrees with the calculated analytical value.

Since $\Delta G \propto \gamma$ it becomes larger as more energy is pumped into the crystal. This phenomenon is due to the fact that gain saturation pulls the gain down harder between pump pulses the harder we pump. ΔG is also proportional to τ_p/τ, hence for materials with short fluorescence lifetimes like Ce:LiCAF ($\tau = 25$ ns) it is larger than for materials with longer fluorescence lifetimes when all other parameters are kept similar. In e.g. Ti:sapphire lasers that feature a fluorescence lifetime of 3.2 μs, the gain is more uniform in comparison to the gain in Ce:LiCAF due to the longer fluorescence lifetime. We return to this in section 5.10.

5.9 Comparison of Experimental and Simulated Results

To verify the results of the numerical model further, the simulated output is compared to the output measured experimentally. Just like figure 4.18 in the previous chapter 4, figure 5.14 shows the time trace measured with a ns-photodiode at a total laser cavity lengths of 0.754 m, which corresponds to a cavity length mismatch to the 3^{rd} harmonic $\Delta l = 120$ mm - recall that for this cavity length the residual modulation was predicted to be minimal and we hence use this cavity length to generate our CW laser output. The output is shown over a time of 150 ns and 42 ns respectively. In addition to the experimental data, in figure 5.14 the laser output as predicted by the simulations ("simulated, unfiltered" line) and the simulated output convolved with the response function of the measurement system ("simulated, filtered" line) are plotted as well. There is a good agreement between the model and the experimental results: Experimentally the modulation was measured to be just ±1% for frequencies below 1 GHz, and the "simulated, filtered" line that simulates the laser output as seen by the used measurement system predicts a residual modulation with the same magnitude. The "simulated, unfiltered" line shows the model predictions for the residual modulation on a faster timescale that can not be resolved by the measurement system used in the experiments. According to the model the modulation on this faster timescale should still be less than ±4%. Nevertheless, for many applications of CW UV lasers, a modulation of the laser output at GHz frequencies will not be resolved just as it is not resolved by our measurement system and is hence not problematic. For these applications the generated laser output is closely equivalent to that from a CW-pumped multi-longitudinal-mode CW laser, and so can be used interchangeably.

Zooming further into the time trace, some components of the fast modulation that are also clearly visible in the RF spectrum of the laser output, can be revealed. Figure 5.15 shows the measured and simulated laser output over a time frame of 6 ns. In addition to the fast modulation with a period of around 2.54 ns that is related to the 5/2 harmonic component of the output, there is a modulation with a period of 0.114 ns that corresponds to the 111/44 harmonic. Even though the 111/44 harmonic is just 10 μm away, its influence is much weaker

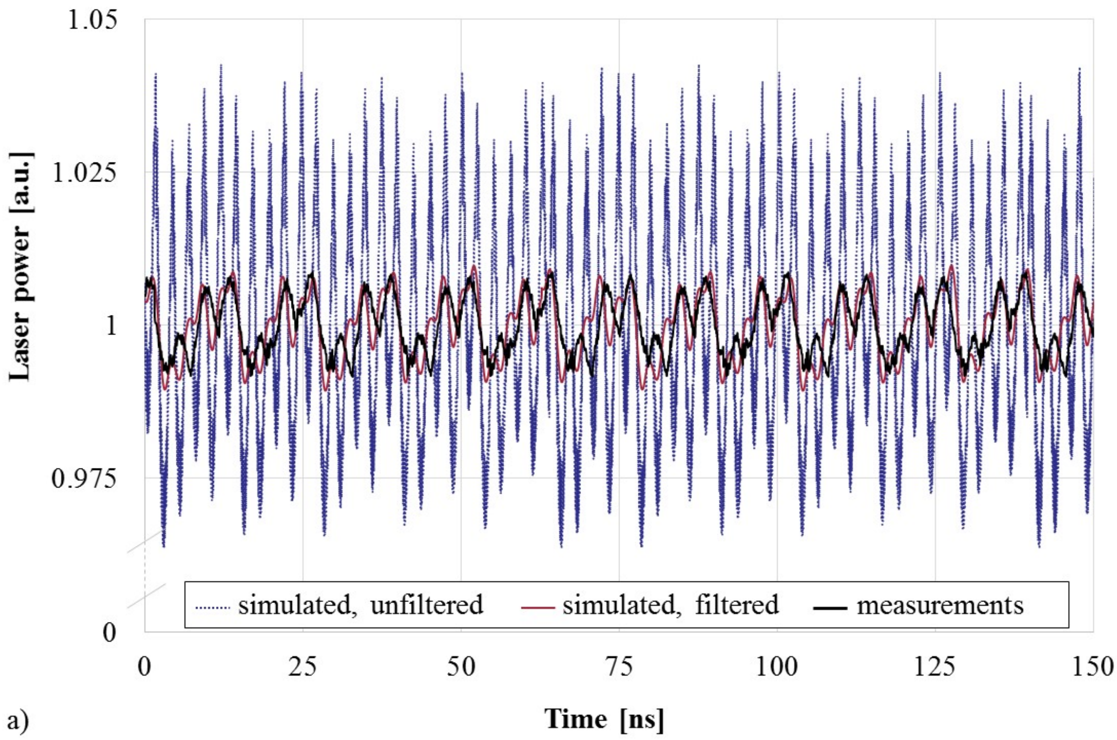

a)

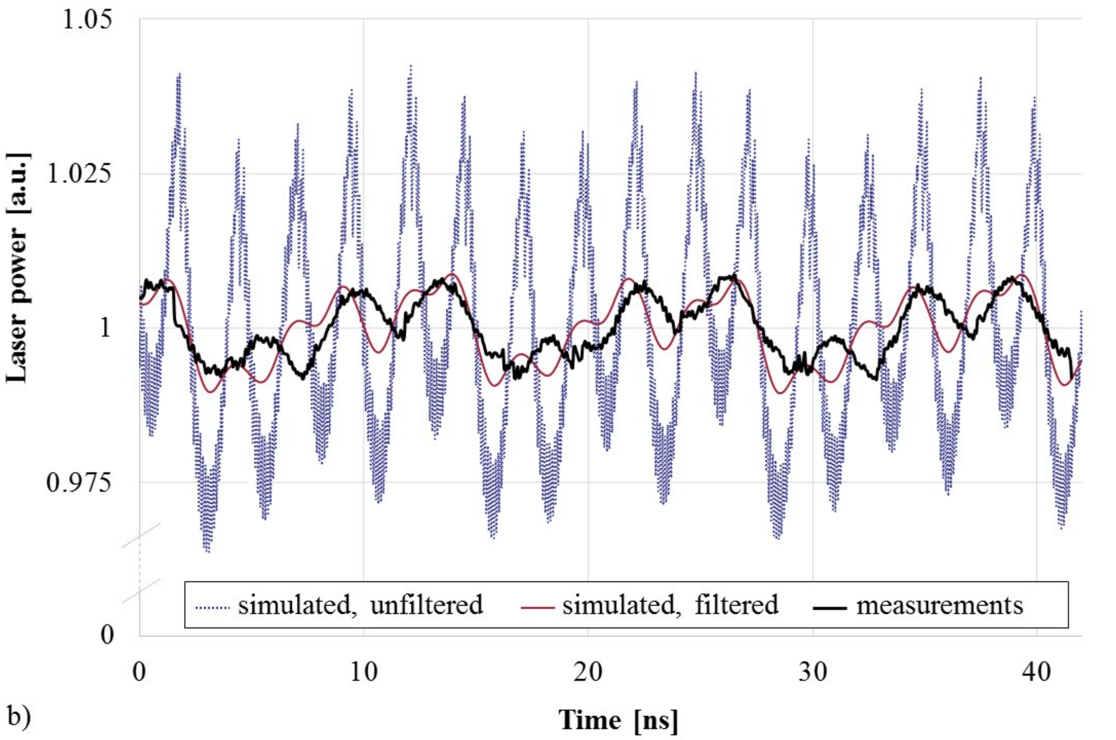

b)

Figure 5.14: Measured and simulated laser output over a time frame of a) 150 ns and b) 42 ns, for a cavity length of Δl = 120 mm. The modulation is of the order of 1% for frequencies below 1 GHz and 4% on faster timescales.

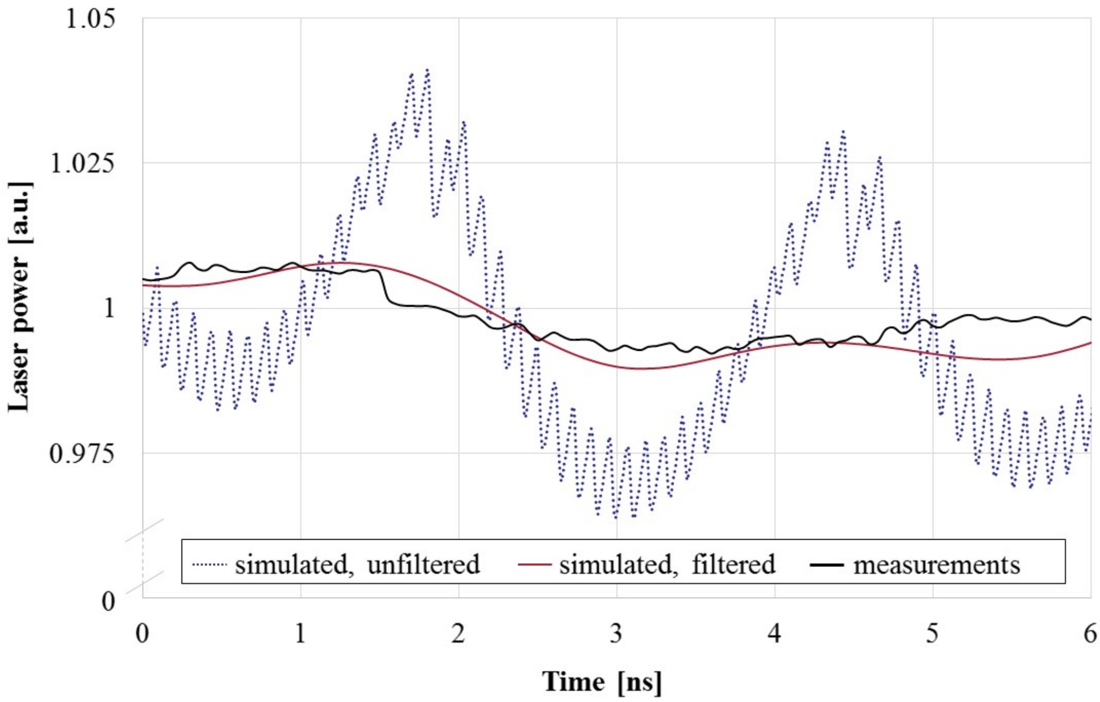

Figure 5.15: Measured and simulated laser output over a time frame of 6 ns at Δl = 120 mm.

than that of the 5/2 harmonic and the overall dominant y = 1 harmonics.

While the residual modulation is minimal at around 120 mm cavity length mismatch, modulated CW output (as oppose to fully modulated pulse trains) can be observed at many other cavity lengths between harmonics as well. In figure 5.16 the laser output at 12 mm cavity length mismatch can be seen. Again, the simulated, filtered output follows the experimental line closely. The residual modulation here is still only of the order of 2% for frequencies below 1 GHz and just about 5% on faster timescales, even though the 3^{rd} harmonic is just 12 mm away.

Finally we confirm that the numerical model agrees with the analytical calculations for total output power. In chapter 4, the slope efficiency of the Ce:LiCAF laser with a cavity length mismatch of 120 mm was determined to be 20%, with a maximum laser output of 288 mW at an input power of 2.80 W and a lasing threshold of 1.37 W as can be seen in figure 4.19 in chapter 4 and here in figure 5.17. By comparing these experimental results with theoretical values calculated using well established literature equations [135], the laser waist size was determined to be ω_l = 13 μm, and the overlap efficiency η_o = 0.81. The simulations that led to the "simulated" line in figure 5.17 were hence done using these values. All used values are also listed in table 5.1. The results of the simulation match those of the experiment and the theoretical calculations perfectly thus confirming the validity of the model.

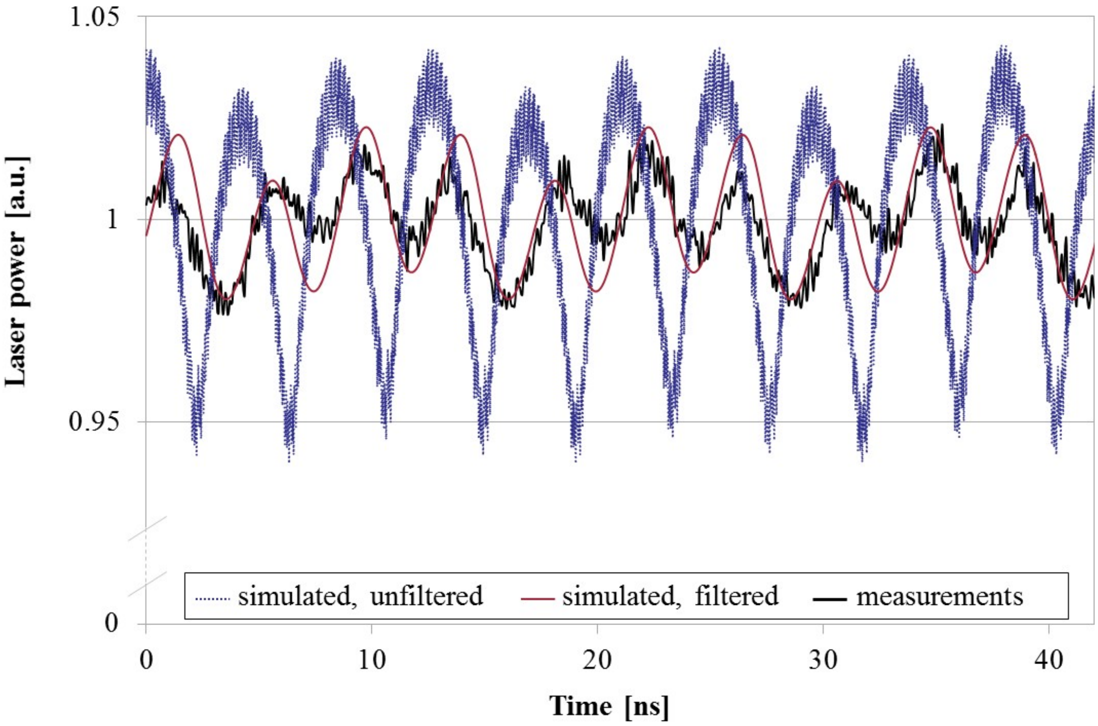

Figure 5.16: Measured and simulated laser output over a time frame of 42 ns, for a cavity length of Δl = 20 mm. The modulation is of the order of 2% for frequencies below 1 GHz and 5% on faster timescales.

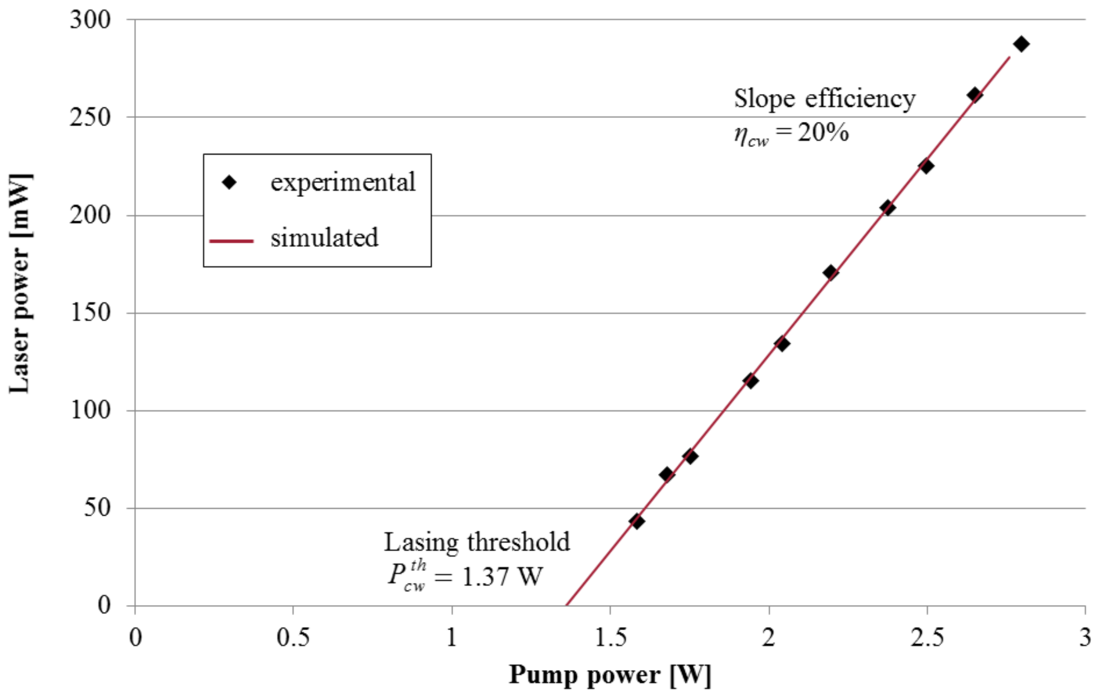

Figure 5.17: Slope efficiency for maximum power output coupling.

5.10 Mode-Locked Pumped CW Ti:sapphire Lasers

Titanium doped sapphire (Ti:sapphire) was introduced as a laser material in 1986 [51] and rapidly became one of the most important solid-state crystals for tunable lasers and ultrashort pulse generation. A short account of some milestones achieved with Ti:sapphire lasers is already given in chapter 2.2.2. Ti:sapphire lasers are also widely used as pump sources for other lasers as they can be tuned to many commonly required pump wavelengths and feature high beam quality as well as high output powers. In chapter 3.2 we compared the approach of using Ce:LiCAF as a laser material to generate tunable UV output to the common method to obtain such UV output, which is based on the frequency conversion of tunable Ti:sapphire laser emission. The many different utilisations of Ti:sapphire lasers are due to the very broad gain bandwidth of Ti:sapphire ranging from 600 nm in the red to around 1100 nm in the infrared (IR) spectral region with an emission peak at around 800 nm. Ti:sapphire and Ci:LiCAF hence have in common, that they both have bandwidths of the order 133 THz. Ce:LiCAF and Ti:sapphire also have many other features in common; they are both very efficient and robust materials and can be set up in all solid-state systems. Due to the many similarities, Ce:LiCAF has been called the "Ti:sapphire of the UV" [113]. Ti:sapphire and Ce:LiCAF can also both be pumped conveniently by harmonics of Nd doped solid-state lasers. While for Ce:LiCAF the fourth harmonic is used as discussed in chapter 3 and chapter 4, for Ti:sapphire the second harmonic (λ = 532 nm) can be used. At this wavelength the pump absorption is only slightly reduced compared to the main absorption peak around 500 nm. The fluorescence lifetime of Ti:sapphire is 3.2 µs, which is significantly longer than the 25 ns lifetime of Ce:LiCAF. When using Ti:sapphire in a mode-locked pumped set-up with a 80 MHz pump source as we do here, the fluorescence lifetime is hence greatly larger than the inter-pulse interval.

An asynchronously mode-locked pumped Ti:sapphire laser was simulated using our model to put our Ce:LiCAF results into perspective. While in practice a CW Ti:sapphire laser can relatively conveniently be pumped with a CW green laser, there may be cases where a picosecond green laser might be more convenient. The parameters used to simulate the Ti:sapphire laser were chosen to match the performance of the Ce:LiCAF laser to be able to compare the results easily. The value of the laser beam waist in the crystal was set to 48.5 µm to provide a similar laser threshold and slope efficiency as for the Ce:LiCAF laser. All used parameters are listed in table 5.2 next to the values used for Ce:LiCAF.

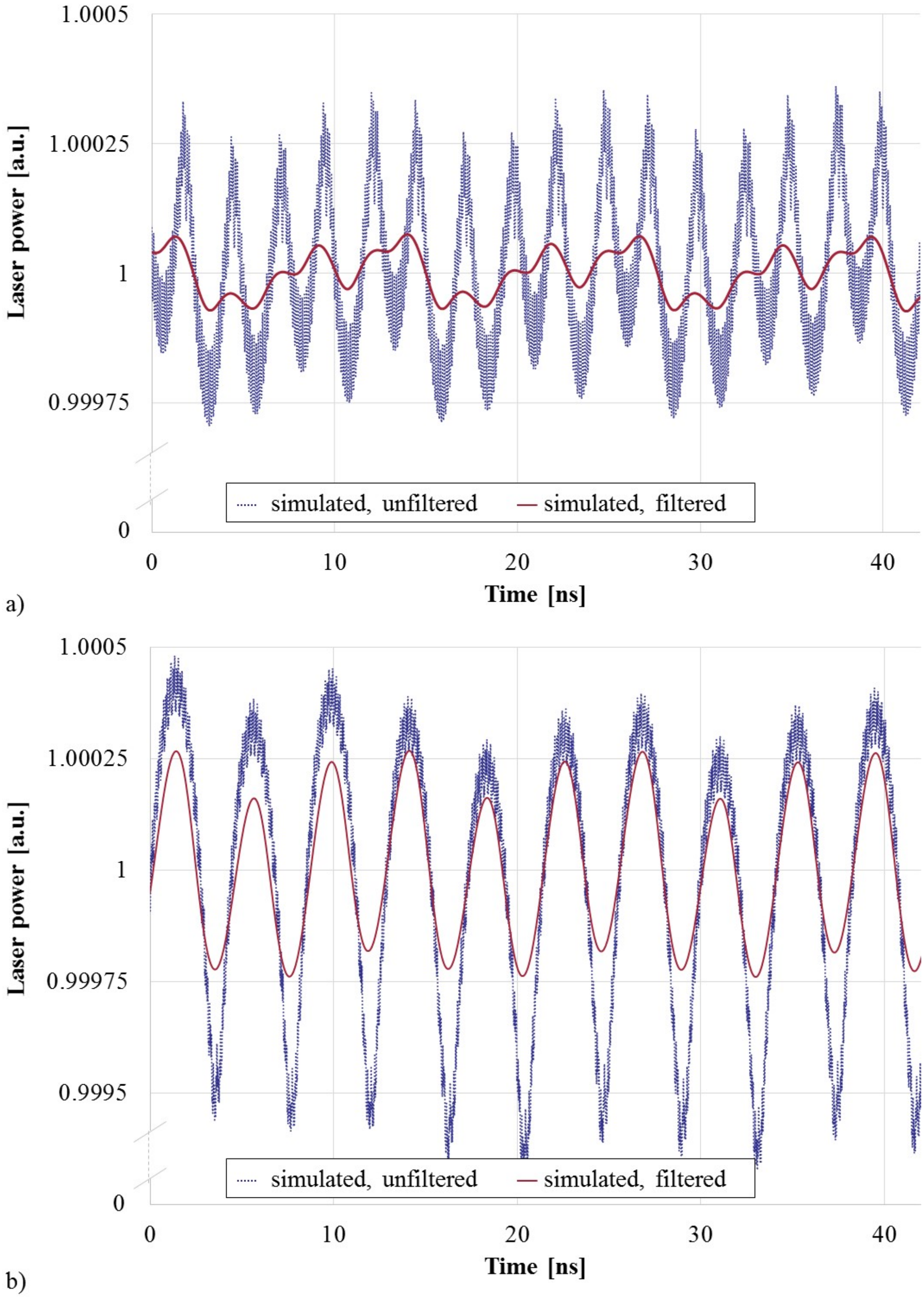

Figure 5.18: Simulated laser output of a mode-locked pumped Ti:sapphire laser over a time frame of 42 ns for a cavity length mismatch of a) Δl = 120 mm and b) Δl = 20 mm.

Table 5.2: Input variables for the numerical model used for simulating the Ce:LiCAF laser and a Ti:sapphire laser respectively.

Variable	**Ce:LiCAF**	**Ti:sapphire**
Measured (average) pump power P_P	2.76 W	2.76 W
Pump repetition rate R_{pump}	78.75 MHz	78.75 MHz
Pump cavity length $l_{pump} = c/(2 \times R_{pump})$	1.902 m	1.902 m
Pump pulse duration	23 ps	23 ps
Transmission of CM_1	91%	91%
Single pass absorption of the crystal α_p	70%	70%
Overlap efficiency η_o	81%	81%
Pump wavelength λ_p	266 nm	532 nm
Laser wavelength λ_l	290 nm	800 nm
Laser beam waist in crystal ω_l	12.9 µm	48.5 µm
Upper laser level lifetime τ	25 ns	3.2 µs
Emission cross section σ_{em}	9.6×10^{-18} cm^2 [103]	41×10^{-18} cm^2 [51]
ESA cross section σ_{ESA}	3.6×10^{-18} cm^2 [103]	0
Refractive index of the crystal (at λ_l) n	1.41	1.76
Output coupling loss L_{OPC}	2.5%	2.5%
Loss of cavity elements L_t	2.45%	2.45%

The simulated laser output of a mode-locked pumped Ti:sapphire laser at a cavity mismatch length of Δl = 120 mm is given in figure 5.18 a). This result is analogous to the plot in figure 5.14 b) for Ce:LiCAF. Just like when simulating the Ce:LiCAF laser, the filtered simulated result that reflects the laser output as seen by the measurement system is shown in addition to the unfiltered simulated laser output. It is clear that the output of the Ti:sapphire laser is much smoother than the output of the Ce:LiCAF laser. The modulation of the Ti:sapphire laser is predicted to be of the order of only 0.01% for frequencies below 1 GHz and of the order of 0.03% on faster timescales. This is expected from the equation of the single pass gain step (see above), since the upper laser level lifetime of Ti:sapphire (τ = 3.2 µs) is much longer than that for Ce:LiCAF (τ = 25 ns), and so the accumulated inversion effectively averages over a long timescale compared to the inter-pulse period of the pump laser. Figure 5.18 b) shows the predicted results for a Ti:sapphire laser with a cavity length mismatch of 20 mm. This is the analogous simulation to the results in figure 5.16 for Ce:LiCAF. Here, the modulation is of the order of 0.03% for frequencies below 1 GHz and of the order of 0.08% for faster timescales.

5.11 Chapter Summary

The chapter explains how a mode-locked pump source can be used to generate CW laser output with only small residual modulation in Ce:LiCAF lasers. The key is to set up the laser system in such a way that asynchronous pumping is achieved. To obtain such asynchronous pumping, laser cavity lengths associated with rational-harmonic mode-locking (as well as harmonic mode-locking) and regions in their immediate surroundings (the "shoulders" of the harmonics) must be avoided, since the modulation of the laser output is intensified at these cavity lengths. It was shown that the larger the numerator x and the denominator y of a rational harmonic x/y are, the narrower the shoulders of this harmonic are. At the same time the intensity of the modulation gets smaller the larger x and y. As a result there exist cavity lengths that feature low output modulation between regions that are influenced by rational harmonics. Simulations revealed that the optimal cavity length to generate a laser output with minimal residual modulation is at 0.3964 normalized cavity length. At this cavity length a residual modulation of the order 1% was measured experimentally using a ns-photodiode and a 6 GHz oscilloscope. The simulated laser output for the same cavity length predicts an additional fast modulation of the order 4% that can not be resolved by the measurement system and in fact will also not be resolved by many potential applications for CW deep-UV light. In addition, simulations of mode-locked pumped Ti:sapphire lasers have been conducted in order to put the Ce:LiCAF results into perspective. For a cavity mismatch of Δl = 120 mm the predicted Ti:sapphire output features a modulation of only 0.01% for frequencies below 1 GHz and 0.03% on faster timescales.

The main results of this chapter were published in: B. Wellmann, D.J. Spence, and D.W. Coutts, "Dynamics of solid-state lasers pumped by mode-locked lasers." Optics Express, Vol.23, No.4, 12. February 2015, pp. 4441-4452 (see appendix A "Publications Arising from this Thesis").

6

Tuning and Linewidth Narrowing

The broad gain spectrum of Ce:LiCAF makes it an ideal material for a tunable laser with a potential continuous tuning range over 35 nm in the deep UV (280 nm to 315 nm). The concept of wavelength control and selection in lasers dates to the early days of laser research and was proposed independently in dye lasers by Sorokin and Lankard [167] and Schäfer *et al.* [168] in 1966. Dye lasers use organic molecules that feature extremely large bandwidths over tens or even hundreds of nanometers. Simple dye lasers without emission control generate broadband emission that may be composed of several transverse modes, each with a multitude of longitudinal modes [169]. The first narrow-linewidth tunable laser was presented in 1972 by Hänsch in the form of a pulsed dye laser incorporating an intracavity beam-expanding telescope and a diffraction grating [170]. This laser introduced by Hänsch featured a rather long (40 cm) cavity due to the intracavity telescope. More compact solutions for tunable narrow-linewidth lasers were realized using grazing-incidence grating cavities [171] and multiple-prism grating oscillators [172]. These cavity designs have since also been applied to other types of lasers, e.g. tunable gas lasers, semiconductor lasers, and solid-state lasers

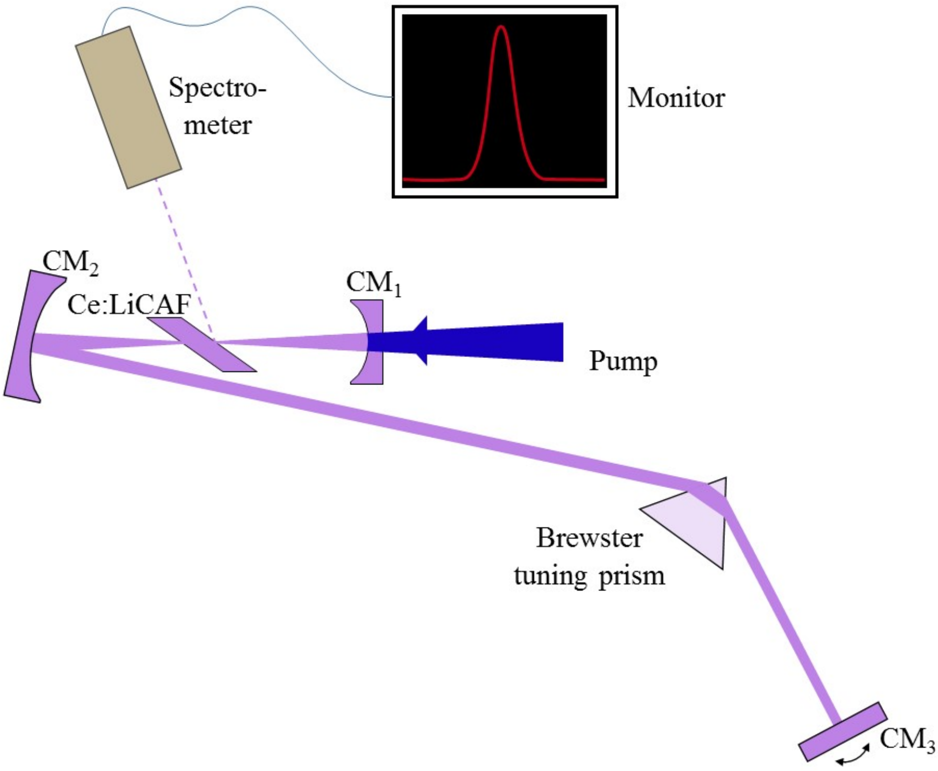

Figure 6.1: Set-up for tuning using a prism

[173]. Of all solid-state lasers, the most common tunable laser is the Ti:sapphire laser with a potential tuning range in the red and infrared from 670 nm to 1100 nm [51]. Typically Ti:sapphire lasers are nowadays tuned using a Lyot filter that is placed inside the laser cavity [174]. Lyot filters use birefringence to select a narrow range of transmitted wavelengths and are usually built with multiple thin plates each plate being half the thickness of the previous one. In this arrangement, the thickest plate determines the linewidth of the laser and the thinnest plate determines the tuning range. In Ti:sapphire lasers, usually quartz is used as a the birefringent material. In this chapter, we use birefringent filtering to tune our Ce:LiCAF laser, but instead of quartz we use magnesium fluoride (MgF_2) as it features larger birefringence in the UV than quartz (see section 6.2 below). Another tuning technique that is widely used in solid-state lasers and that we also exploit for our Ce:LiCAF laser is prism tuning (see section 6.1 below). For many applications it is desirable to generate broadly tunable laser output that also features a very narrow linewidth. Hence laser tuning and linewidth narrowing are often addressed together. Experimental linewidth narrowing of our CW Ce:LiCAF laser is discussed in section 6.3, and section 6.4 explores the theoretical limit of the linewidth of the laser.

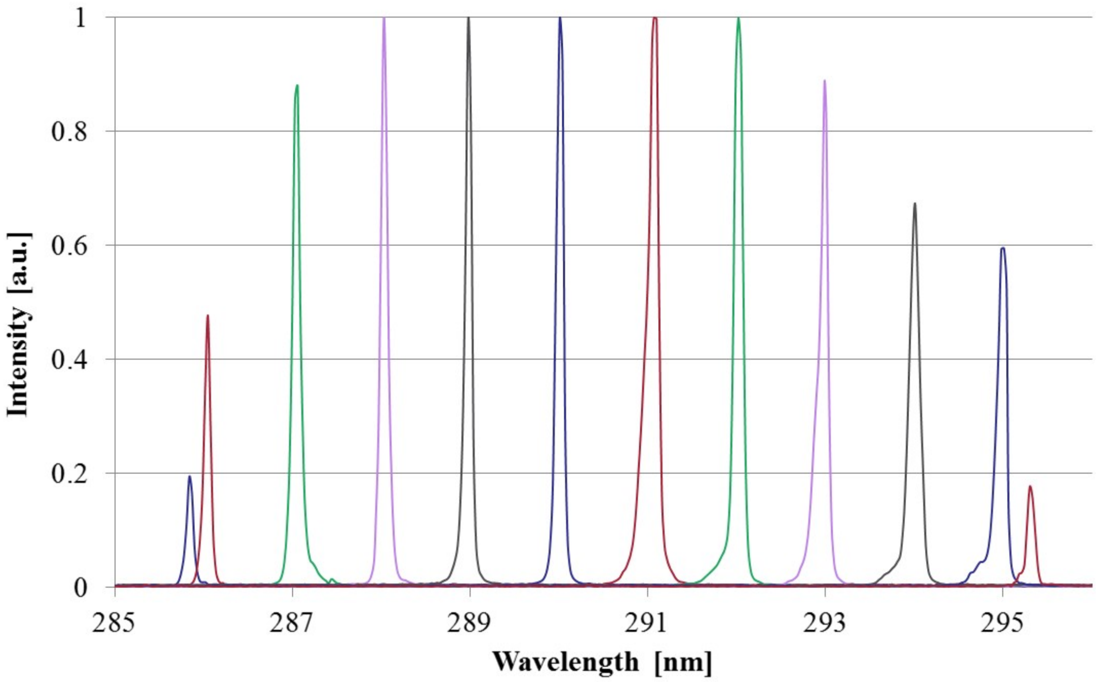

Figure 6.2: Tunability of the CW-laser - laser output spectrum for 12 different angles of the end cavity mirror CM_3

6.1 Prism Tuning

We first investigate tuning our cerium laser using a prism, with a cavity design shown in figure 6.1. By placing a UV grade silica Brewster prism with an apex angle of 67.4° in the long arm of the laser cavity instead of the OPC, the CW Ce:LiCAF laser output wavelength could be tuned by rotating the cavity end mirror CM_2. For such a prism, the input and output beam angles can both be close to Brewster's angle. The laser signal was captured from the Brewster's angle face of the Ce:LiCAF crystal and measured with an Ocean Optics HR4000 spectrometer with a resolution of 0.05 nm. With this set-up, lasing from around 285.85 nm to around 295.30 nm was achieved, with peak performance at around 289 nm (figure 6.2). This tuning range is consistent with the main tuning peak of Ce:LiCAF. Note that the output power corresponding to each spectrum shown in the figure was not measured and the intensities of the individual spectra do not provide accurate quantitative information on the actual output power at the different angles. The full width at half maximum (FWHM) linewidth of the laser with the prism in the longer arm was widest at around 291 nm (0.2 nm) and was narrower towards the extremes of the tuning range (0.1 nm at 286 nm and at 295 nm). While the achieved tuning range of approximately 10 nm is already considerable, nanosecond pulsed

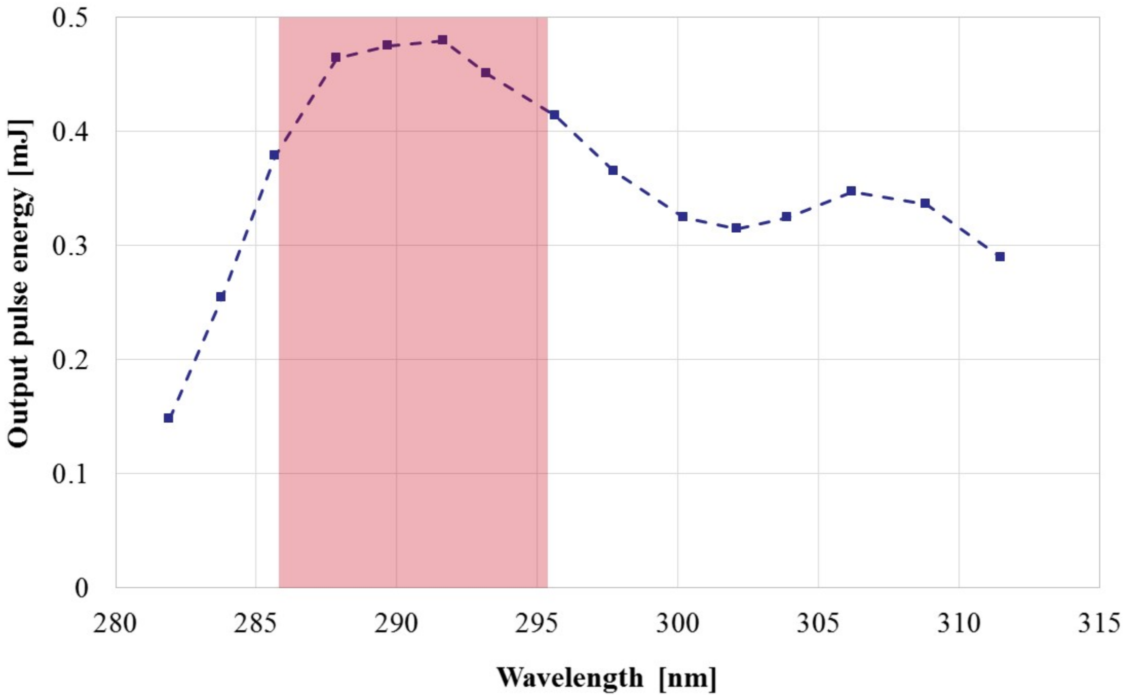

Figure 6.3: Tuning curve of Spence *et al.* [131] (blue) and our tuning range achieved via prism tuning (red).

Ce:LiCAF lasers can be readily tuned from 282 nm to 315 nm [131]. Figure 6.3 shows the tuning curve reported by Spence *et al.* in [131] with our tuning range achieved via prism tuning marked in red. The tuning range was limited by the fact that the laser was running only about a factor of two over threshold. Tuning with a Brewster prism has the disadvantage of preventing double-pass pumping of the crystal since the 266 nm pump light does not get retro-reflected off the cavity end mirror. The resulting reduction in absorbed pump power contributes to the higher threshold of the tuned laser. This problem could be solved by replacing the HR CM_2 with a dichroic mirror and reinjecting the transmitted pump back into the crystal via an external mirror, although the loss for λ = 290 nm of the dichroic coating L_{DC} = 0.45% is higher than the loss of the HR coating L_{HR} = 0.2%, and so a set-up with two dichroic mirrors would involve increasing the total cavity loss significantly and largely removing any potential advantage.

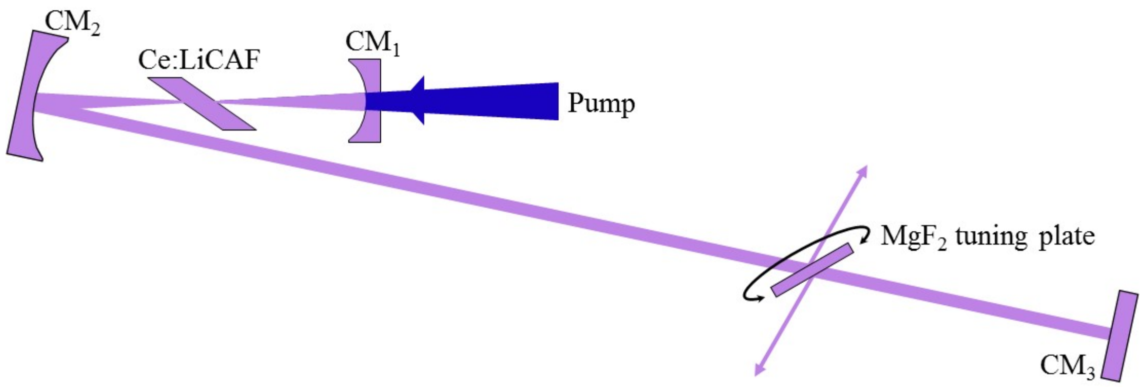

Figure 6.4: Schematic of the laser cavity for birefringent tuning. The MgF_2 tuning plate is placed in the long cavity arm close to Brewster's angle and is simultaneously used as an output coupler.

6.2 Birefringent Tuning

An alternative to prism tuning is birefringent tuning, where a birefringent plate is inserted into the laser cavity at close to Brewster's angle relative to the laser beam path. With the optical axis of the birefringent element set at an angle to the polarisation of the light inside the laser cavity, different wavelengths experience different polarisation rotations and the wavelengths that complete an integer number of polarisation rotations see the lowest loss on the Brewster faces of the birefringent element and the Brewster laser crystal. Figure 6.4 shows a schematic of our Ce:LiCAF laser cavity set-up for birefringent tuning. The birefringent magnesium fluoride (MgF_2) plate was placed in the long cavity arm at close to Brewster's angle similar to the OPC when the laser was running without a tuning element. In this set-up, the MgF_2 plate was simultaneously used as an output coupler.

Using birefringent tuning instead of tuning with a Brewster prism has the advantage that at least part of the unabsorbed single-pass pump light can be recycled back into the laser crystal after being reflected by the HR cavity end mirror, as there is no spatial dispersion between the pump and the laser modes. Pumping efficiency for the return pass is still reduced depending on the rotation of the pump light polarisation in the birefringent element and associated loss on the Brewster faces.

Birefringent tuning has been used effectively with CW dye and Ti:sapphire lasers in the past. The equation used to calculate the transmission T of the birefringent plates (assuming the plate is followed by a linear polariser[1]) can be found in [175].

[1] In the experiments no additional polariser was inserted but due to the four Brewster surfaces in the cavity the laser field is strongly polarised.

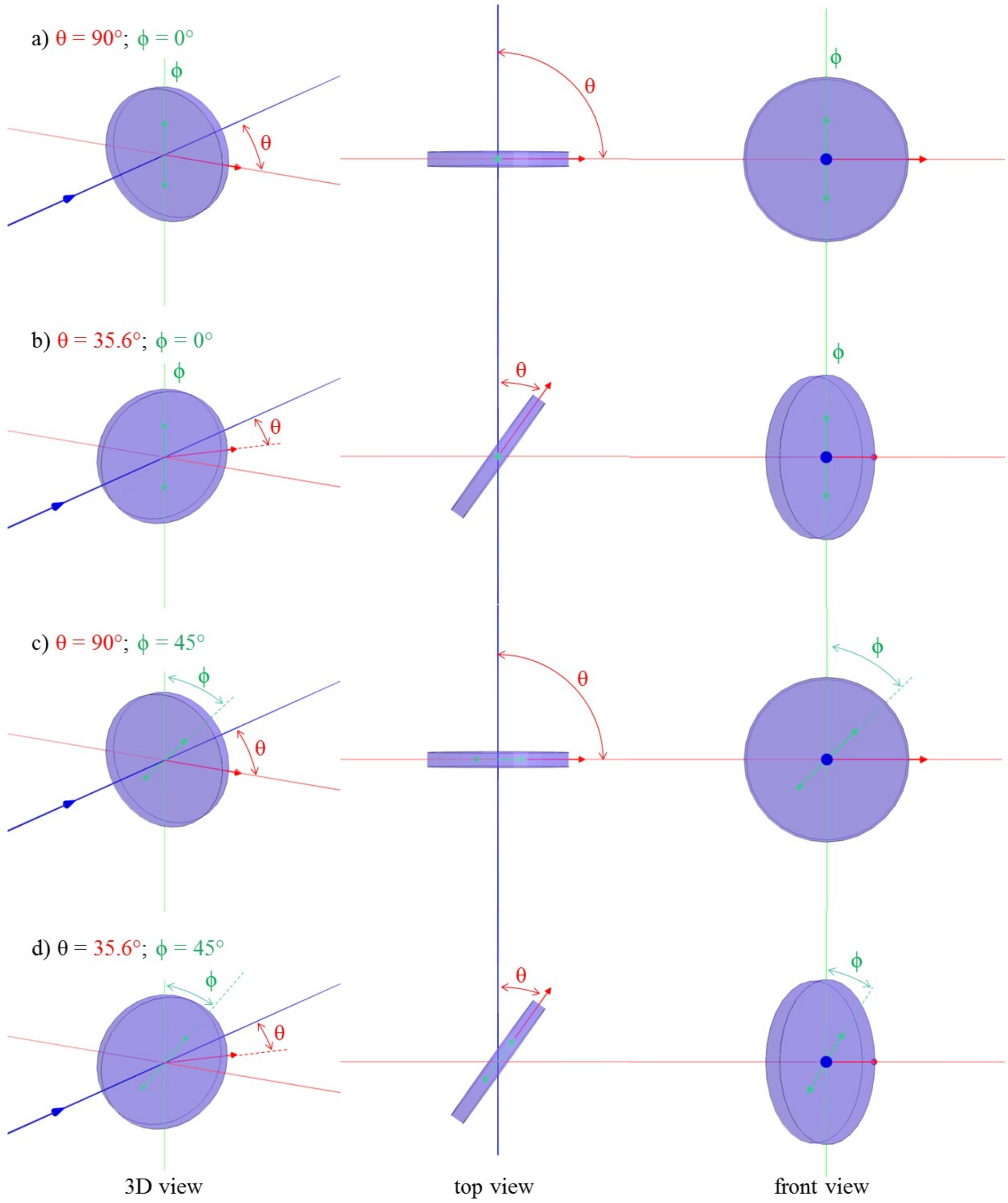

Figure 6.5: Schematic of the angles relevant in birefringent tuning. Plotted are four different cases a) to d) for different combinations of the angles θ and ϕ. The blue arrow marks the path of the laser beam inside the cavity through the birefringent tuning plate. θ is the tilt angle of the plate as a whole with respect to the beam axis. Since the plate is also used as an OPC, θ is also the angle that controls the output coupling fraction. ϕ is the plate rotation angle of the crystal axis and is the "internal" tuning angle of the plate. In the first column the plate is shown in a 3D view for each angle combination, the second column is the top view highlighting the tilt (and OPC) angle θ relative to the laser beam path. The third column shows the plate looking down the beam axis which also best illustrates the internal tuning angle ϕ.

Thus the transmission T is given by

$$T = 1 - \sin^2(2\phi)\,\frac{n_o^4 - n_o^2\cos^2\theta}{\left(n_o^2 - \cos^2\phi\cos^2\theta\right)^2}$$

$$\cdot \sin^2\left[\frac{2\pi d}{\lambda}\left(\frac{n_e\left[1 + \left(\cos^2\theta\cos^2\phi\right)/n_e^2 - \left(\cos^2\theta\cos^2\phi\right)/n_o^2\right]}{\left[1 - (\cos^2\theta\cos^2\phi)/n_e^2 - (\cos^2\theta\cos^2\phi)/n_o^2\right]^{1/2}} - \frac{n_o}{\left[1 - (\cos^2\theta)/n_o^2\right]^{1/2}}\right)\right].$$

Here, ϕ is the plate rotation angle of the crystal birefringent axis, θ is the plate tilt angle as a whole with respect to the beam axis, d is the plate thickness, and n_o and n_e are the principal refractive indices of the uniaxial crystal for light linearly polarised perpendicular and parallel respectively to the optical axis. Note that both n_o and n_e are also wavelength dependent due to material dispersion. To illustrate the two angles relevant for birefringent tuning, schematics of a birefringent tuning plate at different angle combinations are drawn in figure 6.5. In all pictures, the blue arrow marks the path of the laser beam inside the cavity. The first row shows the plate with a tilt angle θ of 90° relative to the beam path, so that the plate is perpendicular to the laser beam. The two-sided green arrow marks the optical axis of the birefringent plate. Here, in case a), the internal rotation angle of the plate ϕ between the optical axis of the plate and the vertical axis of the system is 0°. The first column in figure 6.5 shows the scenario in a 3D view, the second column provides the top view emphasising the tilt angle θ, and the third column gives the front view, which better shows the rotation angle ϕ. In the second row, case b), the plate is tilted by 35.6°, which achieves an incidence angle for the laser beam (90° - θ) of Brewster's angle for a MgF_2 plate at a wavelength of λ = 289 nm, and hence the angle close to which we are operating. In row c) θ is set back to 90°, and now ϕ is moved to 45° to illustrate the rotation of ϕ. Angles close to 45° for ϕ are used to achieve best tuning results as will be discussed in the following. In the last case d), both θ and ϕ are now rotated.

We will now investigate the influence of the two angles θ and ϕ on the transmission T of the plate. We assume that the input laser beam is horizontally polarised and the plate is followed by a linear polariser hence we are assuming full rejection of σ-polarised light. First we will discuss ϕ, the internal rotation angle, that is the tuning angle of the birefringent axis with respect to the polarisation axis. In figure 6.6 transmission curves of a 250 µm thick MgF_2 plate for different angles ϕ are plotted as a function of wavelength in a range relevant for our Ce:LiCAF laser. For these calculated transmission curves, the angle θ was fixed at 35°, which is an angle very close to that for Brewster's angle operation of 35.6°.

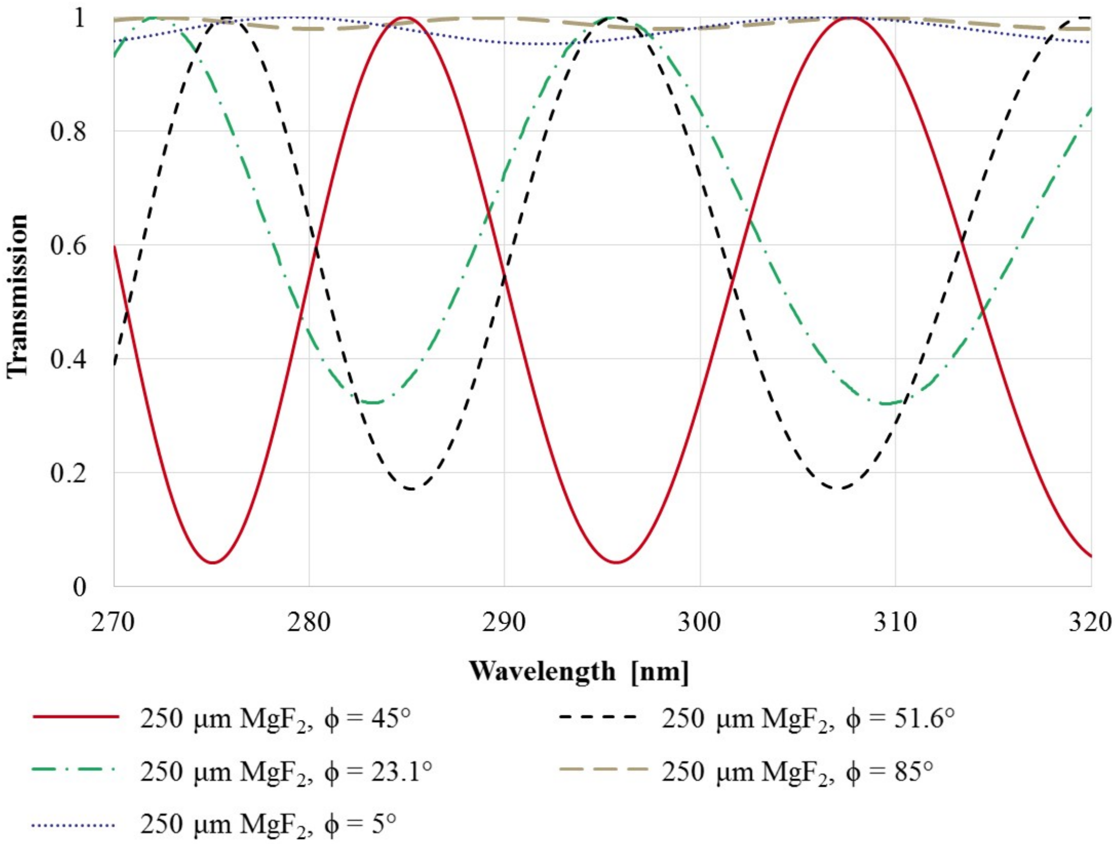

Figure 6.6: Calculated transmission curves of a 250 μm birefringent MgF_2 Brewster tuning plate followed by a linear polariser for different rotation angles ϕ, with the tilt angle $\theta = 35°$.

For wavelengths with a transmission of 1, π-polarised light has its polarisation unchanged or changed by an integer number of polarisation rotations and hence the birefringent plate does not attenuate the incident π-polarised light meaning these wavelengths are most likely to lase. All other wavelengths experience an alteration of polarisation, either elliptical or rotated linear, and suffer loss at the Brewster faces of the birefringent plate and the Brewster laser crystal. For a plate rotation of 45° for example, the two peak wavelengths in the wavelength range examined are 284.9 nm and 307.6 nm. The wavelengths of the transmission peaks shift with angle, which is why birefringent plates can be used to tune a laser in the first place. There are two other characteristics of the transmission curves that also change with the rotation angle ϕ as can be seen in the figure: the free spectral range (FSR) and the minimum transmission. The FSR is the spectral distance between two peaks featuring a transmission of 1. The dependency on ϕ can be seen in the figure: there is a transmission peak at 295.8 nm both for a plate rotation of 51.6° and 23.1°, but while the FSR towards shorter wavelengths for a rotation of 51.6° is 19.9 nm, the FSR for a rotation of 23.1° is 23.6 nm.

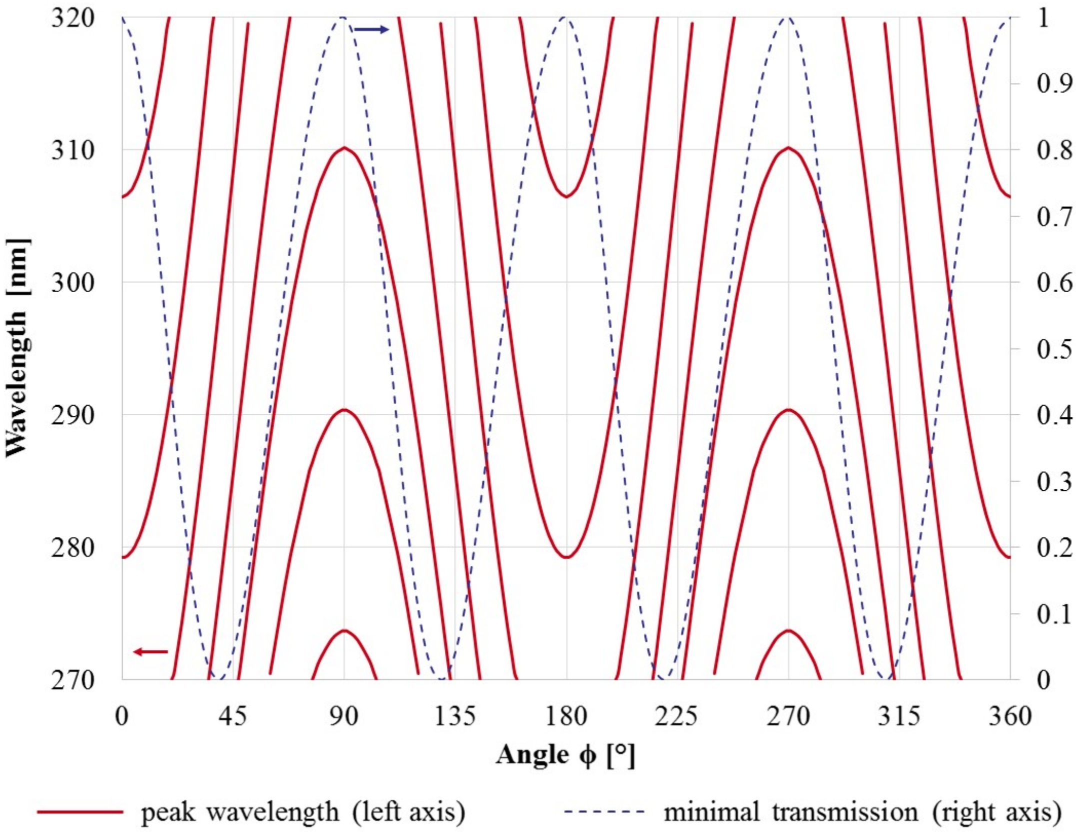

Figure 6.7: Calculated peak wavelengths and minimal transmission of a 250 µm birefringent MgF_2 Brewster tuning plate followed by a linear polariser as functions of the rotation angle ϕ, with the tilt angle $\theta = 35°$.

The dependency of the minimal transmission on the rotation angle is also clearly visible in figure 6.6. The lower the value of the minimal transmission, the stronger is the wavelength selection effect. For a plate rotation of 45° the minimal transmission is 0.042, hence the wavelength selection is strong, while for a plate rotation of 0° and 90° (as well as 180°, 270°, and 360°), that is when the optical axis of the plate is aligned with the vertical axis of the system or perpendicular to the vertical axis of the system respectively, the transmission is uniformly 1 for all wavelengths and no wavelength selection occurs, resulting in a laser spectrum equal to that of the laser running without a tuning element.

Figure 6.7 illustrates the dependencies of the peak wavelengths and the minimal transmission on the rotation angle ϕ for a 250 µm thick MgF_2 plate at a tilt angle of 35°. The minimal transmission periodically varies between 0 and 1 as discussed in the paragraph above. We will see in the discussion of the tilt angle θ below, that in addition to being dependent on ϕ, the minimal transmission is also dependent on θ. For the chosen fixed tilt angle of $\theta = 35°$,

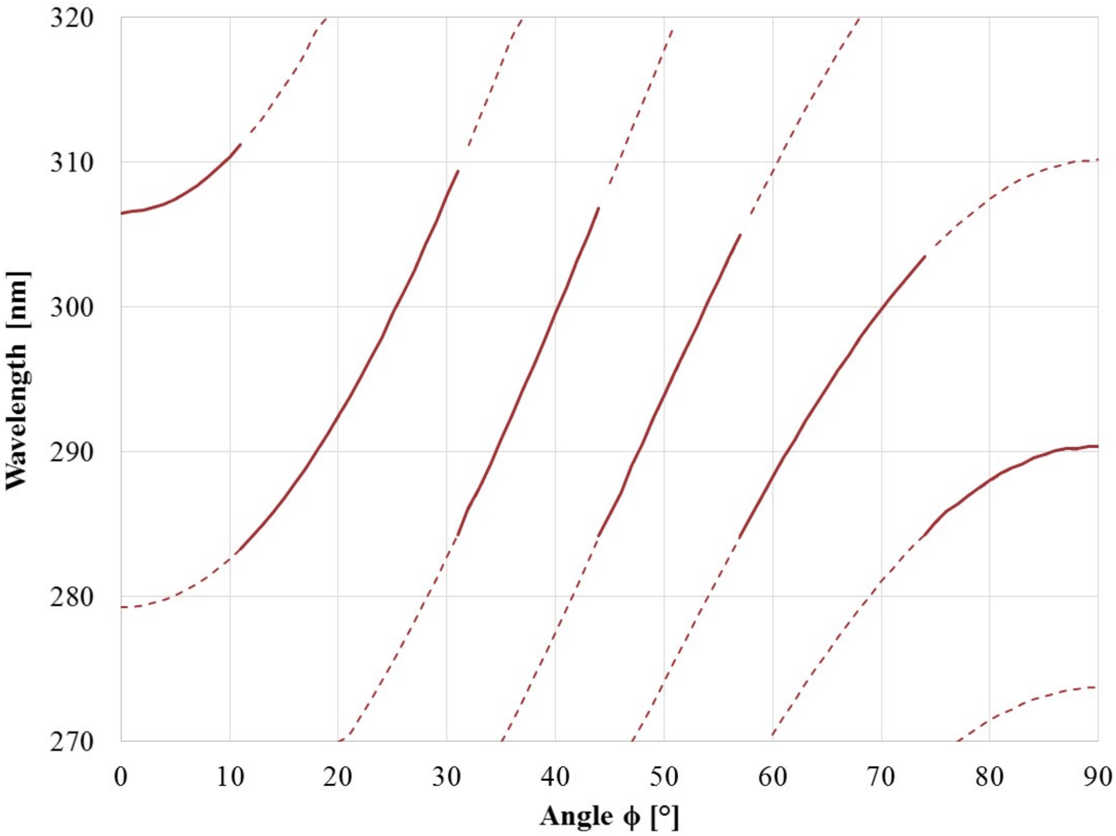

Figure 6.8: Predicted lasing wavelength with a 250 µm birefringent MgF_2 Brewster tuning plate as a function of the rotation angle ϕ as determined by taking a typical Ce:LiCAF tuning curve [131] into account.

the minimal transmission is 0 at a rotation angle ϕ = 40° as well as 130°, 220°, and 310°. The peak wavelengths of the transmission as a function of rotation angle were determined in the wavelength range of 270 nm to 320 nm. The peaks follow a pattern with reversal points at 0°, 90°, 180°, and 270° and multiple peaks at each angle. To determine which one of the peaks is most likely to lase in our Ce:LiCAF laser, a typical tuning curve of a Ce:LiCAF as reported by Spence *et al.* in [131] was taken into account (see e.g. figure 6.3). The result is shown for a rotation angle of 0° < ϕ < 90° in figure 6.8 revealing points of discontinuity in the laser wavelength. Experimentally, these discontinuities and the reversal points in the peak wavelength over angle make it possible to determine the orientation of the optical axis of an unmarked birefringent plate. By rotating the plate continuously in one direction in a running laser, upwards and downwards tuning with jumps between wavelengths can be observed interrupted by reverse points where the spectrum is broad and in the shape of the untuned laser. Thus the orientation of the optical axis can be easily found experimentally.

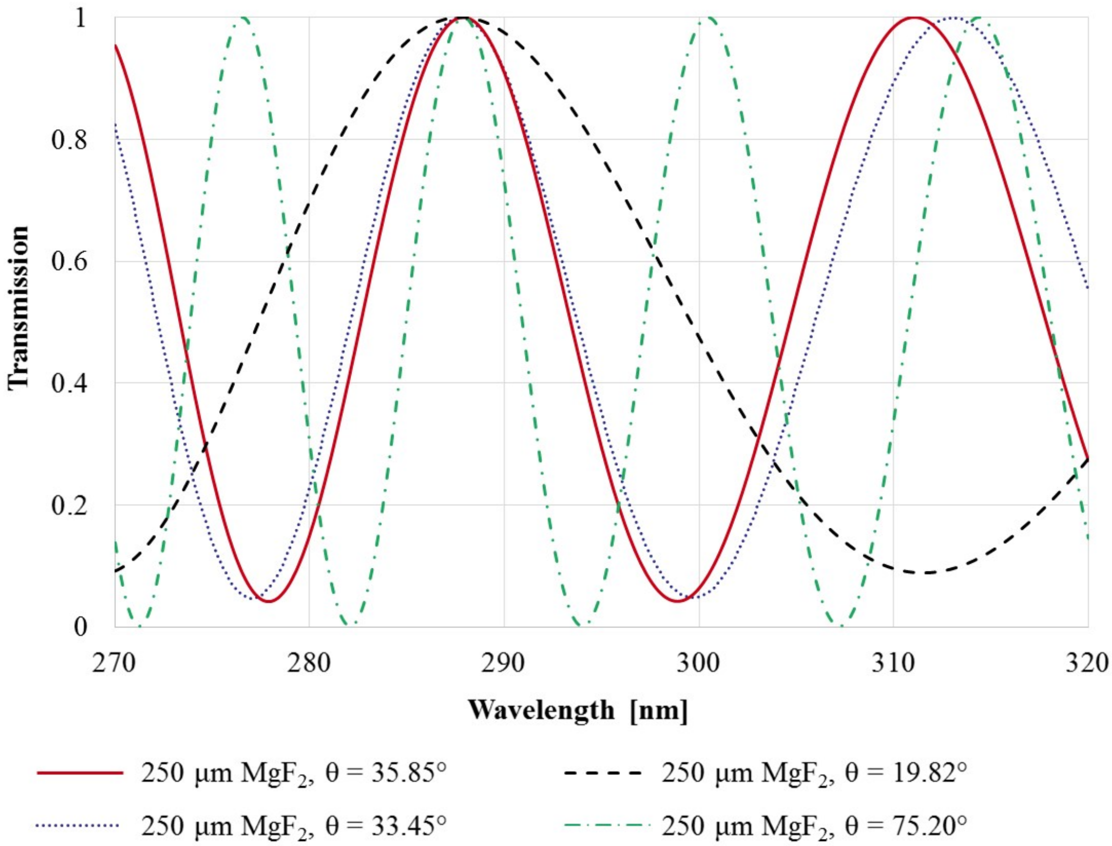

Figure 6.9: Calculated transmission curves of a 250 µm birefringent MgF_2 Brewster tuning plate followed by a linear polariser for different tilt angles θ, with the rotation angle $\phi = 45°$.

To determine the best plate orientation for optimal tuning results we must look at all discussed features of the birefringent tuning plate together. We require a good wavelength selection hence a good wavelength suppression, so the minimal transmission should be as close to 0 as possible. This is given for rotation angles around $\phi = 40°$ when the plate is set to a tilt θ close to Brewster's angle. At the same time the FSR should be as large as possible to allow tuning over a wide range of wavelengths. The FSR is greater for angles between 0° and 45° than it is between angles of 45° and 90°, so combining both features leads to an ideal plate rotation of around 30° to 45° for best tuning results.

Next, we will have a closer look at the tilt angle θ. Figure 6.9 shows transmission curves for the 250 µm MgF_2 plate with a fixed rotation angle of $\phi = 45°$ for different plate tilt angles. In general, placing the birefringent plate in the laser beam path at different tilt angles results in the selection and suppression of different wavelengths similar to when the rotation angle ϕ is changed, but there are certain differences in the behaviour when comparing a rotation of ϕ to a tilt of θ. In figure 6.9 tilt angles were chosen at which the transmission curves all feature

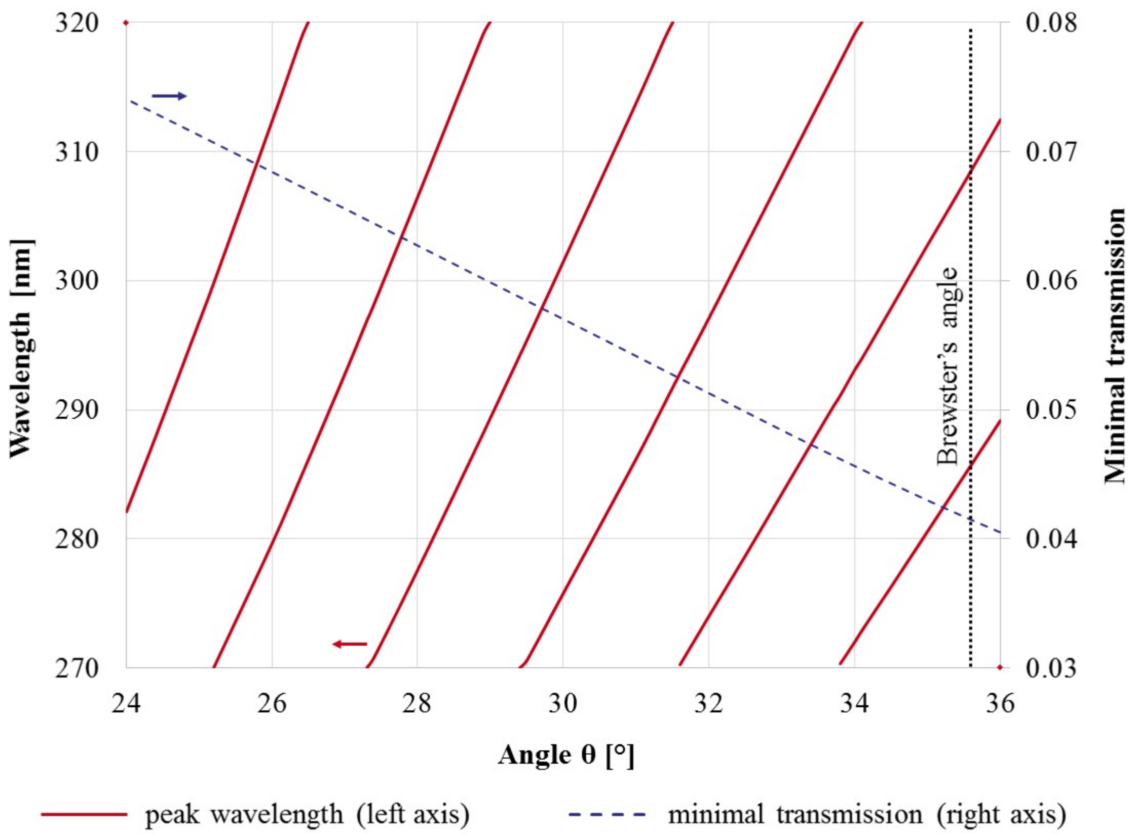

Figure 6.10: Calculated peak wavelengths and minimal transmission of a 250 μm birefringent MgF_2 Brewster tuning plate followed by a linear polariser as functions of the tilt angle θ, with the rotation angle $\phi = 45°$.

a peak at 288 nm. The strong dependency of the FSR on the tilt angle is clearly visible with the FSR being larger for smaller tilt angles. The FSR is smallest at angles close to 90° (and hence also 270°). However, transmission curves at very small or very large tilt angles are of purely theoretical value, since in order to support lasing, the birefringent plate must be placed in the beam with a tilt angle close to Brewster's angle similar to a non-birefringent OPC (see chapter 4). Nevertheless, in order to assure a larger tuning range, it is slightly favourable to tilt the plate towards smaller angles from Brewster's angle when choosing an OPC angle. This is confirmed when comparing the transmission curves for $\theta = 35.85°$ and $\theta = 33.45°$ in figure 6.9. These are the two angles closest to the Brewster angle at 35.6° which feature a transmission peak at 288 nm. It can be seen that the FSR of the 33.45° curve is larger than the FSR of the 35.85° curve.

The minimal transmission also changes with a changing tilt angle θ, but the dependency is much weaker than it is when changing the rotation angle ϕ. At $\theta = 0°$ (grazing), the minimal

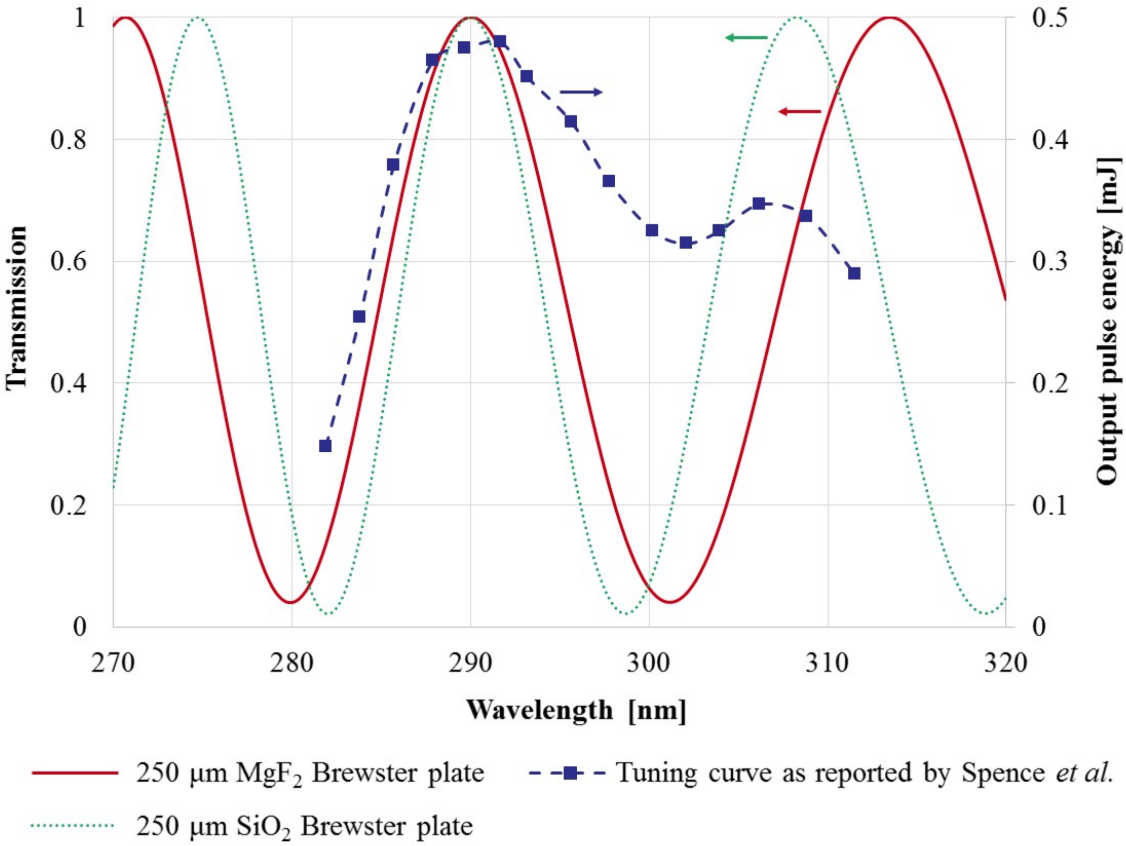

Figure 6.11: Calculated transmission of 250 µm birefringent MgF_2 and SiO_2 Brewster tuning plates and the tuning range achieved by Spence *et al.* in [131].

transmission is just 0.12 (for a plate with a rotation angle of 45°) and it decreases further with increasing θ. At $\theta = 90°$ it is of order 6×10^{-7}. The weak dependency of the minimal transmission on θ is visible in figure 6.9 and also in 6.10, where the minimal transmission and the peak wavelength are plotted for $24° \leq \theta \leq 36°$, that is at Brewster's angle and angles up to around 10° smaller than Brewster's angle where lasing still occurs. The figure confirms that there is an additional strong peak wavelength dependency on θ, that can be used in order to fine tune the laser by adjusting θ over a very small angle range and to reach wavelengths at the limits of the tuning range.

In the visible or infrared, most commonly quartz plates are used as birefringent tuning filters [175]. But in order to ensure a single tuning peak within the broad gain of Ce:LiCAF in the UV (280 nm to 315 nm), very thin quartz plates with thicknesses below 200 µm would be required. In this spectral region, MgF_2 has slightly greater birefringence and lower dispersion than quartz, and thus is the better alternative. The calculated transmission curves for a 250 µm MgF_2 Brewster plate and a 250 µm SiO_2 Brewster plate are plotted in Fig. 6.11

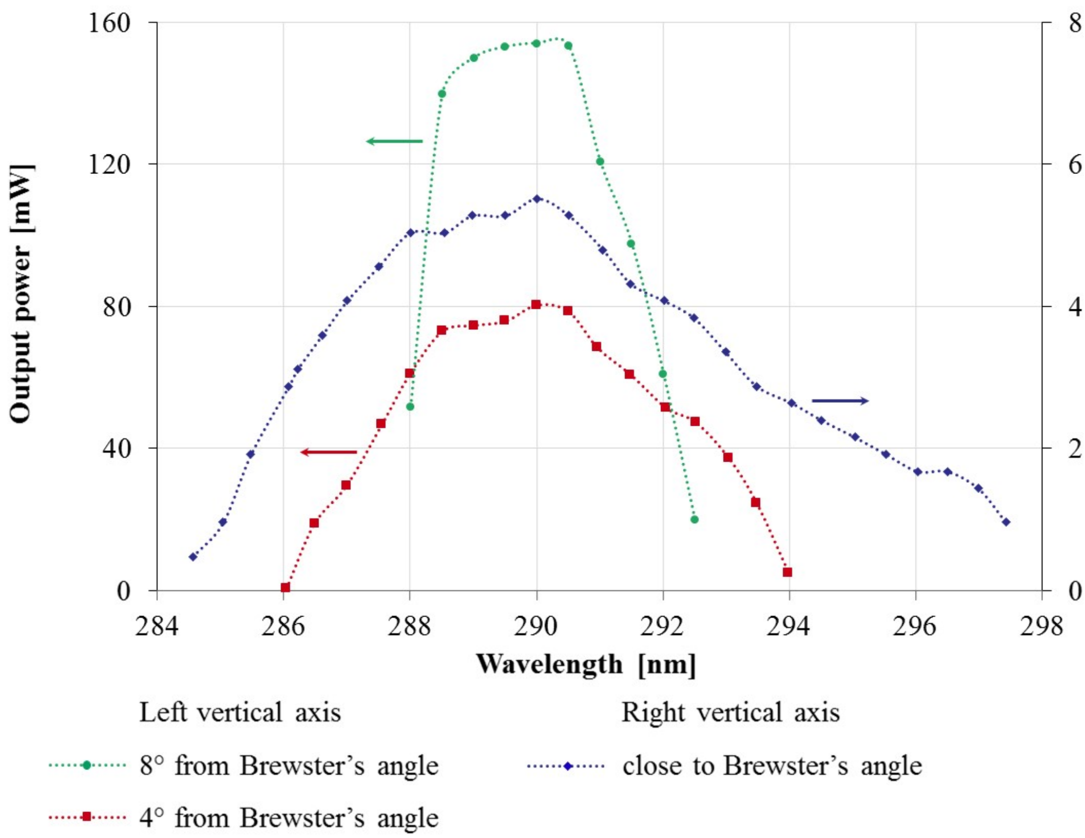

Figure 6.12: Tuning curves using a single 250 µm birefringent MgF_2 plate at different OPC angles.

in addition to the tuning range achieved by Spence *et al.* in [131]. The values for n_o and n_e for quartz were calculated using the Sellmeier coefficients given in [176]. While the FSR of the 250 µm quartz plate at a tilt angle close to Brewster's angle is just 18 nm in the relevant spectral region, the FSR of the 250 µm thick MgF_2 tuning plate is 24 nm.

In Fig. 6.12 tuning curves for the Ce:LiCAF laser with a single 250 µm thick birefringent MgF_2 plate at different output coupling angles are plotted. For low output coupling with the plate at a tilt angle very close to Brewster's angle, continuous tuning over a range of 13 nm from 284.5 nm to 297.5 nm with a maximum output power of 6 mW was achieved. For higher output coupling the tuning range narrowed, but the maximum output power increased, as expected. With the tuning plate at 9° from Brewster's angle, the maximum output power was 154 mW and the tuning range spanned from 288.2 nm to 292.5 nm. Figure 6.13 shows the tuning range reported by Spence *et al.* in [131] with the tuning range of 13 nm achieved at close to Brewster's angle marked in red.

Another factor that influences the tuning characteristics is the plate thickness d. In figure 6.14 we see transmission curves for birefringent MgF_2 plates of different thicknesses, all

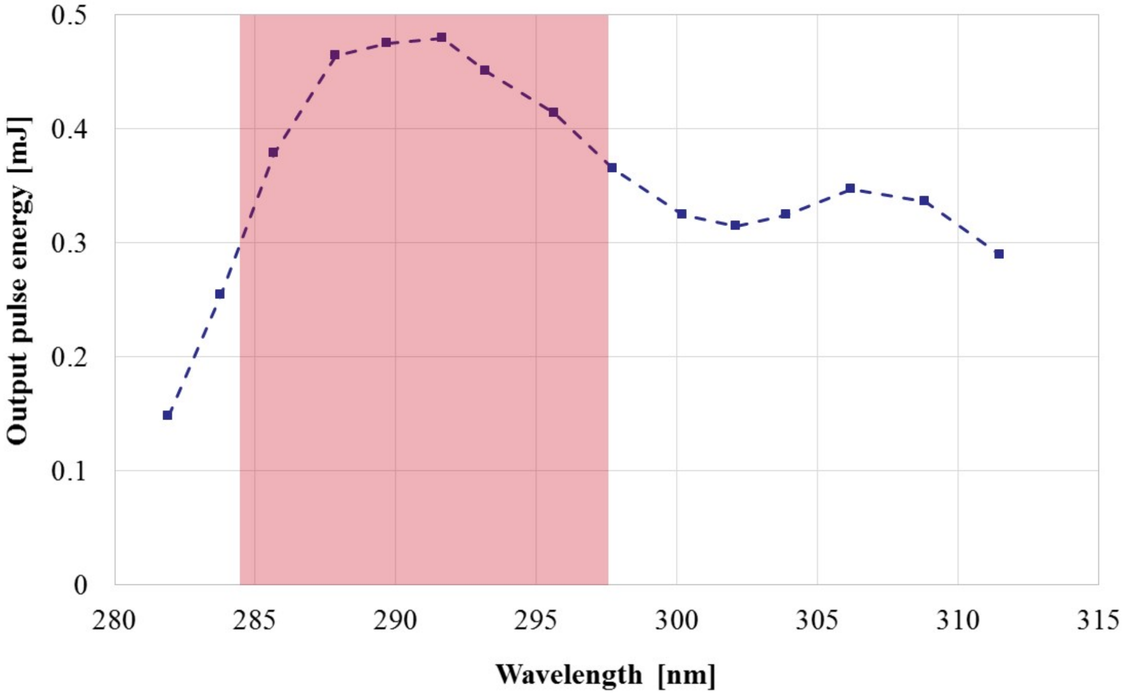

Figure 6.13: Tuning curve of Spence *et al.* [131] (blue) and our tuning range achieved via birefringent tuning with a 250 μm birefringent MgF_2 Brewster tuning plate (red).

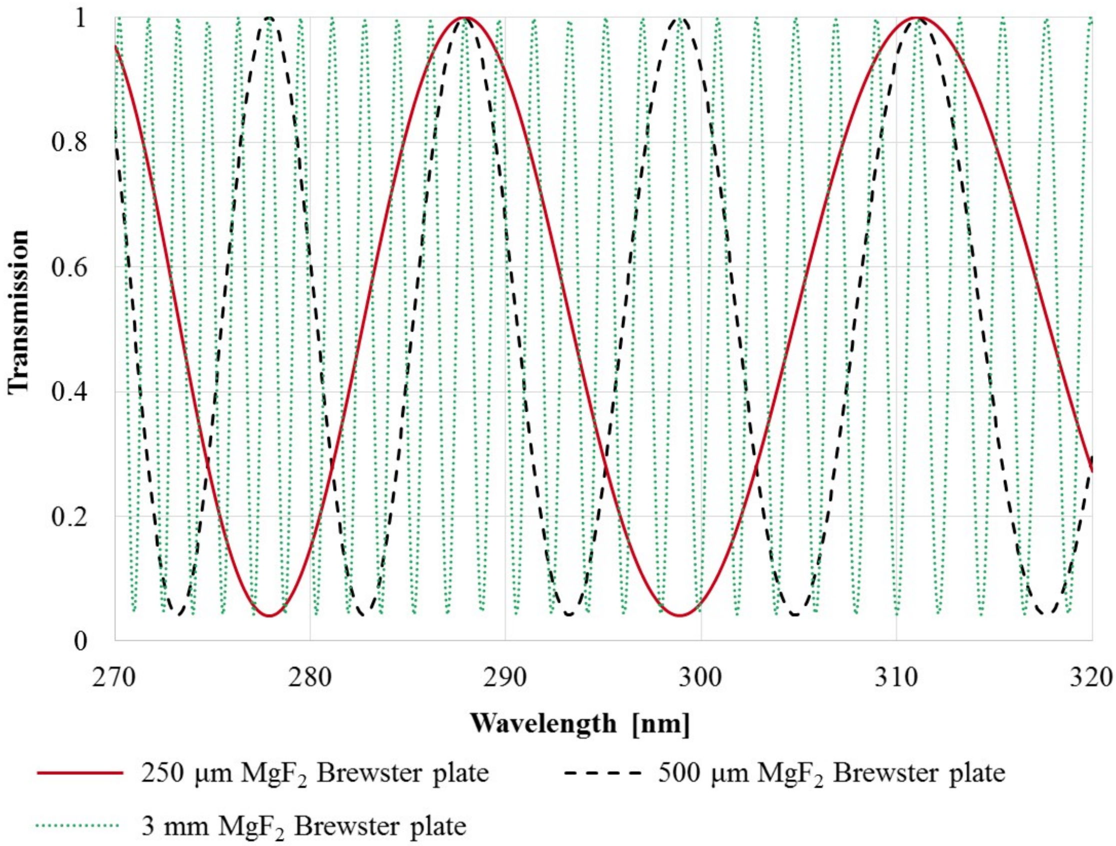

Figure 6.14: Calculated transmission curves for birefringent MgF_2 Brewster tuning plates of different thicknesses, all at a tilt angle of $\theta = 35°$ and a rotation angle of $\phi = 45°$.

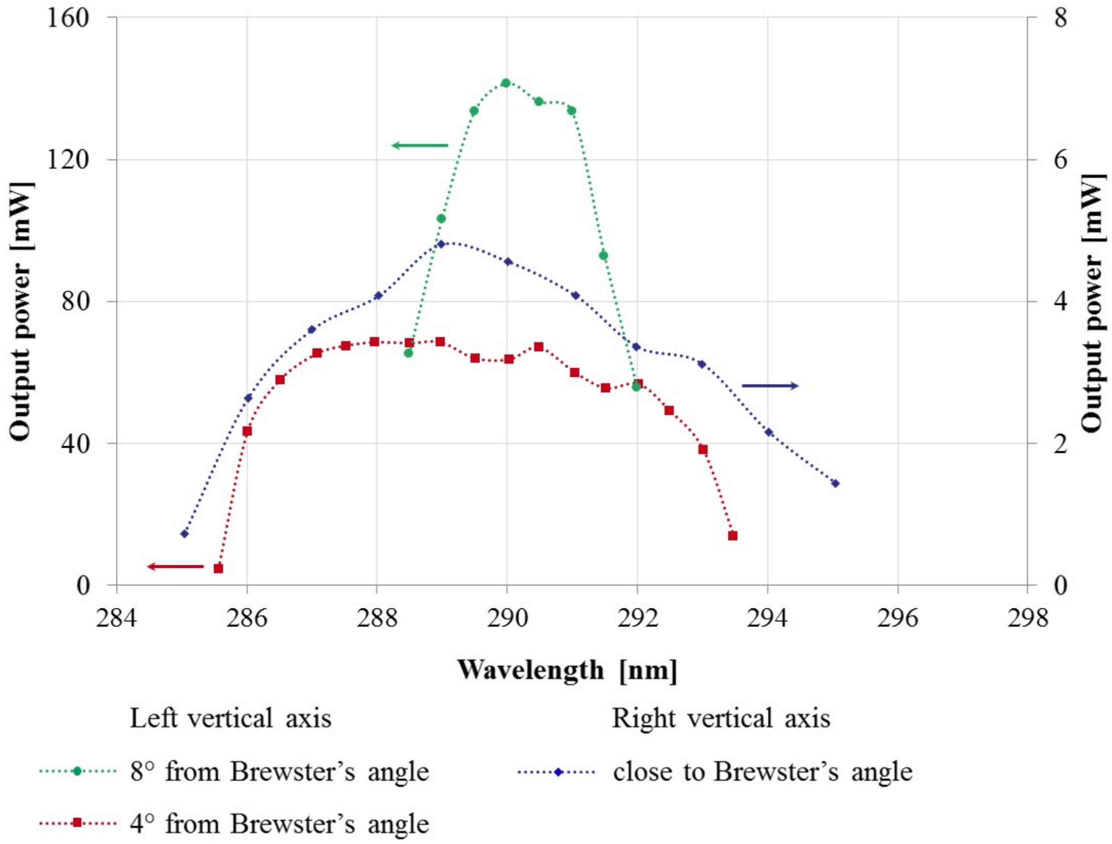

Figure 6.15: Tuning curves using a single 500 μm thick birefringent MgF_2 plate at different output coupling angles.

at a tilt angle of $\theta = 35°$ and a rotation angle of $\phi = 45°$. The minimal transmission and the peak wavelength (288 nm) do not change as we increase the plate thickness by integer multiples, but the FSR decreases proportionally. This means, when interested in a large tuning range regardless the linewidth of a laser, a plate thin enough to feature a FSR of the same order as the width of the gain spectrum of the laser, should be used. Figure 6.15 shows the tuning curves of a 500 μm thick MgF_2 plate at different output coupling angles. At close to Brewster's angle a tuning range of 10 nm from 285.0 nm to 295.0 nm was achieved, which is close to the theoretical FSR of 10.6 nm for this spectral region. In the experimental case the laser continues to lase as the plate is rotated, but jumps from 285 nm to 295 nm (or reverse, see above discussion of the wavelength dependency on the rotation angle), which is a clear sign that the tuning range is limited by the free spectral range and not by the gain properties or lack of pump power. In addition tuning experiments with even thicker MgF_2 plates were conducted. For a 3 mm thick MgF_2 plate, a tuning range of 1.47 nm was achieved (288.45 nm to 289.92 nm), the theoretical FSR for such a plate is 1.6 nm. A 4 mm thick

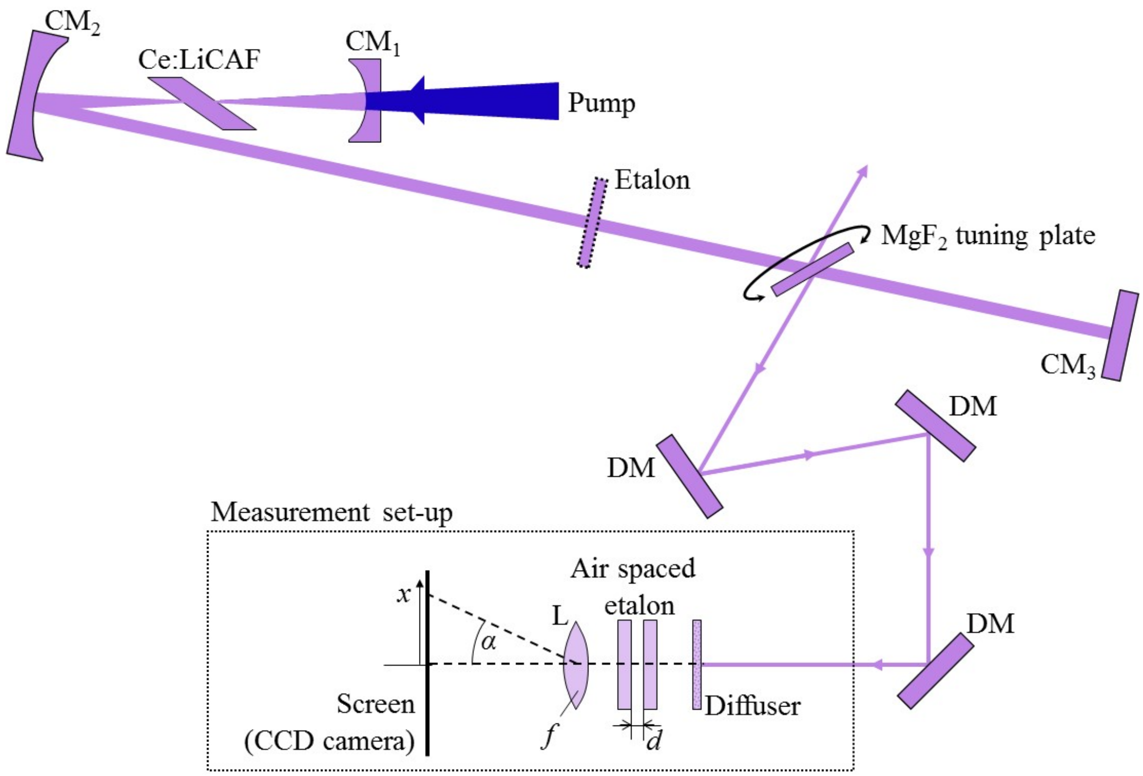

Figure 6.16: Schematic of the cavity set-up for linewidth narrowing and linewidth measurement. For strongest linewidth narrowing an additional etalon was placed in the cavity at close to normal incidence.

MgF_2 plate lead to a 1.16 nm tuning range from 288.63 nm to 289.7 nm with a corresponding theoretical FSR of 1.2 nm and finally a 6 mm MgF_2 plate showed a 0.7 nm tuning range (288.92 nm to 289.62 nm) that is also in good agreement with the theoretical FSR value of 0.8 nm. The tuning ranges of all plates with thicknesses of 500 µm and larger were FSR limited as expected.

6.3 Linewidth Narrowing

To determine the output linewidth of the laser, a measurement set-up using an air-spaced Fabry-Perot etalon and an UV CCD camera was constructed. A schematic of the laser cavity and the measurement set-up for linewidth measurement and linewidth narrowing is shown in figure 6.16. The output off the MgF_2 tuning plate was separated via three dichroic mirrors (DM) and then sent through a diffuser into an air spaced etalon with thickness d realized using two parallel UV mirrors with a nominal reflectivity at 290 nm of $R_{290} = 90\%$. The light transmitted through the etalon was captured on a CCD placed in the focal plane of a lens with the focal length f. To average out strong laser speckle the diffuser was mounted on a rotor and spun while collecting an image. The image captured by the CCD camera was a set of concentric fringes. An example of such a fringe pattern is given in figure 6.17. The captured fringes in the figure were achieved for a set-up with a 4 mm MgF_2 Brewster tuning plate and a 3 mm uncoated narrowing etalon close to normal incidence in the long arm of the laser cavity. Figure 6.17 a) shows the raw image of the fringes captured with the CCD camera. The radial intensity cross section was extracted from this image (white line plotted at the bottom of figure 6.17 a)) as a column average of the intensities over 20 pixels of the middle rows of the pattern and then plotted over the distance x, that is derived by multiplying the pixel number by the size of one pixel. The zero-point of the axis x is matched to the pixel column corresponding to the centre of the pattern. Using the geometrical relationship $\tan(\alpha) = x/f$ the intensity pattern can be given as a function of the angle α. In order to generate a pattern with equidistant peaks, the extracted intensity is then plotted against $1 - \cos(\alpha)$ (figure 6.17 b)). A calculated transmission curve based on the etalon transmission function

$$T = \frac{\Delta\nu}{\Delta\nu + FSR \sin^2\left(\frac{2\pi}{\lambda} 2n(\lambda) d \cos(\alpha)\right)}$$

was then fitted to the extracted intensity pattern. In this equation, $\Delta\nu$ is the linewidth of the pattern, $n(\lambda)$ is the wavelength dependent refractive index, and d is the thickness of the air spaced etalon, that is the distance between the two mirrors. FSR is the free spectral range

$$FSR = \frac{c}{2n(\lambda)d}.$$

Since the transmission is wavelength dependent (and thus frequency dependent), it is crucial to measure the peak wavelength at all times when conducting the linewidth measurement. This was done via the Ocean Optics HR4000 spectrometer that was also used for previous experiments. The measurement was conducted over a timeframe of order 1 second and no frequency drift was observed over a period of minutes. The two variable values in the transmission function that are adjusted to fit the measured intensity pattern, are the pattern linewidth $\Delta\nu$ and the etalon thickness d. In practice a rough value of d is set based on the measurement of the mirror distance using a ruler. Then the fit function scans through an etalon thickness range close to the set value and determines the exact thickness that matches the measured results best for a fine tuning of the value. The step width used for the scan is 0.01 µm, hence the etalon thickness is determined to two decimal places. The fit values can

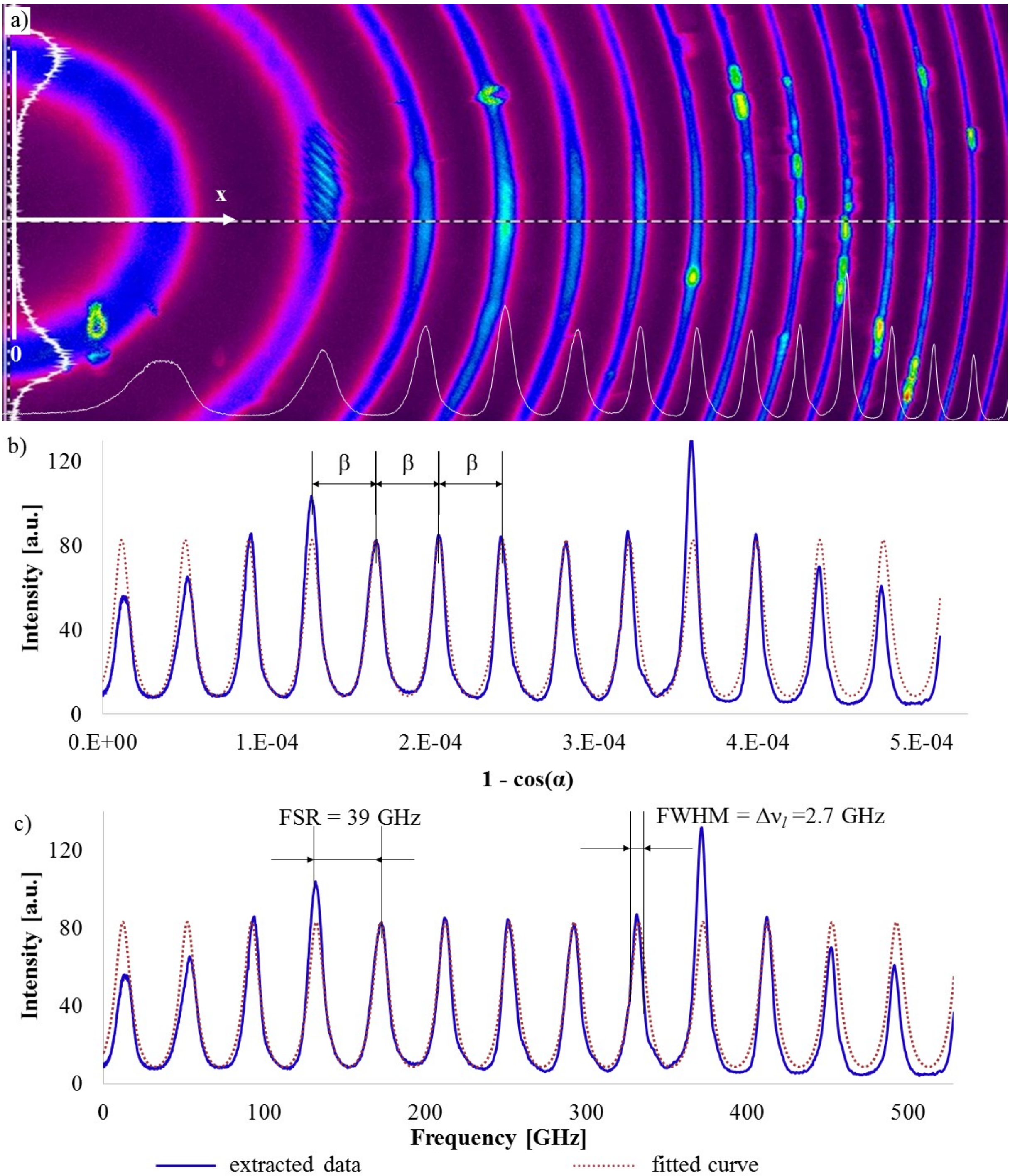

Figure 6.17: Fabry-Perot fringes for the laser with a 4 mm MgF_2 Brewster tuning plate and a 3 mm etalon close to normal incidence, tuned to 290.4 nm. a) raw image of the fringes captured with a CCD camera. Bright spots superimposing the pattern are caused by UV fluorescent contaminations due to organic residue on the CCD. b) Intensity pattern extracted from the raw image and the fitted curve to match the pattern plotted over 1-cos(α) and c) intensity pattern and the fitted curve to match the pattern plotted on a linearised frequency scale. The free spectral range (FSR) is measured to be 39 GHz and the linewidth of the laser is determined to be 2.7 GHz.

finally be used to plot the fringes against a frequency scale (figure 6.17 c)). In order to ensure a good fitting of the calculated curve to the measured pattern, it is necessary to capture a fringe pattern that features valley values between the intensity peaks close to the background noise level. To achieve such analysable patterns, the etalon thickness and the focussing lens used have to be chosen accordingly for each measurement.

The linewidth $\Delta\nu$ of the pattern captured by the CCD camera is a combination of the instrument linewidth $\Delta\nu_F$ and the laser linewidth $\Delta\nu_l$. This means in order to quantify a laser linewidth it must be large compared to the instrument linewidth of the measurement system used. In the etalon set-up used, the instrument linewidth $\Delta\nu_F$ is determined by the finesse F of the system and is the minimal resolvable laser linewidth. In an instrument limited (finesse limited) system, the relationship between F, the free spectral range FSR and the instrument linewidth $\Delta\nu_F$ is

$$F = \frac{FSR}{\Delta\nu_F},$$

which means in an instrument limited measurement the linewidth of the generated pattern changes with the etalon thickness due to a constant limiting F and the transmission T is also a function of F:

$$T = \frac{1}{1 + F\sin^2\left(\frac{2\pi}{\lambda}2n(\lambda)d\cos(\alpha)\right)}.$$

Assuming perfect mirrors without any aberrations are used to build the air spaced measurement etalon, F is solely given by the wavelength dependent reflectivity $R(\lambda)$ of the mirrors

$$F = \frac{4R(\lambda)}{(1 - R(\lambda))^2}.$$

In reality, mirror aberrations can lower the finesse significantly. The mirrors used for the presented linewidth measurements were coated for a nominal reflectivity of $R_{290} = 90\%$ at wavelengths around 290 nm and measuring the transmittance yield a value of $T_{290} = 10\%$ leading to $R_{290} = 90\%$ assuming $R = 100\%$ - T and hence neglecting absorption. The finesse for 290 nm as given by perfect mirrors is thus 360. For an etalon spacing and focal length combination that generates a pattern with a FSR of 39 GHz, the resolution limit is hence 0.11 GHz. To test the system a narrowband (nominally single frequency CW) 266 nm laser was utilised. The transmission of the mirrors was measured to be $T_{266} = 16\%$ for 266 nm light, hence $R_{266} = 84\%$. This gives a reflectivity limited finesse for 266 nm of 131 and a resolution limit for a pattern with a FSR of 39 GHz of 0.30 GHz. The theoretical resolution

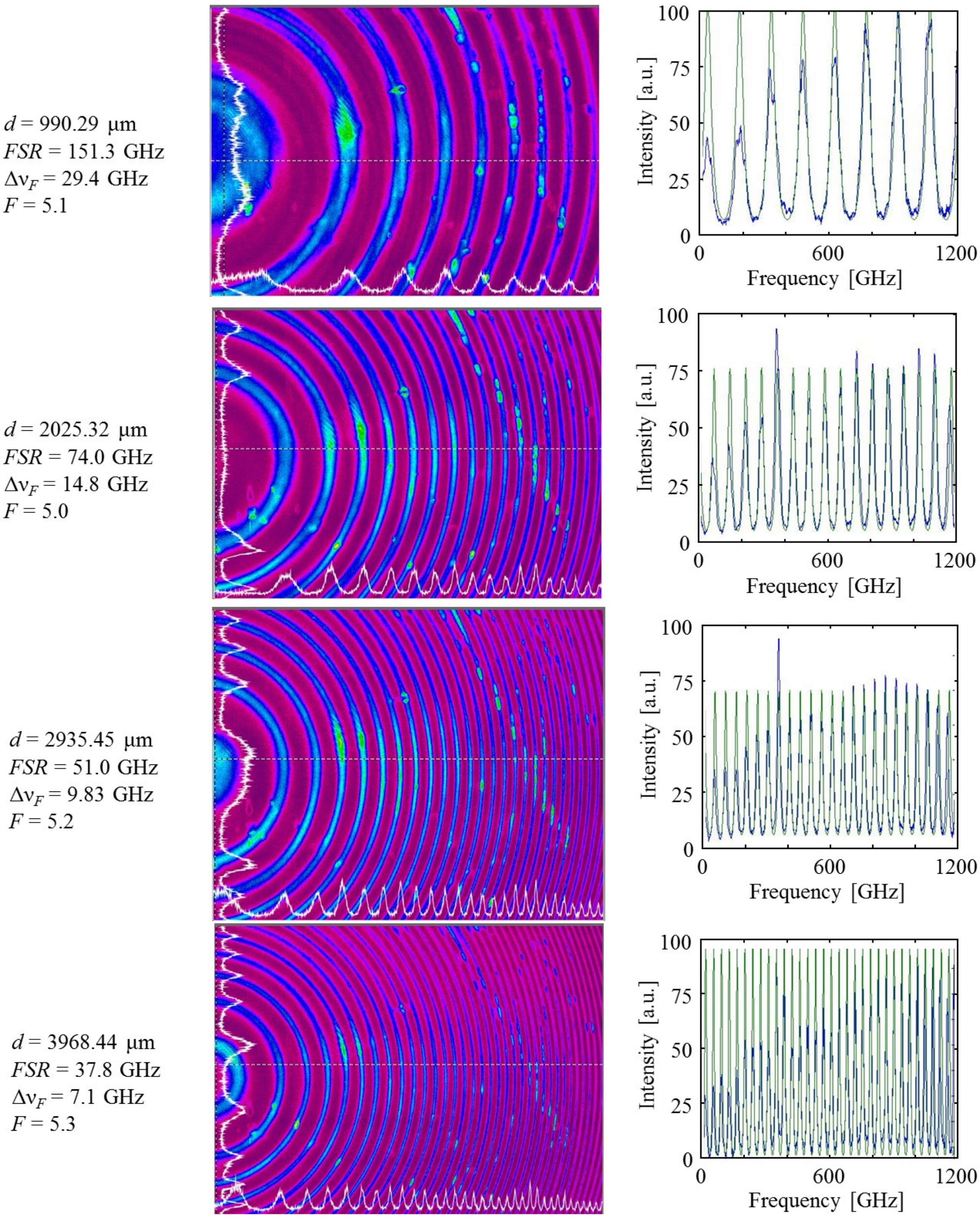

Figure 6.18: Linewidth measurement of a narrowband 266 nm laser using different etalon thicknesses. The determined linewidth was different in all cases and the Finesse F was constant, indicating that the resolution limit was reached.

250 µm BRF tuner
λ = 291.0 nm
d = 1050.37 µm
FSR = 142.6 GHz
$\Delta\nu_l$ = 51.7 GHz

6 mm BRF tuner
λ = 289.6 nm
d = 2253.26 µm
FSR = 71.3 GHz
$\Delta\nu_l$ = 7.1 GHz

6 mm BRF tuner +
500 µm BRF tuner
λ = 290.4 nm
d = 1930.57 µm
FSR = 67.8 GHz
$\Delta\nu_l$ = 15.3 GHz

6 mm BRF tuner +
3 mm etalon
λ = 290.4 nm
d = 2780.42 µm
FSR = 53.5 GHz
$\Delta\nu_l$ = 2.7 GHz

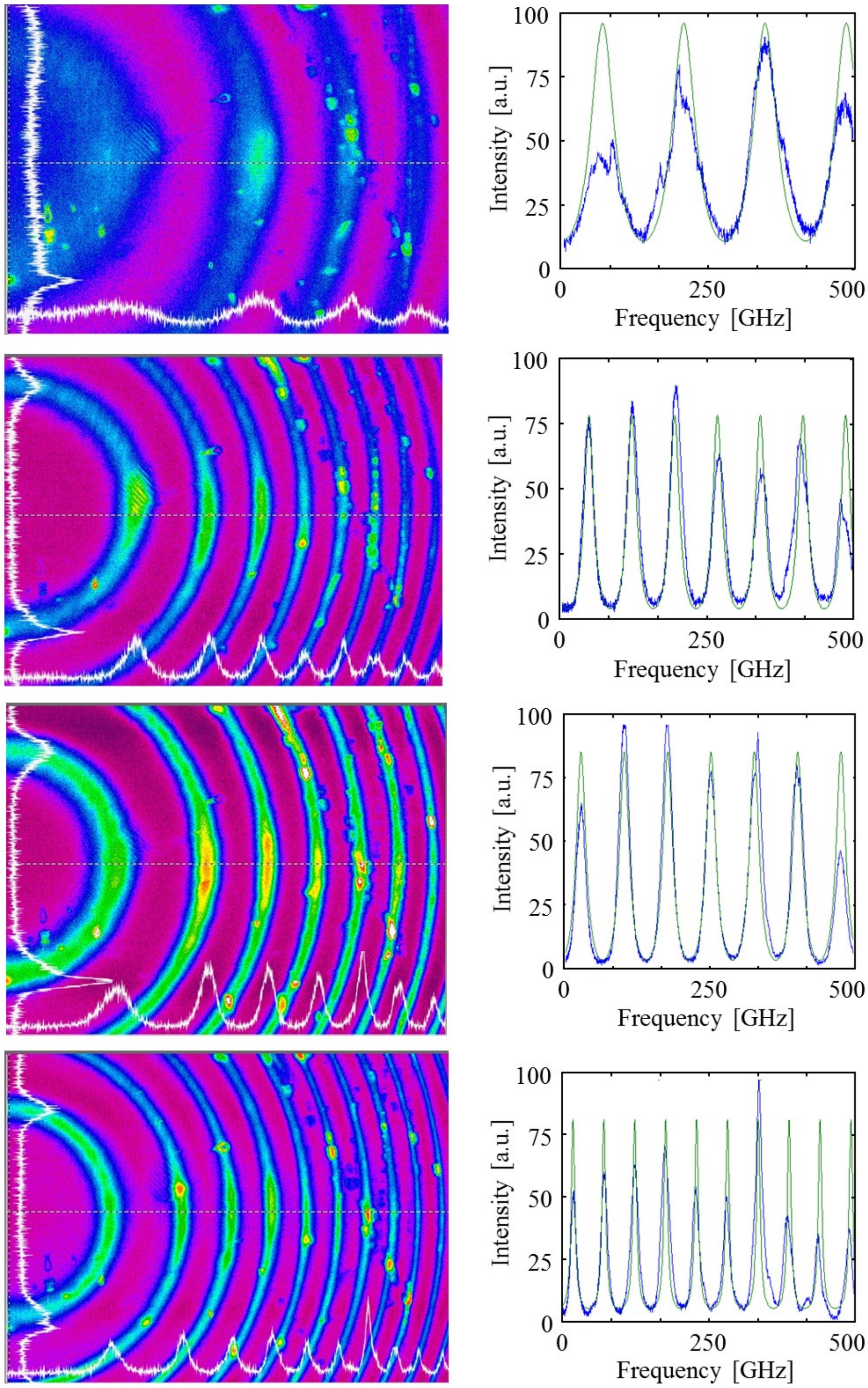

Figure 6.19: Linewidth measurement results for the Ce:LiCAF laser incorporating a single 250 µm MgF_2 plate, a single 6 mm MgF_2 plate, two parallel MgF_2 plates (6 mm and 500 µm), and a 6 mm MgF_2 plate plus an additional 3 mm etalon in the long cavity arm close to normal incidence.

limit assuming perfect mirrors is thus 3 times broader for 266 nm than for 290 nm. Figure 6.18 shows patterns generated with different etalon thicknesses for the narrowband 266 nm laser. With the determined pattern linewidth being different for all cases and $FSR/\Delta\nu$ being constant, the system was determined to be finesse limited for our narrowband 266 nm laser with $F = FSR/\Delta\nu_F = 5$. The measurements show that the actual finesse of the system $F = 5$ is much lower than the theoretical value of 131 indicating significant mirror aberrations.

Since we did not have access to a single-frequency 290 nm light source, it was not possible to determine the effective finesse of our measurement system for 290 nm (the theoretical limit assuming perfect mirrors was calculated to be 0.11 GHz as discussed above). Therefore, to quantify the linewidth of the Ce:LiCAF laser around 290 nm, we ensured that the pattern linewidth was independent of etalon thickness, hence verifying that the laser linewidth was broad compared to the instrument linewidth and thus was the determining value. Applying this method, the linewidth can only be overestimated.

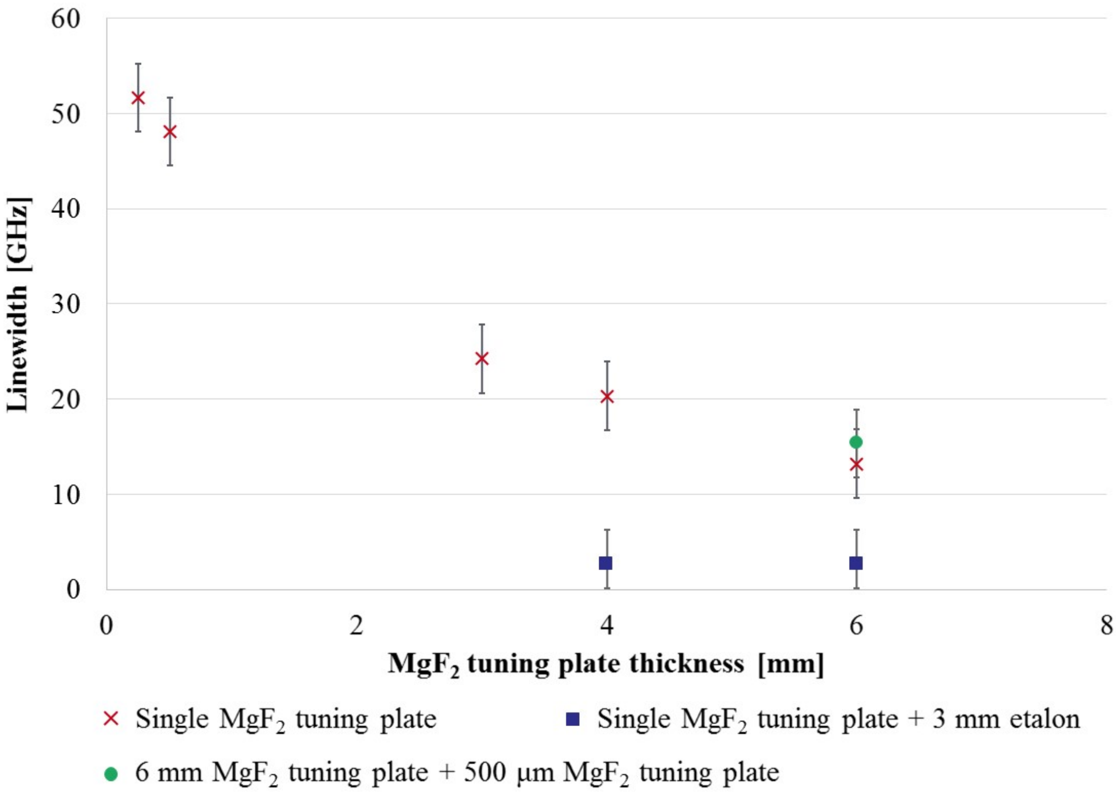

Figure 6.20: Overview of the measured linewidths for tuning with a single MgF_2 plate, a MgF_2 plate plus an additional 3 mm etalon in the long cavity arm close to normal incidence, and two parallel MgF_2 plates (6 mm and 500 µm) close to Brewster's angle.

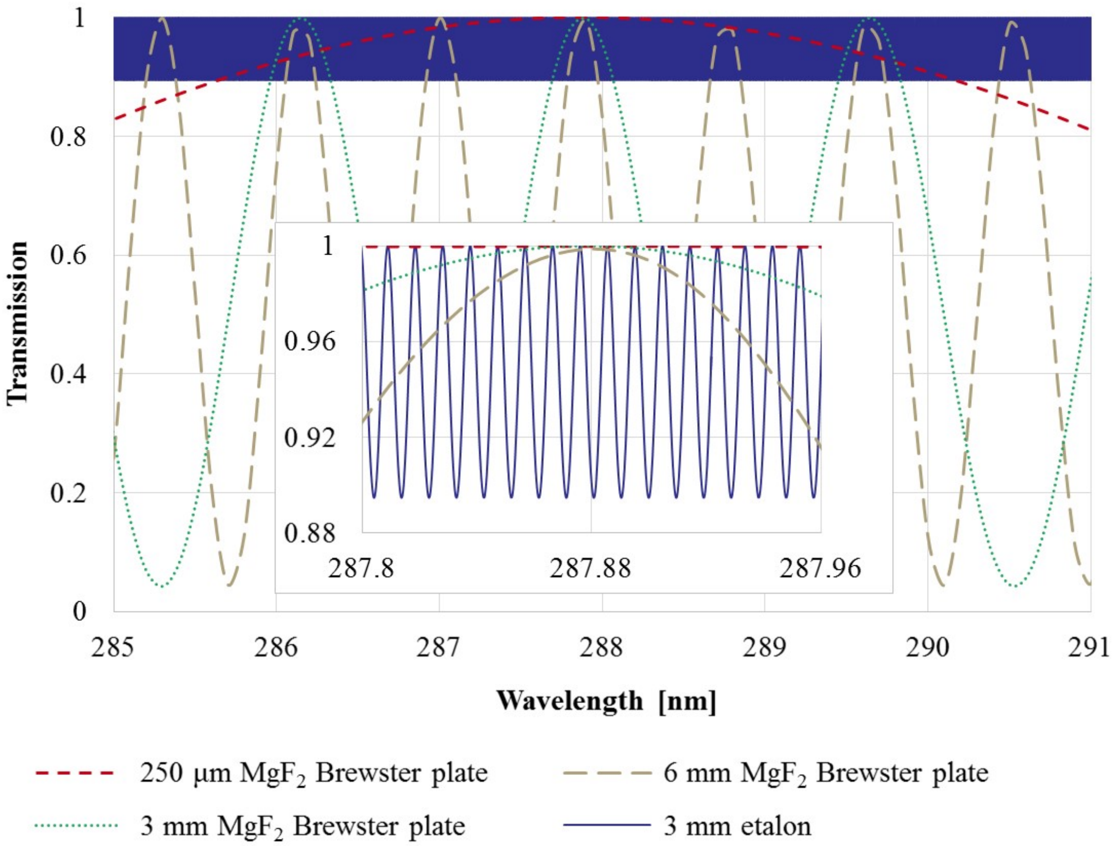

Figure 6.21: Theoretical transmission curves for a 6 mm MgF_2 Brewster tuning plate with an internal rotation of 45°, and a 3 mm etalon at close to normal incidence.

An overview of the linewidth measurement results for the Ce:LiCAF laser is given in figure 6.20 and figure 6.19 shows exemplary measurement results for key combinations of plates. To determine the linewidth of the Ce:LiCAF lasers with tuning plates with different thicknesses, the measurement was performed as the laser was tuned to various wavelengths over the whole achievable tuning range for the specific plate. Measurements were also performed for different etalon thicknesses at each wavelength. The pictures shown in figure 6.19 are hence just a small selection of captured and analysed fringe patterns to illustrate the general appearance of the experimental results. For each plate combination, the determined linewidths were independent of etalon thickness and wavelength, confirming that the system was not finesse limited for the Ce:LiCAF laser light around 290 nm. When using a single 250 µm MgF_2 tuning plate, the FWHM linewidth was 51.7 GHz. Using thicker MgF_2 plates resulted in narrower linewidths, down to 13.2 GHz for a 6 mm thick MgF_2 plate. However, using a single but thicker tuning plate naturally decreased the tuning range of the laser; the free spectral range of a 6 mm thick MgF_2 Brewster plate is just 0.8 nm as illustrated in figure

6.21. To achieve a relatively narrow linewidth, while keeping a relatively broad tuning range, a combination of two parallel MgF_2 tuning plates was used. For tuning with a 500 μm plate and an additional 6 mm tuning plate, both at 7° from Brewster's angle, tuning from 286.8 nm to 293.1 nm was achieved with a linewidth of 15.3 GHz. For further linewidth narrowing a 3 mm uncoated etalon was inserted close to normal incidence in the long cavity arm. The transmission curve for this etalon is also given in figure 6.21. A combination of a 6 mm tuning plate and a 3 mm uncoated etalon led to a FWHM linewidth of only 2.7 GHz which corresponds to 0.09 cm^{-1}. The longitudinal mode spacing for our 0.75 m long cavity is 0.2 GHz, which means there are only about 13 longitudinal modes oscillating in the CW Ce:LiCAF laser.

6.4 Single Longitudinal Mode Operation

Single longitudinal mode (SLM) operation refers to a laser oscillator that operates on only one longitudinal mode leading to a very narrow laser linewidth. Such SLM lasers are also called single frequency lasers. To achieve SLM operation, a laser first needs to be set up for single transverse mode lasing (usually supporting the fundamental transverse electromagnetic TEM_{00} mode) by aligning the cavity accordingly, and then the axial longitudinal modes of the TEM_{00} need to be restricted to a single one. With only one longitudinal mode oscillating in the cavity, the emission linewidth of a laser can be extremely narrow compared to the longitudinal mode spacing of the resonator.

For our narrowed mode-locked pumped CW laser we measured a FWHM linewidth of 2.7 GHz, which indicates that there are only of order 13 longitudinal modes oscillating in the cavity. It is interesting to contemplate if it is theoretically possible for our mode-locked pumped Ce:LiCAF laser to operate single frequency. In pulse-pumped CW laser there is an unavoidable gain step that leads to a residual intensity modulation, as discussed in chapter 4. This modulation must be associated with spectral bandwidth. When narrowing the linewidth of the laser e.g. by using thicker MgF_2 tuning plates and etalons, the power in the higher frequency components of the amplitude modulation gets cut off and the effects of the steps in the gain are smoothed. However, even rather smooth steps in the output result in intensity noise that imposes a limit to the achievable minimum linewidth. To estimate the relations, we take a look at the mode spectrum of a narrowband laser in the frequency domain (see

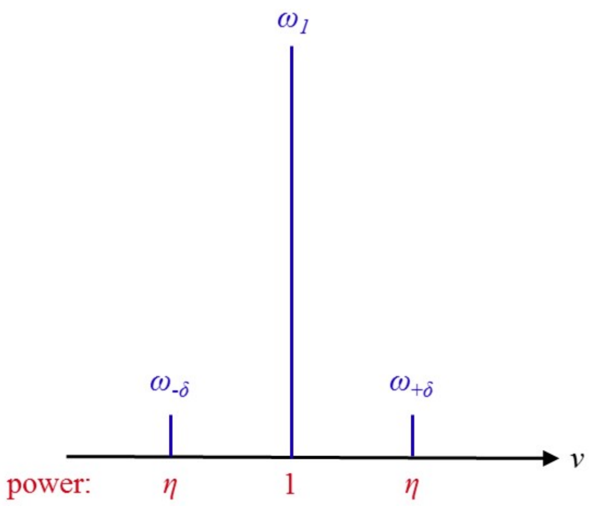

Figure 6.22: Mode spectrum of a narrowband laser in the frequency domain.

figure 6.22). A single frequency laser lases on just one central mode (ω_1) containing all available power. For a (narrowband) laser with two side-modes ($\omega_1 - \delta$ and $\omega_1 + \delta$), the amplitude $A(t)$ is the sum of the three modes

$$A(t) = \sum_{i=-\delta}^{\delta} a_i \cos(\omega_i t) .$$

For simplicity we assume that the intensity $I(t)$ and $A(t)$ are related via

$$A(t) = \sqrt{I(t)}$$

and presume a laser running predominantly on one mode, with the side modes each containing a relative power η and a relative phase relation resulting in an amplitude modulation only. Hence

$$a_1 = 1 \quad \text{and} \quad a_{-\delta} = a_{+\delta} = \eta^{1/2}.$$

From this it follows that

$$A(t) = \cos(\omega_1 t) + \eta^{1/2}\cos(\omega_{-\delta} t) + \eta^{1/2}\cos(\omega_{+\delta} t)$$

and with $\omega_{\pm\delta} = \omega_1 \pm \delta$

$$A(t) = \cos(\omega_1 t)\left(1 + 2\eta^{1/2}\cos(\delta t)\right).$$

It follows finally that the intensity is given by

$$I(t) = \cos^2(\omega_1 t)\left(1 + 4\eta^{1/2}\cos(\delta t)\right).$$

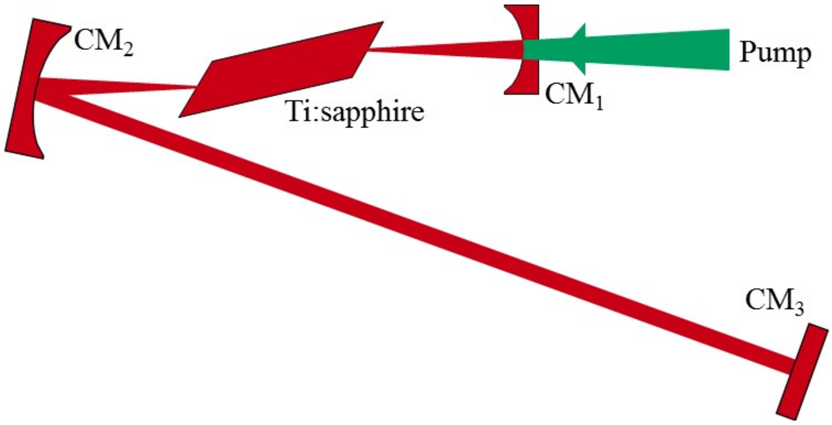

Figure 6.23: Schematic of the Ti:sapphire laser set-up. CM_1, dichroic cavity input coupling mirror with a radius of curvature (ROC = 100 mm; CM_2, high reflective (HR) cavity folding mirror with ROC = 150 mm; CM_3, plane output coupling mirror with a reflectivity of $R = 95\%$. The optical path distance between CM_1 and CM_2 was 181 mm with the Ti:sapphire crystal being 8 mm long. The length of the long cavity arm spanning from CM_2 to CM_3 was adjusted according to the operation mode desired (synchronous or asynchronous).

This shows that an intensity modulation of ε requires a relative power of $\varepsilon^2/16$ in the side modes. The intensity modulation we predict for our CW Ce:LiCAF laser is of order 4% for high frequencies (see chapter 5). Following the considerations above, to cause such an intensity modulation of 4%, only a very small amount of power needs to be contained in the side modes: $\eta^{1/2} = 0.01$ and hence $\eta = 1 \times 10^{-4}$ for an intensity modulation of 4%. This estimation suggests that lasing on predominantly one mode is indeed possible in our mode-locked pumped Ce:LiCAF laser. Despite the residual modulation, we should hence be able to achieve relatively pure single mode operation.

To test if a mode-locked pumped solid-state laser can lase SLM, we built a Ti:sapphire laser with a set-up comparable to our Ce:LiCAF laser. A schematic of the set-up can be seen in figure 6.23. The Ti:sapphire laser cavity was set up as a three-mirror resonator similar to the Ce:LiCAF one. All three mirrors were fabricated and coated by Melles Griot for ideal performance in the IR. CM_1, the dichroic input coupling mirror, had a radius of curvature (ROC) of 100 mm, CM_2 had a ROC of 150 mm and CM_3 was a plane output coupling mirror with a reflectivity of $R = 95$ %. The Ti:sapphire crystal was 8 mm long, cut at Brewster's angle with the c axis perpendicular to the propagation direction and in the horizontal plane. The total length of the short cavity arm from CM_1 to CM_2 (including the optical path through the crystal) was 18.1 cm. The folding angle α was set to 20° to compensate the

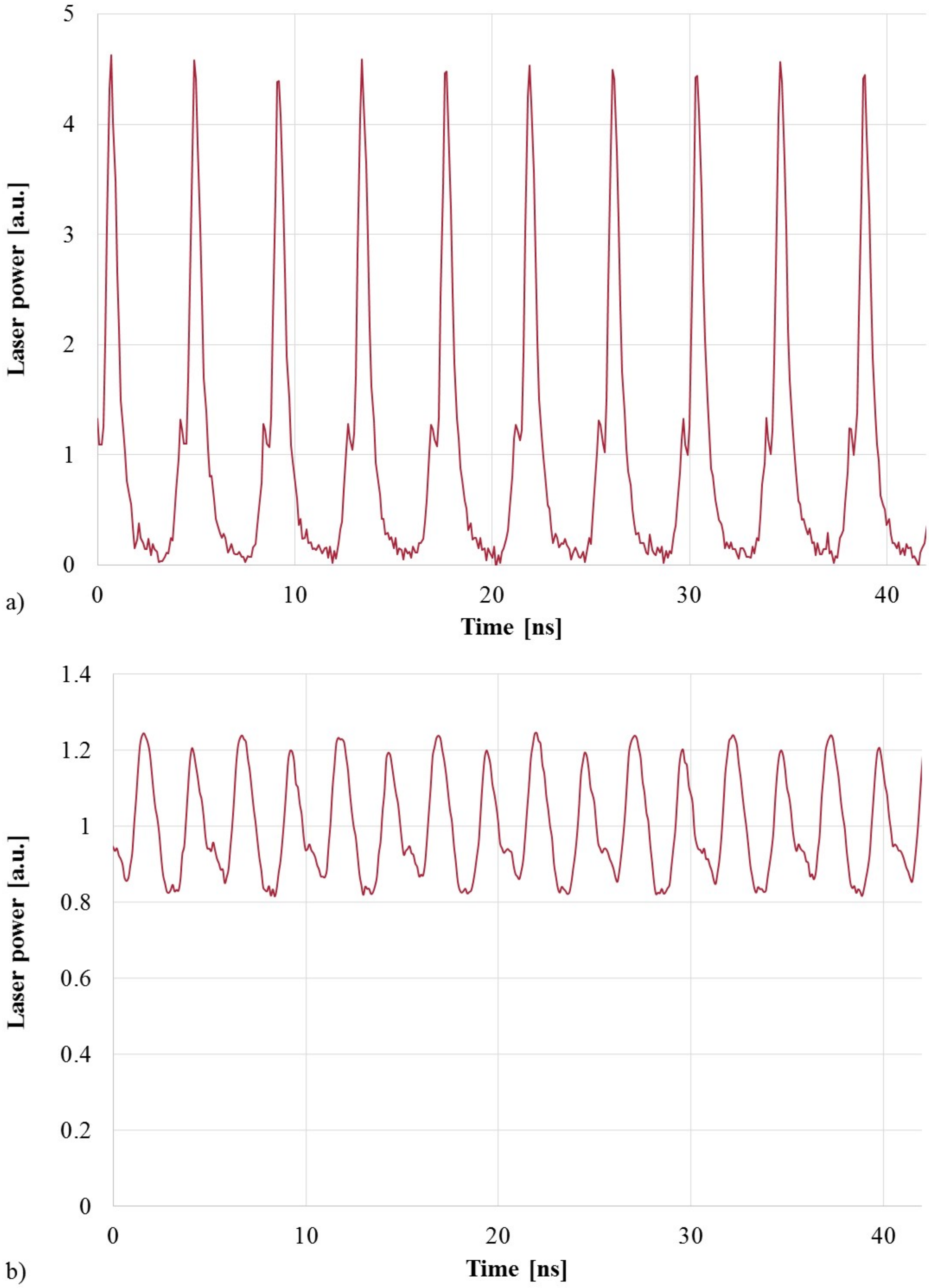

Figure 6.24: Output of the Ti:sapphire laser at a) the 3^{rd} harmonic and b) the 5/2 harmonic

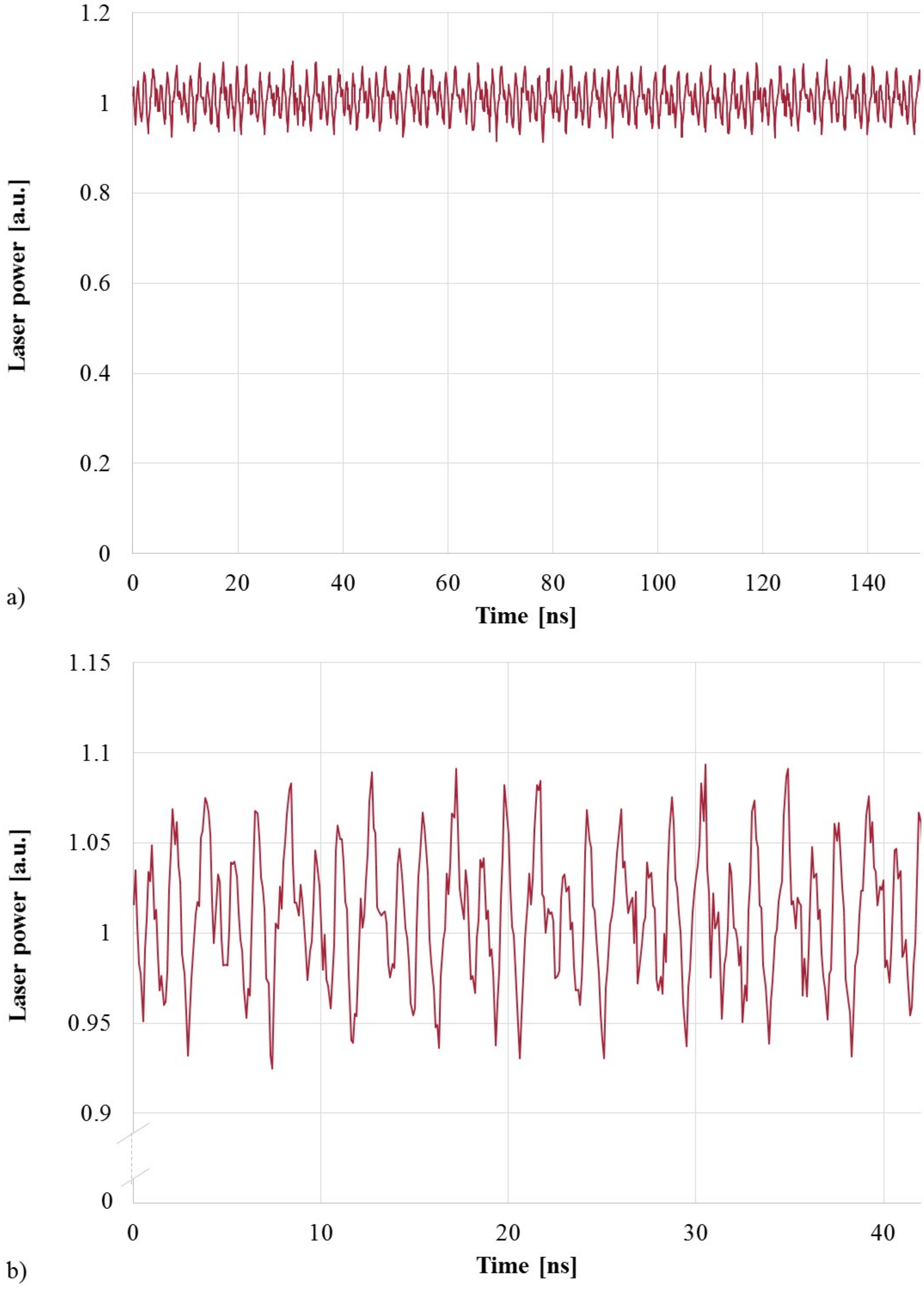

Figure 6.25: Output of the Ti:sapphire laser at the CW location (Δl = 120 mm) a) over 150 ns and b) zoomed over 42 ns

astigmatism introduced by the Brewster crystal and the folding mirror (see chapter 4). The Ti:sapphire laser cavity was pumped with the second harmonic of our Nd:YVO_4 laser, that is the 78.75 MHz pulses of 532 nm light produced by the LBO frequency doubling stage (see chapter 4.1). Accordingly, to set up the cavity at the 3^{rd} harmonic of the 78.75 MHz pump, the length of the long cavity arm must be set to 45.35 cm. For the 5/2 harmonic, the long cavity arm must be set to 58.05 cm and to achieve asynchronous pumping to generate CW light we used a configuration with the long cavity arm set to 56.6 cm. Figures 6.24 and 6.25 show the measured laser outputs at the 3^{rd} harmonic, the 5/2 harmonic, and at CW cavity length.

The upper laser level lifetime of Ti:sapphire (τ = 3.2 µs) is much longer than that of Ce:LiCAF (τ = 25 ns) and thus the gain step experienced by mode-locked pumped Ti:sapphire lasers is much smaller than in mode-locked pumped Ce:LiCAF lasers. As a result, the predicted residual modulation of an asynchronously pumped Ti:sapphire laser at the ideal CW cavity length is only 0.03% on fast timescales (see chapter 5.10). Clearly, the experimentally measured output of our CW Ti:sapphire laser features a modulation of order 1% that is much higher than predicted. The measured output at at 5/2 harmonic on the other hand does not show a full modulation down to zero, but only a modulation of order 20%. This indicates that there are other crucial factors present in the Ti:sapphire laser built affecting the performance. The nature of these factors has yet to be investigated. One factor could be that our Ti:sapphire laser operated not far over threshold.

However, by placing multiple etalons in the long arm of the Ti:sapphire laser cavity at CW cavity length, similar to the linewidth narrowing etalons in the Ce:LiCAF laser, it seems to be possible to achieve SLM lasing. For example, we could narrow the output linewidth from the around 10 nm free running value down to below the resolution limit of our Ocean Optics HR4000 spectrometer, which we used to monitor the output spectrum. Figure 6.26 shows the output trace of the CW Ti:sapphire laser with a 30 mm etalon, a 6 mm MgF_2 BRF plate, a 5 mm etalon, and a 250 µm 30% (1064 nm) coated etalon all in the long cavity arm. The measured output features a 4.55 µs ripple that we also observe in our Ce:LiCAF laser and is caused by a 220 kHz modulation on the pump laser. It is not related to the dynamics associated with mode-locked pumped CW lasers and can hence be neglected (see chapter 4.5). In figures 6.26 a) and 6.26 b) we see a transition in the output around 260 µs from low to high modulation. Figure 6.26 d) reveals that the high modulation is associated with a

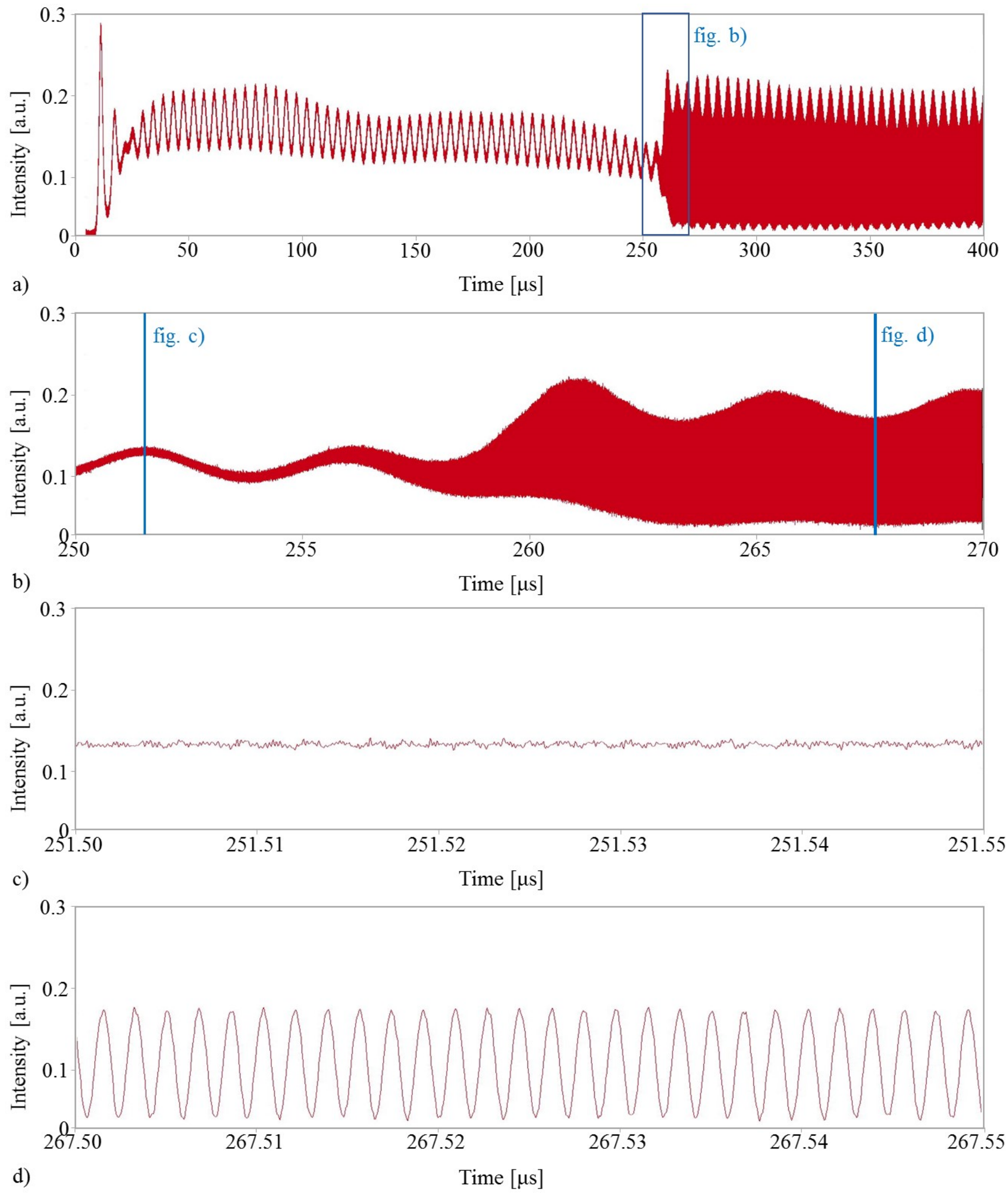

Figure 6.26: Ti:sapphire laser transitioning from SLM to two mode operation

fast modulation that is not present during the low modulation as seen in figure 6.26 c). The fast modulation observed in 6.26 d) follows the typical mode beating characteristics of two equal amplitude modes that happen to be separated by three times the cavity FSR. We thus interpret the transition occurring to be due to the laser switching between single and two-mode operation. The laser was observed to randomly switch back and forth between single mode and two-mode operation presumably in response to thermal drift in the system. While additional investigations are needed to fully explain the characteristics of our Ti:sapphire laser output, the results achieved support the proposition that mode-locked pumped solid-state lasers can indeed operate SLM, or at least very close to SLM. Of course both the Ce:LiCAF and the Ti:sapphire lasers investigated had linear cavities where spatial hole burning makes achieving SLM output particularly challenging. To obtain SLM operation it would be preferable to use a unidirectional ring resonator.

The main results of this chapter were published in: B. Wellmann, O. Kitzler, D.J. Spence, and D.W. Coutts, "Linewidth narrowing of tunable mode-locked pumped continuous-wave Ce:LiCAF laser." Optics Letters, Vol. 40, No. 13, 1st July 2015, pp. 3065-3068 (see appendix A "Publications Arising from this Thesis").

7

Conclusion and Future Work

Cerium doped solid-state crystals have been studied for many years starting in 1973 by Elias *et al.* [97] and their huge potential as a UV laser material has been proven [103]. Ce:LiCAF has even been described as the "Ti:sapphire of the UV" [113]. Ti:sapphire has had a tremendous impact on science and applications, and Ce:LiCAF being compared to it foreshadows the bright future Ce:LiCAF may have as a broadband laser material. Just like Ti:sapphire, Ce:LiCAF is a very efficient and robust crystal, that can be integrated in a convenient all-solid-state laser system set-up. Even more importantly, its broad gain spectrum spanning from 280 nm to 315 nm in the UV features the same bandwidth in order 133 THz as the gain spectrum of Ti:sapphire in the infrared (IR) spectral region (600 nm to 1100 nm). This broad bandwidth is in principle enough to support 4.5 fs pulses, but while the single cycle limit of Ti:sapphire in the IR is 2.7 fs, the one of Ce:LiCAF in the UV is only 970 as. To date, this theoretical limit is still out of reach, but it beautifully illustrates the potential of Ce:LiCAF as a laser material.

The "Unlocking the Ultraviolet" project at the MQ Photonics research centre was founded with the aim to develop a new laser platform based on Ce:LiCAF. In addition to providing what is needed to generate pulses in the attosecond regime, Ce:LiCAF has other advantages over Ti:sapphire, so that applications using Ti:sapphire systems today can possibly be enhanced by switching to Ce:LiCAF systems in the future once they are fully developed. This is true for both pulsed and CW Ce:LiCAF laser systems. Since Ce:LiCAF has a three times higher carrier frequency compared to Ti:sapphire, its laser beams can be focussed to tighter spots, with a diffraction limit three times smaller compared to Ti:sapphire. This is beneficial for many applications where a higher resolution and a finer control of processes are crucial, for example in laser materials processing. Moving to a shorter wavelength also has the advantage of working with higher photon energies. This allows interactions with materials featuring large bandgaps such as diamond, glass and wide-bandgap semiconductors. In addition, many molecules, atoms, and biological species have absorption bands in the UV and can be excited by Ce:LiCAF laser light. Another research area where Ce:LiCAF lasers are a promising tool, is plasma physics. An ultra-intense UV laser amplified to megawatt peak powers presents an auspicious new excitation source with the capability of allowing laser-plasma interactions that exceed what is obtainable when working with IR lasers. Additionally, the efficiency of high harmonic generation is predicted to be proportional to λ^{-6} [177], so working with Ce:LiCAF instead of Ti:sapphire should theoretically increase the harmonic yield by a factor of order 500 (although longer wavelengths do have the advantage of producing higher maximum harmonics). Thus in theory it will be possible to generate 100 attosecond pulses with microjoule energies or at kHz pulse rates.

One reason the research in Ce:LiCAF lasers has not progressed faster to date has been the lack of suitable reliable high power pump sources. Ce:LiCAF can be pumped conveniently by the fourth harmonic of Nd doped solid-state lasers ($\lambda = 266$ nm), yet at present the availability of such high power 266 nm pump lasers is still very limited. Indeed just recently high power (around 20 W average) 40 MHz 266 nm sources have become available commercially (EdgeWave GmbH, Ultrashort Pulse InnoSlab Lasers PX-Series). These lasers are still very expensive, but their availability bodes well for future enhancement and commercialisation of Ce:LiCAF lasers. To date, high power CW 266 nm sources are even more uncommon, but are likely to emerge in the near future, e.g. Coherent sells 200 mW 266 nm CW lasers with prospect of higher powers in the future. The "Unlocking the Ultraviolet" project was thus founded at an opportune time, providing key achievements in Ce:LiCAF laser research simultaneously to the rise of the commercial availability of suitable pump sources. For the experiments conducted during the course of this PhD project, we built our own pump source. The mode-locked output of a Nd:YVO4 laser was frequency quadrupled via two doubling stages (based on LBO and BBO respectively) generating pump pulses of 266 nm light with 23 ps duration at a repetition rate of 78.75 MHz and a maximum average output power of 2.80 W. The major challenge in this approach is the thermal lensing that occurs in the BBO doubling stage at high powers. In order to avoid such thermal effects, the average input power of the pump pulse train was decreased by chopping with a duty cycle of 8.3% giving on-periods of 400 µs. Since the Ce:LiCAF reached steady-state within times of order 10 µs, the chopping could be disregarded for our purposes, but for future applications it might not be an option. Hence, future work will include the optimisation of the pump light generation with the aim to provide stable, unchopped 266 nm pump pulses. Potential alternatives to frequency doubling via BBO for the generation of 266 nm pump light are frequency doubling using CLBO [178], or fluxless BBO [179], and sum-frequency mixing in CBO [180], I-PCA [181], or LBO [182]. Of all the approaches named, frequency doubling in CLBO is the most advanced alternative. CBLO has been used very efficiently (49% internal efficiency were reported in a CLBO-OPO [183]) and without damage in high-power systems [184]. Recently, studies on the degradation, regeneration and improvement of use [185] were published, providing the knowledge needed to set up an elaborate doubling stage.

Within the "Unlocking the Ultraviolet" project of the MQ Photonics Research Center, this PhD thesis covers one major stream: It is the account of the development and characterisation of mode-locked pumped Ce:LiCAF lasers, and led to the demonstration of the first ever stable CW Ce:LiCAF laser. As a result, a deep understanding of the dynamics in Ce:LiCAF lasers that are pumped by a mode-locked source was developed and a valid alternative to generating CW light in solid-state lasers by using a CW source was identified and established successfully. The method used is a technique we call asynchronous pumping that to the best of our knowledge has never been exploited before to obtain narrow band CW laser light from solid-state laser crystals. Asynchronous pumping is achieved by deliberately setting up a mode-locked pumped laser system in a way that pump timing resonances in the laser cavity are avoided. This means 'rational-harmonic mode-locking' needs to be prevented by selecting the laser cavity lengths carefully. To determine the ideal laser cavity length for asynchronous pumping, simulations with a model based on the laser rate equations were conducted. The optimal laser cavity length for CW lasing in Ce:LiCAF lasers pumped by a mode-locked source was hence calculated to be at normalized cavity length of 0.3964, which in the present case was a length of 120 mm detuned from the third harmonic of the 78.75 MHz pump. The CW output generated by a laser set up with this cavity length featured a residual modulation of only 1% for frequencies below 1 GHz and 4% on faster timescales. The slope efficiency was 20% and the laser threshold 1.37 W.

In addition to revealing the ideal cavity length for CW lasing in mode-locked pumped Ce:LiCAF lasers, the model enables us to predict the output behaviour of the system for various cavity lengths, input powers and other parameter changes. The model can also be adjusted to represent other solid-state lasers, such as e.g. Ti:sapphire, and was used to predict the residual modulation of a mode-locked pumped Ti:sapphire laser set up for CW operation with a normalized cavity length of 0.3964 to be just 0.01% for frequencies below 1 GHz and 0.03% on faster timescales.

When choosing a cavity length for synchronous pumping instead of asynchronous pumping, that is when setting up the laser system in a way that the ratio between the lengths of the pump cavity and the laser cavity is a rational number, ‘rational-harmonic mode-locking’ is obtained and short laser pulses can be generated. Since our laser set-up was a three mirror Z-folded cavity with the laser crystal in the focal position of the short cavity arm, the laser cavity length could be adjusted easily by moving the plane cavity end mirror of the long cavity arm. Thus the transition between CW behaviour and rational-harmonic mode-locking could be realised easily and in addition to the CW output, mode-locked output with pulse repetition rates up to 1.1 GHz was achieved. This represents the highest pulse repetition frequency yet reported for a Ce:LiCAF laser.

Birefringent tuning of the CW Ce:LiCAF laser using single and multiple magnesium fluoride (MgF_2) Brewster plates has also been investigated. Depending on the thickness of the MgF_2 plates used, continuous tuning over a range of up to 13 nm from 284.5 nm to 297.5 nm with a full width at half maximum linewidth of 50 GHz was achieved. By combining MgF_2 plates with etalons, the linewidth of the laser was narrowed down to 2.7 GHz, which means given the 0.75 m long cavity featuring a longitudinal mode spacing of 0.2 GHz, there were only about 13 modes oscillating in the cavity.

In conclusion, the results achieved in the course of the PhD project are milestones in Ce:LiCAF laser development. A solid foundation in the understanding of the dynamics in

Ce:LiCAF lasers has been built and crucial lessons in what is important when setting up a Ce:LiCAF laser system have been learned. This includes general alignment procedures and measurement methods as well as daily cleaning mechanisms of the UV optics and handling strategies for the many components involved. As a result, confidence in the capabilities of Ce:LiCAF as a laser material has been reinforced which will help to push the research on Ce:LiCAF further in the future with prospective work targeting CW pumped Ce:LiCAF lasers as well as mode-locking.

The knowledge gained will especially be essential in the development of CW pumped CW Ce:LiCAF lasers. Indeed at the MQ Photonics Research Centre there is ongoing research in the area of CW pumped CW lasers using the same basic set-up, characterisation techniques and measurement systems that were established during the work presented in this thesis. The first results achieved in this area are being published simultaneously to the finalisation of this thesis. While we do not expect our mode-locked pumped Ce:LiCAF laser to emit on a single frequency due to the unavoidable steps in the gain, the results obtained in the linewidth narrowing experiments suggest that it will be possible to achieve single frequency operation with a CW pumped Ce:LiCAF laser. However, in order to realise such a CW pumped SLM Ce:LiCAF laser it might be necessary to switch to a ring cavity to prevent spatial hole burning.

Another prospect is the development of ultrafast pulses using Ce:LiCAF. The pulses generated with the system set up for rational-harmonic mode-locking during the course of this PhD thesis were not characterised in terms of their pulse duration. Measuring the pulse duration in the UV spectral region is not trivial and cannot be done using simple methods. At the MQ Photonics Research Centre a new technique based on asynchronous sampling using a $\chi^{(2)}$ cross-correlation was developed to provide a measurement method suitable for low energy UV pulses. Using this measurement method, pulses of a Ce:LiCAF cavity set up for 1^{st} harmonic mode-locking were measured to be 6 ps long [5]. While these pulses are the shortest pulses obtained by a Ce:LiCAF system to date, they are obviously far from the potential duration limit of 970 as. However, building on the knowledge gained during the recent breakthroughs, we are now ready to address pulse duration reduction. Since Ce:LiCAF and Ti:sapphire are similar in many aspects, techniques that have proven to work successfully when it comes to reducing the pulse durations of Ti:sapphire lasers can in principle be adopted to reduce the pulse durations of Ce:LiCAF lasers as well. There will be additional challenges to overcome due to working in the UV instead the IR, such as increased dispersion and higher

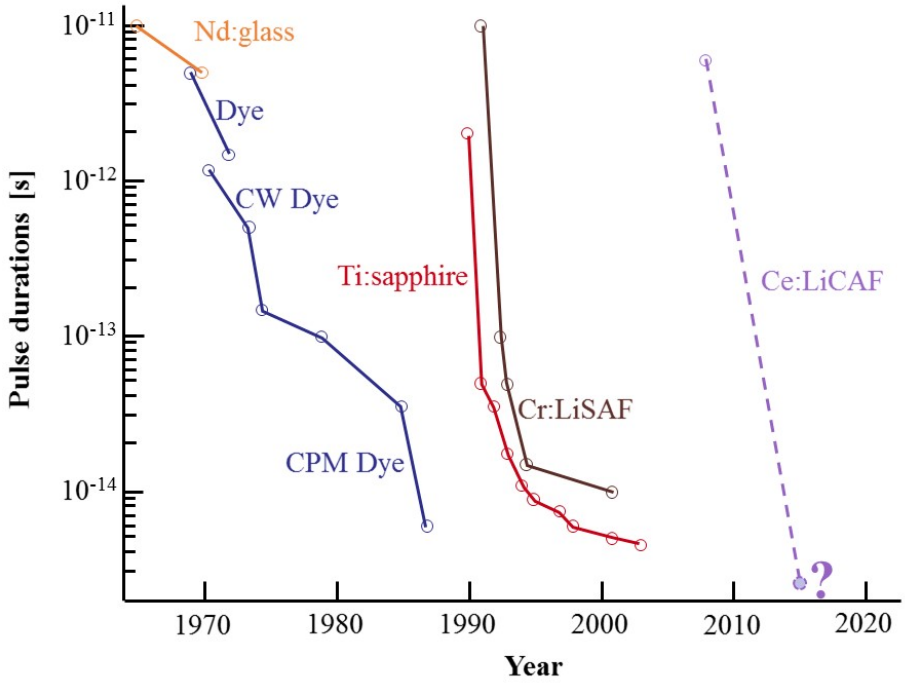

Figure 7.1: Overview of achieved pulse durations over time. Ultrashort pulses were initially generated in dye lasers and pulses with durations of only 27 ps were obtained at a wavelength of 630 nm. When the Ti:sapphire laser emerged in the 1990s, pulses at 800 nm were rapidly shortened into the femtosecond regime. In 2009 first Ce:LiCAF pulses with a duration of 6 ps were published. It is expected that the progress in decreasing the pulse duration of Ce:LiCAF lasers will be fast as well, with the final goal of crossing the sub-femtosecond barrier.

losses. Figure 7.1 shows an overview of the pulse durations reached over time for different laser systems. Looking at the fast development that happened in the other laser systems, the reduction of Ce:LiCAF pulse durations is expected to progress rapidly as well.

Once active mode-locking (synchronous pumping) is optimised successfully, it is planned to implement Kerr-lens mode-locking (KLM). KLM exploits the optical Kerr effect, which is a third-order nonlinear process which causes an intensity dependency of the refractive index of an optical material [186]. The refractive index can thus be described as

$$n(\lambda, I) = n_0(\lambda) + n_2(\lambda, I),$$

where n_0 and n_2 are the intensity independent and intensity dependent refractive indices, respectively. KLM is well established for Ti:sapphire as well as for Cr:LiSAF and Cr:LiCAF lasers, which use the same crystal host as Ce:LiCAF. Among the Cr-doped colquiriite crystals, LiCAF has the highest quantum efficiency and the most favourable thermal properties [187]. It is a high gain material that it is suitable for multipass amplifiers, although the short lifetime

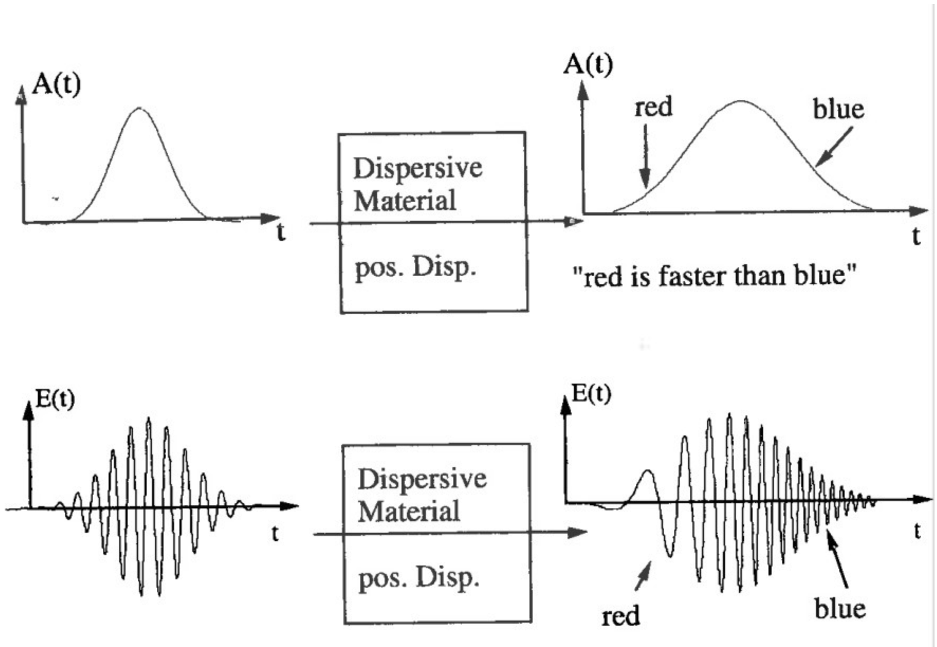

Figure 7.2: Pulse broadening due to positive dispersion [41]

makes it impractical for regenerative amplifiers. Similar to Ti:sapphire, Cr:LiCAF emits in the IR region with its gain spectrum spanning from 700 nm to 1000 nm [187]. But while the nonlinear, intensity dependent refractive index of sapphire is $n_2 \approx 3 \cdot 10^{-16}$ cm^2/W in this spectral region [188], the one of LiCAF is only half of that [189]. This means for effective KLM, pulse peak powers in Cr:LiCAF must be significantly higher than in Ti:sapphire. However, with the intensity dependent refractive index n_2 of the LiCAF increasing with shorter wavelengths, KLM is expected to be efficiently achievable for the UV wavelengths of Ce:LiCAF.

In order to further shorten the pulse duration of our Ce:LiCAF laser, dispersion correction will be implemented. To generate ultrashort pulses, the cavity round-trip time T_R must be frequency independent, otherwise the frequency components that experience a different cavity round-trip time do not interfere constructively which leads to a pulse width broadening [190]. In the laser cavity the main phenomenon causing a frequency dependent shift of the round-trip time is dispersion in the laser crystal due to the wavelength dependence of the refractive index [41]. Solid-state crystals such as Ti:sapphire and Ce:LiCAF exhibit normal (positive) dispersion, which results in a broadening of the pulse inside the cavity. Figure 7.2 illustrates this pulse broadening due to positive dispersion. As shown in the figure, in a material with positive dispersion longer wavelengths travel faster than shorter ones, which means the pulse experiences a red-shift. This is normally expressed with a frequency dependent change of

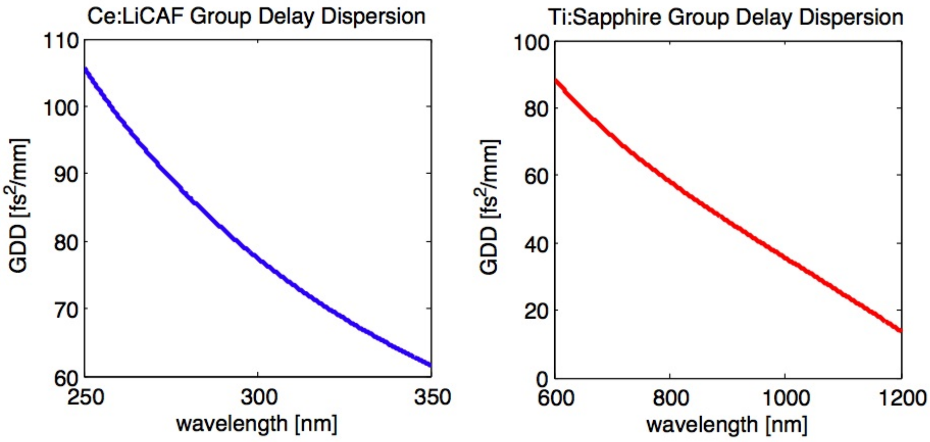

Figure 7.3: Group delay dispersion induced by (a) Ce:LiCAF in the UV and (b) Ti:sapphire in the IR, both as calculated in [4]

group velocity v_g [190]

$$\frac{dv_g}{dv} = -v_g^2 \beta'',$$

where β'' is the group dispersion of the material, which is positive for materials with a normal dispersion $\beta'' > 0$. Figure 7.3 shows the group delay dispersion (GDD) induced by Ce:LiCAF for UV-wavelengths and the GDD induced by Ti:sapphire for IR-wavelengths (as calculated in [4]). It is clearly visible that the dispersion is higher for smaller wavelengths with a dispersion of higher than 70 fs^2/mm for wavelengths shorter than 300 nm in Ce:LiCAF. This dispersion must be compensated in order to generate ultrashort pulses.

There are two common techniques for dispersion compensation: One is the use of a prism pair inside the laser cavity, the other, more recently developed technique is based on chirped mirrors which can either be used in addition to the prisms or as a replacement [62]. A schematic of dispersion correction with two prisms is shown in figure 7.4. The beam is sent through two prisms onto a plane reflector from where it travels back on the same path through the prisms again. Although the glasses of the prisms have normal dispersion, by this arrangement a negative overall dispersion can be introduced to the beam. Mathematically the group velocity dispersion induced by a prism pair can be described as the second derivative of the pathlength l with respect to the wavelength [190]

$$\frac{d^2 l}{d\lambda^2} = 4d \left[\left[\frac{d^2 n_0}{d\lambda^2} + \left(2n_0 - \frac{1}{n_0^3} \right) \left(\frac{dn_0}{d\lambda} \right)^2 \right] \sin\left(\alpha_p\right) - 2 \left(\frac{dn_0}{d\lambda} \right)^2 \cos\left(\alpha_p\right) \right].$$

Here, α_p is the angle difference between $\theta_f(\lambda_1) - \theta_f(\lambda_2)$ where λ_1 and λ_2 are the cut-off wavelengths of the laser. The second part of the equation is responsible for the desired

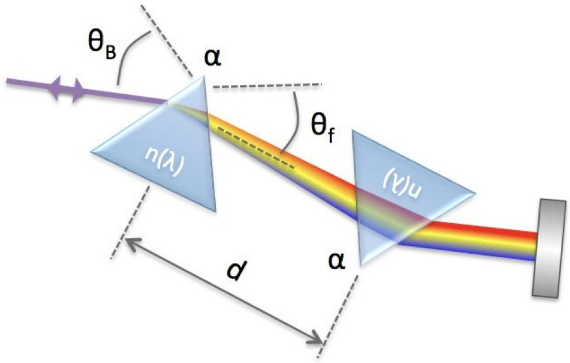

Figure 7.4: Prism pair for dispersion compensation [4]

negative dispersion. Therefore the first part has to be made as small as possible, which is realised by letting the beam pass through the prisms as close to the apex as possible. For UV wavelengths possible materials for prism pairs include fused silica, calcium fluoride or magnesium fluoride, as these materials have low losses at UV-wavelengths.

The second technique to compress the positive dispersion of the laser crystal is by using chirped mirrors. Figure 7.5 shows a schematic of a double-chirped mirror designed for dispersion control. Group delay dispersion in chirped mirrors occurs because different wavelengths are reflected at different depths in the mirror [191]. The mirror consists of many alternating layers with different refractive indices. The optical thickness of the layers is varied monotonically close to a thickness of a quarter wavelength of the selected center wavelength λ_0. This monotonic thickness variation results in a different penetration depth for different wavelengths around the centre wavelength and hence the group delay varies monotonically with wavelength [190]. In double-chirped mirrors additionally the local coupling of the incident wave to the reflected wave is chirped as well by slowly increasing the high-index layer thickness in every layer pair so that the total optical thickness of each pair remains approximately $\lambda_0/2$, which corresponds to an adiabatic matching of the impedance [41].

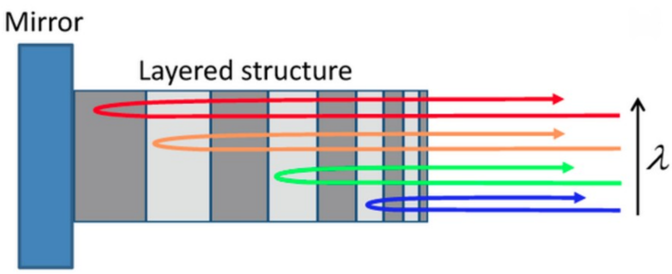

Figure 7.5: General structure of a chirped mirror for dispersion compensation [191]

Chirped mirrors are nowadays available for wavelengths in the range from 220 nm in the deep UV to 4500 nm in the IR [192] and are often referred to as "dispersive mirrors" due to the utilisation of resonant effects (e.g. in Gires-Tournois resonance cavities [193]). In addition, there are multilayer coatings and dispersive mirrors available for wavelengths below 60 nm in the extreme UV (10 nm to 60 nm) and the soft X-ray range (0.1 nm to 10 nm) [194–197]. Chirped mirrors for the deep UV wavelength range are fabricated using hafnium oxide (HfO_2) as a high-index material and silicon dioxide (SiO_2) as a low-index material with fused silica as the base material. The first mirror of this type was presented in 2007 as an ultraband chirped mirror (UBCM) for wavelengths from 300 nm to 900 nm [198]. The mirror was realised as a structure with 83 alternating layers resulting in an average reflectivity of $R = 93\%$ over the whole wavelength range and a GDD of -20 fs^2 at 450 nm. In the following years other dispersive mirrors using the same material combination were published reaching wavelengths even lower than 300 nm [193, 199]. Dispersive mirrors for the deep UV based on HfO_2/SiO_2 typically consist of 80 to 90 alternating layers and feature average reflectivities around 92% and average GDD of around -75 fs^2 [192].

An additional reduction of the pulse duration can be achieved by compressing the pulses after they have left the laser cavity. Depending on the characteristic of the pulses the compression can be done in a single step or requires a sequence of consecutive steps. Single step compression is applicable to chirped pulses where the compression is achieved by removing (or reducing) the chirp. In general this can be realised with the same method as used for dispersion correction: a set-up in which negative dispersion is applied to the pulses is arranged (linear compression). Suitable set-ups can be based on a pair of prisms [201], a pair of diffraction gratings (a grating compressor) [202, 203], optical fiber filters [204], chirped mirrors [205] or chirped Bragg gratings[206]. The duration of the chirp-free pulses is then dependent on the optical bandwidth, which is not modified by the linear compression. We expect our free running synchronous pumped Ce:LiCAF pulses to be chirped, hence subsequent pulse compression can also be an alternative approach to apply to the free running system without intracavity dispersion control.

Pulses that are chirp-free (or only feature a very small chirp) can be compressed by nonlinear pulse compression. This is realised by first broadening the bandwidth of the pulses and subsequently compressing these broadened pulses. The spectral broadening is achieved with a nonlinear interaction such as self-phase modulation, which usually results in

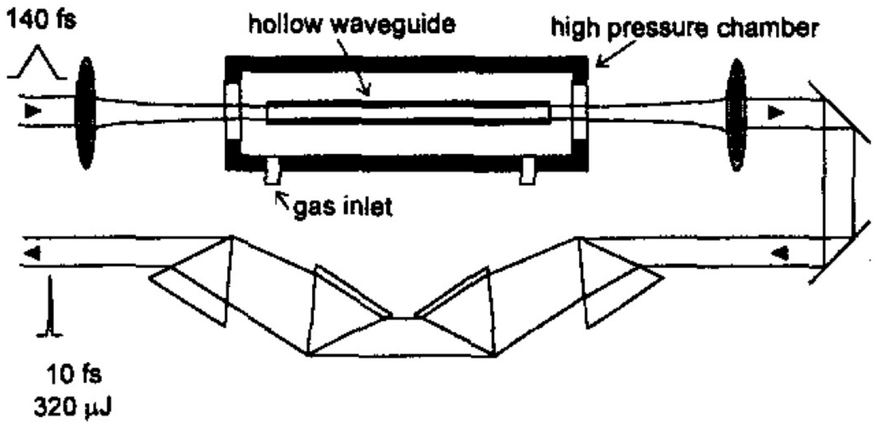

Figure 7.6: Experimental set-up for spectral broadening with a gas-filled hollow fiber and compression using prisms [200]

chirped pulses with longer durations than the original pulse. Subsequently the pulses can be compressed by linear compression as described above, which removes or decreases the chirp. For low intensity pulses the spectral broadening can be attained using a normally dispersive optical fiber [207]. For high-intensity pulses the spectral broadening can be performed in gas-filled hollow fibers [200]. Figure 7.6 shows the experimental set-up used in [200] to broaden and compress 660 μJ 140 fs pulses to 10 fs pulses.

The key technique to amplify ultrafast pulses effectively is chirped pulse amplification (CPA). Here, chirp is applied to the pulses without spectral broadening (stretching) and they are compressed subsequently. When using this method it is possible to amplify the pulses between the stretching and compression step without changing other parameters and thus to reach even higher pulse peak powers without reshaping the pulses [95]. Figure 7.7 shows the schematic of a pulse stretching, amplification and compression sequence. CPA has already been demonstrated for 290 ns pulses with Ce:LiCAF as the amplifying material [129].

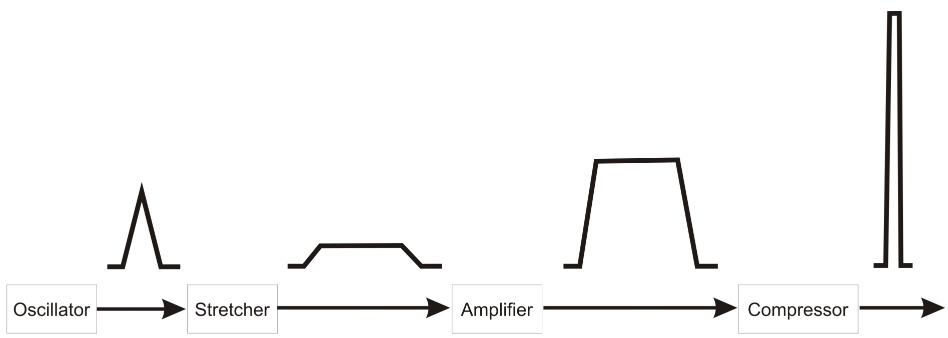

Figure 7.7: Schematic of a pulse broadening, amplification and compression sequence [95]

In summary, the achievements reported in this PhD thesis are crucial milestones on the way to reaching the full potential of Ce:LiCAF lasers. Without doubt the research in Ce:LiCAF lasers has not come close to its limits yet and many improvements and innovations will follow until Ce:LiCAF will truly be the Ti:sapphire of the UV, the workhorse of the ultraviolet.

A

Publications Arising from this Thesis

1. B. Wellmann, D.J. Spence, and D.W. Coutts, "Tunable continuous-wave deep-ultraviolet laser based on Ce:LiCAF", Optics Letters, Vol. 39, No. 5, March 1, 2014, pp. 1306-1309

2. B. Wellmann, D.J. Spence, and D.W. Coutts, "Dynamics of solid-state lasers pumped by mode-locked lasers", Optics Express, Vol. 23, No. 4, February 12, 2015, pp. 4441-4452

3. B. Wellmann, O. Kitzler, D.J. Spence, and D.W. Coutts, "Linewidth narrowing of a tunable mode-locked pumped continuous-wave Ce:LiCAF laser", Optics Letters, Vol. 40, No. 13, July 1, 2015, pp. 3065-3068

1306 OPTICS LETTERS / Vol. 39, No. 5 / March 1, 2014

Tunable continuous-wave deep-ultraviolet laser based on Ce:LiCAF

Barbara Wellmann,* David J. Spence, and David W. Coutts

MQ Photonics Research Centre, Department of Physics and Astronomy, Faculty of Science, Macquarie University, New South Wales 2109, Australia

**Corresponding author: barbara.wellmann@mq.edu.au*

Received November 26, 2013; revised January 23, 2014; accepted January 23, 2014; posted January 24, 2014 (Doc. ID 201920); published February 27, 2014

We demonstrate chopped-cw lasing in a Ce:LiCAF oscillator directly generating deep-UV light around 290 nm. The cw output was achieved by asynchronous pumping of a Ce:LiCAF oscillator by a mode-locked frequency quadrupled $Nd:YVO_4$ laser that generates 23 ps pulses of 266 nm light at a repetition rate of 80 MHz. The pump laser was chopped with 8.3% duty cycle to minimize thermal effects in the frequency quadrupling stage. The maximum output power achieved was 384 mW when pumped with 3.3 W of pulsed 266 nm light, with a slope efficiency of 33%. The laser output was tunable from 286 to 295 nm with the potential to be broadened over the full gain bandwidth of Ce:LiCAF from 280 to 315 nm.

OCIS codes: (140.3600) Lasers, tunable; (140.3610) Lasers, ultraviolet.
http://dx.doi.org/10.1364/OL.39.001306

A large variety of atoms, molecules, and compound materials feature unique absorption bands in the ultraviolet (UV), driving the demand for UV lasers to detect, probe, and control those materials. Continuous-wave (cw) UV lasers can, for example, be used in high-resolution spectroscopy [1,2], atom cooling and trapping [3,4], and biological applications like flow cytometry for the detection of pathogens [5].

The most common approach to generate tunable cw UV light is to convert the wavelength of a standard infrared laser, using a combination of optical parametric conversion and sum-frequency and higher-order harmonic generation to achieve the desired shorter wavelengths [6–8]. The techniques to achieve tunable cascaded nonlinear conversion can often be complex and normally require sensitive locked resonant cavities to enhance the laser intensity so reasonable conversion efficiencies can be achieved.

Our approach is to convert the fixed-wavelength pump light to the UV, and then generate the tunable cw laser light directly in the UV using a suitable solid-state laser crystal. This approach has the promise of giving higher conversion efficiency using a simpler experimental arrangement. The crystal we are using is cerium-doped $LiCaAlF_6$ (Ce:LiCAF), a material that is well established for nanosecond-pulse lasers [9,10]. Ce:LiCAF features a gain bandwidth of 35 nm in the UV (280–315 nm), with a maximum gain at 290 nm, while its absorption spectrum shows a peak at 260–270 nm [11]. Thus it can be pumped conveniently by the fourth harmonic of solid-state Nd lasers ($\lambda_p = 266$ nm). The desired UV lasing occurs on the 5d → 4f transition, which has an upper laser level lifetime of 25 ns. In the nanosecond-pulsed domain, Ce:LiCAF lasers have already been scaled to Watt-level average power [12], 100 mJ pulse energy [13] and have shown high efficiencies (of order 50% [14,15]). We have demonstrated mode-locked picosecond operation of a Ce:LiCAF oscillator [16], and in this Letter we extend that work to demonstrate tunable cw laser output generated by asynchronous pumping of a Ce:LiCAF oscillator by a mode-locked pump source.

Figure 1 shows the experimental setup of our laser system. As a pump source a commercial diode-pumped mode-locked picosecond $Nd:YVO_4$ laser (Photonic Industries PS-1064-25) was used, which generated 1064 nm, 28 ps pulses at a repetition rate of 80 MHz with an average output power of 23 W. This pump light was frequency quadrupled using a 3.5 cm long lithium triborate (LBO) crystal heated to 151.4°C followed by a 4 mm long β-barium borate (BBO) crystal at 50°C. In order to avoid thermal effects in these two subsequent doubling stages, the pump light was chopped before being focused into the LBO. The chopper had an open:closed ratio of 1 : 12, passing 400 μs long bursts of mode-locked pulses every 4.8 ms. Note that all powers are given as the average power during the 400 μs burst; the average powers over the full chopper cycle therefore are 1/12 of the stated powers. The power of the 532 nm light after the first

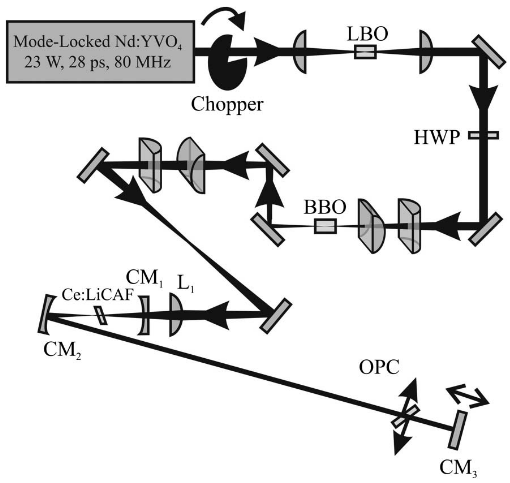

Fig. 1. Schematic of the experimental setup. HWP, half-wave plate at 532 nm; L_1, spherical focusing lens; CM_1, dichroic cavity mirror with a radius of curvature (ROC) = 5 cm; CM_2, HR cavity mirror with ROC = 10 cm; OPC, output coupler; CM_3, HR plane cavity mirror.

doubling stage was measured to be 13.2 W. Using two crossed cylindrical lenses, this radiation was elliptically focused into the BBO generating 3.5 W of 266 nm UV light, with individual mode-locked pulses having a duration of 23 ps. The 266 nm light was subsequently collected using two crossed cylindrical lenses and finally focused by a spherical focussing lens with focal length $f = 75.6$ mm through the dichroic cavity mirror (CM_1) into the laser cavity, providing a slightly elliptical pump spot with a waist (radius at $1/e^2$ of the peak intensity) of 15 μm × 18 μm.

We used a 1.25 mm long 3.5% cerium-doped LiCAF crystal cut at Brewster's angle with the c axis perpendicular to the propagation direction and in the horizontal plane. The single-pass absorption at 266 nm of this crystal was measured to be 70%, and the single-pass loss at 290 nm was 0.7%. The laser cavity was set up as a three-mirror resonator (see Fig. 1) with a folding angle of 12° to compensate the astigmatism introduced by the Brewster-angle-cut Ce:LiCAF crystal [17]. In order to keep the cavity losses at a minimum, all three cavity mirrors were custom coated for minimum absorption and transmission (coated by Advanced Thin Film). A 4 mm thick UV-grade silica plate at close to Brewster's angle was placed in the long cavity arm near to CM_3 as an output coupler (OPC). Using a Brewster plate in this way allowed us to tune the output coupling fraction to optimize the efficiency of the laser.

In this setup, the length of the long cavity arm of the cerium laser cavity (between CM_2 and CM_3) determines the laser operation mode. By carefully adjusting the cavity length to an integer fraction of that of the mode-locked pump laser, harmonic synchronous mode locking can be achieved, and the laser emits a train of short pulses (see [16]); the laser cavity can tolerate a length mismatch of a few tens of micrometers while still generating a full modulated mode-locked pulse train. Further mismatching of the cavity length up to a few millimeters results in cw output that is partially modulated at the harmonic of the pump laser repetition rate.

Strong mismatching of several centimeters generates a stable cw output with sub percent modulation. In order to achieve laser operation in this cw regime, we set the length of the shorter cavity arm to 10.5 cm and the length of the longer cavity arm to 53 cm for a total cavity length of 127 cm, which equates to a cavity round-trip time of 4.2 ns. This cavity length corresponds to a mismatch of 2 cm compared to the third harmonic of the 80 MHz repetition rate of the pump laser. Figure 2 shows the achieved cw-laser output during one opening of the chopper, measured on a nanosecond photodiode (accordingly with a maximum bandwidth of 1 GHz) displayed with an oscilloscope sample rate of 10 GBit/s. The inset gives a detailed view of the cw-laser output and underlying pump pulse train and clearly shows small modulation at three times the pump mode-lock frequency. Note that the pump laser pulse train also had a small 220 kHz amplitude modulation which produced approximately 5% amplitude modulation on the cerium laser output when observed on microsecond time scales.

An additional unavoidable effect of pumping a cw laser with a mode-locked laser is that each pump pulse produces a step increase in the gain during the 23 ps pump

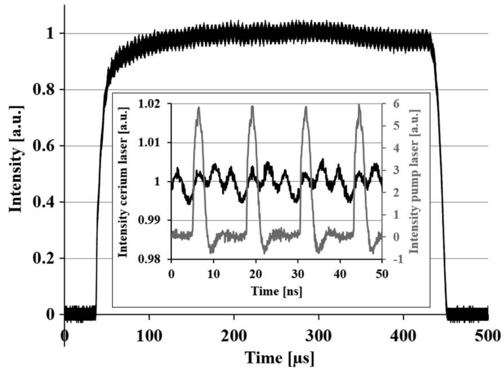

Fig. 2. Cw-laser output during one opening of the chopper, measured on a nanosecond photodiode displayed with an oscilloscope sample rate of 10 GBit/s. Inset: zoomed laser output showing the modulation on the primary y axis (black) and pulse train from the pump laser on the secondary y axis (gray).

pulse duration, which then decays due to stimulated and spontaneous emission, leading to a saw-tooth modulation ripple on the cw laser output. An approximate analysis of the gain modulation shows that for a linear resonator where the intracavity field passes through the gain medium twice on each round trip, the step in the gain has an amplitude ΔG given by

$$\Delta G = \frac{1}{2} \cdot r \cdot (T + L) \cdot \frac{t_p}{\tau_f},$$

where r is the number of times above threshold, T is the output coupling loss, L is the round-trip loss, t_p is the pump pulse period, and $\tau_f = 25$ ns is the fluorescence lifetime. Where the pump pulse also makes a double pass of the Ce:LiCAF crystal such as in the present case, two lower-amplitude gain steps are produced. For the 80 MHz pump laser used, the pump pulse interval equals half the Ce:LiCAF fluorescence lifetime, and with 5% total cavity loss, the gain step is predicted to be just 1.4% at the maximum output power obtained. The resulting modulations in the intracavity field and laser output depend on the cavity length detuning and are expected to be of the same order of magnitude as the gain step for optimum detuning. These intensity modulations will be on a fast time scale compared to the cavity round-trip time and so will be in the multi-gigahertz range and will not be resolved in Fig. 2.

We note that this is a slightly unusual cw laser. Normally a cw laser would be pumped by a cw energy source, and the laser field would reach a steady equilibrium with the inversion, perhaps with sub-round-trip beating noise in a multi-longitudinal-mode cw laser. In the present laser we are pumping with a pulsed energy source, but nevertheless the laser output is always on and is predicted to have only few-percent intensity noise on the time scale of the 13 ns round trip time of the pump laser. Thus the form of the laser output is closely comparable to a cw-pumped multi-longitudinal-mode cw laser and will be equivalent for applications of such lasers.

1308 OPTICS LETTERS / Vol. 39, No. 5 / March 1, 2014

To ensure high laser efficiency, the cavity losses and the additional output coupling losses were measured and optimized using cavity ringdown. A collimated probe beam from a nanosecond cerium laser ($\lambda = 290$ nm) was directed into the laser cavity through the plane cavity end mirror (CM_3) and matched to the cavity mode size, resulting in a focal spot between the two curved cavity mirrors of approximately 15 μm. A photomultiplier tube module (Hamamatsu H10720-20) was used to measure the cavity ringdown time of the nanosecond probe pulse by capturing the leakage through one of the cavity mirrors. Using the results of the ringdown measurements using different combinations of mirrors and with and without the crystal we retrieved the losses of the cavity components: the high-reflective (HR) mirrors had 0.2% loss per reflection, the dichroic cavity mirror had 0.45% loss per reflection, and the single-pass loss of the crystal was 0.7%. The total cavity loss without the OPC was $L = 2.45\%$. The OPC provided a variable additional loss to the cavity that served as the output coupling; this increasing output coupling as the plate was rotated away from Brewster's angle was measured using the ringdown method while the laser output power was recorded. Figure 3 shows the laser output power in milliwatts as a function of the additional round-trip output coupling loss introduced by the OPC for a pump power incident on the crystal of 3.0 W. All reflections off the OPC plate were included in this power measurement. As the graph in Fig. 3 shows, the maximum laser output power was observed for a measured output coupling loss of $T = 2.5\%$ (which corresponds to an angle of 7.5° relative to Brewster's angle). The power measurements described in the following were taken with the OPC at this optimum angle.

The laser output power as a function of the pump input is shown in Fig. 4. The slope efficiency for the given setup with the OPC optimized to maximum output power was thus determined to be 33%, and the lasing threshold in this configuration was 2.2 W. The maximum measured laser output was 385 mW when pumped with 3.3 W of 266 nm. (Recall that all powers are the average powers during the open period of the chopper.)

In [18] Payne *et al.* discuss models to calculate the slope efficiency and the lasing threshold for Ce:LiCAF cw lasers theoretically. Alderighi *et al.* verified these equations in [19]. The cw slope efficiency η_{cw} can thus be calculated as

$$\eta_{\mathrm{cw}} = \eta_p \eta_a T_{\mathrm{DM}} \left(\frac{\lambda_p}{\lambda_c}\right) \left(\frac{T}{T+L}\right) \left(\frac{\sigma_{\mathrm{em}} - \sigma_{\mathrm{ESA}}}{\sigma_{\mathrm{em}}}\right).$$

Here, η_p is the pump efficiency, η_a is the pump absorption, T_{DM} is the transmission of the dichroic input mirror for the pump beam, the term in the first bracket describes the quantum efficiency η_q, and the term in the second bracket is the output coupling efficiency η_{opc}. The effect of excited-state absorption (ESA) of the laser radiation in Ce:LiCAF is taken into account by the term in the third bracket. Marshall *et al.* estimate the ESA cross section σ_{ESA} for Ce:LiCAF to be $3.6 \cdot 10^{-18}$ cm^2 and measured the emission cross section $\sigma_{\mathrm{em}} = 9.6 \cdot 10^{-18}$ cm^2 [20]. Setting $\eta_p = 1$, $\eta_a = 90\%$ (this includes absorption of the residual pump during its second pass through the cerium crystal), $T_{\mathrm{DM}} = 91\%$, we calculate a theoretically predicted efficiency of $\eta_{\mathrm{cw}} = 23.7\%$. This theoretical value is significantly lower than our measured value of 33%. This seems most likely to be due to a lower value of the ESA cross section than the estimated value given by Marshall *et al.* The cw lasing threshold $P_{\mathrm{cw}}^{\mathrm{th}}$ is calculated using the model

$$P_{\mathrm{cw}}^{\mathrm{th}} = \frac{\pi \omega^2 h \nu_p (T+L) n}{2(\sigma_{\mathrm{em}} - \sigma_{\mathrm{ESA}}) \tau_f \eta_p \eta_a T_{\mathrm{DM}}},$$

where ω is the radius of the cavity mode waist in the laser cavity, ν_p is the laser frequency, τ_f is the fluorescence lifetime, and $n = 1.41$ is the refractive index (which appears here owing to the Brewster crystal). The radius of the cavity mode waist ω is calculated to be 17 μm, and the pump spot was more tightly focused in the presented laser. For our system the model gives a lasing threshold of $P_{\mathrm{cw}}^{\mathrm{th}} = 1.91$ W, in reasonable agreement with the observed value of 2.2 W.

The output spectrum shown in the inset of Fig. 4 was measured for a free-running laser without the OPC in the long cavity arm. The laser signal was captured off the Brewster's angle of the Ce:LiCAF crystal and measured with an Ocean Optics HR4000 spectrometer with a resolution of 0.05 nm. As shown in the figure the peak wavelength of the laser was at 289.31 nm with a FWHM linewidth of 0.23 nm. With the OPC in the long cavity arm for maximum output the laser operated at 289.51 nm with a linewidth of 0.2 nm.

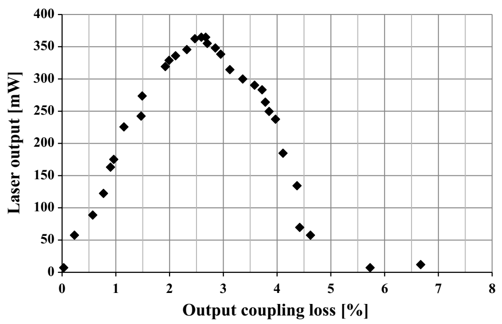

Fig. 3. Measured laser output in milliwatts as a function of the output coupling loss.

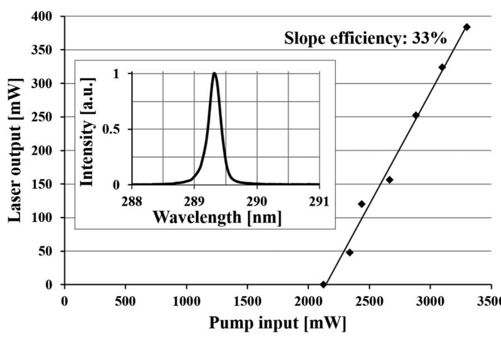

Fig. 4. Slope efficiency for maximum power output coupling. Inset: Spectrum for the free-running laser without OPC.

By placing a UV-grade prism with an apex angle of 67.4° in the long arm of the laser cavity instead of the OPC, we tuned the laser output wavelength. We achieved lasing from around 285.84 nm to around 295.30 nm with peak performance at around 289 nm. This corresponds to the gain spectrum of Ce:LiCAF between 285 and 295 nm and its main tuning peak. While an approximately 10 nm tuning range is already considerable, we note that nanosecond pulsed Ce:LiCAF lasers can be readily tuned from 280 to 315 nm; thus we expect to be able to broaden the tuning range of the laser even further in the future, for instance by implementing birefringent tuning instead of tuning with a prism. In particular, the prism tuning arrangement used did not allow for double-pass pumping, thereby reducing the pump absorption to the single-pass value of $\eta_a = 0.7$. The FWHM linewidth of the laser with the prism in the longer arm was 0.2 nm at around 291 nm, and was narrower toward the extremes of the tuning range (0.1 nm at 286 nm and at 295 nm).

In summary, we have demonstrated the first ever stable tunable chopped cw lasing in a cerium oscillator. The maximum output power measured with the described configuration was 384 mW when pumped with 3.3 W of 266 nm light. The laser output was tunable from 286 to 295 nm. By changing the length of the long cavity arm to match the repetition rate of the pump input, ultrafast laser pulses instead of cw lasing can be generated, which indicates that our demonstrated resonator is an ideal base for a new Ce:LiCAF laser platform for cw and ultrafast pulsed operation in the UV spectral region. These lasers will also benefit from further developments in the engineering of high-power. high-beam-quality 266 nm mode-locked and cw pump sources which presently limit the performance of cw cerium lasers.

B. Wellmann acknowledges support from Macquarie University through an International Macquarie University Research Excellence Scholarship. The authors also acknowledge the support of an Australian Research Council Discovery Grant for this work (DP110102754).

References

1. T. Andreae, W. König, R. Wynands, D. Leibfried, F. Schmidt-Kaler, C. Zimmermann, D. Meschede, and T. W. Hänsch, Phys. Rev. Lett. **69**, 1923 (1992).
2. M. Scheid, F. Markert, J. Walz, J. Wang, M. Kirchner, and T. W. Hänsch, Opt. Lett. **32**, 955 (2007).
3. H. Kumagai, IEEE J. Sel. Top. Quantum Electron. **10**, 1252 (2004).
4. T. Rosenband, D. B. Hume, P. O. Schmidt, C. W. Chou, A. Brusch, L. Lorini, W. H. Oskay, R. E. Drullinger, T. M. Fortier, J. E. Stalnaker, S. A. Diddams, W. C. Swann, N. R. Newbury, W. M. Itano, D. J. Wineland, and J. C. Bergquist, Science **319**, 1808 (2008).
5. H. M. Shapiro, *Practical Flow Cytometry* (Wiley, 1994).
6. Y. Zhang, R. Hoshi, D. Yamaguchi, Y. Okada-Shudo, M. Watanabe, M. Hyodo, Y. Zhu, X. Wang, Y. Zhu, G. Wang, C. Chen, T. Kanai, and S. Watanabe, Opt. Commun. **295**, 176 (2013).
7. Y. Kaneda, J. M. Yarborough, L. Li, N. Peyghambarian, L. Fan, C. Hessenius, M. Fallahi, J. Hader, J. V. Moloney, Y. Honda, M. Nishioka, Y. Shimizu, K. Miyazono, H. Shimatani, M. Yoshimura, Y. Mori, Y. Kitaoka, and T. Sasaki, Opt. Lett. **33**, 1705 (2008).
8. A. Richter, N. Pavel, E. Heumann, G. Huber, D. Parisi, A. Toncelli, M. Tonelli, A. Diening, and W. Seelert, Opt. Express **14**, 3282 (2006).
9. T. Le, S. J. Schowalter, W. Rellergert, J. Jeet, G. Lin, N. Yu, and E. R. Hudson, Opt. Lett. **37**, 4961 (2012).
10. D. J. Spence, H. Liu, and D. W. Coutts, Opt. Commun. **262**, 238 (2006).
11. N. Sarukura, M. A. Dubinskii, L. Zhenlin, V. V. Semashko, A. K. Naumov, S. L. Korableva, R. Y. Abdulsabirov, K. Edamatsu, Y. Suzuki, T. Itoh, and Y. Segawa, IEEE J. Sel. Top. Quantum Electron. **1**, 792 (1995).
12. D. W. Coutts and A. J. S. McGonigle, IEEE J. Sel. Top. Quantum Electron. **40**, 1430 (2004).
13. Z. Liu, K. Shimamura, T. Fukuda, T. Kozeki, Y. Suzuki, and N. Sarukura, Opt. Mater. **19**, 123 (2002).
14. S. Ono, Y. Suzuki, T. Kozeki, H. Murakami, H. Ohtake, N. Sarukura, H. Sato, S. Machida, K. Shimamura, and T. Fukuda, Appl. Opt. **41**, 7556 (2002).
15. V. A. Fromzel and C. R. Prasad, in *OSA Topical Meeting on Advanced Solid-State Photonics (ASSP)*, Vol. **83** of Trends in Optics and Photonics Series (2003), p. 203.
16. E. Granados, D. W. Coutts, and D. J. Spence, Opt. Lett. **34**, 1660 (2009).
17. H. W. Kogelnik, E. P. Ippen, A. Dienes, and C. V. Shank, IEEE J. Quantum Electron. **8**, 373 (1972).
18. S. A. Payne, L. L. Chase, H. W. Newkirk, L. K. Smith, and W. F. Krupke, IEEE J. Quantum Electron. **24**, 2243 (1988).
19. D. Alderighi, G. Toci, M. Vannini, D. Parisi, and M. Tonelli, Opt. Express **13**, 7256 (2005).
20. C. D. Marshall, J. A. Speth, S. A. Payne, W. F. Krupke, G. J. Quarles, V. Castillo, and B. H. T. Chai, J. Opt. Soc. Am. B **11**, 2054 (1994).

Dynamics of solid-state lasers pumped by mode-locked lasers

Barbara Wellmann,* **David J Spence, and David W Coutts**

MQ Photonics Research Centre, Department of Physics and Astronomy, Faculty of Science and Engineering, Macquarie University, Balaclava Road, North Ryde, New South Wales 2109, Australia
*barbara.wellmann@mq.edu.au

Abstract: We analyze the dynamics of mode-locked pumped solid-state lasers focusing on the transition between mode-locked and CW behavior. Where the ratio of the pump and laser cavity lengths is a rational number, 'rational-harmonic mode-locking' is obtained. When the cavity length is detuned away from such resonances, modulated continuous output is generated. The transition from mode-locked to modulated CW operation is explored experimentally for a Ce:LiCAF laser operating at 290 nm and pumped by a 78.75 MHz mode-locked frequency quadrupled Nd:YVO_4 laser. Both CW output and mode-locked output with pulse repetition rates up to 1.1 GHz were achieved. A rate equation model is developed to predict optimum cavity lengths for achieving CW output with minimized modulation.

OCIS codes: (140.3580) Lasers, solid-state; (140.3610) Lasers, ultraviolet; (140.4050) Mode-locked lasers; (140.5560) Pumping.

References and links

1. Q. Fu, G. Mak, and H. M. van Driel, "High-power, 62-fs infrared optical parametric oscillator synchronously pumped by a 76-MHz Ti:sapphire laser," Opt. Lett. **17**(14), 1006–1008 (1992).
2. H. M. van Driel, "Synchronously pumped optical parametric oscillators," Appl. Phys. B **60**(5), 411–420 (1995).
3. G. A. Mourou and T. Sizer II, "Generation of pulses shorter than 70 fs with a synchronously-pumped cw dye laser," Opt. Commun. **41**(1), 47–48 (1982).
4. C. Wu and N. K. Dutta, "High-repetition-rate optical pulse generation using a rational harmonic mode-locked fiber laser," IEEE J. Quantum Electron. **36**(2), 145–150 (2000).
5. C. D. Marshall, J. A. Speth, S. A. Payne, W. F. Krupke, G. J. Quarles, V. Castillo, and B. H. Chai, "Ultraviolet laser emission properties of Ce^{3+}-doped $LiSrAlF_6$ and $LiCaAlF_6$," J. Opt. Soc. Am. B **11**(10), 2054–2065 (1994).
6. N. Sarukura, M. A. Dubinskii, L. Zhenlin, V. V. Semashko, A. K. Naumov, S. L. Korableva, R. Y. Abdulsabirov, K. Edamatsu, Y. Suzuki, T. Itoh, and Y. Segawa, "Ce^{3+}-activated fluoride crystals as prospective active media for widely tunable ultraviolet ultrafast lasers with direct 10-ns pumping," IEEE J. Sel. Top. Quantum Electron. **1**(3), 792–804 (1995).
7. D. Alderighi, G. Toci, M. Vannini, D. Parisi, S. Bigotta, and M. Tonelli, "High efficiency UV solid state lasers based on Ce: $LiCaAlF_6$ crystals," Appl. Phys. B **83**(1), 51–54 (2006).
8. D. J. Spence, H. Liu, and D. W. Coutts, "Low-threshold miniature Ce:LiCAF lasers," Opt. Commun. **262**(2), 238–240 (2006).
9. D. W. Coutts and A. J. McGonigle, "Cerium-doped fluoride lasers," IEEE J. Quantum Electron. **40**(10), 1430–1440 (2004).
10. Z. Liu, K. Shimamura, T. Fukuda, T. Kozeki, Y. Suzuki, and N. Sarukura, "High-energy pulse generation from solid-state ultraviolet lasers using large Ce: fluoride crystals," Opt. Mater. **19**(1), 123–128 (2002).
11. S. Ono, Y. Suzuki, T. Kozeki, H. Murakami, H. Ohtake, N. Sarukura, H. Sato, S. Machida, K. Shimamura, and T. Fukuda, "High-energy, all-solid-state, ultraviolet laser power-amplifier module design and its output-energy scaling principle," Appl. Opt. **41**(36), 7556–7560 (2002).
12. V. A. Fromzel and C. R. Prasad, "A tunable, narrow linewidth, 1 kHz Ce: LiCAF laser with 46% efficiency," In *2003 OSA Topical Meeting on Advanced Solid-State Photonics (ASSP) (Trends in Optics and Photonics Series)* p. 203. (Optical Society of America, February 2003, San Antonio, Tex.).
13. E. Granados, D. W. Coutts, and D. J. Spence, "Mode-locked deep ultraviolet Ce:LiCAF laser," Opt. Lett. **34**(11), 1660–1662 (2009).
14. B. Wellmann, D. J. Spence, and D. W. Coutts, "Tunable continuous-wave deep-ultraviolet laser based on Ce:LiCAF," Opt. Lett. **39**(5), 1306–1309 (2014).
15. J. Farey, "LXXIX. On a curious property of vulgar fractions," Philos. Mag. **47**(217), 385–386 (1816).

#226438 - $15.00 USD Received 6 Nov 2014; revised 5 Feb 2015; accepted 6 Feb 2015; published 12 Feb 2015
(C) 2015 OSA 23 Feb 2015 | Vol. 23, No. 4 | DOI:10.1364/OE.23.004441 | OPTICS EXPRESS 4441

16. A. Zavadilová, V. Kubeček, and J. Šulc, "Pulse repetition rate multiplication in an intracavity synchronously pumped ring optical parametrical oscillator," Laser Phys. Lett. **10**(11), 115401 (2013).
17. J. P. Zheng, U. Sen, D. M. Benenson, and H. S. Kwok, "Observation of periodicity multiplication in a synchronously pumped dye laser," Opt. Lett. **11**(10), 632–634 (1986).
18. H. Kogelnik, E. P. Ippen, A. Dienes, and C. V. Shank, "Astigmatically compensated cavities for cw dye lasers," IEEE J. Quantum Electron. **8**(3), 373–379 (1972).
19. J. Lee and J. H. Lee, "Experimental investigation of the cavity modulation frequency detuning effect in an active harmonically mode-locked fiber laser," J. Opt. Soc. Am. B **30**(6), 1479–1485 (2013).

1. Introduction

Continuous power sources such as continuous wave (CW) lasers are typically used to pump mode-locked and CW lasers. However mode-locked pulsed lasers are also useful pump sources, most commonly for synchronously pumping of other mode-locked lasers such as optical parametric oscillators [1,2] and dye lasers [3]. In these cases, the pump and laser cavity lengths are carefully matched to ensure the pump pulses are synchronous with the circulating pulse in the laser cavity, in which case the pulse repetition frequency of the mode-locked laser matches that of the pump laser.

Where the pump and laser optical cavity lengths are different, but their ratio is given by a rational number, 'rational-harmonic' mode-locking [4] can occur, in which case more than one pulse may circulate in the laser cavity and each circulating pulse is only synchronous with a pump pulse after an integer number of round trips. This approach is particularly useful for solid-state and fiber lasers where the gain persists, as such systems allow generation of output pulses at rational harmonics of the pump repetition frequency. Alternatively, for fully asynchronous pumping, where the pump and laser round trip times are far from a harmonic resonant condition, the laser may operate CW even though it is pumped with a mode-locked source.

In this paper, we explore experimentally and numerically the dynamics of solid-state lasers when pumped synchronously and asynchronously by a mode-locked laser, including the transition from rational-harmonic mode-locking to CW operation. We focus on mode-locked pumped Ce:LiCAF solid-state lasers; Ce:LiCAF has an upper laser level lifetime of 25 ns [5] which is of the same order as the pump laser inter-pulse interval for a typical 80 MHz mode-locked solid-state pump laser, potentially leading to complex dynamics. Ce:LiCAF can be pumped conveniently by the fourth harmonics of solid-state Nd lasers (λ_p = 266 nm) as this wavelength is well matched to the peak of the absorption spectrum. For practical reasons it is advantageous to pump Ce:LiCAF lasers with mode-locked lasers, since at present the availability of high power CW 266 nm pump lasers is limited, while it is relatively easy to obtain pulsed high power 266 nm from frequency quadrupling mode-locked Nd lasers.

Ce:LiCAF is an efficient ultraviolet (UV) laser material with an overall gain bandwidth that spans over 35 nm from 280 nm to 315 nm with a maximum gain at 290 nm [6]. Ce:LiCAF is a well-established material for nanosecond-pulse tunable UV lasers. In this domain [7,8], Ce:LiCAF lasers have already been scaled to Watt-level average power [9], have reached 100 mJ pulse energy [10] and have shown laser slope efficiencies of the order of 50% [11,12]. We have also demonstrated synchronously-pumped mode-locked picosecond operation of a Ce:LiCAF oscillator [13]. Finally, we recently reported the generation of tunable chopped-CW laser output in a mode-locked pumped Ce:LiCAF oscillator using asynchronous pumping [14]. In this paper we discuss in detail mode-locked pumping of solid-state lasers for the generation of both CW laser output and rational-harmonic mode-locked output. We have developed an analytical model based on the laser rate equations and investigate the dynamics in the Ce:LiCAF laser cavities based both on simulation and experimental results. Our findings confirm that mode-locked pump sources can indeed be used to generate stable CW laser output with only small residual modulations using asynchronous pumping, and also to generate pulse trains with over 1 GHz pulse repetition frequency using rational-harmonic pumping of a Ce:LiCAF laser.

2. Synchronous and asynchronous pumping

When pumping a solid-state laser with a mode-locked pump source, the length of the laser cavity determines the laser operation mode. Each successive pulse from the mode-locked pump is incident at the laser crystal with some specific timing relative to the circulating laser cavity field. If that timing is the same for every pump pulse, then we have synchronous mode-locking, where a single pulse is formed in the laser cavity field, and that pulse arrives at the gain crystal synchronized with each pump pulse. Clearly this occurs when the pump cavity length and laser cavity lengths are matched; it also occurs when the laser cavity length is any integer fraction of the pump cavity length. For *n*-th harmonic locking, the laser cavity is *n*-times shorter than the pump cavity, and the pulse in the laser cavity makes *n* round trips between each synchronized pump event. The relative timing of the pump pulse and the intracavity laser pulse for the third harmonic are shown schematically in Figs. 1(a) and 1(b).

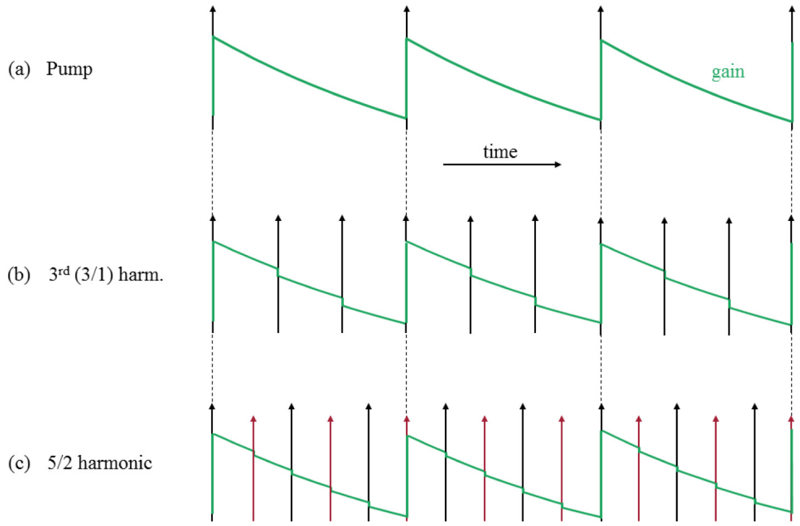

Fig. 1. Comparison of pulse timing for different cavity lengths. (a) The pump pulse train arriving at the laser crystal. The green line represents the gain curve. (b) The laser pulse train of the 3rd harmonic of the pump. There is one pulse in the cavity which is synchronized with a pump pulse every 3rd round-trip. (c) The laser pulse train for the '5/2 harmonic'. There are two pulses in the cavity (represented by the black and red arrows, arbitrarily drawn with different heights to distinguish them), each synchronous with a pump pulse every 5th round-trip.

There are also more complex harmonics, for which multiple locations in the laser cavity field are each synchronized with a subset of the arriving pump pulses, and each of the locations experience pump events in sequence. This occurs when the ratio of the cavity lengths is any rational number, giving rise to 'rational-harmonic' mode-locking. For example, if the laser cavity length is 2/5 of the pump cavity length, there are two locations in the laser field that are each synchronized with every second pump pulse. We can call this the 5/2 harmonic. Figure 1(c) illustrates the timing for the 5/2 harmonic; there are two laser pulses in the cavity with each pulse synchronous with a pump pulse every five round trips. In general, the *x/y* harmonic has *y* pulses in the laser cavity, each of which makes *x* round trips between its pump events. The output repetition rate is *x*-times that of the pump laser. Note that the gain persists between pump events (shown schematically in Fig. 1), so that the laser pulses see gain at every pass through the crystal whether or not that pass is synchronous with a pump pulse.

#226438 - $15.00 USD Received 6 Nov 2014; revised 5 Feb 2015; accepted 6 Feb 2015; published 12 Feb 2015
(C) 2015 OSA 23 Feb 2015 | Vol. 23, No. 4 | DOI:10.1364/OE.23.004441 | OPTICS EXPRESS 4443

Figure 2 shows a plot of the range of rational harmonics, where the horizontal axis is the normalized cavity length $l/l_{pump} = y/x$, and the vertical axis the normalized laser repetition rate $R/R_{pump} = x$. The plot includes all harmonics for which $x \leq 100$, and $y/x \leq 0.5$. The blue dotted lines connect harmonics with the same y thus having the same number of intracavity pulses. So the lowest line connects the 2nd, 3rd, etc. harmonics with cavity lengths 0.5, 0.33, etc. The next lowest line connects the 5/2, 7/2, etc. harmonics with normalized cavity lengths 2/5, 2/7, etc. The complete set of reduced rational fractions that define the harmonics are known as the Farey sequence [15]. Rational-harmonic mode-locking allows access to a wide range of repetition rates for relatively minor changes in the laser cavity length. Rational-harmonic mode-locking has been reported in synchronously pumped ring optical parametrical oscillators (OPOs) e.g. [16]. and synchronously pumped dye lasers e.g. [17].

For a fixed pump power, the more pulses there are in the laser cavity (y), the less energy is in each - the extent of gain saturation thus decreases as the number of pulses increases, and so the strength of the pulse-forming effect must decrease. We thus expect the laser cavity field for complex rational harmonics (x/y) with larger denominators y to become progressively less modulated, limiting the theoretically-infinite set of complex harmonics to a more limited number. The resonances also get narrower as the numerator x increases, since each circulating pulse becomes synchronous with a pump pulse less frequently, imposing tighter limits on the exact cavity length. Hence, at cavity lengths between those corresponding to harmonics that have small denominators, there are cavity lengths for which there is no strong modulation of the laser cavity field – this is asynchronous pumping.

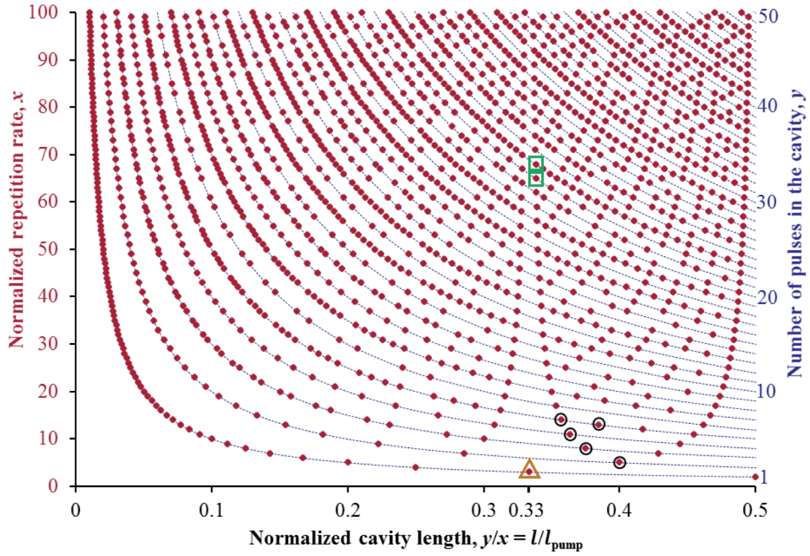

Fig. 2. A visualization of harmonics as a function of the normalized cavity length ($l / l_{pump} = y/x$). The vertical axis is the normalized laser repetition rate $R/R_{pump} = x$. The plot includes all harmonics for which $x \leq 100$, and $y/x \leq 0.5$. The solid lines connect harmonics with the same y thus having the same number of intracavity pulses. Harmonic points marked are explored in detail later in this paper.

3. Experimental setup and analytical model

We have constructed a Ce:LiCAF laser to illustrate the behavior of asynchronous solid-state lasers and to study the transition between mode-locked output and continuous output. The laser system setup we used for our experiments, shown in Fig. 2, is similar to that described in

[14]. In summary, the chopped frequency quadrupled mode-locked output of a Nd:YVO_4 laser was used to pump a Ce:LiCAF laser cavity. Pump pulses of 266 nm light with 23 ps duration at a repetition rate of 78.75 MHz were generated with a maximum average output power of 2.80 W. This pulse train was chopped with a duty cycle of 8.3% to avoid thermal effects in the second frequency doubling stage [14], with on-periods of 400 µs; the Ce:LiCAF laser was observed to reach steady-state on times of order 10 µs, and so the chopping is disregarded henceforth. The laser cavity was a three-mirror resonator with a folding angle of 12° to compensate the astigmatism introduced by the Brewster-angle-cut 1.25 mm long 3.5% cerium-doped LiCAF crystal [18]. All three cavity mirrors were custom coated for minimum absorption and transmission, and as an output coupler (OPC), a 4 mm thick UV-grade silica plate at close-to Brewster's angle was placed in the long cavity arm. In this laser cavity, the length of the long cavity arm (between CM_2 and CM_3) determined the laser operation mode [14].

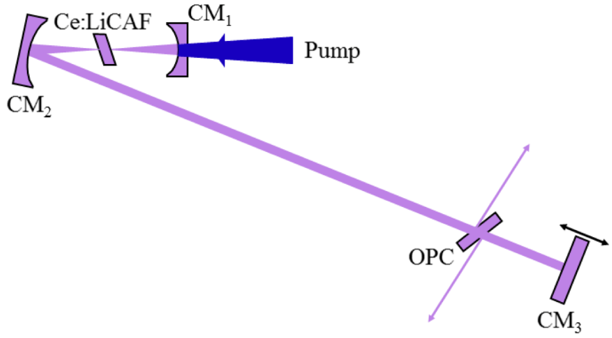

Fig. 3. Schematic of the Ce:LiCAF laser cavity. CM1: dichroic input coupling cavity mirror with a radius of curvature (ROC) = 5 cm; CM2: high reflective (HR) cavity mirror with ROC = 10 cm; OPC: output coupler; CM3: HR plane cavity mirror.

To analyze the behavior of our laser system for various cavity lengths, we compiled an analytical model based on the laser rate equations. In this model, the bi-directional cavity field is divided into an integer number (typically 1000) of small elements, and the evolution of that laser field is calculated as the field circulates in the cavity. We assume that laser crystal is thin. To determine the rate of change of the inversion, we need the current left- and right-travelling laser field at the crystal location (I_L^+ and I_L^-). Combined with time-dependent absorbed pump power $P_P^{abs}(t)$ that tracks the train of pump pulses arriving at the crystal, the total number N of inverted ions in the laser crystal can be written

$$\frac{dN}{dt} = \frac{P_P^{abs}(t)}{e_p} - \frac{\sigma_{em} N (I_L^+ + I_L^-)}{e_l} - \frac{N}{\tau} \tag{1}$$

in which e_p and e_l are the phonon energies of the pump and laser photons, τ is the upper laser level lifetime, and σ_{em} is the emission cross-section of the laser transition. We model the incident pump pulse train as a sequence of pulses with temporal Gaussian profile. The single-pass absorption of our crystal was measured to be α_p = 70%. The cavity mirrors (CM_2 and CM_3 in Fig. 3) were not only highly-reflective for the laser wavelength, but also for the pump wavelength. Thus, in addition to being pumped by the forwards travelling pump light through CM_1, the crystal is also pumped by the backwards traveling residual pump that is reflected inside the cavity. This second pump pass results in the absorption of a further 21% of the initial pump energy – we include this secondary absorption in the model, suitably offset in time from the main absorption pass.

The laser field is amplified during its forward and backward pass through the crystal according to

$$dI_L^{\pm} = \frac{\sigma_{eff} N I_L^{\pm}}{An}, \tag{2}$$

where $\sigma_{eff} = \sigma_{em} - \sigma_{ESA}$ is an effective gain coefficient that accounts for the reduction in effective gain caused by excited state absorption with coefficient σ_{ESA}. Parameter A is the focal area of the pump laser, which is expanded by a factor n in the tangential plane within the Brewster-cut crystal.

The output coupling is modeled as a loss T_{opc} applied at a single specific location in the cavity with current field value I_L^{opc}; the remaining cavity losses L are also collected here, resulting in

$$dI_L^{opc} = (T_{opc} + L) I_L^{opc}. \tag{3}$$

The output coupling T_{opc} = 2.5% and the round-trip loss L = 2.45% were measured accurately (to ± 0.05%) using a cavity ringdown method, and sum to a total loss of 4.95% [14]. Finally, we calculate the laser output power P_L as

$$P_L = T_{opc} I_L^{opc} An. \tag{4}$$

The model was used to predict the behavior and the form of the output of Ce:LiCAF lasers with parameters summarized in Table 1 as a function of cavity length. Note that the behavior is insensitive to minor changes in the listed parameters other than the cavity length. The model neglects dispersion and gain bandwidth that will affect the duration of strongly mode-locked pulses; it also neglects nonlinear effects such as self phase modulation and self-focusing that can cause passive mode-locking and soliton generation. Thus the model is not suitable for understanding the laser performance at locations that generate very short pulses, and we do not present or consider pulse durations for strongly mode-locked pulse trains in this work. The model is designed for investigating the behavior for cavity lengths between strongly mode-locked locations, where the peak intensities are low, and the structure in the cavity field is on multi-picosecond timescales: here the laser behavior is determined mostly by gain modulation and gain saturation. The good agreement shown below between the model and experiment for such asynchronous cavity lengths attests that the simplified model provides a useful tool for understanding the behavior of this laser.

4. Results

Figure 4 shows experimental and modeling results for the slope efficiency of the Ce:LiCAF laser for a cavity length of 0.754 m (120 mm mismatched from the 3rd harmonic), where CW laser output with a modulation of just ± 1% for frequencies below 1 GHz was obtained (discussed in detail later). The laser threshold was determined to be 1.37 W, and the maximum laser output power achieved was 288 mW at an input power of 2.80 W. The parameters used to match the model and experimental data are listed in Table 1.

#226438 - $15.00 USD Received 6 Nov 2014; revised 5 Feb 2015; accepted 6 Feb 2015; published 12 Feb 2015
(C) 2015 OSA 23 Feb 2015 | Vol. 23, No. 4 | DOI:10.1364/OE.23.004441 | OPTICS EXPRESS 4446

Table 1. Input variables for the numerical model used for simulating the Ce:LiCAF laser.

Variable	Value
Measured (average) pump power P_P	2.76 W
Pump repetition rate R_{pump}	78.75 MHz
Pump cavity length $l_{pump} = c/(2 \cdot R_{pump})$	1.902 m
Pump pulse duration	23 ps
Transmission of the dichroic input coupling mirror (CM_1)	91%
Single pass absorption of the crystal α_p	70%
Overlap efficiency	81%
Pump wavelength	266 nm
Laser wavelength	290 nm
Laser beam waist in crystal ω_l	12.9 µm
Upper laser level lifetime τ	25 ns
Emission cross section σ_{em}	$9.6 \cdot 10^{-18}$ cm^2 [5]
ESA cross section σ_{ESA}	$3.6 \cdot 10^{-18}$ cm^2 [5]
Refractive index of the crystal (at laser wavelength) n	1.41
Output coupling loss T_{opc}	2.5%
Loss of cavity elements L	2.45%

Using this Ce:LiCAF laser, we have studied the complex harmonics close to the 3rd harmonic (alternatively called the 3/1 harmonic), that is located at a cavity length $l_3 = l_{pump}/3 \approx 0.634$ m, where l_{pump} is the length of the pump laser resonator. The 3rd harmonic is marked with an orange triangle in Fig. 2. From here on, we refer to cavity length mismatch $\Delta l = l - l_3$, which is the cavity length referenced to that for the 3rd harmonic. We focus on harmonics that occur for cavity lengths close to but longer than for the third harmonic, i.e. $x/y \lesssim 3$ so that $l_{x/y} = l_{pump} \times y/x$, as this length range probes the full range of expected behavior for a synchronously pumped Ce:LiCAF laser.

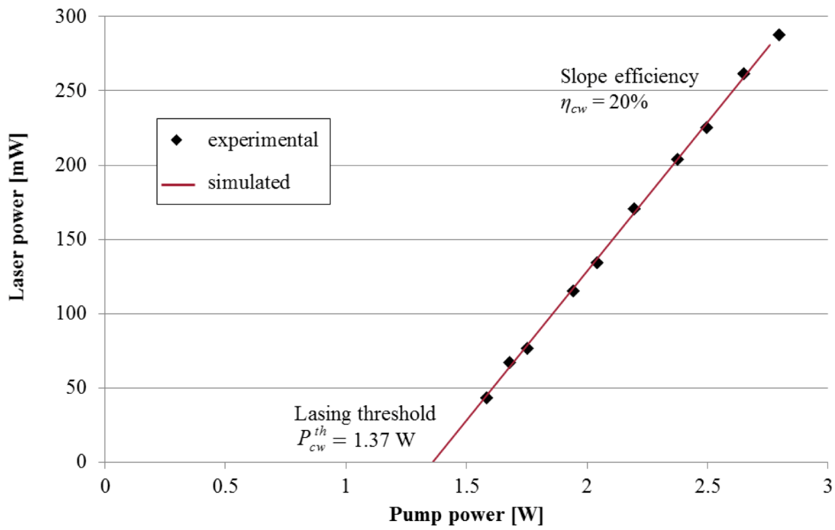

Fig. 4. Measured and simulated slope efficiencies, for a cavity length of 0.754 m (120 mm mismatched from the 3rd harmonic), where CW laser output with a modulation of just ± 1% for frequencies below 1 GHz was obtained.

#226438 - $15.00 USD Received 6 Nov 2014; revised 5 Feb 2015; accepted 6 Feb 2015; published 12 Feb 2015

23 Feb 2015 | Vol. 23, No. 4 | DOI:10.1364/OE.23.004441 | OPTICS EXPRESS 4447

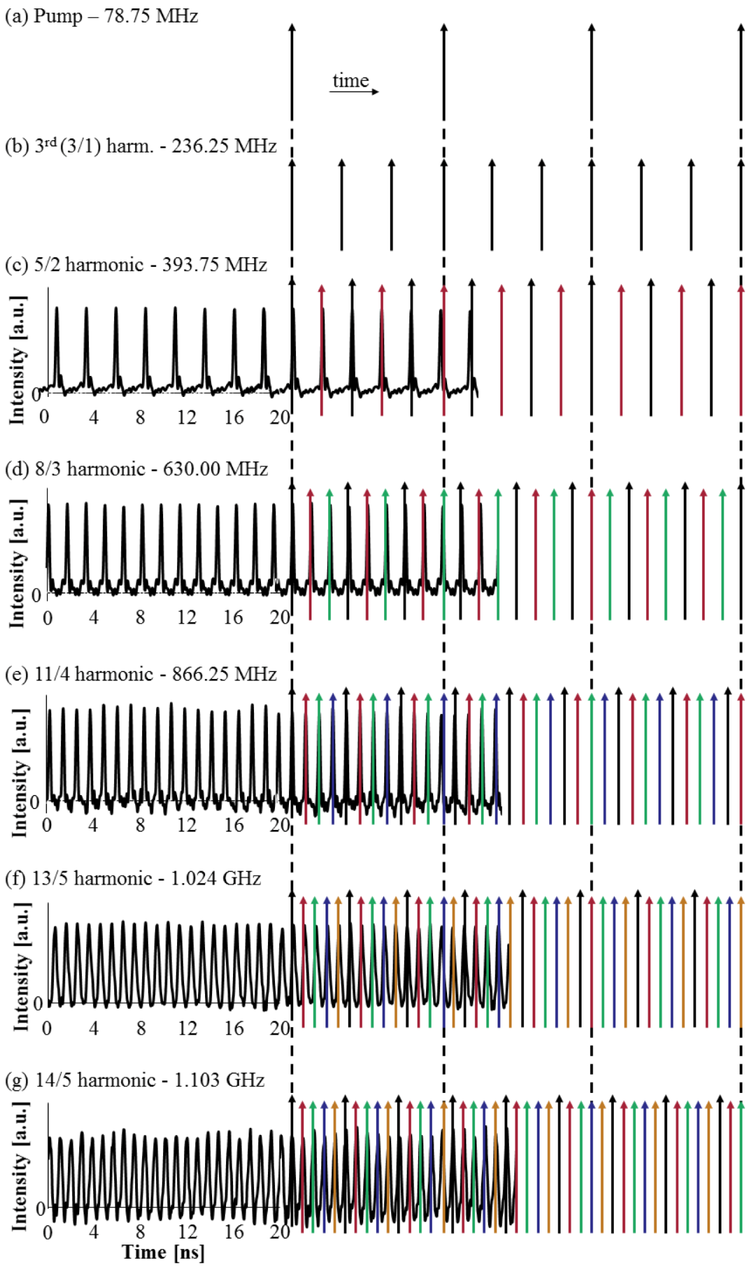

Fig. 5. Time domain measurement of a selection of rational harmonics, showing full modulation of the cerium laser cavity field overlapped with the schematic diagram showing the pulse timing for the pump laser and the harmonics. For each harmonic, each of the distinct pulses within the laser cavity is marked with a different color, with one arbitrarily marked taller to assist the reader.

#226438 - $15.00 USD Received 6 Nov 2014; revised 5 Feb 2015; accepted 6 Feb 2015; published 12 Feb 2015
(C) 2015 OSA 23 Feb 2015 | Vol. 23, No. 4 | DOI:10.1364/OE.23.004441 | OPTICS EXPRESS 4448

We have experimentally observed a range of rational harmonics using a fast photodiode. The traces shown in Fig. 5(c)-5(g) were measured using an ALPHALAS UPD-50-UP ultrafast photodetector with a 50 ps rise time, and 6 GHz oscilloscope. We thus expect to be able to detect harmonics with repetition rates = 6 GHz; with our 78.75 MHz pump laser, this corresponds to harmonics x/y with x = 60. Figure 5 shows a selection of the observed higher order harmonics corresponding to the group of rational harmonics circled in black in Fig. 2, each appearing at the predicted cavity length $l_{pump} \times y/x$, showing fully modulated pulse trains; the maximum measured repetition rate is 78.75 GHz × 14 = 1.103 GHz corresponding to the 14/5 harmonic.

Figure 5 also shows schematically the timing for each of these different harmonics. The timing of the arrival of pump pulses at the laser crystal is shown in panel (a); the remaining panels show the timing of arrival of pulses in the laser cavity. The color-coded arrows represent the distinct pulses within the laser cavity at the higher harmonics – recall that for the x/y harmonic, there are y distinct pulses in the laser cavity. The arrow marking the specific pulse that is synchronous at the left is drawn slightly larger to assist the reader to track the different pulses in the cavity. Comparing the 13/5 and the 14/5 harmonic [Fig. 5(f) and 5(g)] is particularly instructive; in both cases there are 5 distinct pulses in the cavity. For the 13/5 harmonic, the repetition rate is 78.75 GHz × 13 = 1.024 GHz, and each pulse is synchronous after making 13 round trips – the pulses are synchronous with the pump pulse in the order 1-3-5-2-4-1-3-… For the 14/5 harmonic, the repetition rate is 78.75 GHz × 14 = 1.103 GHz, and each pulse is synchronous after making 14 round trips – the pulses experience pump events in the order 1-5-4-3-2-1-5-…

The main aim of the work presented in this paper is to discuss the general form of the laser operation mode of mode-locked pumped solid-state lasers for a large range of cavity lengths, concentrating on the transition between mode-locked and CW behavior. A detailed characterization of the pulses at rational harmonics (e.g. pulse widths, stability) is thus not included in this paper. We note that we have previously measured the pulse duration of a similar laser, mode-locked at the 1st harmonic, to be 6 ps [13].

In general the pulse trains generated at rational harmonics will have relatively uniform energy, since the gain persists between pumping events (see Fig. 1 and section 2) and so pulses are amplified even on round trips for which they are not synchronous with the pump; the precise variation between the pulses will be different for each harmonic. In contrast, rational-harmonic OPOs have pronounced pulse energy variation, since pulses see gain only during their own pump events and so decay in amplitude on each round trip between pump events [16]. In fiber lasers, that feature a long energy storage time compared to the laser round trip time, strong Q-switching has been observed when the laser cavity is detuned from a harmonic [19]. Due to the short upper laser level lifetime of Ce:LiCAF (τ = 25 ns), such Q-switching modulation would not be expected to be significant.

We now use the simulated output from our numerical model to explore the behavior of the laser for a small range of cavity lengths. Figure 6 shows the modulation depth of the simulated laser output, defined as $(I_{max} - I_{min}) / (I_{max} + I_{min})$, as a function of cavity length mismatch. Also marked are the expected positions of all rational harmonics with x < 390 in this cavity length range. Note that this cavity length mismatch range of 9.3 mm to 9.8 mm, corresponds to a very narrow selection of potential harmonics, covering normalized cavity lengths of 0.3382 to 0.3385; the two dominant harmonics (68/23 and 65/22) are marked with green squares both in Fig. 6 and in Fig. 2. Using the numerical model, we specifically sampled the locations and surrounding cavity lengths for the noted harmonics, to find the range of cavity lengths over which each harmonic has influence. We see that the model predicts strong modulation of the cavity field at the location of each harmonic, with the modulation depth decreasing somewhat with increasing x; thus there is a continuous transition between trains of well separated pulses and a modulated CW cavity field as the number of pulses in the cavity increases.

#226438 - $15.00 USD Received 6 Nov 2014; revised 5 Feb 2015; accepted 6 Feb 2015; published 12 Feb 2015
(C) 2015 OSA 23 Feb 2015 | Vol. 23, No. 4 | DOI:10.1364/OE.23.004441 | OPTICS EXPRESS 4449

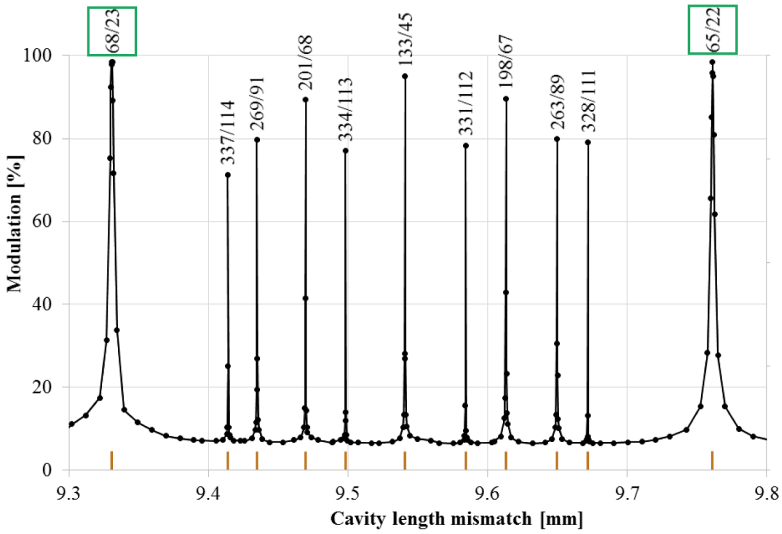

Fig. 6. Modulation depth of the laser output from numerical simulation as a function of cavity length mismatch Δl, showing a set of higher harmonics interspersed by regions of lower modulation. The location of harmonics with x < 390 are indicated near the x-axis. The harmonic labels marked with a square correspond to the points marked with a square in Fig. 2.

The resonances become much sharper for higher harmonics: e.g. for the 68/23 harmonic, the resonance has a width of Δl = 100 µm, but for the 198/67 or 263/89 harmonic, the resonances have a width of only Δl = 10 µm. The decreasing modulation depth and decreasing width of the resonances for the higher harmonics means that despite there being an infinite number of possible harmonics, in practice there are significant regions between the resonances that have relatively little modulation. Modelling for cavity lengths between the marked resonances show modulation of under 10%. We can see that in these regions the laser can be described as providing continuous laser output with a small superimposed intensity ripple.

We have explored experimentally and theoretically the regions of lower modulation between the harmonics. Figure 7 shows a series of experimental measurements at different cavity mismatch lengths that avoid rational-harmonic mode-locking, and where the resulting modulation is small. Note that these experimental measurements were recorded using a photodiode with a 1 ns response and an oscilloscope with 6 GHz bandwidth, since the instantaneous output power was not sufficient for our faster photodiode. These measurements are compared to the model output, as well as the model output convolved with the response function of our measurement system to simulate the experimental results (the curve marked "simulated, filtered" in Fig. 7). The simulations were carried out at cavity lengths representative of the low-modulation regions, avoiding the narrow peaks corresponding to high-order harmonics. The curves were plotted for an input power of 2.80 W, so about twice above threshold. The modulation of the simulated filtered output and the experimentally measured output match each other closely, giving confidence in the output of the model. The modulation decreases with increasing cavity length mismatch Δl from the third harmonic – this is because we are moving off the extended shoulder of the third harmonic resonance, which is significant for a wide range of cavity lengths. The model predicts that for cavity lengths around Δl = 120 mm, corresponding to a normalized cavity length l_n of 0.3964, the residual modulation is minimized. This minimum is formed by the decreasing modulation due to the third harmonic (l_n = 0.33) being balanced by the increasing modulation due to the second harmonic (l_n = 0.5). These two y = 1 harmonics dominate the behavior - while this minimum location is relatively close to the location of the 5/2 harmonic at Δl = 126.8 mm (l_n = 0.4), this higher harmonic only has influence over a range of 5 mm.

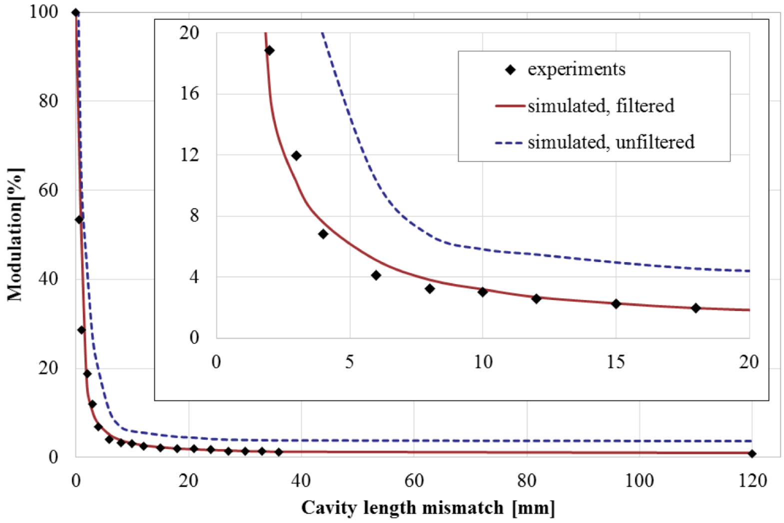

Fig. 7. Measured and simulated laser output fluctuation as a function of the cavity length mismatch. These points cover normalized cavity lengths from 0.3333 to 0.3964.

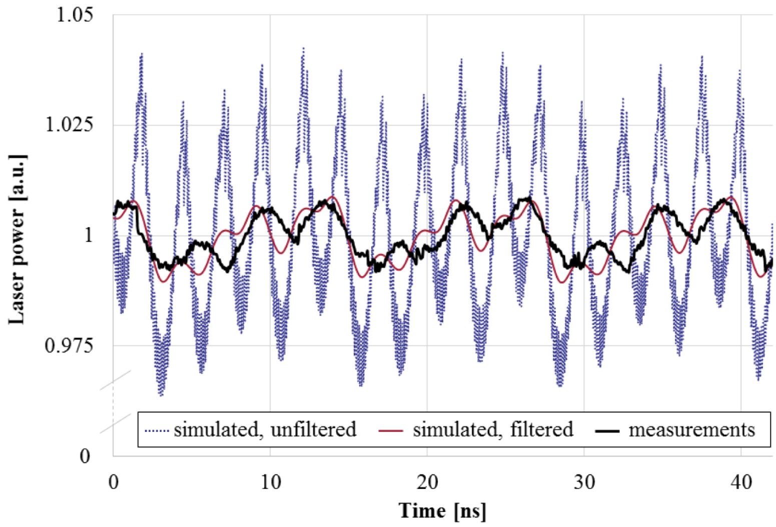

Fig. 8. Measured and simulated laser output for a cavity length Δl of 120 mm, for a Ce:LiCAF laser - the modulation is of the order of 1% for frequencies below 1 GHz and 4% on faster timescales.

#226438 - $15.00 USD Received 6 Nov 2014; revised 5 Feb 2015; accepted 6 Feb 2015; published 12 Feb 2015

23 Feb 2015 | Vol. 23, No. 4 | DOI:10.1364/OE.23.004441 | OPTICS EXPRESS 4451

Figure 8 shows the measured and simulated Ce:LiCAF laser output plotted as a function of time for *Δl* of 120 mm. We see good agreement between the model and the experimental results: We measured experimentally the modulation to be just ± 1% for frequencies below 1 GHz, and according to the model the modulation should be less than ± 4% on faster timescales. For many applications of CW UV lasers, modulation of the laser output at GHz frequencies may not be problematic. For these applications our generated laser output is closely equivalent to that from a CW-pumped multi-longitudinal-mode CW laser, and so can be used interchangeably.

An unavoidable effect of pumping a CW laser with a mode-locked laser is that each pump pulse produces a step increase in the gain (increasing on the timescale of the pump pulse duration), which then decays due to stimulated and spontaneous emission; this gain step must lead to some modulation in the laser output and is thus a limiting factor that we can quantify as follows. In steady-state, the average gain must equal the round trip loss, which in the present case is 4.95%. We can estimate the gain step before and after the arrival of a pump pulse using the equation given in [14]:

$$\Delta G = \frac{1}{2} r (T_{opc} + L) \frac{1}{R_{pump} \cdot \tau} \tag{5}$$

where *r* is the ratio of the pump power to the threshold value. For the parameters given in Table 1 for Ce:LiCAF, a laser threshold of 1.37 W, and assuming single pass pumping, we predict a gain step of 5.1%; for the case of 70% and 21% of the total pump power being absorbed in two temporally-separated events, the bigger of the two gain steps is now $\Delta G = 3.2\%$. We can estimate then that the lowest possible modulation of the laser intensity consistent with the variations in the laser field that this pulsed pumping must create is ± 1.6%. This represents a lower limit to the modulation that might optimally be achieved.

5. Conclusion

We have analyzed the behavior of solid-state lasers pumped synchronously and asynchronously by a mode-locked pump laser. As the cavity length changes, we find regions of rational-harmonic mode-locking interspersed by regions of continuous laser output. Numerical modelling for an ultraviolet Ce:LiCAF laser system provides an understanding of the fast dynamics for mode-locked pumped lasers, and enables us to predict the output behavior of the system for various cavity lengths, input powers and other parameter changes. The agreement between the measured and simulated data over a wide range of laser cavity lengths gives confidence that the model predictions are valid. Experimentally we observed rational-harmonic mode-locking of a Ce:LiCAF laser at harmonics up to 14/5, corresponding to a pulse repetition frequency of 1.103 GHz. This represents the highest pulse repetition frequency yet reported for a Ce:LiCAF laser. This same laser is predicted numerically to operate mode-locked at much higher rational harmonics such as 68/23 which corresponds to a pulse repetition frequency of 5.3 GHz. We find that the cavity length of the laser can also be tuned to avoid resonances with rational harmonics, resulting in continuous laser output. For our experimental Ce:LiCAF laser, this output had intensity modulations at the 1% level for detection frequencies below 1 GHz, and is predicted to have 4% modulation for faster timescales. While our approach is clearly not suited for generating single-longitudinal mode CW laser output, we believe that mode-locked-pumped CW lasers will nevertheless be suitable for many applications of CW light.

Acknowledgments

B. Wellmann acknowledges support from Macquarie University through an International Macquarie University Excellence Scholarship. The authors also acknowledge the support of an Australian Research Council Discovery Grant for this work (DP110102754).

Letter Vol. 40, No. 13 / July 1 2015 / Optics Letters 3065

Optics Letters

Linewidth narrowing of a tunable mode-locked pumped continuous-wave Ce:LiCAF laser

BARBARA WELLMANN,* ONDREJ KITZLER, DAVID J. SPENCE, AND DAVID W. COUTTS

MQ Photonics Research Centre, Department of Physics and Astronomy, Faculty of Science and Engineering, Macquarie University, New South Wales 2109, Australia

**Corresponding author: barbara.wellmann@mq.edu.au*

Received 23 April 2015; revised 3 June 2015; accepted 3 June 2015; posted 4 June 2015 (Doc. ID 239672); published 23 June 2015

We report birefringent tuning using single and multiple magnesium fluoride (MgF_2) Brewster tuning plates in a mode-locked pumped continuous-wave Ce:LiCAF laser. Depending on the thickness of the MgF_2 plates used, continuous tuning over a range of up to 13 nm from 284.5 to 297.5 nm with a full width at half-maximum linewidth of 14 pm (50 GHz) was achieved. By combining MgF_2 plates with etalons, the linewidth of the laser was narrowed down to 0.75 pm (2.7 GHz). This generated narrowband output is suitable for many applications in spectroscopy, cold-atom manipulation, and sensing.

OCIS codes: (140.3580) Lasers, solid-state; (140.3600) Lasers, tunable; (140.3610) Lasers, ultraviolet.

http://dx.doi.org/10.1364/OL.40.003065

Narrowband tunable ultraviolet (UV) lasers are needed for applications in spectroscopy, cold-atom manipulation, and sensing. Typically, tunable UV laser output is obtained by using nonlinear optical processes (harmonic and sum-frequency generation) to frequency up-convert the output from visible or infrared tunable lasers. For continuous wave (CW) sources however, the nonlinear frequency conversion is inefficient and requires complex resonant enhancement cavities [1–3]. An alternative approach to obtain CW output in the UV is to use a laser medium, which itself operates directly in the ultraviolet. Cerium (Ce)-doped fluoride lasers do just that; they produce output tunable in the 285 to 315 nm spectral range [4]. We have recently shown that Ce^{3+}:$LiCaAlF_6$ (Ce:LiCAF) lasers can be operated as mode-locked [5] and CW sources [6]. In this Letter, we now report narrowband tunable operation of a chopped continuous-wave Ce:LiCAF laser.

Ce:LiCAF lasers are all-solid-state tunable UV lasers that are well established in the nanosecond-pulse regime, offering broad tunability and efficient operation [7–9]. Conveniently, Ce:LiCAF can be pumped by the fourth harmonic of neodymium (Nd)-doped lasers at 266 nm, which is well matched to the peak of the main absorption band. This route to tunable UV is thus based on frequency quadrupling of a high power, high beam quality, fixed wavelength source and is used to pump a Ce:LiCAF laser, which provides wavelength tunability. Lasing occurs on the $5d \rightarrow 4f$ transition in Ce^{3+}, which has an upper state lifetime of 25 ns [10]. This lifetime is of the same order as the inter-pulse interval for a typical 80 MHz mode-locked solid-state laser, and so mode-locked lasers are also potentially useful as pump sources. We have indeed shown that a frequency quadrupled 80 MHz mode-locked Nd laser can efficiently pump a Ce:LiCAF laser [5,6,11], with the advantage that the peak power of a mode-locked 1064 nm laser allows efficient frequency quadrupling to 266 nm without needing a resonant enhancement cavity. The Ce:LiCAF laser system can either generate short laser pulses with pulse repetition rates up to 1.10 GHz when setup for rational-harmonic mode-locking or generate CW output when pumped asynchronously [6,11]. The transition between mode-locked and CW behavior can be achieved easily by adjusting the length of the laser cavity. In [11] we discussed the dynamics of this laser system showing that using a mode-locked pump laser to generate CW laser output inevitably leads to steps in the gain and hence to a residual intensity modulation. Our reported CW laser output at 290 nm features a residual modulation in the order of only 1% for frequencies below 1 GHz and 4% on faster timescales. Due to this unavoidable residual modulation we do not expect the laser to run on a single longitudinal mode; however, we show here that it is still possible with this configuration to obtain narrowband tunable output that is suitable for many applications.

Figure 1 shows a schematic of the laser cavity. The setup is similar to that described in [6] and [11]. The pump laser was a 78.75 MHz frequency quadrupled $Nd:YVO_4$ laser. In order to avoid thermal effects in the β-barium borate (BBO) crystal used for the second frequency doubling stage, the 1064 nm pump light was chopped with a duty cycle of 1/12, passing 400 µs long bursts of mode-locked 23 ps pulses every 4.8 ms. Note that all powers are given as the average power during the 400 µs chopper opening time; the average powers over the full chopper cycle therefore are 1/12 of the stated powers. The 1.25 mm long Brewster cut 3.5% Ce-doped LiCAF crystal was placed in the focal position of a three-mirror cavity with the c axis perpendicular to the propagation direction and in the horizontal plane. The single-pass absorption at 266 nm

0146-9592/15/133065-04$15/0$15.00 © 2015 Optical Society of America

3066 Vol. 40, No. 13 / July 1 2015 / *Optics Letters* Letter

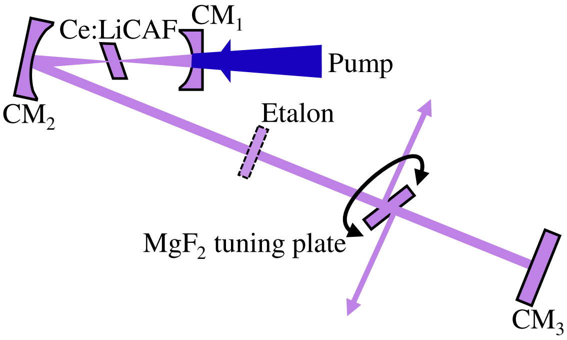

Fig. 1. Schematic of the Ce:LiCAF laser cavity. CM_1, dichroic input coupling cavity mirror with a radius of curvature (ROC) = 5 cm; CM_2, HR cavity mirror with ROC = 10 cm; CM_3, HR plane cavity mirror. The MgF_2 tuning plate is placed in the long cavity arm close to Brewster's angle and is simultaneously used as an output coupler. For further linewidth narrowing an uncoated etalon is inserted close to normal incidence in the long arm of the cavity.

of this crystal was measured to be 70% and the single-pass loss at 290 nm was 0.7%. The laser cavity was set up as a three-mirror resonator with a folding angle of 12° to compensate the astigmatism introduced by the Brewster-angle cut Ce:LiCAF crystal [12]. In order to keep the cavity losses at a minimum, all three cavity mirrors were custom coated for minimum absorption and transmission (coated by Advanced Thin Film). Using these mirrors and with careful alignment, most of the 30% residual pump power could be returned to the crystal after being back reflected by the high-reflective (HR) cavity mirrors for a second absorption pass to improve the laser efficiency.

To achieve CW output with minimal residual modulation, the cavity length was set to 0.754 m, which equals the pump cavity length $l_{pump} \times 0.3964$ and corresponds to a mismatch of 120 mm from the third harmonic of the pump cavity length [11]. The build-up time for the CW lasing with this configuration was typically under 20 µs, so that the laser operated in steady-state for most of the 400 µs chopper opening time. The free running laser with no tuning element and a nonbirefringent output coupler (a 4 mm thick UV-grade silica plate at close to Brewster's angle) in the long cavity arm produced a maximum output power of 288 mW when pumped with 2.80 W of 266 nm light (recall that all powers are the average powers during the open period of the chopper). The slope efficiency for CW operation was 20% and the laser threshold was 1.37 W, which is in good agreement with the theoretical values determined in [13]. The free running wavelength was 289.5 nm with a full width at half-maximum (FWHM) linewidth of 0.2 nm (see [11] for a detailed description).

For nanosecond cerium lasers, tuning can be achieved by injection seeding [14] or Brewster prisms, with possible additional line narrowing using etalons [8,9]. In [6] we already report tuning of a CW Ce:LiCAF laser using a Brewster prism over a range of 9.5 nm from 285.8 to 295.3 nm. The FWHM linewidth was 0.2 nm at around 291 nm and was narrower toward the extremes of the tuning range (0.1 nm at 286 nm and at 295 nm). However, tuning with a Brewster prism has the disadvantage of preventing double-pass pumping of the crystal. This problem could be solved by replacing the HR CM_2 with a dichroic mirror, except that the loss for $\lambda = 290$ nm of the dichroic coating $L_{DC} = 0.45\%$ is higher than the loss of the HR coating $L_{HR} = 0.2\%$, hence a setup with two dichroic mirrors would involve increasing the total cavity loss significantly with corresponding loss of laser performance. Using birefringent tuning instead of prism tuning allows at least part of the unabsorbed single-pass pump light to be recycled back into the laser crystal after being reflected by the HR cavity end mirror, as there is no spatial separation between the pump and the laser modes.

Birefringent tuning has been used effectively with CW dye and Ti:sapphire lasers in the past. In the visible or infrared, most commonly quartz plates are used as birefringent tuning filters [15]. To ensure a single tuning peak within the broad gain of Ce:LiCAF in the UV (280 to 315 nm), very thin quartz plates with thicknesses below 200 µm would be required. In this spectral region, magnesium fluoride (MgF_2) has greater birefringence and lower dispersion than quartz, and thus is the better alternative. The calculated transmission curves for a 250 µm MgF_2 Brewster plate and a 250 µm SiO_2 Brewster plate are plotted in Fig. 2(a) in addition to the approximated gain curve for Ce:LiCAF.

For birefringent tuning, an MgF_2 plate was inserted in the long cavity arm at close to Brewster's angle. The tuning plate also acted as an output coupler. In Fig. 3 tuning curves for the

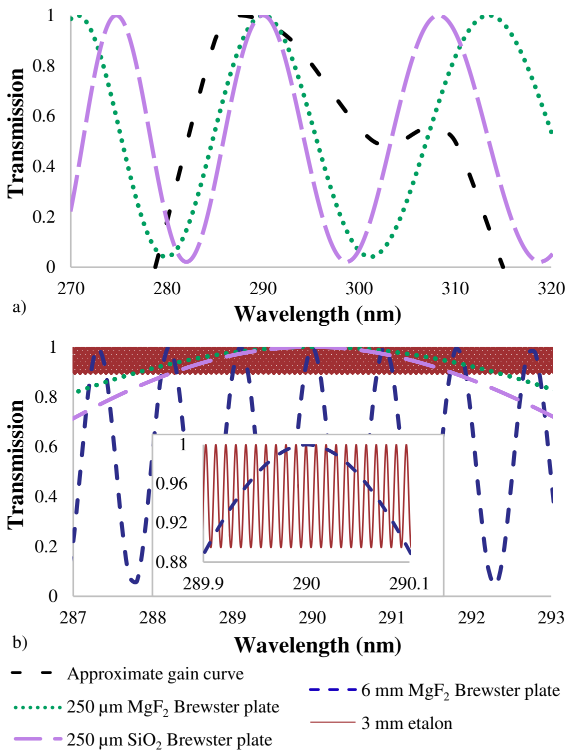

Fig. 2. (a) Calculated transmission of 250 µm birefringent MgF_2 and SiO_2 Brewster tuning plates and the approximated gain curve for Ce:LiCAF. (b) Calculated transmission for the same 250 µm MgF_2 and SiO_2 plates, a 6 mm MgF_2 Brewster tuning plate, and a 3 mm uncoated etalon at normal incidence.

Letter Vol. 40, No. 13 / July 1 2015 / Optics Letters 3067

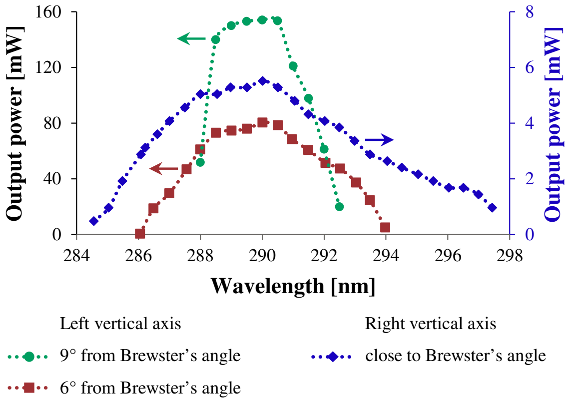

Fig. 3. Tuning curves using a single 250 μm thick birefringent MgF_2 plate at different output coupling angles.

Ce:LiCAF laser with a single 250 μm thick birefringent MgF_2 plate at different output coupling angles are plotted. The free spectral range of the 250 μm thick tuning plate was calculated to be 24 nm. For low output coupling with the plate very close to Brewster's angle, continuous tuning over a range of 13 nm from 284.5 to 297.5 nm with a maximum output power of 6 mW was achieved. For higher output coupling the tuning range narrowed, but the maximum output power increased. With the tuning plate at 9° from Brewster's angle, maximum output power was 154 mW and the tuning range spanned from 288.2 to 292.5 nm.

We investigated the linewidth of the laser output for a range of different tuning arrangements. The output linewidth was measured using an air-spaced Fabry–Perot etalon and a UV CCD camera. An example of captured fringes for an arrangement with a 4 mm MgF_2 Brewster tuning plate and a 3 mm uncoated narrowing etalon close to normal incidence in the long arm of the laser cavity are shown in Fig. 4. Figure 4(a) shows the raw image of the fringes captured with the CCD camera. The radial intensity cross section was extracted from this image [white line plotted at the bottom of Fig. 4(a)] and then plotted on a linearized frequency scale [Fig. 4(b)]. To determine the free spectral range and FWHM linewidth, a calculated curve based on the etalon transmission function was fitted to the extracted intensity pattern. An overview of the linewidth measurement results is given in Fig. 5. When using a single 250 μm MgF_2 tuning plate, the FWHM linewidth was 14 pm. Using thicker MgF_2 plates resulted in narrower linewidths, down to 3.7 pm for a 6 mm thick MgF_2 plate. However, using a single but thicker tuning plate naturally decreased the tuning range of the laser; the free spectral range of a 6 mm thick MgF_2 Brewster plate is just 0.8 nm as illustrated in Fig. 2(b). To achieve a relatively narrow linewidth, while keeping a relatively broad tuning range, a combination of two parallel MgF_2 tuning plates was used. For tuning with a 500 μm plate and an additional 6 mm tuning plate, both at 7° from Brewster's angle, tuning from 286.8 to 293.1 nm was achieved with a linewidth of 4.3 pm. For further linewidth narrowing a 3 mm uncoated etalon was inserted close to normal incidence in the long cavity arm. The transmission curve for this etalon is also given in Fig. 2(b). A combination of a 6 mm tuning plate

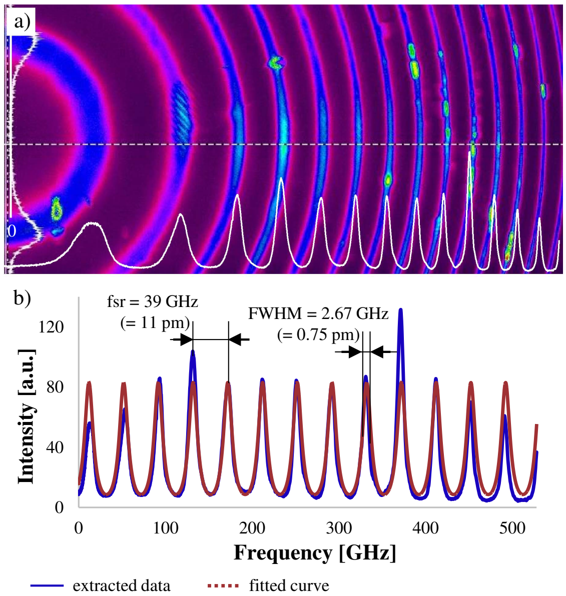

Fig. 4. Fabry–Perot fringes for the laser with a 4 mm MgF_2 Brewster tuning plate and a 3 mm etalon close to normal incidence, tuned to 290.4 nm. (a) Raw image of the fringes captured with a CCD camera. (b) Intensity pattern extracted from the raw image plotted on a linearized frequency scale and the fitted curve to match the pattern. The free spectral range (fsr) is measured to be 11 pm and the linewidth of the laser is determined to be 0.75 pm.

and a 3 mm uncoated etalon led to a FWHM linewidth of only 0.75 pm, which corresponds to a bandwidth of 2.67 GHz or 0.09 cm^{-1}. Since we did not have access to a single-frequency 290 nm light source to determine the finesse of our measurement system, it is possible that we have reached the instrument limit of the measuring etalon. (We note that achieving high finesse is difficult in the UV owing to significant absorption of mirror coatings.)

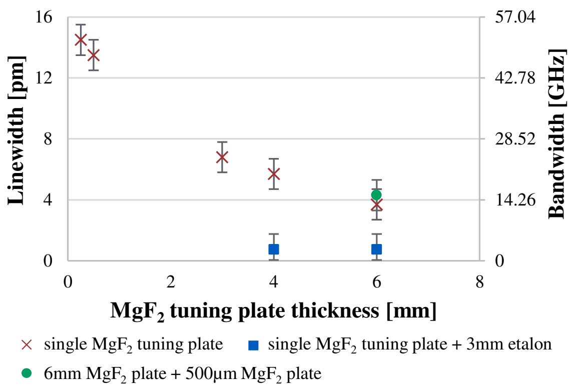

Fig. 5. Overview of the measured linewidths for tuning with a single MgF_2 plate, an MgF_2 plate plus an additional 3 mm etalon in the long cavity arm close to normal incidence and two parallel MgF_2 plates (6 mm and 500 μm) close to Brewster's angle.

Since the laser is pumped with an 80 MHz pulsed pump source, there are, as mentioned, unavoidable gain steps that continually create small intensity steps associated with each pump pulse [6,11]. When narrowing the linewidth of the laser by using thicker MgF_2 tuning plates and etalons, the power in the higher noise frequencies associated with this modulation can be suppressed but not eliminated, imposing a limit to the achievable minimum linewidth. Our measured bandwidth of 2.67 GHz may come close to this limit: The longitudinal mode spacing for the 0.75 m long cavity is 0.20 GHz, which means there are only about 13 longitudinal modes oscillating in the CW Ce:LiCAF laser.

In conclusion we showed that birefringent tuning using single or multiple MgF_2 plates is the preferred alternative to prism tuning in Ce:LiCAF lasers producing broader tunability and narrower linewidths. By combining the MgF_2 tuning plates with etalons, the linewidth of the laser can be narrowed down to 0.75 pm. These results are promising and suggest that single frequency operation will be achieved with CW pumped CW Ce lasers, although it will likely be necessary to move to a ring architecture to avoid spatial hole burning.

Australian Research Council (ARC) (DP110102754); Macquarie University.

REFERENCES

1. J. I. Kim and D. Meschede, Opt. Express **16**, 10803 (2008).
2. K. Devi, S. C. Kumar, and M. Ebrahim-Zadeh, Opt. Express **21**, 24829 (2013).
3. C. E. Wagstaff and M. H. Dunn, J. Phys. D **12**, 355 (1979).
4. D. W. Coutts and A. J. S. McGonigle, IEEE J. Sel. Top. Quantum Electron. **QE-40**, 1430 (2004).
5. E. Granados, D. W. Coutts, and D. J. Spence, Opt. Lett. **34**, 1660 (2009).
6. B. Wellmann, D. J. Spence, and D. W. Coutts, Opt. Lett. **39**, 1306 (2014).
7. D. Alderighi, G. Toci, M. Vannini, D. Parisi, S. Bigotta, and M. Tonelli, Appl. Phys. B **83**, 51 (2006).
8. S. V. Govorkov, A. O. Wiessner, T. Schroder, U. Stamm, W. Zschocke, and D. Basting, Adv. Solid State Lasers **19**, 2 (1998).
9. D. J. Spence, H. Liu, and D. W. Coutts, Opt. Commun. **262**, 238 (2006).
10. C. D. Marshall, J. A. Speth, S. A. Payne, W. F. Krupke, G. J. Quarles, V. Castillo, and B. H. T. Chai, J. Opt. Soc. Am. B **11**, 2054 (1994).
11. B. Wellmann, D. Spence, and D. Coutts, Opt. Express **23**, 4441 (2015).
12. H. W. Kogelnik, E. P. Ippen, A. Dienes, and C. V. Shank, IEEE J. Quantum Electron. **QE-8**, 373 (1972).
13. D. Alderighi, G. Toci, M. Vannini, D. Parisi, and M. Tonelli, Opt. Express **13**, 7256 (2005).
14. M. A. Dubinskii, K. L. Schepler, R. Y. Abdulsabirov, and S. L. Korableva, J. Mod. Opt. **45**, 1993 (1998).
15. D. R. Preuss and J. L. Gole, Appl. Opt. **19**, 702 (1980).

B

Conference Presentations

1. B. Wellmann, S.P. Stark, D.J. Spence, and D.W. Coutts, "Mode-Locked Deep UV Lasers Based on Ce:LiCAF", IONS - KOALA 2012 (International OSA Network of Students - Conference on Optics, Atoms and Laser Applications),2. - 7. December 2012, Brisbane, Australia, Poster presentation

2. B. Wellmann, S.P. Stark, D.J. Spence, and D.W. Coutts, "Mode-Locked Deep UV Lasers Based on Ce:LiCAF", 20th Congress of the Australian Institute of Physics (AIP), 9. - 13. December 2012, Sydney, Australia, Poster presentation

3. B. Wellmann, D.J. Spence, and D.W. Coutts, "Tunable Deep-UV Laser Based on Ce:LiCAF", Australian and New Zealand Conference on Optics and Photonics (ANZCOP) 2013, 7. - 12. December 2013, Fremantle, Australia, Oral presentation

4. B. Wellmann, O. Kitzler, D.J. Spence, and D.W. Coutts, "Tunable Continuous Wave Ultraviolet Cerium LiCAF Lasers", Advanced Solid State Lasers (ASSL) 2014, 16. - 21. November 2014, Shanghai, China, Poster presentation

5. B. Wellmann, O. Kitzler, D.J. Spence, and D.W. Coutts, "Asynchronously pumped Ce:LiCAF lasers", 21st Congress of the Australian Institute of Physics (AIP), 7. - 12. December 2014, Canberra, Australia, Oral presentation

6. B. Wellmann, O. Kitzler, D.J. Spence, and D.W. Coutts, "Birefringent Filter Tuning and Linewidth Narrowing in a Mode-Locked Pumped Deep-Ultraviolet Continuous-Wave Ce:LiCAF Laser", Conference on Lasers and Electro-Optics/Europe (CLEO/Europe) 2015, 21. - 25. June 2015, Munich, Germany, Oral presentation

7. O. Kitzler, B. Wellmann, D.J. Spence, and D.W. Coutts, "Continuous-Wave Ultraviolet Ce:LiCAF Laser", Advanced Solid State Lasers (ASSL) 2015, 4. - 9. October 2015, Berlin, Germany, Oral presentation

C

MatLab Code of Cavity Model

```
%%%%%%%%%%%%%%%%%%%%%%%%%%%%%%%%%%%%%%%%%%%%%%%%%%%%%%%%%%%%%%%%%%%%%%%%%%%%%%
%This script calculates the laser field in a z-folded 3 mirror laser      %
%resonator that is pumped by a pulsed source. The length of the laser     %
%resonator can be set to different lengths in order to mismatch the cavity%
%round trip time from the pump round trip time to achieve asynchronous    %
%pumping. The laser output can be plotted over multiple round trip times  %
%and can also be shown "filtered" (as seen when using the measurement     %
%tools available in the lab (ns-photodiode and 2GBit/s oscilloscope)).    %
%                                                                          %
%Features of the simulation:                                               %
%The laser resonator is divided into elements and the laser crystal sweeps%
%through the elements. Parallel to the "main" crystal, a "second crystal",%
%that simulates the backwards pumping of the crystal, and the output      %
%coupler are sweeping through the cavity.                                  %
%                                                                          %
%                                                                          %
%To simulate a realistic initialisation of the lasing, the pump is ramped %
%up and the initial cavity field is set up as an exponential decay with a %
%step up at the output coupler position.                                   %
%                                                                          %
%for the filter of the output, a convolution with the pump pulse response %
%(approximated from the measured pump pulse response in the lab) is used. %
%%%%%%%%%%%%%%%%%%%%%%%%%%%%%%%%%%%%%%%%%%%%%%%%%%%%%%%%%%%%%%%%%%%%%%%%%%%%%%

function ce_licaf_final

clear all
close all
clc
```

```
% simulation variables
N=500; % number of elements the resonator is divided into
number_loops=2500; %number of roundtrip times that are simulated
plot_start=2000; % number of roundtrips after which data is collected for the plots
%(should be set at a number after which steady state is reached). Must obviously be
%smaller than number loops.
plot_time=15; % number of roundtrips the laser output is displayed over in the figure

%plotting/calculation options - choose as little as needed, otherwise the simulation
%gets reeeeeaaaaaally slow
slope_threshold_paper=0; %if slope and threshold should be calculated (using the
%equations used in the paper) set to 1
plot_every_round_trip=0; %if output should be plotted "live" every round trip, set to 1
plot_mulit_rt=1; %if multi-round trip output should be plotted every time the trigger
%goes off, set to 1
sig_val_unfiltered=1; %if significant values for unfiltered output should be
%calculated, set to 1
plot_filtered_output=0; %if filtered output should be plotted, set to 1
plot_fluc_curve=0; %if curve of fluctuation over different resonator lengths should be
%plotted, set to 1
plot_conv=0; %if convolution function should be plotted, set to 1

%set-up variables as measured in lab
length_resonator=[ 1.28896]; %in m
pump_power_measured=[ 2.76 ]; %measured (average) pump power in W
Pfrequ=78.75*10^6; %pump frequency in Hz
Ppulse_duration=23*10^-12; %pump pulse duration in s
opc=0.025; %unitless loss of the output coupler (2.5%)
loss=0.024; %unitless loss of the cavity elements other than opc (2.4%)
dis_cry_opc=0.625; %distance between crystal and the opc in m
dis_cry_DCM1=0.05; %distance between crystal and dichroic cavity mirror 1 (the input
%coupling mirror) in m

%other system variables
lambda_pump=266*10^-9; %pump wavelength in m Ce:LiCAF: 266*10^-9, Ti:sapp: 532*10^-9
lambda_laser=290*10^-9; %laser wavelength in m Ce:LiCAF: 290*10^-9, Ti:sapp: 800*10^-9
waist=12.9; %waist of the laser field in micrometer
pump_area=pi*(waist*10^-6)^2; %pump area inside the crystal in m^2
tau=25*10^-9; %upper laser level lifetime in s Ce:LiCAF: 25*10^-9, Ti:sapp: 3.2*10^-6
sigma_em=9.6*10^-22; %emission cross section in m^-2 Ce:LiCAF: 9.6*10^-22, Ti:sapp:
%41*10^-24
sigma_esa=3.6*10^-22; %excited state absorption cross section in m^-2 Ce:LiCAF:
%3.6*10^-22, Ti:sapp:0
pump_absorption=0.7; %unit less pump absorption (70%)
overlap_eff=0.81; %pump efficiency (adjust to match slope efficiency)
trans_DCM=0.91; %transmittance of the dichroic cavity mirror (91%)
ref_index=1.41; %refractive index of the laser crystal Ce:LiCAF: 1.41, Ti:sapp: 1.76

%natural constants
c=299792458; %in m/s
h=6.62606957*10^-34; %in Js

%check how many different resonator lengths/ pump powers were entered
quantity_length_input=size(length_resonator,2);
quantity_power_input=size(pump_power_measured,2);

%pump pulse calculations
length_pump_res=(c/Pfrequ); %length of the pump pulse resonator
length_pump_pulse=(c*Ppulse_duration); %"length" of the pump pulse duration
pump_absorption_back=(1-pump_absorption)*pump_absorption; %pump absorption when pumped
%backwards ("second crystal")
pump_peak_power=ones(quantity_power_input);
syms x;
integral_pump_function=int(exp(-4*log(2)*((x-
length_pump_res/2))^2/length_pump_pulse^2)),0,length_pump_res);

%threshold and slope as calculated in paper
if slope_threshold_paper==1
```

```
    threshold_cal=pump_area*h*(c/lambda_pump)*(opc+loss)*ref_index/(2*(sigma_em-
    sigma_esa)*tau*overlap_eff*(pump_absorption+pump_absorption_back)*trans_DCM);
    slope_cal=100*overlap_eff*(pump_absorption+pump_absorption_back)*trans_DCM*
    (lambda_pump/lambda_laser)*(opc/(opc+loss))*((sigma_em-sigma_esa)/sigma_em);
end

%since the filter has a rise time, later some elements have to be cut off
%the output array (and other arrays). Therefore - in order to display the number of
%chosen round trip times - it is needed to add on some "dummy" elements to the
%plot_time that can be cut off later
plot_time_cal=plot_time+6;

%definition of dummy arrays to reserve space for later used large arrays
%(that otherwise would change size after every loop)
output_power_y=zeros(quantity_power_input,N); %array for power output
output_power_y_figure=zeros(quantity_power_input,N*plot_time_cal); %dummy array for
%plot of multiple roundtrips (before cutting the rise time)
output_power_y_figure2=zeros(quantity_power_input,N*(plot_time)); %dummy array for plot
%of multiple roundtrips (after cutting the rise time)dummy arrays for fluctuation
%calculation
overall_I_mean=ones(quantity_power_input);
overall_I_max=ones(quantity_power_input);
overall_I_min=ones(quantity_power_input);
overall_Fluc=ones(quantity_power_input);
mean_overall_I_mean=ones(quantity_power_input);
mean_overall_I_max=ones(quantity_power_input);
mean_overall_I_min=ones(quantity_power_input);
mean_overall_Fluc=ones(quantity_power_input);
output_Fluc=ones(quantity_length_input);

%constants/dummy arrays that are needed for the convolution
time_conv=14.8*10^-9; %length of the convolution function in s
length_conv=time_conv*c; %length of the convolution function in m

%constantes that are used in loops
a=length_pump_res/integral_pump_function;
b=number_loops/10;
d=-4*log(2);
e=length_pump_res/2;
f=length_pump_pulse^2;
g=trans_DCM*pump_absorption*overlap_eff;
j=h*(c/lambda_pump)*pump_area*ref_index;
k=sigma_em/(h*(c/lambda_laser));
m=sigma_em-sigma_esa;
n=pump_area*ref_index*opc;
o=opc+loss;
p=3*N+1:N*(plot_time_cal-3);

for count_length_input=1:quantity_length_input
    %this loop works through the different resonator lengths that were preset
    x_axis=linspace(0,length_resonator(count_length_input),N); %deviding a "x-axis" (in
    %m) into elements
    time_x=(x_axis/c); %x-axis in s
    delta_x=length_resonator(count_length_input)/N; %length (in m) of one element
    dis_cry_opc_index=round(dis_cry_opc/delta_x); %distance between the crystal and the
    %opc in number of elements
    dis_cry2=length_resonator(count_length_input)-2*dis_cry_DCM1; %distance between the
    %crystal when pumped forwards and when pumped backwards in m
    dis_cry2_index=round(dis_cry2/delta_x); %distance between the crystal when pumped
    %forwards and when pumped backwards in number of elements
    output_power_x=linspace(0,(length_resonator(count_length_input)-delta_x)*10^9/c,N);
    %x-axis of the output plot (for a single roundtrip) -> time in ns
    output_power_x_multiRT=linspace(0,((length_resonator(count_length_input)*
    plot_time)-delta_x)/c,N*plot_time); %x-axis of the output plot (for multiple
    %roundtrips) -> time in s
    output_power_x_multiRT_ns=linspace(0,((length_resonator(count_length_input)*
    plot_time)-delta_x)*10^9/c,N*plot_time); %x-axis of the output plot (for multiple
    %roundtrips)-> time in ns
```

```
store_dummy=ones(1,N*(plot_time)); %dummy array for the output that will be stored
%creating the convolution function
number_elements_conv=4*round((length_conv/delta_x)/4); %number of elements the
%convolution function is long (one element has the same length as one element of
%the resonator)
time_conv_x=linspace(0,time_conv,number_elements_conv); %x-axis for the convolution
%function
conv_x_function=zeros(number_elements_conv,1); %dummy_array for the convolution
%function
conv_x_function_original=zeros(number_elements_conv,1); %dummy_array for the
%convolution function
for count=1:number_elements_conv/4 %writing the first hump of the convolution
%function
   conv_x_function_original(count)=10.5931284*sin(0.87373312*10^9*time_conv_x
   (count))*exp(-time_conv_x(count)*10^9/2.5894032);
end
for count=number_elements_conv/4+1:number_elements_conv/2 %writing the second hump
   %of the convolution function
    conv_x_function_original(count)=200*sin(0.881*10^9*time_conv_x(count))*exp(-
    time_conv_x(count)*10^9/0.8);
end
conv_x_function_original=conv_x_function_original/sum(conv_x_function_original);
%normalizing the convolution function
conv_x_function(number_elements_conv/2+1:number_elements_conv)=conv_x_function
_original(1:number_elements_conv/2); %conv_function is the shifted sine function
%with the maximum of the sine in the middle of the resonator length

if plot_conv==1
    figure (1) %plot of the convolution function
    plot(time_conv_x*10^9,conv_x_function);
    xlabel('time [ns]');
    xlim([0 14.8]);
end

%trigger - the multiple roundtrip time plot is triggered by the
%incomming pump pulse
trigger=0; %initial value for trigger
trigger_count=0; %not really needed for simulation, just in case we want to know
%how many times the trigger was activated
plot_number=zeros(quantity_power_input); %not really needed for simulation, just in
%case we want to know how many times the output was plotted (the number of plots
%the averaged output was averaged over)
trigger_start=length_pump_res/2-delta_x; %number of element in which the pump pulse
%was seen by the crystal

%constants used in this loop (resonator length dependent)
l=delta_x/c;
q=((length_resonator(count_length_input)*(plot_time-1))/c)*10^9;

for count_power_input=1:quantity_power_input
    %this loop works through the different preentered pump power values
    inversion=0; %start value of the inversion
    %set up a self-consistent initial cavity field with exponential decay
    alpha = -1*log(1-opc-loss)/length_resonator(count_length_input);
    intensity_x=ones(1,N);
    for r=1:N
        if r<(1+dis_cry_opc_index)
            intensity_x(r)=exp(-alpha*r*delta_x);
        else
            intensity_x(r)=exp(-alpha*r*delta_x)/(1-opc-loss);
        end
    end

    %calculation of the pulse peak power
    pump_peak_power_syms=pump_power_measured(count_power_input)*a;
    pump_peak_power(count_power_input)=double(pump_peak_power_syms);

    for loops=1:number_loops %loops until preentered number of loops (=roundtrip
```

```
%times) is reached

    for crystal_index=1:N
        %this loop is the heart of the simulation. Here the crystal (and the
        %opc and the "second crystal") is looped through the elements of the
        %resonator and the inversion and cavity field are calculated for each
        %element.
        if loops<b %this loop ramps up the pump power
            ramp=((loops+crystal_index/N)/b)^2;
        else
            ramp=1;
        end

        %position of the crystal when pumped backwards
        crystal_index_2=mod_new(crystal_index-dis_cry2_index+1,N); %position of
        %the crystal when pumped backwards, dependened on position of the
        %crystal, the length of the resonator and the predefined distance
        %between the crystal and the dichroic cavity mirror 1

        %1. pump the crystal forwards
        %look where the crystal is in regards to the pump function
        crystal_pump=crystal_index*delta_x + (loops-1)*length_resonator
        (count_length_input);
        crystal_pump=mod_new(crystal_pump,length_pump_res);
        pump_x_1=ramp*pump_peak_power(count_power_input)*exp(d*(crystal_pump -
        e)^2/f);

        %2. pump the crystal backwards
        %look where the crystal is in regards to the pump function
        crystal_pump_2=crystal_index_2*delta_x + (loops-
        2)*length_resonator(count_length_input);
        crystal_pump_2=mod_new(crystal_pump_2,length_pump_res);
        pump_x_2=ramp*pump_peak_power(count_power_input)*exp(d*(crystal_pump_2
        - e)^2/f);

        %3. pump crystal if it is in a position where the pump pulse function
        %is larger than zero
        inversion_new=inversion + ((pump_x_1*g+pump_x_2*pump_absorption_back*
        overlap_eff)/j - inversion*(intensity_x(crystal_index)+intensity_x(
        crystal_index_2))*k - inversion/tau)*l;
        %gain
        %add intensities of crystal at forwards and backwards pumping positions
        intensity_x_total_old=intensity_x(crystal_index)+intensity_x
        (crystal_index_2);
        %gain for total intensity
        intensity_x_total_new=intensity_x_total_old + m *intensity_x_total_old
        *inversion;
        %split total intensity into intensity at forward and backwards pumping
        %positions

        intensity_x(crystal_index)=intensity_x_total_new*intensity_x
        (crystal_index)/intensity_x_total_old +inversion*10^-16;  %added in
        %spontaneous emission here and below, not at line above.
        intensity_x(crystal_index_2)=intensity_x_total_new*intensity_x
        (crystal_index_2)/intensity_x_total_old +inversion*10^-16;

        inversion=inversion_new; %set inversion as inversion_new to start with
        %inversion_new in next loop

        %loss at opc position
        opc_index=mod_new(crystal_index+dis_cry_opc_index,N); %position of the
        %opc, dependened on position of the crystal and the predefined distance
        %between the crystal and the opc
        output_power_y(count_power_input,crystal_index)=intensity_x
        (opc_index)*n; %this is our output off the opc
        intensity_x(opc_index)=intensity_x(opc_index) - intensity_x
        (opc_index)*o; %intensity inside the cavity is reduced by the output
```

```
    %trigger - here the trigger is set to 1 whenever a pump pulse arrives
    %and the output is not currently already being recorded for a multiple-
    %roundtrip plot
    if loops>plot_start && crystal_pump>=trigger_start && crystal_pump<=
     length_pump_res/2&& trigger==0
       trigger=1;
       trigger_count=trigger_count+1;
       trigger_element=crystal_index;
    end

end

if plot_every_round_trip==1 %output is plotted "live" every roundtrip time,
 %if option was chosen initially
    if mod(loops,10)==1
        set(figure(count_power_input^2),'Position',[50 570-count_power_
        input^9 600 400]);
        figure (count_power_input^2)
        plot(output_power_x,output_power_y(count_power_input,:));
        xlim([0 (length_resonator/c)*10^9]);
        xlabel('time [ns]');
        drawnow;
    end
end

%start recording data (from as many roundtrip times as predefined), when
%trigger was set to 1
if trigger == 1
    trigger=trigger+1;
    output_power_y_figure(count_power_input,1:N-trigger_element+1)=
    output_power_y(count_power_input,trigger_element:N); %record first
    %roundtrip output after trigger went off
elseif trigger>1 && trigger < plot_time_cal %continue recording until
    %plot_time_cal is reached
    trigger=trigger+1;
    output_power_y_figure(count_power_input,(trigger-1)*N+2-
    trigger_element:N*trigger-trigger_element+1)=output_power_y(count_power
    _input,1:N);
elseif trigger == plot_time_cal %stop recording when plot_time_cal is
    %reached
    output_power_y_figure(count_power_input,(trigger-1)*N+2-
    trigger_element:N*(trigger-1))=output_power_y(count_power_input
    ,1:trigger_element-1);
    plot_number(count_power_input)=plot_number(count_power_input)+1;
    trigger=0;

    %convolution
    convolved_output(count_power_input,:)=conv(output_power_y_figure
   (count_power_input,:),conv_x_function,'same'); %the pump (one round
    %trip) is convolved with the convolution function

    %cut off the filter build-up time
    output_power_y_figure2(count_power_input,:)=output_power_y_figure
    (count_power_input,p); %unfiltered output must be cut as well, so that
    %the length of the unfiltered output matches the length of the filtered
    %output (otherwise the two can't be plotted in the same plot).
    filter_output2(count_power_input,:)=convolved_output(count_power_
    input,p); %cut filtered output
    if plot_mulit_rt==1 %the multi rt data is plotted every time it is
       %recorded, if option was chosen initially.

        figure (1)
        plot(output_power_x_multiRT_ns,output_power_y_figure2
        (count_power_input,:),output_power_x_multiRT_ns,real(filter_output2
        (count_power_input,:)),'*r');
        xlim([0 q]);
        %ylim([0 1]);
        xlabel('time [ns]');
```

```
                drawnow;
                assignin('base','unfiltered_output1',output_power_y_figure2(1,:));
                assignin('base','filtered_output1',filter_output2(1,:));
            end
            store_dummy=vertcat(store_dummy,filter_output2(count_power_input,:));
            %every filtered
            %output is stored in this matrix (every time the data is recorded, a
            %new line is created)
        end
    end
    trigger=0; %trigger is set to 0 again, so that it can be set to 1 again in the
    %next loop when a pump pulse comes in.

    %calculate significant values for unfiltered output (if this option is chosen
    %initially)
    if sig_val_unfiltered==1
        overall_I_mean(count_power_input)=mean(output_power_y_figure2
       (count_power_input,:));
        overall_I_max(count_power_input)=max(output_power_y_figure2
       (count_power_input,:));
        overall_I_min(count_power_input)=min(output_power_y_figure2
       (count_power_input,:));
        overall_Fluc(count_power_input)=((overall_I_max(count_power_input)-
        overall_I_min(count_power_input))/(overall_I_max(count_power_input)
        +overall_I_min(count_power_input)))*100;
    end

end
if quantity_power_input==1 %if just one pump power is entered, (almost) all lines
  %in the store are averaged to get the averaged output. The first 12 lines are cut
  %off because of build up time.
    store_output(1,:)=mean(store_dummy(12:end,:));
    if plot_filtered_output==1 %if option was activated the averaged output is
     %plotted
        set(figure (300),'Position',[1300 569 600 400]);
        figure (300)
        plot(output_power_x_multiRT_ns,real(store_output(1,:)));
        xlim([0 q]);
        xlabel('time [ns]');
        drawnow;
    end
elseif quantity_power_input==2 %if there were 2 pump powers entered, the store is
     %split accordingly and than the averages are calculated
    store_output(1,:)=mean(store_dummy(12:plot_number(1)+1,:));
    store_output(2,:)=mean(store_dummy(plot_number(1)+12:plot_number(1)+
    plot_number(2)+1,:));
    if plot_filtered_output==1 %if option was activated the averaged outputs are
      %plotted
        set(figure (300),'Position',[1300 569 600 400]);
        figure (300)
        plot(output_power_x_multiRT_ns,real(store_output(1,:)));
        xlim([0 q]);
        xlabel('time [ns]');
        drawnow;
        set(figure (6),'Position',[1300 58 600 400]);
        figure (6)
        plot(output_power_x_multiRT_ns,real(store_output(2,:)));
        xlim([0 q]);
        xlabel('time [ns]');
        drawnow;
    end
end

%calculate significant values for filtered output (this is possible for one or two
%entered input powers)
for z=1:quantity_power_input
    store_cal(z,:)=real(store_output(z,1:N*(plot_time-1)));
    mean_overall_I_mean(z)=mean(store_cal(z,:));
    mean_overall_I_max(z)=max(store_cal(z,:));
```

```
        mean_overall_I_min(z)=min(store_cal(z,:));
        mean_overall_Fluc(z)=((mean_overall_I_max(z)-mean_overall_I_min(z))/
        (mean_overall_I_max(z)+mean_overall_I_min(z)))*100;
    end

    if quantity_power_input==2 %if two input powers are entered, the slope efficiency
       %and the threshold are calculated
        slope=(overall_I_mean(2)-overall_I_mean(1))/(pump_power_measured(2)-
        pump_power_measured(1));
        slope_sim=slope*100; %slope in %
        threshold_sim=-(overall_I_mean(2)-slope*pump_power_measured(2))/slope;
    end

    %%write function variables (stored in function workspace) into base workspace
    %%(uncomment the ones you want to be able to access in the base workspace)
% assignin('base','N',N);
    % assignin('base','loops',loops);
    % %assignin('base','delta_x',delta_x);
    % assignin('base','length_resonator',length_resonator);
    % %assignin('base','overall_I_max',overall_I_max);
    % %assignin('base','overall_I_min',overall_I_min);
     assignin('base','overall_I_mean1',overall_I_mean(1));
    % %assignin('base','overall_I_mean2',overall_I_mean(2));
     assignin('base','overall_Fluc1',overall_Fluc(1));
    % %assignin('base','overall_Fluc2',overall_Fluc(2));
    % assignin('base','mean_overall_I_max',mean_overall_I_max);
    % assignin('base','mean_overall_I_min',mean_overall_I_min);
     assignin('base','mean_overall_I_mean1',mean_overall_I_mean(1));
    % %assignin('base','mean_overall_I_mean2',mean_overall_I_mean(2));
     assignin('base','mean_overall_Fluc1',mean_overall_Fluc(1));
    % %assignin('base','mean_overall_Fluc2',mean_overall_Fluc(2));
    % %assignin('base','threshold_cal',threshold_cal);
    % %assignin('base','threshold_sim',threshold_sim);
    % assignin('base','pump_power_measured1',pump_power_measured(1));
    % %assignin('base','pump_power_measured2',pump_power_measured(2));
    % assignin('base','waist',waist);
    % assignin('base','trans_DCM',trans_DCM);
    % assignin('base','pump_peak_power1',pump_peak_power(1));
    % %assignin('base','pump_peak_power2',pump_peak_power(2));
    % %assignin('base','slope_sim',slope_sim);
    % %assignin('base','solpe_cal',slope_cal);
    % assignin('base','filter_var',filter_var);
    assignin('base','averaged_filtered_output',real(store_output(1,:)));
    assignin('base','x_axis_ns',output_power_x_multiRT_ns);
    % assignin('base','plot_number1',plot_number(1));
    % %assignin('base','plot_number2',plot_number(2));

    %calculated fluctuation in % for the filtered, averaged output for entered pump
    %power (1) is written in array
    output_fluc(count_length_input)=mean_overall_Fluc(1);
end
%calculations of fluctuation (if more than one resonator length was entered)
%assignin('base','Fluc',output_fluc);
diff_l=1.249135-length_resonator;
if plot_fluc_curve==1 %plot of fluc over resonator length if option selected
    figure(7)
    plot(diff_l,real(output_fluc));
end
end

function [position_output] = mod_new(position_input,length_max)
%slight variation to the existing mod function that returns the max. value instead of a
%0 when max is given
position_output = mod(position_input,length_max);
if position_output == 0
    position_output = length_max;
end
end
```

Acknowledgements

Acknowledgements commonly start with the academics advisors, but I would like to dedicate this first paragraph to you, Dennis. 4 years = 2 kids + 2 PhDs on the other side of the world. It was pretty damn hard at times, but amazingly it looks like we actually manage(d) to pull this off... Thank you for being you and for being a true partner - me being able to submit a PhD thesis at all is your achievement as much as it is mine. ♡

The other two men without whom this PhD thesis would not have been possible are my supervisors David Spence and David Coutts. I learned a lot from you and I would like to thank you for your endless patience, understanding, encouragement and support. During my PhD I watched three postdocs come and two of them go, with long stretches when there was no postdoc at all. Both Davids were always there for me throughout my whole PhD, but they especially stepped up when it was just the three of us working on the cerium project: On top of being "just" my supervisors they were my lab partners and work companions - thank you!

Over time, there were three postdocs engaged in this project: Sebastian (Paul) Stark, Teoman Gün, and Ondrej Kitzler, each of whom contributed to the project in their own way. Thanks to all of you for your input and for sharing your experiences and knowledge with me. Ondra, you are the last one standing - I am glad I didn't cause you to leave as well :) I hope you will keep the project (and the CW laser) running for a loooooong time (unchopped).

Other academics and students, who were involved in this or related projects at one point or another, include Guido Palmer, Alexander Fürbach, Fedor Gubarev, Caleb Seal, and Adam Sharp. One time I think there were even !6! people sitting in our weekly cerium meeting. Thank you all for your valuable insights and feedback.

Also thanks to Eduardo Granados. His name was mention a gazillion times in regards to the cerium project and reading his PhD thesis helped me a lot to get started. I really hope to meet him someday to finally be able to put a face to the name...

I also want to thank the rest of the MQ Photonics Research Team and my friends and office-mates at Uni. Thanks for making my PhD experience a truly fabulous and memorable time! VeRy SpEcIaL thanks go to (in order of appearance) Jana, Andy, Annie, Varun, Katya, and Tristan. I could elaborate, but I read that saying things like "Thank you for looking after me when I passed out drunk", "Thanks for organising the best Aussie-style beach weekends with BBQs and surfing sessions ever", or "Thanks for letting me use your dryer and introducing me to the West Wing when it rained for weeks non-stop" in academic acknowledgements is very unprofessional, so I won't. Just want to - professionally - send ExTrA VeRy SpEcIaL thanks to Tristan for proofreading. Wednesday will always be our day!

My PhD was funded by an iMQRES scholarship, and the project was funded by an ARC Discovery Grant (DP110102754), so I gratefully acknowledge this financial support[1].

I also want to acknowledge the support I received outside the University: Dana, my champion sister-in-law - you are a lifesaver and mega-aunty-superstar. I don't know what we would have done without you. Thank you heaps! All of my friends and family (partly in the northern hemisphere): thank you for fun times at the beach, cafés, clubs, and playgrounds and/or your visits, photos, emails, calls, texts, letters, presents, etc. etc. Even though some of you were far away physically (most of the time), you were with us emotionally and helped us to continue and to believe in ourselves.

Thanks to the staff at Gumnut Cottage, especially the Blue Room team of 2014. The positive and loving atmosphere you created made it much easier for me to leave my little baby girl "in the hands of strangers" and to continue with my PhD.

Finally I want to appreciate my wonderful children Ronja and Tom. Both were with me in the lab for 9 months each, but thankfully have not been growing third arms or similar due to extensive UV light exposure (yet)... I enjoy watching you develop and explore the world every day and am (already) extremely proud of you. Just *please* never decide to do a PhD and have kids 16000 km away from home!

[1] Although I want to state how disappointed I was to not be granted a second paid maternity leave. It is just an additional 12-weeks pay for the very few female PhD students who are giving birth a second time during their candidature, which accounts to almost nothing in the budget of the University, but does help these PhD students and their families A LOT. Especially since Macquarie declares itself to be a flagship University in regards to equity and diversity, a second paid maternity leave should be granted without any discussion.

List of Symbols and Abbreviations

α	angle
α_p	single-pass absorption
β	angle
β''	group dispersion
γ	number of times over threshold
ε	field amplitude
η_a	pump absorption
η_{CW}	continuous wave slope efficiency
η_o	overlap efficiency
η_{OPC}	output coupling efficiency
η_p	pump efficiency
η_q	quantum efficiency
θ	angle
λ	wavelength
λ_0	centre wavelength
λ_l	laser wavelength
λ_p	pump wavelength
ν	frequency
ν_0	centre frequency
ν_g	group velocity of a laser pulse
ν_l	laser frequency
ν_m	modulation frequency
ν_R	pulse repetition frequency

$\Delta\nu_c$	cavity bandwidth
$\Delta\nu_F$	minimal resolvable laser linewidth
$\Delta\nu_l$	laser linewidth
σ_{eff}	effective gain cross section
σ_{em}	emission cross section
σ_{ESA}	excited-sate absorption cross section
τ	upper laser level lifetime
τ_I	decay time of the intensity
τ_p	pulse duration
ϕ	angle
ω	angular frequency
ω_l	laser beam waist size
ω_p	pump beam waist size
A	focal area of the pump
B_{in}	incoming forward travelling beam
B_{out}	outgoing forward travelling beam
B_r	reflected forward travelling beam
B_t	transmitted forward travelling beam
c	speed of light
d	distance; plate thickness
d_s	effective distance in the sagittal plane
d_t	effective distance in the tangential plane
d_{eff}	effective nonlinearity coefficient
e_l	photon energy of the laser
e_p	photon energy of the pump
E_p	pump energy
E_{pu}	pulse energy
$E_{sat,a}$	saturation energy of a saturable absorber
$E_{sat,g}$	saturation energy of a gain medium
f	focal length
f_s	focal length in the sagittal plane

f_t	focal length in the tangential plane
F	finesse
F_{in}	incoming forward travelling beam
F_{out}	outgoing forward travelling beam
F_r	reflected forward travelling beam
F_t	transmitted forward travelling beam
FSR	free spectral range
G	gain
G_{th}	gain at threshold
ΔG	step in the gain at each pump pulse
ΔG_{sp}	single pass step in the gain
h	Planck's constant
I	intensity
I_b	background intensity
I_{CW}^{th}	continuous wave lasing threshold intensity
I_L^{OPC}	intensity of the current travelling laser field at the OPC
I_L^+	intensity of the left travelling laser field at the crystal location
I_L^-	intensity of the right travelling laser field at the crystal location
I_{max}	maximum intensity
I_{min}	minimal intensity
k_B	Boltzmann constant
l	length
l_3	cavity length of the 3^{rd} harmonic
l_{pump}	cavity length of the pump laser
Δl	cavity length mismatch from the 3^{rd} harmonic
L	loss
L_{DC}	loss of the dichroic cavity mirror coating
L_{em}	loss of the empty cavity (all mirrors)
L_{HR}	loss of the high reflective cavity mirror coating
L_{OPC}	loss introduced by the OPC
L_t	total cavity loss introduced by all mirrors and the crystal
n	refractive index

n_e	refractive index for light linearly polarized in vertical direction
n_o	refractive index for light linearly polarized in horizontal direction
N	natural number
N_i	number of inverted ions
N_{max}	maximum number of inverted ions (in steady state)
N_{min}	minimal number of inverted ions (in steady state)
N_{th}	number of inverted ions at threshold
ΔN	step in the inversion at each pump pulse
Out	laser output beam
P_{CW}^{th}	continuous wave laser threshold power
P_l	laser output power
P_p^{abs}	absorbed pump power
q	complex Gaussian beam parameter
r	radius
R	reflectivity
R_c	repetition rate of the cavity
R_l	laser beam curvature
R_{pump}	repetition rate of the pump laser cavity
R_s	reflectivity for σ-polarized light
ΔR	modulation depth of the reflectivity
t	time
t_p	pump pulse period
T	transmission
T_{DM}	transmission of the dichroic input coupling mirror
T_p	temperature
T_R	round-trip time
T_s	transfer matrix for the sagittal plane
T_t	transfer matrix for the tangential plane
x	pulse repetition rate
Δx	length mismatch
y	number of pulses in the laser cavity

AR	anti-reflective
ATF	Advanced Thin Film
BBO	low-temperature BaB_2O_4 - β-Barium borate
CB	conduction band
CC	colour centre
Ce:LaF	Ce^{3+}:LaF_3 - cerium doped lanthanum fluoride
Ce:LiCAF	Ce^{3+}:$LiCaAlF_6$ - cerium doped lithium calcium aluminium fluoride
Ce:LiLuF	Ce^{3+}:$LiLuF_4$ - cerium doped lithium lutetium fluoride
Ce:LiSAF	Ce^{3+}:$LiSrAlF_6$ - cerium doped lithium strontium aluminium fluoride
Ce:YAG	Ce^{3+}:$Y_3Al_5O_{12}$ - cerium doped yttrium aluminium garnet
Ce:YLF	Ce^{3+}:$YLiF_4$ - cerium doped yttrium lithium fluoride
CM	cavity mirror
CL	cylindrical lens
CLBO	$CsLiB_6O_{10}$ - caesium lithium borate
CPA	chirped pulse amplification
Cr:YAG	Cr^{4+}:$Y_3Al_5O_{12}$ - chromium doped yttrium aluminium garnet
CVL	copper vapour laser
CW	continuous wave
DM	dichroic mirror
ESA	excited-state absorption
FEL	free electron laser
FFT	Fast Fourier Transformation
FM	frequency modulation
FWHM	full width at half maximum
GDD	group delay dispersion
HfO_2	hafnium oxide
HR	high reflective
HWHM	half width at half maximum
HWP	half-wave plate
IBS	ion-beam sputtering
IR	infrared
KLM	Kerr-Lens mode-locking

L	lens
LBO	LiB_3O_5 - lithium triborate
M	mirror
MgF_2	magnesium fluoride
Nd:YVO	$Nd^{3+}:YVO_4$ - neodymium doped yttrium orthovanadate
OPC	output coupler
OPO	optical parametric oscillator
PMT	photomultiplier tube
Q-factor	quality factor
ROC	radius of curvature
SESAM	semiconductor saturable absorber mirror
SHG	second-harmonic generation
SiO_2	silicon dioxide
SLM	single longitudinal mode
TEM_{00}	fundamental transverse electromagnetic mode
Ti:sapphire	$Ti^{3+}:Al_2O_3$ - titanium doped sapphire
UBCM	ultraband chirped mirror
UV	ultraviolet
WGM	whispering gallery modes

List of Figures

References

[1] T. Maiman. *Stimulated optical radiation in ruby*. Nature **187**(4736), 493 (1960).

[2] G. Mourou and T. Tajima. *More intense, shorter pulses*. Science **331**(6013), 41 (2011).

[3] U. Keller. *Recent developments in compact ultrafast lasers*. Nature **424**(6950), 831 (2003).

[4] E. Granados Mateo. *Mode Locked Lasers in the Deep Ultraviolet and the Visible*. Ph.D. thesis, Macquarie University, Faculty of Science, Department of Physics & Astronomy (2010).

[5] E. Granados, D. Coutts, and D. Spence. *Mode locked deep ultraviolet Ce:LiCAF laser*. Optics Letter **34**(11), 1660 (2009).

[6] T. Andreae, W. König, R. Wynands, D. Leibfried, F. Schmidt-Kaler, C. Zimmermann, D. Meschede, and T. Hänsch. *Absolute frequency measurement of the hydrogen 1S-2S transition and a new value of the Rydberg constant*. Physical Review Letters **69**(13), 1923 (1992).

[7] M. Scheid, F. Markert, J. Walz, J. Wang, M. Kirchner, and T. Hänsch. *750 mW continuous-wave solid-state deep ultraviolet laser source at the 253.7 nm transition in mercury*. Optics Letters **32**(8), 955 (2007).

[8] H. Kumagai. *Development of a continuous-wave, deep-ultraviolet, and single-frequency coherent light source - challenges toward laser cooling of silicon*. IEEE Journal of Selected Topics in Quantum Electronics **10**(6), 1252 (2004).

[9] T. Rosenband, D. Hume, P. Schmidt, C. Chou, A. Brusch, L. Lorini, W. Oskay, R. Drullinger, T. Fortier, J. Stalnaker, S. Diddams, W. Swann, N. Newbury, W. Itano, D. Wineland, and J. Bergquist. *Frequency ratio of Al+ and Hg+ single-ion optical clocks; metrology at the 17th decimal place*. Science **319**(5871), 1808 (2008).

[10] H. Shapiro. *Practical Flow Cytometry* (Wiley Liss, New York, NY, 1994), 3rd edition ed.

[11] A. Assion, T. Baumert, M. Bergt, T. Brixner, B. Kiefer, V. Seyfried, M. Strehle, and G. Gerber. *Control of chemical reactions by feedback-optimized phase-shaped femtosecond laser pulses*. Science **282**(5390), 919 (1998).

[12] J. Valdmanis and G. Mourou. *Subpicosecond electrooptic sampling: Principles and applications*. Quantum Electronics, IEEE Journal of **22**(1), 69 (1986).

[13] T. Roberti, N. Cherepy, and J. Zhang. *Nature of the power-dependent ultrafast relaxation process of photoexcited charge carriers in II-VI semiconductor quantum dots: Effects of particle size, surface, and electronic structure*. The Journal of Chemical Physics **108**, 2143 (1998).

[14] X. Liu, D. Du, and G. Mourou. *Laser ablation and micromachining with ultrashort laser pulses*. Quantum Electronics, IEEE Journal of **33**(10), 1706 (1997).

[15] A. Rousse, C. Rischel, S. Fourmaux, I. Uschmann, S. Sebban, G. Grillon, P. Balcou, E. Förster, J. Geindre, P. Audebert, J. Gauthier, and D. Hulin. *Non-thermal melting in semiconductors measured at femtosecond resolution*. Nature **410**(6824), 65 (2001).

[16] A. Baum, P. Scully, W. Perrie, D. Liu, and V. Lucarini. *Mechanisms of femtosecond laser-induced refractive index modification of poly (methyl methacrylate)*. Journal of the Optical Society of America B-Optical Physics **27**(1), 107 (2010).

[17] W. Denk, J. Strickler, and W. Webb. *Two-photon laser scanning fluorescence microscopy*. Science **248**(4951), 73 (1990).

[18] C. Crotti, F. Deloison, D. Peyrot, M. Savoldelli, J. Legeais, F. Roger, and K. Plamann. *Wavelength optimization in femtosecond laser corneal surgery: Experimental results*. In *Proceedings of SPIE- The International Society for Optical Engineering*, vol. 7373, p. 73730J (SPIE, 2009).

[19] N. Suhm, M. Götz, J. Fischer, F. Loesel, W. Schlegel, V. Sturm, J. Bille, and R. Schröder. *Ablation of neural tissue by short-pulsed lasers: A technical report*. Acta Neurochirurgica **138**(3), 346 (1996).

[20] F. Loesel, J. Fischer, M. Götz, C. Horvath, T. Juhasz, F. Noack, N. Suhm, and J. Bille. *Non-thermal ablation of neural tissue with femtosecond laser pulses*. Applied Physics B: Lasers and Optics **66**(1), 121 (1998).

[21] C. Townes. *The first laser*. A Century of Nature: Twenty-One Discoveries that Changed Science and the World p. 107 (2003).

[22] N. Bloembergen. *From nanosecond to femtosecond science*. Reviews of Modern Physics **71**(2), 283 (1999).

[23] R. Hellwarth. *Control of fluorescent pulsations*. In *Advances in Quantum Electronics*, vol. 1, p. 334 (1961).

[24] F. McClung and R. Hellwarth. *Giant optical pulsations from ruby*. Applied Optics **1**(101), 103 (1962).

[25] F. Kneubühl and M. Sigrist. *Laser*, chap. Gaslaser (Vieweg + Teubner, Springer Science + Buisness Media, Wiesbaden, 2008), 7 ed.

[26] R. Hellwarth. *Advances in Lasers*, chap. IV Q-Modulation of Lasers, pp. 253–294 (Dekker, M., New York, 1966).

[27] B. Lengyel. *Introduction to Laser Physics* (Wiley New York, 1966).

[28] H. Haken. *Handbuch der Physik Bd. 25/2c*, chap. Laser Theory (1970).

[29] H. Haus. *Mode-locking of lasers*. Selected Topics in Quantum Electronics, IEEE Journal of **6**(6), 1173 (2000).

[30] K. Gürs and R. Müller. *Breitband-Modulation durch Steuerung der Emission eines Optischen Masers (Auskoppelmodulation)*. Physics Letters **5**(3), 179 (1963).

[31] K. Gürs, P. Grivet, and N. Bloembergen. *Beats and modulation in optical ruby-masers(ruby laser emissions modulated by changing focal length of mirror and lens)*. In *Quantum Electronics, Proceedings of the Third International Congress Paris, France, Feb. 11-15, 1963.*, 6, pp. 1113–1119 (Columbia University Press, 1964).

[32] H. Statz, C. Tang, P. Grivet, and N. Bloembergen. *Zeeman effect and nonlinear interactions between oscillating laser modes*. Quantum Electronics III pp. 469–498 (1964).

[33] M. DiDomenico. *Small-signal analysis of internal (coupling type) modulation of lasers*. Journal of Applied Physics **35**, 2870 (1964).

[34] L. Hargrove, R. Fork, and M. Pollack. *Locking of He–Ne laser modes induced by synchronous intractivity modulation*. Applied Physics Letters **5**, 4 (1964).

[35] A. Yariv. *Internal modulation in multimode laser oscillators*. Journal of Applied Physics **36**, 388 (1965).

[36] L. Siegman. *Lasers*, chap. 27 Active Laser Mode Coupling, pp. 1041–1103 (University Science Books, Mill Valley, CA, 1986).

[37] A. Seilmeier, B. Sens, K. Drexhage, and W. Kaiser. *Tunable picosecond pulses around 1.3 μm generated by a synchronously pumped infrared dye laser*. Optics Letters **8**(4), 205 (1983).

[38] W. Jiang, R. Mirin, and J. Bowers. *Mode-locked GaAs vertical cavity surface emitting lasers*. Applied Physics Letters **60**(6), 677 (1992).

[39] C. Siders, E. Gaul, M. Downer, A. Babine, and A. Stepanov. *Self-starting femtosecond pulse generation from a Ti: sapphire laser synchronously pumped by a pointing-stabilized mode-locked Nd: YAG laser*. Review of Scientific Instruments **65**(10), 3140 (1994).

[40] C. Spielmann, F. Krausz, T. Brabec, E. Wintner, and A. Schmidt. *Femtosecond pulse generation from a synchronously pumped Ti: sapphire laser*. Optics Letters **16**(15), 1180 (1991).

[41] U. Keller. *Advances in Lasers and Applications, Proceedings of the Fifty Second Scottish Universities Summer School in Physics, St. Andrews, September 1998*, chap. Laser Sources - Ultrashort Pulse Generation (Scottish Universities Summer School in Physics and Institute of Physics Publishing, Bristol and Philadelphia, 1999).

[42] L. Siegman. *Lasers*, chap. 28 Passive Mode Locking, pp. 1104–1128 (University Science Books, Mill Valley, CA, 1986).

[43] J. Fleck Jr. *Ultrashort-pulse generation by Q-switched lasers*. Physical Review B **1**(1), 84 (1970).

[44] H. Mocker and R. Collins. *Mode competition and self-locking effects in a Q-switched ruby laser*. Applied Physics Letters **7**, 270 (1965).

[45] A. DeMaria, D. Stetser, and H. Heynau. *Self mode-locking of lasers with saturable absorbers*. Applied Physics Letters **8**(7), 174 (1966).

[46] U. Keller, D. Miller, G. Boyd, T. Chiu, J. Ferguson, and M. Asom. *Solid-state low-loss intracavity saturable absorber for Nd:YLF lasers: an antiresonant semiconductor fabry-perot saturable absorber*. Optics Letters **17**(7), 505 (1992).

[47] E. Ippen, C. Shank, and A. Dienes. *Passive mode locking of the cw dye laser*. Applied Physics Letters **21**, 348 (1972).

[48] C. Shank and E. Ippen. *Subpicosecond kilowatt pulses from a mode-locked cw dye laser*. Applied Physics Letters **24**(8), 373 (1974).

[49] J. Valdmanis and R. Fork. *Design considerations for a femtosecond pulse laser balancing self phase modulation, group velocity dispersion, saturable absorption, and saturable gain*. Quantum Electronics, IEEE Journal of **22**(1), 112 (1986).

[50] R. Fork, C. Cruz, P. Becker, and C. Shank. *Compression of optical pulses to six femtoseconds by using cubic phase compensation*. Optics Letters **12**(7), 483 (1987).

[51] P. Moulton. *Spectroscopic and laser characteristics of Ti:Al_2O_3*. Journal of the Optical Society of America. B, Optical physics **3**(1), 125 (1986).

[52] Y. Ishida, N. Sarukura, and H. Nakano. *Soliton-like pulse shaping in a cw passively mode-locked Ti:Al_2O_3 laser*. In C. Harris, E. Ippen, G. Mourou, and A. Zewail, eds., *Ultrafast Phenomena VII: Proceedings of the 7^{th} international conference*, vol. 53 of *Springer Series in Chemical Physics*, p. pp 75 (Springer Verlag, Berlin, 1990).

[53] D. Spence, P. Kean, and W. Sibbett. *Sub-100 fs pulse generation from a self-modelocked titanium-sapphire laser*. In *Digest of Conference on Lasers and Electro-Optics*, p. pp 629 (Optical Society of America, Washington D.C., 1990).

[54] D. Spence, P. Kean, and W. Sibbett. *60-fsec pulse generation from a self-mode-locked Ti:sapphire laser*. Optics Letters **16**(1), 42 (1991).

[55] U. Keller, G. Thooft, W. Knox, and J. Cunningham. *Femtosecond pulses from a continuously self-starting passively mode-locked Ti:sapphire laser*. Optics letters **16**(13), 1022 (1991).

[56] F. Salin, J. Squier, and M. Piche. *Mode locking of Ti:sapphire lasers and self-focusing: a gaussian approximation*. Optics Letters **16**(21), 1674 (1991).

[57] M. Piché and F. Salin. *Self-mode locking of solid-state lasers without apertures*. Optics Letters **18**(13), 1041 (1993).

[58] G. Cerullo, S. DeSilvestri, V. Magni, and L. Pallaro. *Resonators for Kerr-lens mode-locked femtosecond Ti:sapphire lasers*. Optics Letters **19**(11), 807 (1994).

[59] G. Cerullo, S. DeSilvestri, and V. Magni. *Self-starting Kerr-lens mode locking of a Ti:sapphire laser*. Optics Letters **19**(14), 1040 (1994).

[60] U. Keller, W. Knox, and G. tHooft. *Ultrafast solid-state mode-locked lasers using resonant nonlinearities*. Quantum Electronics, IEEE Journal of **28**(10), 2123 (1992).

[61] U. Keller, K. Weingarten, F. Kartner, D. Kopf, B. Braun, I. Jung, R. Fluck, C. Honninger, N. Matuschek, and J. Aus der Au. *Semiconductor saturable absorber mirrors (SESAM's) for femtosecond to nanosecond pulse generation in solid-state lasers*. Selected Topics in Quantum Electronics, IEEE Journal of **2**(3), 435 (1996).

[62] R. Szipöcs, K. Ferencz, C. Spielmann, and F. Krausz. *Chirped multilayer coatings for broadband dispersion control in femtosecond lasers*. Optics Letters **19**(3), 201 (1994).

[63] F. Kärtner, N. Matuschek, T. Schibli, U. Keller, H. Haus, C. Heine, R. Morf, V. Scheuer, M. Tilsch, and T. Tschudi. *Design and fabrication of double-chirped mirrors*. Optics Letters **22**(11), 831 (1997).

[64] N. Matuschek, F. Kartner, and U. Keller. *Analytical design of double-chirped mirrors with custom-tailored dispersion characteristics*. Quantum Electronics, IEEE Journal of **35**(2), 129 (1999).

[65] N. Matuschek, L. Gallmann, D. Sutter, G. Steinmeyer, and U. Keller. *Back-side-coated chirped mirrors with ultra-smooth broadband dispersion characteristics*. Applied Physics B: Lasers and Optics **71**(4), 509 (2000).

[66] D. Sutter, G. Steinmeyer, L. Gallmann, N. Matuschek, F. Morier-Genoud, U. Keller, V. Scheuer, G. Angelow, and T. Tschudi. *Semiconductor saturable-absorber mirror assisted Kerr-lens mode-locked Ti:sapphire laser producing pulses in the two-cycle regime*. Optics Letters **24**(9), 631 (1999).

[67] R. Ell, U. Morgner, F. Kärtner, J. Fujimoto, E. Ippen, V. Scheuer, G. Angelow, T. Tschudi, M. Lederer, A. Boiko, and B. Luther-Davies. *Generation of 5-fs pulses and octave-spanning spectra directly from a Ti:sapphire laser*. Optics Letters **26**(6), 373 (2001).

[68] M. Nisoli, S. De Silvestri, O. Svelto, R. Szipöcs, K. Ferencz, C. Spielmann, S. Sartania, and F. Krausz. *Compression of high-energy laser pulses below 5 fs*. Optics Letters **22**(8), 522 (1997).

[69] B. Schenkel, J. Biegert, U. Keller, C. Vozzi, M. Nisoli, G. Sansone, S. Stagira, S. DeSilvestri, and O. Svelto. *Generation of 3.8-fs pulses from adaptive compression of a cascaded hollow fiber supercontinuum*. Optics Letters **28**(20), 1987 (2003).

[70] E. Matsubara, K. Yamane, T. Sekikawa, and M. Yamashita. *Generation of 2.6 fs optical pulses using induced-phase modulation in a gas-filled hollow fiber*. Journal of the Optical Society of America B **24**(4), 985 (2007).

[71] P. Paul, E. Toma, P. Breger, G. Mullot, F. Augé, P. Balcou, H. Muller, and P. Agostini. *Observation of a train of attosecond pulses from high harmonic generation*. Science **292**(5522), 1689 (2001).

[72] P. Antoine, A. L'Huillier, and M. Lewenstein. *Attosecond pulse trains using high-order harmonics*. Physical Review Letters **77**(7), 1234 (1996).

[73] P. Agostini and L. DiMauro. *The physics of attosecond light pulses*. Reports on Progress in Physics **67**, 813 (2004).

[74] C. Hönninger, R. Paschotta, F. Morier-Genoud, M. Moser, and U. Keller. *Q-switching stability limits of continuous-wave passive mode locking*. Journal of the Optical Society of America B: Optical Physics **16**(1), 46 (1999).

[75] A. Javan, W. Bennett Jr, and D. Herriott. *Population inversion and continuous optical maser oscillation in a gas discharge containing a He-Ne mixture*. Physical Review Letters **6**(3), 106 (1961).

[76] A. White and J. Rigden. *Continuous gas maser operation in visible*. Proceedings of the Institute of Radio Engineers **50**(7), 1697 (1962).

[77] W. Zinth, A. Laubereau, and W. Kaiser. *The long journey to the laser and its rapid development after 1960*. The European Physical Journal H **36**(2), 153 (2011).

[78] B. Zhdanov and R. Knize. *Diode-pumped 10 W continuous wave cesium laser*. Optics Letters **32**(15), 2167 (2007).

[79] W. Krupke, R. Beach, V. Kanz, and S. Payne. *Resonance transition 795-nm rubidium laser*. Optics Letters **28**(23), 2336 (2003).

[80] D. Nelson and W. Boyle. *A continuously operating ruby optical maser*. Applied Optics **1**(101), 99 (1962).

[81] K. Nakahara, M. Kondow, T. Kitatani, M. Larson, and K. Uomi. *1.3-μm continuous-wave lasing operation in GaInNAs quantum-well lasers*. Photonics Technology Letters **10**(4), 487 (1998).

[82] A. Ferguson and M. Dunn. *A tunable, frequency-doubled, continuous-wave dye laser using ADA*. Optics Communications **23**(2), 177 (1977).

[83] L. Siegman. *Lasers*, chap. 3 Electric-dipole transition in real atoms, pp. 118–175 (University Science Books, Mill Valley, CA, 1986).

[84] B. Saleh and M. Teich. *Grundlagen der Photonik*, chap. 13 Photonen und Atome, pp. 571–634 (Wiley-Vch, Weinheim, 2008).

[85] J. Eichler and H. Eichler. *Laser - Bauformen, Strahlführung, Anwendungen*, chap. 18 Frequenzselektion und -abstimmung, pp. 333–343 (Springer, Berlin, 2006), 6 ed.

[86] A. Schawlow and C. Townes. *Infrared and optical masers*. Physical Review **112**(6), 1940 (1958).

[87] M. Lax. *Classical noise. v. noise in self-sustained oscillators*. Physical Review **160**(2), 290 (1967).

[88] R. Paschotta, H. Telle, and U. Keller. *Noise of solid state lasers*. Solid-State Lasers and Applications **7**, 473 (2007).

[89] P. A. Franken, A. E. Hill, C. W. Peters, and G. Weinreich. *Generation of optical harmonics*. Physical Review Letters **7**, 118 (1961).

[90] S. Haroche. *Essay: Fifty years of atomic, molecular and optical physics in physical review letters*. Physical Review Letters **101**, 160001 (2008).

[91] H. Heard. *Ultra-violet gas laser at room temperature*. Nature **200**, 667 (1963).

[92] N. Basov, V. Danilychev, Y. Popov, and D. Khodkevich. *Laser operating in the vacuum region of the spectrum by excitation of liquid xenon with an electron beam*. Soviet Journal of Experimental and Theoretical Physics Letters **12**(10), 329 (1970).

[93] F. Houtermans. *Über Massen-Wirkung im Optischen Spektralgebiet und die Möglichkeit Absolut Negativer Absorption für einige Fälle von Molekülspektren (Licht-Lawine)*. Helvetica Physica Acta **33**, 933 (1960).

[94] D. Basting, K. Pippert, and U. Stamm. *History and future prospects of excimer laser technology*. Riken Review pp. 14–22 (2002).

[95] J. Eichler and H. Eichler. *Laser - Bauformen, Strahlführung, Anwendungen*, chap. UV-Moleküllaser (Springer, Berlin, 2006), 6 ed.

[96] K. Jain, C. Willson, and B. Lin. *Ultrafast deep UV lithography with excimer lasers*. Electron Device Letters, IEEE **3**(3), 53 (1982).

[97] L. Elias, W. Heaps, and W. Yen. *Excitation of UV fluorescence in LaF_3 doped with trivalent cerium and praseodymium*. Physical Review B **8**(11), 4989 (1973).

[98] D. Ehrlich, P. Moulton, and R. Osgood Jr. *Ultraviolet solid-state Ce:YLF laser at 325 nm*. Optics Letters **4**(6), 184 (1979).

[99] D. Ehrlich, P. Moulton, and R. Osgood Jr. *Optically pumped Ce:LaF$_3$ laser at 286 nm*. Optics Letters **5**(8), 339 (1980).

[100] D. Coutts and A. McGonigle. *Cerium-doped fluoride lasers*. Quantum Electronics, IEEE Journal of **40**(10), 1430 (2004).

[101] M. Dubinskii, V. Semashko, A. Naumov, R. Abdulsabirov, and S. Korableva. *Spectroscopy of a new active medium of a solid-state UV laser with broadband single-pass gain*. Laser Physics **3**, 216 (1993).

[102] M. Dubinskii, R. Abdulsabirov, S. Korableva, A. Naumov, and V. Semashko. *A new active medium for a tunable solid-state UV laser with an excimer pump*. Laser Physics **4**, 480 (1994).

[103] C. Marshall, J. Speth, S. Payne, W. Krupke, G. Quarles, V. Castillo, and B. Chai. *Ultraviolet laser emission properties of Ce^{3+}-doped LiSrAlF$_6$ and LiCaAlF$_6$*. Journal of the Optical Society of America, Part B: Optical Physics **11**(10), 2054 (1994).

[104] L. Ziegler, J. Morais, Y. Zhou, S. Constantine, M. Reed, M. Steiner-Shepard, and D. Lommel. *Tunable 50-fs pulse generation in the 250-310-nm ultraviolet range*. Quantum Electronics, IEEE Journal of **34**(9), 1758 (1998).

[105] K. Kosma, S. Trushin, W. Schmid, and W. Fuß. *Vacuum ultraviolet pulses of 11 fs from fifth-harmonic generation of a Ti:sapphire laser*. Optics Letters **33**(7), 723 (2008).

[106] M. Ghotbi, A. Esteban-Martin, and M. Ebrahim-Zadeh. *Tunable, high-repetition-rate, femtosecond pulse generation in the ultraviolet*. Optics Letters **33**(4), 345 (2008).

[107] C. Durfee III, S. Backus, H. Kapteyn, and M. Murnane. *Intense 8-fs pulse generation in the deep ultraviolet*. Optics Letters **24**(10), 697 (1999).

[108] T. Fuji, T. Horio, and T. Suzuki. *Generation of 12 fs deep-ultraviolet pulses by four-wave mixing through filamentation in neon gas*. Optics Letters **32**(17), 2481 (2007).

[109] N. Aközbek, A. Iwasaki, A. Becker, M. Scalora, S. Chin, and C. Bowden. *Third-harmonic generation and self-channeling in air using high-power femtosecond laser pulses*. Physical Review Letters **89**(14), 143901 (2002).

[110] S. Trushin, K. Kosma, W. Fuß, and W. Schmid. *Sub-10-fs supercontinuum radiation generated by filamentation of few-cycle 800 nm pulses in argon*. Optics Letters **32**(16), 2432 (2007).

[111] P. Baum, S. Lochbrunner, and E. Riedle. *Tunable sub-10-fs ultraviolet pulses generated by achromatic frequency doubling*. Optics Letters **29**(14), 1686 (2004).

[112] U. Graf, M. Fieß, M. Schultze, R. Kienberger, F. Krausz, and E. Goulielmakis. *Intense few-cycle light pulses in the deep ultraviolet*. Optics Express **16**(23), 18956 (2008).

[113] S. Ono, Y. Suzuki, T. Kozeki, H. Murakami, H. Ohtake, N. Sarukura, H. Sato, S. Machida, K. Shimamura, and T. Fukuda. *High-energy, all-solid-state, ultraviolet laser power-amplifier module design and its output-energy scaling principle*. Applied Optics **41**(36), 7556 (2002).

[114] Y. Zhang, R. Hoshi, D. Yamaguchi, Y. Okada-Shudo, M. Watanabe, M. Hyodo, Y. Zhu, X. Wang, Y. Zhu, G. Wang, C. Chenc, T. Kanaid, and S. Watanabee. *Generation of quasi-cw deep ultraviolet light below 200nm by an external cavity with a Brewster-input KBBF prism coupling device*. Optics Communications **295**, 176 (2013).

[115] Y. Kaneda, J. Yarborough, L. Li, N. Peyghambarian, L. Fan, C. Hessenius, M. Fallahi, J. Hader, J. Moloney, Y. Honda, M. Nishioka, Y. Shimizu, K. Miyazino, H. Shimatani, M. Yoshimura, Y. Mori, Y. Kitaoka, and T. Sasaki. *Continuous-wave all-solid-state 244 nm deep-ultraviolet laser source by fourth-harmonic generation of an optically pumped semiconductor laser using $CsLiB_6O_{10}$ in an external resonator*. Optics Letters **33**(15), 1705 (2008).

[116] A. Richter, N. Pavel, E. Heumann, G. Huber, D. Parisi, A. Toncelli, M. Tonelli, A. Diening, and W. Seelert. *Continuous-wave ultraviolet generation at 320 nm by intracavity frequency doubling of red-emitting praseodymium lasers*. Optics Express **14**(8), 3282 (2006).

[117] J. Kim and D. Meschede. *Continuous-wave coherent ultraviolet source at 326 nm based on frequency trippling of fiber amplifiers*. Optics Express **16**(14), 10803 (2008).

[118] K. Devi, S. Kumar, and M. Ebrahim-Zadeh. *Tunable, continuous-wave, ultraviolet source based on intracavity sum-frequency-generation in an optical parametric oscillator using BiB_3O_6*. Optics Express **21**(21), 24829 (2013).

[119] C. Wagstaff and M. Dunn. *A second-harmonic, ring dye laser for the generation of continuous-wave, single-frequency UV radiation*. Journal of Physics D: Applied Physics **12**(3), 355 (1979).

[120] M. Weber. *Nonradiative decay from 5d states of rare earths in crystals*. Solid State Communications **12**(7), 741 (1973).

[121] B. Henderson and R. Bartram. *Crystal-Field Engineering of Solid-State Laser Materials*, vol. 25 (Cambridge University Press, 2005), digitally printed first paperback version ed.

[122] N. Sarukura, M. Dubinskii, Z. Liu, V. Semashko, A. Naumov, S. Korableva, R. Abdulsabirov, K. Edamatsu, Y. Suzuki, T. Itoh, and Y. Segawa. *Ce^{3+}-activated fluoride crystals as prospective active media for widely tunable ultraviolet ultrafast lasers with direct 10-ns pumping*. Selected Topics in Quantum Electronics, IEEE Journal of **1**(3), 792 (1995).

[123] M. Dubinskii, V. Semashko, A. Naumov, R. Abdulsabirov, and S. Korableva. *Ce^{3+}-doped colquiriite: A new concept of all-solid-state tunable ultraviolet laser*. Journal of Modern Optics **40**(1), 1 (1993).

[124] Z. Liu, N. Sarukura, M. Dubinskii, V. Semashko, A. Naumov, S. Korableva, and R. Abdulsabirov. *Tunable ultraviolet short-pulse generation from a Ce:LiCAF laser amplifier system and its sum-frequency mixing with an Nd:YAG laser*. Japanese Journal of Applied Physics **37**, L36 (1998).

[125] J. Pinto, L. Esterowitz, and T. Carrig. *Extended wavelength coverage of a Ce^{3+}:LiCAF laser between 223 and 243 nm by sum frequency mixing in β-barium borate*. Applied Optics **37**(6), 1060 (1998).

[126] A. Petersen, C. Marshall, and G. Quarles. *High-repetition-rate Ce:LiCAF tunable UV laser*. In *CLEO '96., Summaries of papers presented at the Conference on Lasers and Electro-Optics*, p. CTuJ1 (The Optical Society of America, Anaheim, CA, USA, 1996).

[127] M. Dubinskii, K. Schepler, R. Abdulsabirov, and S. Korableva. *Tunable UV Ce:LiCAF injection-seeded laser for high spectral brightness applications*. Advanced Solid State Lasers - UV Laser Sources **UL2**, 6 (1998).

[128] Z. Liu, N. Sarukura, M. Dubinskii, R. Abdulsabirov, and S. Korableva. *All-solid-state subnanosecond tunable ultraviolet laser sources based on Ce^{3+}-activated fluoride crystals*. Journal of Nonlinear Optical Physics and Materials **8**, 41 (1999).

[129] Z. Liu, T. Kozeki, Y. Suzuki, N. Sarukura, K. Shimamura, T. Fukuda, M. Hirano, and H. Hosono. *Chirped-pulse amplification of ultraviolet femtosecond pulses by use of $Ce^{3+}:LiCaAlF_6$ as a broadband, solid-state gain medium.* Optics Letters **26**(5), 301 (2001).

[130] A. McGonigle, D. Coutts, and C. Webb. *530-mW 7-kHz cerium LiCAF laser pumped by the sum-frequency-mixed output of a copper-vapor laser*. Optics Letters **24**(4), 232 (1999).

[131] D. Spence, H. Liu, and D. Coutts. *Low-threshold miniature Ce:LiCAF lasers*. Optics Communications **262**(2), 238 (2006).

[132] Z. Liu, K. Shimamura, T. Fukuda, T. Kozeki, Y. Suzuki, and N. Sarukura. *High-energy pulse generation from solid-state ultraviolet lasers using large Ce: fluoride crystals*. Optical Materials **19**(1), 123 (2002).

[133] V. Fromzel and C. Prasad. *A tunable, narrow linewidth, 1kHz Ce:LiCAF laser with 46% efficiency*. 2003 OSA Topical Meeting on Advanced Solid-State Photonics (ASSP) (Trends in Optics and Photonics Series) **83**, 203 (2003).

[134] T. Le, S. Schowalter, W. Rellergert, J. Jeet, G. Lin, N. Yu, and E. Hudson. *Low-threshold ultraviolet solid-state laser based on a Ce^{3+}: $LiCaAlF_6$ crystal resonator*. Optics Letters **37**(23), 4961 (2012).

[135] D. Alderighi, G. Toci, M. Vannini, D. Parisi, and M. Tonelli. *Experimental evaluation of the cw lasing threshold for a Ce:LiCaAlF$_6$ laser*. Optics Express **13**(19), 7256 (2005).

[136] S. Payne, L. Chase, H. Newkirk, L. Smith, and W. Krupke. *LiCaAlF$_6$:Cr^{3+}: A promising new solid-state laser material*. IEEE Journal of Quantum Electronics **24**(11), 2243 (1988).

[137] S. Rausch, T. Binhammer, A. Harth, J. Kim, R. Ell, F. Kärtner, and U. Morgner. *Controlled waveforms on the single-cycle scale from a femtosecond oscillator*. Optics Express **16**(13), 9739 (2008).

[138] T. Ukachi, R. Lane, W. Bosenberg, and C. Tang. *Measurements of noncritically phase-matched second-harmonic generation in a LiB$_3$O$_5$ crystal*. Applied Physics Letters **57**(10), 980 (1990).

[139] J. Huang, Y. Shen, C. Chen, and B. Wu. *Noncritically phase-matched second-harmonic generation and optical parametric amplification in a lithium triborate crystal*. Applied Physics Letters **58**(15), 1579 (1991).

[140] C. Chen, Y. Wu, A. Jiang, B. Wu, G. You, R. Li, and S. Lin. *New nonlinear-optical crystal: LiB$_3$O$_5$*. Journal of the Optical Society of America B **6**(4), 616 (1989).

[141] B. Wu, N. Chen, C. Chen, D. Deng, and Z. Xu. *Highly efficient ultraviolet generation at 355 nm in LiB$_3$O$_5$*. Optics Letters **14**(19), 1080 (1989).

[142] T. Kojima, S. Konno, S. Fujikawa, K. Yasui, K. Yoshizawa, Y. Mori, T. Sasaki, M. Tanaka, and Y. Okada. *20-W ultraviolet-beam generation by fourth-harmonic generation of an all-solid-state laser*. Optics Letters **25**(1), 58 (2000).

[143] J. Sakuma, Y. Asakawa, and M. Obara. *Generation of 5-W deep-UV continuous-wave radiation at 266nm by an external cavity with a CsLiB$_6$O$_{10}$ crystal*. Optics Letters **29**(1), 92 (2004).

[144] S. Tidwell, J. Seamans, D. Lowenthal, G. Matone, and G. Giordano. *Efficient high-power UV generation by use of a resonant ring driven by a cw mode-locked IR laser*. Optics Letters **18**(18), 1517 (1993).

[145] M. Oka, L. Liu, W. Wiechmann, N. Eguchi, and S. Kubota. *All solid-state continuous-wave frequency-quadrupled Nd:YAG laser*. IEEE Journal of Selected Topics in Quantum Electronics **1**(3), 859 (1995).

[146] H. Kogelnik, E. Ippen, A. Dienes, and C. Shank. *Astigmatically compensated cavities for cw dye lasers*. IEEE Journal of Quantum Electronics **QE-8**, 373 (1972).

[147] R. Jacobs, W. Krupke, and M. Weber. *Measurement of excited-state-absorption loss for Ce^{3+} in $Y_3Al_5O_{12}$ and implications for tunable $5d \rightarrow 4f$ rare-earth lasers*. Applied Physics Letters **33**(5), 410 (1978).

[148] W. Miniscalco, J. Pellegrino, and W. Yen. *Measurements of excited-state absorption in Ce^{3+}: YAG*. Journal of Applied Physics **49**(12), 6109 (1978).

[149] C. Pedrini, F. Rogemond, and D. McClure. *Photoionization thresholds of rare-earth impurity ions. Eu^{2+}:CaF_2, Ce^{3+}:YAG, and Sm^{2+}:CaF_2*. Journal of Applied Physics **59**(4), 1196 (1986).

[150] D. Hamilton, S. Gayen, G. Pogatshnik, R. Ghen, and W. Miniscalco. *Optical-absorption and photoionization measurements from the excited states of Ce^{3+}: $Y_3Al_5O_{12}$*. Physical Review B **39**(13), 8807 (1989).

[151] J. Lawson and S. Payne. *Excited-state absorption spectra and gain measurements of CaF_2:Sm^{2+}*. Journal of the Optical Society of America B **8**(7), 1404 (1991).

[152] J. Owen, P. Dorain, and T. Kobayasi. *Excited-state absorption in Eu^{2+}:CaF_2 and Ce^{3+}:YAG single crystals at 298 and 77 K*. Journal of Applied Physics **52**(3), 1216 (1981).

[153] J. Lawson and S. Payne. *Excited-state absorption of Eu^{2+}-doped materials*. Physical Review B **47**(21), 14003 (1993).

[154] B. Wellmann, D. J. Spence, and D. W. Coutts. *Tunable continuous-wave deep-ultraviolet laser based on Ce: LiCAF*. Optics Letters **39**(5), 1306 (2014).

[155] J. Farey. *LXXIX. On a curious property of vulgar fractions*. Philosophical Magazine Series 1 **47**(217), 385 (1816).

[156] J. Zheng, U. Sen, D. Benenson, and H. Kwok. *Observation of periodicity multiplication in a synchronously pumped dye laser*. Optics Letters **11**(10), 632 (1986).

[157] N. Onodera, A. Lowery, L. Zhai, Z. Ahmed, and R. Tucker. *Frequency multiplication in actively mode-locked semiconductor lasers*. Applied Physics Letters **62**(12), 1329 (1993).

[158] J. Jiang and T. Hasama. *Synchronously pumped femtosecond optical parametric oscillator based on an improved pumping concept*. Optics Communications **220**(1), 193 (2003).

[159] A. Zavadilová, V. Kubeček, and J. Šulc. *Pulse repetition rate multiplication in an intracavity synchronously pumped ring optical parametrical oscillator*. Laser Physics Letters **10**(11), 115401 (2013).

[160] L. Zhan, Z. Gu, J. Zhang, and Y. Xia. *Critical behavior of a passively mode-locked laser: Rational harmonic mode locking*. Optics Letters **32**(16), 2276 (2007).

[161] J. Lee and J. Lee. *Experimental investigation of the cavity modulation frequency detuning effect in an active harmonically mode-locked fiber laser*. Journal of the Optical Society of America B **30**(6), 1479 (2013).

[162] M. Shikatani and M. Izutsu. *A study of a higher order fm mode-locking laser with double phase modulators*. Electronics and Communications in Japan (Part II: Electronics) **86**(3), 1 (2003).

[163] H. Lee, K. Kim, and H. Kim. *Pulse-amplitude equalization of rational harmonic mode-locked fiber laser using a semiconductor optical amplifier loop mirror*. Optics Communications **160**(1), 51 (1999).

[164] Y. Shiquan, L. Zhaohui, Z. Chunliu, D. Xiaoyi, Y. Shuzhong, K. Guiyun, and Z. Qida. *Pulse-amplitude equalization in a rational harmonic mode-locked fiber ring laser by using modulator as both mode locker and equalizer*. Photonics Technology Letters, IEEE **15**(3), 389 (2003).

[165] L. Zhan, P. Wang, Z. Gu, S. Luo, and Y. Xia. *Amplitude-equalized high-order arbitrary numerator rational harmonic mode-locked pulse generation in fiber-ring lasers using nonlinear polarization rotation*. Optics Express **13**(3), 836 (2005).

[166] L. Krainer, R. Paschotta, S. Lecomte, M. Moser, K. Weingarten, and U. Keller. *Compact Nd:YVO$_4$ lasers with pulse repetition rates up to 160 GHz.* Quantum Electronics, IEEE Journal of **38**(10), 1331 (2002).

[167] P. Sorokin and J. Lankard. *Stimulated emission observed from an organic dye, chloro-aluminum phthalocyanine*. IBM Journal of Research and Development **10**(2), 162 (1966).

[168] F. Schäfer, W. Schmidt, and J. Volze. *Organic dye solution laser*. Applied Physics Letters **9**(8), 306 (1966).

[169] F. Duarte, P. Kelley, L. Hillman, and P. Liao. *Dye Laser Principles* (Academic Press, 1990).

[170] T. Hänsch. *Repetitively pulsed tunable dye laser for high resolution spectroscopy*. Applied Optics **11**(4), 895 (1972).

[171] I. Shoshan, N. Danon, and U. Oppenheim. *Narrowband operation of a pulsed dye laser without intracavity beam expansion*. Journal of Applied Physics **48**(11), 4495 (1977).

[172] O. Peterson, S. Tuccio, and B. Snavely. *CW operation of an organic dye solution laser*. Applied Physics Letters **17**(6), 245 (1970).

[173] F. Duarte. *Tunable Laser Optics* (CRC Press, 2015).

[174] B. Lyot. *Optical apparatus with wide field using interference of polarized light*. CR Academic Science (Paris) **197**, 1593 (1933).

[175] D. R. Preuss and J. Gole. *Three-stage birefringent filter tuning smoothly over the visible region: Theoretical treatment and experimental design*. Applied Optics **19**(5), 702 (1980).

[176] P. Hlubina and D. Ciprian. *Birefringence dispersion in a quartz crystal retrieved from a channeled spectrum resolved by a fiber-optic spectrometer*. Optics Communications **284**(12), 2683 (2011).

[177] M. Frolov, N. Manakov, and A. Starace. *Wavelength scaling of high-harmonic yield: Threshold phenomena and bound state symmetry dependence*. Physical Review Letters **100**(17), 173001 (2008).

[178] I. Mori, Y.and Kuroda, S. Nakajima, T. Sasaki, and S. Nakai. *New nonlinear optical crystal: cesium lithium borate*. Applied Physics Letters **67**(13), 1818 (1995).

[179] R. Bhandari, T. Taira, A. Miyamoto, Y. Furukawa, and T. Tago. *> 3 MW peak power at 266 nm using Nd: YAG/Cr 4+: YAG microchip laser and fluxless-BBO*. Optical Materials Express **2**(7), 907 (2012).

[180] Y. Wu, P. Fu, J. Wang, Z. Xu, L. Zhang, Y. Kong, and C. Chen. *Characterization of CsB_3O_5 crystal for ultraviolet generation*. Optics Letters **22**(24), 1840 (1997).

[181] M. Kitazawa, R. Higuchi, M. Takahashi, T. Wada, and H. Sasabe. *Ultraviolet generation at 266 nm in a novel organic nonlinear optical crystal: l-pyrrolidone-2-carboxylic acid*. Applied Physics Letters **64**(19), 2477 (1994).

[182] D. Nikitin, O. Byalkovskiy, O. Vershinin, V. Tyrtyshnyy, and B. Davydov. *Sum frequency generation of UV laser radiation at 266 nm in LBO crystal*. In *Laser Optics, 2014 International Conference*, pp. 1–1 (IEEE, 2014).

[183] B. Köhler, A. Nebel, and R. Wallenstein. *266 nm pumped cw mode-locked $CsLiB_6O_{10}$ (CLBO)-OPO tunable in the blue and red spectral range*. In *Conference on Lasers and Electro-Optics*, p. CMG1 (Optical Society of America, 1999).

[184] G. Wang, A. Geng, H. Bo, Y.and Li, Z. Sun, Y. Bi, D. Cui, Z. Xu, X. Yuan, and X. Wang. *28.4 W 266nm ultraviolet-beam generation by fourth-harmonic generation of an all-solid-state laser*. Optics Communications **259**(2), 820 (2006).

[185] M. Yoshimura, Y. Oeki, Y. Takahashi, H. Adachi, and Y. Mori. *Ultraviolet laser-induced degradation of $CsLiB_6O_{10}$*. In *Advanced Solid State Lasers*, pp. AM5A–11 (Optical Society of America, 2015).

[186] R. Stolen and A. Ashkin. *Optical Kerr effect in glass waveguide*. Applied Physics Letters **22**(6), 294 (1973).

[187] P. Wagenblast, U. Morgner, F. Grawert, T. Schibli, F. Kärtner, V. Scheuer, G. Angelow, and M. Lederer. *Generation of sub-10-fs pulses from a Kerr-lens mode-locked Cr^{3+}: LiCAF laser oscillator by use of third-order dispersion-compensating double-chirped mirrors*. Optics Letters **27**(19), 1726 (2002).

[188] A. Major, F. Yoshino, I. Nikolakakos, J. Aitchison, and P. Smith. *Dispersion of the nonlinear refractive index in sapphire*. Optics Letters **29**(6), 602 (2004).

[189] P. Wagenblast. *Ultrashort Pulse Generation in Kerr-lens Mode Locked Colquiriite Lasers* (Cuvillier Verlag, 2004).

[190] W. Koechner. *Solid-State Laser Engineering*, vol. 1 (Springer Verlag, 2006).

[191] S. Yefet and A. Pe'er. *A review of cavity design for Kerr lens mode-locked solid-state lasers*. Applied Sciences **3**(4), 694 (2013).

[192] V. Pervak, O. Razskazovskaya, I. Angelov, K. Vodopyanov, and M. Trubetskov. *Dispersive mirror technology for ultrafast lasers in the range 220–4500 nm*. Advanced Optical Technologies **3**(1), 55 (2014).

[193] C. Rivera, S. Bradforth, and G. Tempea. *Gires-Tournois interferometer type negative dispersion mirrors for deep ultraviolet pulse compression*. Optics Express **18**(18), 18615 (2010).

[194] A.-S. Morlens, P. Balcou, P. Zeitoun, C. Valentin, V. Laude, and S. Kazamias. *Compression of attosecond harmonic pulses by extreme-ultraviolet chirped mirrors*. Optics Letters **30**(12), 1554 (2005).

[195] A. Wonisch, U. Neuhäusler, N. Kabachnik, T. Uphues, M. Uiberacker, V. Yakovlev, F. Krausz, M. Drescher, U. Kleineberg, and U. Heinzmann. *Design, fabrication, and analysis of chirped multilayer mirrors for reflection of extreme-ultraviolet attosecond pulses*. Applied Optics **45**(17), 4147 (2006).

[196] M. Suman, G. Monaco, M.-G. Pelizzo, D. Windt, and P. Nicolosi. *Realization and characterization of an XUV multilayer coating for attosecond pulses*. Optics Express **17**(10), 7922 (2009).

[197] M. Hofstetter, M. Schultze, M. Fieß, B. Dennhardt, A. Guggenmos, J. Gagnon, V. Yakovlev, E. Goulielmakis, R. Kienberger, and E. Gullikson. *Attosecond dispersion control by extreme ultraviolet multilayer mirrors*. Optics Express **19**(3), 1767 (2011).

[198] V. Pervak, F. Krausz, and A. Apolonski. *Dispersion control over the ultraviolet-visible-near-infrared spectral range with HfO_2/SiO_2-chirped dielectric multilayers*. Optics Letters **32**(9), 1183 (2007).

[199] O. Razskazovsaya, M. Hassan, E. Goulielmakis, F. Krausz, and V. Pervak. *HfO_2/SiO_2 chirped multilayer mirrors for broadband dispersion management in the ultraviolet spectral range*. Dig. XVIII International Conference on Ultrafast Phenomena **36B**, THU.PIII.17 (2012).

[200] M. Nisoli, S. De Silvestri, and O. Svelto. *Generation of high energy 10 fs pulses by a new pulse compression technique*. Applied Physics Letters **68**(20), 2793 (1996).

[201] R. Fork, O. Martinez, and J. Gordon. *Negative dispersion using pairs of prisms*. Optics Letters **9**(5), 150 (1984).

[202] E. Treacy. *Optical pulse compression with diffraction gratings*. Quantum Electronics, IEEE Journal of **5**(9), 454 (1969).

[203] O. Martinez, J. Gordon, and R. Fork. *Negative group-velocity dispersion using refraction*. Journal of the Optical Society of America A **1**(10), 1003 (1984).

[204] H. Winful. *Pulse compression in optical fiber filters*. Applied Physics Letters **46**(6), 527 (1985).

[205] M. Zavelani-Rossi, G. Cerullo, S. De Silvestri, L. Gallmann, N. Matuschek, G. Steinmeyer, U. Keller, G. Angelow, V. Scheuer, and T. Tschudi. *Pulse compression over a 170-THz bandwidth in the visible by use of only chirped mirrors*. Optics Letters **26**(15), 1155 (2001).

[206] N. Broderick, D. Taverner, D. Richardson, M. Ibsen, and R. Laming. *Optical pulse compression in fiber Bragg gratings*. Physical Review Letters **79**(23), 4566 (1997).

[207] W. Tomlinson, R. Stolen, and C. Shank. *Compression of optical pulses chirped by self-phase modulation in fibers*. Journal of the Optical Society of America B **1**(2), 139 (1984).